

AD-786 467

SUPERSONIC JET EXHAUST NOISE INVESTIGATION

Paul R. Knott

General Electric Company

Prepared for:

Air Force Aero Propulsion Laboratory

June 1974

DISTRIBUTED BY:

NTIS

**National Technical Information Service
U. S. DEPARTMENT OF COMMERCE
5285 Port Royal Road, Springfield Va. 22151**

NOTICE

When Government drawings, specifications, or other data are used for any purpose other than in connection with a definitely related Government procurement operation, the United States Government thereby incurs no responsibility nor any obligation whatsoever; and the fact that the government may have formulated, furnished, or in any way supplied the said drawings, specifications, or other data, is not to be regarded by implication or otherwise as in any manner licensing the holder or any other person or corporation, or conveying any rights or permission to manufacture, use, or sell any patented invention that may in any way be related thereto.

NOTIS
BY

A

Copies of this report should not be returned unless return is required by security considerations, contractual obligations, or notice on a specific document.

16

AD - 786 467

REPORT DOCUMENTATION PAGE		READ INSTRUCTIONS BEFORE COMPLETING FORM
1 REPORT NUMBER AFADL-TR-74-25	2 GOVT ACCESSION NO	3 RECIPIENT'S CATALOG NUMBER
4 TITLE (and Subtitle) SUPERSONIC JET EXHAUST NOISE - PROGRESS REPORT		5 TYPE OF REPORT & PERIOD COVERED Interim Report (December 72 through December 73)
		6 PERFORMING ORG. REPORT NUMBER
7 AUTHOR(s) Paul R. Knott		8 CONTRACT OR GRANT NUMBER(s) F33615-73-C-2031
9 PERFORMING ORGANIZATION NAME AND ADDRESS General Electric Company Evendale, Ohio		10 PROGRAM ELEMENT, PROJECT, TASK AREA & WORK UNIT NUMBERS Project No. 3066 Task 14 Work Unit 07
11 CONTROLLING OFFICE NAME AND ADDRESS		12 REPORT DATE June 1974
		13 NUMBER OF PAGES 282
14 MONITORING AGENCY NAME & ADDRESS (if different from Controlling Office) Air Force Aero Propulsion Laboratory Wright-Patterson AFB, Ohio		15 SECURITY CLASS. (of this report) Unclassified
		15a DECLASSIFICATION/DOWNGRADING SCHEDULE
16 DISTRIBUTION STATEMENT (of this Report) Approved for Public Release; Distribution Unlimited		
17 DISTRIBUTION STATEMENT (of the abstract entered in Block 20, if different from Report)		
18 SUPPLEMENTARY NOTES NATIONAL TECHNICAL INFORMATION SERVICE Springfield, VA 22161		
19 KEY WORDS (Continue on reverse side if necessary and identify by block number) Acoustics, Turbulence, Jet Noise, Laser Doppler Velocimeter, Supersonic Jets		
20 ABSTRACT (Continue on reverse side if necessary and identify by block number) This progress report summarizes the major theoretical and experimental efforts performed during the first year of a two-year program sponsored by the Air Force and the Department of Transportation on Supersonic Jet Exhaust Noise. The overall objective of the program is to develop the technology to significantly reduce supersonic aircraft propulsion system noise with minimum associated performance and weight penalties. To reach the objectives of this program a varied and comprehensive research program is being carried out to		

Unclassified

SECURITY CLASSIFICATION OF THIS PAGE(When Data Entered)

Block No. 20 (Continued)

develop the basic theory and experimental methods for understanding and quantizing the acoustic characteristics of simple supersonic jets for a range of velocities and temperatures typical of present and future military and commercial supersonic aircraft propulsion systems. A comprehensive aero-acoustic model, relating the local fluid dynamic properties of the jet to the jet acoustic nature, is being developed. Major advances in the development of a Laser Velocimeter to measure turbulence spectra in a high temperature high velocity jet are presented. Detailed discussion and results are also presented on the evaluation of in-jet static pressure fluctuation probes for source location in high velocity jets.

Unclassified

SECURITY CLASSIFICATION OF THIS PAGE(When Data Entered)

19

SUPERSONIC JET EXHAUST NOISE INVESTIGATION

P. R. KNOTT

TECHNICAL REPORT AFAPL-TR-74-25

JUNE 1974

APPROVED FOR PUBLIC RELEASE;
DISTRIBUTION UNLIMITED

1.c

FOREWORD

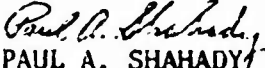
This interim report was prepared by the Advanced Engineering and Technology Programs Department, Aircraft Engine Group of the General Electric Company, Evendale, Ohio under the joint sponsorship of the Air Force Aero Propulsion Laboratory, Wright-Patterson Air Force Base, Ohio and the Department of Transportation, Washington, D. C. under Contract F33615-73-C-2031. The inclusive dates of this interim program activity were December 1972 through December 1973. The work described is part of a program to define and control the noise emission of aircraft propulsion systems.

Mr. Paul A. Shahady of the Air Force Aero Propulsion Laboratory (AFAPL/TBC) was the Project Engineer. The program is being conducted under Project 3066, Task 14.

The principal technical contributors to this report are: R. Mani, C. Merkle, P. Scott, P. Mossey, R. Kantola, K. R. Bilwakesh, J. Wang, J. F. Brausch, H. S. Ribner and S. P. Pao.

This document covers interim results of theoretical and experimental investigations necessary to reveal the basic mechanisms of supersonic exhaust noise typical of present and future military and commercial supersonic aircraft propulsion systems. The program was conducted by the General Electric Company under the direction of Dr. Paul R. Knott. The report was submitted by the author(s) on 15 February 1974.

Publication of this report does not constitute Air Force approval of the report's findings or conclusions. It is published only for the exchange and stimulation of ideas.


PAUL A. SHAHADY
Project Engineer

FOR THE COMMANDER


ERNEST C. SIMPSON
Director, Turbine Engine Division

ABSTRACT

This interim report summarizes the major theoretical and experimental task efforts performed at General Electric during the first year of a two year follow-on program sponsored jointly by the Air Force and the Department of Transportation on Supersonic Jet Exhaust Noise. The overall objective of the Program is to develop the technology to significantly reduce supersonic aircraft propulsion system noise with minimum associated performance and weight penalties. To reach the objectives of this program a varied and comprehensive research program is being carried out to develop the basic theory and experimental methods for understanding and quantizing the acoustic characteristics of simple supersonic jets for a range of velocities and temperatures typical of present and future military and commercial supersonic aircraft propulsion systems. A comprehensive aero-acoustic model, which had its origin in the first phase of effort, relating the local fluid dynamic properties of the jet to the jet acoustic nature is continuing in its development. The main thrust in the development of this aero-acoustic model has been 1) to refine the calculation of the aerodynamic input by including the effects of shock waves on heated jet flow properties, and 2) to more clearly delineate the acoustic model to account for heretofore paradoxical jet acoustic observations. It is shown that the shock structure and turbulent fluid dynamic properties for a heated supersonic exhaust jet can be accurately predicted. Further, comprehensive analyses are presented which explicitly account for the non-classical density dependence of jet noise, the influence of mean flow on the real radiative efficiency of moving sources and some fundamental theoretical questions regarding the interplay between convection and refraction in jet acoustic propagation. Preliminary results of parametric far-field and near-field acoustic experiments are presented. Results are displayed in such a way as to illustrate many of the salient features of the velocity, density and spectral dependency of heated supersonic jets. Major advances in developing General Electric's Laser Velocimeter for performing turbulence spectra measurements in heated high velocity jets is discussed. Results are presented which clearly show General Electric's Laser Velocimeter to be a viable non-contact type probe capable of performing turbulence rms and spectra measurements in a heated high velocity jet, and to perform in-jet to far-field acoustic noise source location measurements. Detailed discussions and results are also presented on the evaluation of in-jet static pressure fluctuations probes source location in high velocity jets.

TABLE OF CONTENTS

	<u>Page</u>
<u>INTRODUCTION</u>	1
<u>Section</u>	
I. THEORETICAL DEVELOPMENTS OF THE AERODYNAMICS OF SUPERSONIC JETS.	5
1.0 Description of the Aerodynamic Model	6
2.0 Derivation of the Equations Used in the Inner Region	8
3.0 Calculation of the Turbulence Field.	11
4.0 Matching Between the Inner and Outer Solutions	13
5.0 Shock Reflection from Axis of Symmetry	14
6.0 Results for Shock Structure Computations	18
II. THEORETICAL ACOUSTIC MODEL OF TURBULENCE JETS	34
1.0 Moving Source Models for Jet Noise	34
1.1 First Model Problem	34
1.2 Asymmetric Line of Source Convection.	43
1.3 Effect of Finite Shear on Model Problem Studies in Section 1.1.	50
1.4 Jet Density Exponent Issue for Noise of Heated Subsonic Jets	54
1.5 Computed Results and Inferences	63
1.6 Directivity of Subsonic Jet Noise	65
2.0 Aerodynamic Noise Emission from Turbulent Shear Layers	79
2.1 The Effects of Jet Density on Sound Emission.	79
2.2 The Effects of Refraction and Convection.	83
2.3 Phillips-Pao Model for Detailed Predictions	85
3.0 The Question of Convection and Refraction Coupling in Jet Noise Turbulent Mixing Theories.	88
3.1 Does the Lighthill Equation account for Refrac- tion? Yes or no.	88
3.2 Separation of Convection and Refraction Effects by Use of Green's Function.	89
APPENDIX II-1	94

TABLE OF CONTENTS (Cont.)

<u>Section</u>	<u>Page</u>
III. EXPERIMENTAL INVESTIGATION OF HEATED SUPERSONIC JET ACOUSTIC CHARACTERISTICS.	129
1.0 Far-Field Acoustic Experiments	129
2.0 Near-Field Acoustic Experiments.	136
3.0 Photographic and Some Shock Noise Experiments.	138
IV. IN-JET NOISE SOURCE LOCATION STUDIES.	189
1.0 The Laser Velocimeter and Turbulence Spectra	189
1.1 Theoretical Analysis for Turbulent Spectra.	189
1.2 Method for Obtaining Spectra.	190
1.3 Error Analysis.	194
1.4 Experimental Set-Up Used for Laser Velocimeter Turbulent Spectra and RMS Turbulent Plume Surveys	197
1.5 Laser Velocimeter Turbulent Spectra Measure- ments	199
1.6 Laser Velocimeter Jet Plume Surveys	200
2.0 Static Pressure Probe Development for Jet Noise Source Correlation Studies	204
2.1 Theoretical Background.	204
2.2 Probe Selection	206
2.3 Experiments	209
2.4 In-Jet Correlations	215
APPENDIX IV-1	219
REFERENCES I-IV	260

LIST OF ILLUSTRATIONS

<u>Figure</u>		<u>Page</u>
1.	The Flowfield of an Inviscid Two-Dimensional Supersonic Jet	22
2.	The Flowfield of an Ideally Expanded Viscous Jet.	22
3.	Subdivision of the Jet into Inner and Outer Regions. Outer Region Shown Shaded	23
4.	Amplification of Turbulence by a Shock Wave as Predicted by Ribner's Shock-Turbulence Theory	24
5.	Outline of Complete Computational Procedure	25
6.	Mach Disk Model	26
7.	Predicted Shock Shape and Outer Boundary Shape-Inviscid	27
8.	Intersection of Shock With Axis of Symmetry	28
9.	Height of Mach Disk	29
10.	Shock Shape Prediction on Schlieren Photograph.	30
11.	Cross-Stream Variation of Predicted Total Pressure and Static Pressure for Ideally Expanded Jet. $M_{exit} = 1.60$, $P_{amb}/P_{Tref} = .242$	31
12.	Cross-Stream Variation of Predicted Total Pressure and Static Pressure for Slightly Underexpanded Jet, Showing Total Pressure Loss Due to Both Shocks and Mixing. $M_{exit} = 1.25$, $P_{amb}/P_{Tref} = .242$	31
13.	Cross-Stream Variation of Predicted Total Pressure and Static Pressure for Jet From Convergent Nozzle, Showing Total Pressure Loss Due to Both Shocks and Mixing. $M_{exit} = 1.0$, $P_{amb}/P_{Tref} = .242$	32
14.	Comparison Between Predicted Shock Shapes Using Inviscid Prediction Technique and Coupled (Inner-Out : Analysis) Viscous Technique. Shaded Region Represents Flow Which Is Significantly Affected by Mixing. $M_{exit} = 1.25$, $P_{amb}/P_{Tref} = .242$	32
15.	Comparison of the Theory Predicted Shock Structure and a Schlieren Photograph.	33
16.	First Model Problem	100
17.	Convective Amplification as a Function of M and k_{0a}	100
18.	Implications for Strouhal Scaling	100
19.	Peak Strouhal Number as a Function of Jet Mach Number	101

LIST OF ILLUSTRATIONS (Cont.)

<u>Figure</u>		<u>Page</u>
20.	Second Model Problem.	101
21.	Results of Second Model Problem	102
22.	Application to Ribner - Miles Problem	103
23.	Application to Problem of Reference 1	104
24.	Power Spectrum Prediction for a Freely Moving Source; $M_0 = 0.7$	105
25.	Power Spectrum Prediction for a Freely Moving Source; $M_j = 0.9$	106
26.	Third Model Problem	107
27.	η as a Function of $(St)_0$ for $M_0 = 0.5$	108
28.	η as a Function of $(St)_0$ for $M_0 = 0.7$	108
29.	η as a Function of $(St)_0$ for $M_0 = 0.9$	109
30.	Normalized Power Spectra.	109
31.	Jet Density Exponent.	109
32.	η as a Function of (w_{0a}/c_0) for Various M_0	110
33.	Schematic of a Moving Source.	111
34.	Schematic of Moving Source With Finite Lifetime	112
35.	Directivity Predictions for a Freely Moving Point Source; $M_j = .366$	113
36.	Directivity Predictions for a Freely Moving Point Source; $M_j = .57$	114
37.	Directivity Predictions for a Freely Moving Point Source; $M_j = .878$	115
38.	Directivity Predictions for a Freely Moving Point Source; $M_j = .366$	116
39.	Directivity Predictions for a Freely Moving Point Source; $M_j = .57$	117
40.	Directivity Predictions for a Freely Moving Point Source; $M_j = .878$	118
41.	Dependence of Sound Power on Jet Density Ratio.	119
42.	Theory-Data Comparison of Sound Power as a Function of Density Ratio and Exit Convection Mach Number	120
43.	The Density Ratio Power Index at Various Levels of M_j	121
44.	The Generalized Sound Power Correlation	122

LIST OF ILLUSTRATIONS (Cont.)

<u>Figure</u>		<u>Page</u>
45.	Directivity Pattern for a Typical Slice of Jet With $M_j = 1.0$	123
46.	Directivity for a Typical Slice of Jet With $M_j = 2.0$	124
47.	Effects of Attenuation and the Coupled Effects of Con- vection and Refraction, $M_j = 1.0$	125
48.	Effects of Attenuation and the Coupled Effects of Con- vection and Refraction, $M_j = 2.0$	126
49.	Comparison of Theoretical Results and Experimental Data	127
50.	Comparison of Theoretical Results and Experimental Data	128
51.	Sketch of Narrowband Directivity Due to Convection and Refraction.	92
52.	Acoustic Far-Field Measuring Stations	141
53.	Acoustic Near-Field Measuring Stations.	142
54.	4.3 Inch Throat Diameter Water-Cooled Parallel Flow Con- vergent/Divergent Nozzle.	143
55.	4.3 Inch Exit Diameter Water-Cooled Conical Convergent Nozzle.	144
56.	Theory-Data Comparison of Sound Power as a Function of Density Ratio and Exit Convection Mach Number	145
57.	Effect of Temperature on OAPWL.	146
58.	Effect of Jet Density on Peak OASPL	147
59.	Effect of Jet Density on Jet Noise at $\Theta = 90^\circ$	148
60.	Velocity Dependence of Overall Power Level.	149
61.	Velocity Dependence of 1/3 Octave Band SPL at Source Strouhal Numbers From 0.1 to 10.0	150
62.	Velocity Dependence of 1/3 Octave Band SPL at Source Strouhal Numbers From 0.1 to 10.0	151
63.	Velocity Dependence of 1/3 Octave Band SPL at Source Strouhal Numbers From 0.1 to 10.0	152
64.	Velocity Dependence of 1/3 Octave Band SPL at Source Strouhal Numbers From 0.1 to 10.0	153
65.	Velocity Dependence of 1/3 Octave Band SPL at Source Strouhal Numbers From 0.1 to 10.0	154
66.	Velocity Dependence of 1/3 Octave Band SPL at Source Strouhal Numbers From 0.1 to 10.0	155

LIST OF ILLUSTRATIONS (Cont.)

<u>Figure</u>		<u>Page</u>
67.	Velocity Dependence of 1/3 Octave Band SPL at Source Strouhal Numbers From 0.1 to 10.0	156
68.	Velocity Dependence of 1/3 Octave Band SPL at Source Strouhal Numbers From 0.1 to 10.0	157
69.	Effect of Jet Temperature on 1/3 Octave Band Directivity Pattern at a Constant Source Strouhal Number of 1.0 . . .	158
70.	Effect of Jet Temperature on 1/3 Octave Band Directivity Pattern at a Constant Source Strouhal Number of 1.0 . . .	159
71.	Effect of Jet Temperature on 1/3 Octave Band Directivity Pattern at a Constant Observed Strouhal Number of 1.0 . .	160
72.	Effect of Jet Temperature on 1/3 Octave Band Directivity Pattern at a Constant Observed Strouhal Number of 1.0 . .	161
73.	View of the Near-Field Microphone Array and Traversing Mechanism	162
74.	Close-Up View of the Near-Field Microphone Array.	163
75.	Microphone Array for Detailed Near-Field Acoustic Data. .	164
76.	Variation of OASPL With Axial Distance From Nozzle Exit Plane at Different Radial Locations. 4.31 Inch Diameter Conical Nozzle.	165
77.	Variation of OASPL With Axial Distance From Nozzle Exit Plane at Different Radial Locations. 4.31 Inch Diameter Conical Nozzle.	166
78.	Variation of OASPL With Axial Distance From Nozzle Exit Plane at Different Radial Locations. 4.31 Inch Diameter Conical Nozzle.	167
79.	Variation of OASPL With Axial Distance From Nozzle Exit Plane at Different Radial Locations. 4.31 Inch Throat Diameter C/D Nozzle	168
80.	Variation of OASPL With Axial Distance From Nozzle Exit Plane at Different Radial Locations. 4.31 Inch Throat Diameter C/D Nozzle	169
81.	Comparison of OASPL Versus X/D Profiles for Conical and C/D Nozzles. $M \approx 1.55$, $V_j = 2800$ fps, $T_g = 2000^\circ R$	170
82.	1/3 Octave Band Spectra From Conical and C/D Nozzles. . .	171
83.	Overall Sound Pressure Level Contours: 4.31 Inch Throat Diameter C/D Nozzle, $V_j = 3100$ fps, $T_T = 2400^\circ R$	172
84.	Simulated Setup for Schlieren System.	173

LIST OF ILLUSTRATIONS (Cont.)

<u>Figure</u>		<u>Page</u>
85.	JENOTS - Schlieren "Still" Photographic System.	174
86.	JENOTS - Schlieren "High Speed" Movie System.	175
87.	JENOTS - Schlieren Light Source Systems Setup for Still Flash Pictures.	176
88.	JENOTS - Schlieren Light Source Systems - Setup for High Speed Movies.	177
89.	Schlieren Photograph of Shock Free Nozzle at Exit Plane.	178
90.	Schlieren Photograph of Thin Lip Conic Nozzle at Exit Plane	179
91.	Schlieren Photograph of Thin Lip Conic Nozzle Downstream.	180
92.	Schlieren Photograph of Thick Lip Conic Nozzle at Exit Plane	181
93.	Schlieren Photograph of Thick Lip Conic Nozzle Down- stream.	182
94.	Spark Schlieren Photograph of Shock Free Nozzle at Exit Plane	183
95.	Spark Schlieren Photograph of Thin Lip Conic Nozzle at Exit Plane.	184
96.	Spark Schlieren Photograph of Thick Lip Conic Nozzle at Exit Plane.	185
97.	Far-Field Narrowband Spectra Comparison of C/D and Conical Thin and Thick Lip Nozzles. $\theta = 30^\circ$, $V_j = 2500$ fps, T_T $= 1400^\circ R$	186
98.	Far-Field Narrowband Spectra Comparison of C/D and Conical Thin and Thick Lip Nozzles. $\theta = 130^\circ$, $V_j = 2500$ fps, $T_T = 1400^\circ R$	187
99.	Far-Field Narrowband Spectra Comparison of C/D and Conical Thin and Thick Lip Nozzles. $\theta = 140^\circ$, $V_j = 2500$ fps, $T_T = 1400^\circ R$	188
100.	Sketch of Finite Width Time Grid for Bias Errors.	194
101.	Sketch of Frequency Domain for Error Analysis	196
102.	Laser Velocimeter Optics Package.	222
103.	Laser Velocimeter Setup at JENOTS	223
104.	Laser Velocimeter Estimated Autocorrelated Function and Inter-Particle Arrival Histogram.	224

LIST OF ILLUSTRATIONS (Cont.)

<u>Figure</u>		<u>Page</u>
105.	Velocity Histogram.	225
106.	Comparison of Laser Velocimeter and Hot Film Turbulence Spectra. $M_j = 0.5$, $X/D = 5$, $r/r_0 = 1$; 80 Hz Band Width .	226
107.	Autocorrelation Function.	227
108.	Velocity Histogram.	228
109.	Measured Laser Velocimeter Turbulent Spectrum for a Hot Sonic Jet: $M_j = 1.0$, $T_g = 1500^\circ R$, $X/D = 10$, $r/r_0 = 0$. .	229
110.	Hot Film Arrangement on Laser Velocimeter Cart.	230
111.	Axial Variations of Mean Velocity; Comparison of LV With Hot Film: $M_j \sim 0.5$	231
112.	Mean Velocity Profile Comparison of LV With Hot Film; $X/D = 2.0$, $M_j = 0.5$	232
113.	Axial Variation of Turbulence Intensity Comparisons of LV With Hot Film: $M_j = 0.5$	233
114.	Laser Velocimeter Measured Axial Profile of Mean Velocity for a Perfectly Expanded, Hot Supersonic Jet: $M_j = 1.55$, $T_T = 1500^\circ R$	234
115.	Laser Velocimeter Measured Mean Velocity and Turbulence Intensity Radial Profiles: $M_j = 1.55$, $T_T = 1500^\circ R$, $X/D = 9.6$	235
116.	Laser Velocimeter Measured Axial Variation of Turbulence Intensity for Shock-Free Flow: $M_j = 1.55$, $T_T = 1500^\circ R$. .	236
117.	Schematic Arrangement for Correlation Analysis.	237
118.	In-Jet Static Pressure "RMS" Profile.	238
119.	In-Jet Static Pressure "RMS" Profile.	239
120.	In-Jet Static Pressure "RMS" Profile.	240
121.	In-Jet Static Pressure "RMS" Profile.	241
122.	In-Jet Fluctuating Pressure Maximum Level and Radial Position Versus Downstream Distance, X. Convergent Jet $D = 2$ Inch, $Pr = 2$	242
123.	Jet Pressure 1/3 Octave Band Spectrum	243
124.	Axial Distributions of Mean Velocity and Axial and Radial Turbulence Velocities Using Cross Hot Film.	244
125.	Probe Contamination of Far-Field SPL Versus Far-Field Microphone Position	245

LIST OF ILLUSTRATIONS (Cont.)

<u>Figure</u>		<u>Page</u>
126.	Normalized Cross-Correlation of In-Jet Microphone With Far-Field Microphone. In-Jet Microphone at Point of Peak "RMS" Signal	246
127.	Unfiltered Cross-Correlation of In-Jet Microphone and Far-Field Microphone: 2 Inch Diameter Convergent Jet at Pr = 2; In-Jet at X = 20 Inch on Centerline; Far-Field at R = 10 ft. 43.8° From Centerline.	247
128.	Unfiltered Cross-Correlation of In-Jet Microphone and Far-Field Microphone: 2 Inch Diameter Convergent Jet at Pr = 2; In-Jet at X = 20 Inch on Centerline; Far-Field at R = 10 ft. 33.6° From Centerline	248
129.	Unfiltered Cross-Correlation of In-Jet Microphone and Far-Field Microphone: 2 Inch Diameter Convergent Jet at Pr = 2; In-Jet at X = 20 Inch on Centerline; Far-Field at R = 10 ft. 19.1° From Centerline	249
130.	Block Diagram for the Cross-Correlation Measurements. . .	250
131.	Normalized Cross-Correlation of V_r^2 and Far-Field Acoustics	251
132.	Normalized Cross-Correlation Coefficient for In-Jet Microphones	252
133.	Radial Cross Correlation Function	253
134.	Radial Cross Correlation Function	254
135.	Circumferential Cross-Correlation Unfiltered Microphone .	255
136.	Normalized Cross-Correlation Function of Unsteady Velocity, U' , and Jet Pressure, p'	256
137.	Eddy Convection Velocity as a Function of Probe Separation.	257
138.	Axial Cross-Correlation Coefficient of Unsteady U_1 and Jet Pressure, p'	258
139.	Axial Cross-Correlation Coefficient of Unsteady Velocity Squared, $(U')^2$, and Jet Pressure, p'	259

INTRODUCTION

With the advent of larger and more powerful military and commercial aircraft propulsion systems, it is increasingly apparent that to improve the general community environment greater efforts must be taken to reduce jet engine noise. A considerable effort has been spent in the last twenty years in the development of jet noise suppressors, but because of a lack of clear understanding and detailed mathematical specification of the dominant noise producing sources necessary for the establishment of meaningful prediction procedures for even the most simple nozzles, only partial success has been met in reducing the noise with acceptable jet nozzle performance.

The overall objective of this joint Air Force and Department of Transportation Supersonic Jet Exhaust Noise investigation is to develop the technology to significantly reduce supersonic aircraft propulsion system noise with minimum associated performance and weight penalties. To reach the Program objectives a varied and comprehensive research program is being carried out to develop the basic theory and experimental methods necessary for understanding and quantizing the acoustic characteristics of simple supersonic jets over a range of velocities and temperatures typical of present and future military and commercial supersonic aircraft propulsion systems.

This interim report summarizes the major theoretical and experimental task efforts performed at General Electric during the first year of a two year program. This two year program is a result of an initial exploratory research program initiated by the Air Force Aero Propulsion Laboratory during FY 71. During the initial phase of work the general framework for General Electric's method of approach was established. At the time of the initial phase of work, a thorough review of various competing mathematical models used to explain supersonic jet noise generation processes was performed, and preliminary experimental instrumentation and procedures were demonstrated. One result of General Electric's initial efforts was establishment of a comprehensive turbulent mixing aero-acoustic model capable of computing all the main acoustic properties: overall sound power level, power spectra, overall sound pressure level, sound pressure level spectra and the jet's detailed directivity characteristics. Additionally, the procedure was extended for acoustic noise source location

predictions such as axial power distributions for subsonic and supersonic exhaust jets, acoustic peak frequency distribution, and the effects of initial turbulence intensity on jet noise. The primary emphasis in thinking was to computationally link the detailed mean and turbulent flow aerodynamic properties to selected turbulent mixing acoustic models. This computational scheme was completed and a great deal of success^{1,2} was achieved for shock free supersonic high temperature jets. The computational scheme was so designed as to enable the acoustic predictions to be based on aerodynamic input which could be predicted or measured, thus allowing the scheme to be compatible with exhaust nozzle suppressor investigations where the detailed aerodynamic properties cannot as yet be predicted.

To complement the theoretical investigations, experimental instrumentation was developed to measure the detailed in-jet flow properties of heated supersonic exhaust jets. It was demonstrated that General Electric's laser velocimeter was an ideal in-jet, non-contact type probe, capable of measuring the detailed mean and turbulence velocity of supersonic high temperature jets, thus offering the option of using measured flow properties as the aerodynamic input to the acoustic prediction models developed.

It was found during the first phase of effort that the original models developed, which were based on the concepts of Lighthill, Ribner and Ffowcs-Williams, had certain limitations and difficulties with regard to properly accounting for the density dependence of jet noise, the influence of moving sound sources on the acoustics of the problem, the interplay between convective and refractive coupling and the assessment of the degree each plays in understanding the directivity characteristics of jet noise, and the influence of shock turbulence interaction on the aerodynamic and the acoustic properties of high velocity and high temperature supersonic jets.

Section I of this report deals with the aerodynamic input which serves as the starting point for the acoustic calculations of General Electric's Comprehensive Model. The shock free solutions for the aerodynamic input have been dealt with in detail in the first phase report.¹ Here Section I deals with inclusion of shock waves into the general aerodynamic flow model. A comprehensive account is given of the theoretical and computational foundations for formulating and computing the shock structure and the mean and turbulent flow properties of heated, shocked supersonic jets.

Section II deals with the acoustic input of the aeroacoustic model. Here, detailed discussions and theory development is given which will be used in the refinement of the acoustic input for the comprehensive aero-acoustic model development. Since the predictive capacity of the model has been well demonstrated in the Phase I report, only the newer theory developments of jet noise will be discussed. Particular emphasis is directed toward solutions for moving sources and the new insights this model gives for explaining the reasons of increased low frequency convective amplification at shallow jet angles, the density dependence of turbulent mixing noise, and correct velocity scaling of jet noise. The Phillips-Pao turbulent shear-layer model is also discussed. Particular attention is devoted toward formulating this model in a way acceptable for aero-acoustic predictions, and the way this theory accounts for convective/refractive coupling, source radiative efficiency and the temperature dependency of jet noise. Additionally, a section is devoted to forming a generalized Green's function approach from the Lighthill/Ribner jet noise theory point of view to unify the concepts regarding moving and stationary noise source models, and how the theory can be used to establish the framework for acoustic refraction studies that will be carried out in the next year's effort.

Section III gives preliminary results from a set of detailed far field, near field acoustic parametric studies, and some results from photographic studies. The results are presented in a form which will be useful for future theory/data comparisons and noise source location investigations.

Section IV reports on the recent advances made in developing instrumentation for performing in-jet noise source location studies on high temperature high velocity exhaust jets. Section IV discusses the theory and error analysis necessary to construct turbulence spectra using General Electric's laser velocimeter. Results of demonstration experiments for measuring turbulence spectra in subsonic cold and heated high velocity jets are given. Preliminary comparisons of LV measured turbulent flow properties with hot film measurements are also discussed. Additionally a detailed discussion of in-jet pressure probe and in-jet to far-field acoustic probe correlation investigations is given for a sonic jet. How these studies compare with work performed at low velocities, and the usefulness of in-jet pressure probes for high speed flow investigations are reviewed.

Section V reviews the work planned for the completion of the Program activities.

REFERENCES

1. M.J. Benzakein and P.R. Knott, "Supersonic Jet Exhaust Noise," Air Force Aero Propulsion Laboratory, AFAPL-TR-72-52, July 1972.
2. P.R. Knott and M.J. Benzakein, "Analytical and Experimental Supersonic Jet Noise Research," AIAA 73-188 (1973).
3. R. Mani, "A Moving Source Problem Relevant to Jet Noise," GE Class I Report, May 1972.

I. THEORETICAL DEVELOPMENTS OF THE AERODYNAMICS OF SUPERSONIC JETS

C.L. Merkle

There are two distinct techniques which have been used to analyze the aerodynamic flow field in a supersonic jet. In the first approach, the jet is treated as a viscous, boundary layer flow. The resulting flow field is of the type depicted in Figure 1. According to the usual boundary layer approximations, the radial velocity components are assumed small in comparison to their axial counterparts, and, in addition, the pressure is taken to be constant throughout the whole flow field. These approximations implicitly assume that the static pressure at the jet exit plane is identical to the ambient pressure and that Prandtl-Meyer expansions and/or shock waves are not present in the flow field. Consequently, this viscous boundary layer analysis can only be applied to subsonic jets, or to supersonic jets which are ideally (or nearly ideally) expanded.

In contrast to this viscous analysis, the second traditional technique for analyzing supersonic jets completely ignores the effects of turbulent mixing. In this second (inviscid) analysis, the full two-dimensional equations of motion are used, and strong radial and axial pressure gradients can occur. These pressure gradients have their origin at the nozzle exit plane where the static pressure is generally significantly different from the ambient pressure. In adjusting to the ambient pressure, the flow field generally develops a series of shock waves and Prandtl-Meyer expansions in a nearly periodic, cell-like fashion. A schematic description of the qualitative features of a jet described by this two-dimensional analysis is shown on Figure 2.

As indicated above, both of these approximate models are applicable to the analysis of a certain class of supersonic jet. However, as might be expected, neither model applies to all supersonic jets. Thus, for example, the effects of friction can never be entirely removed from the jet. Further, supersonic jets are seldom uniform, parallel ideally expanded jets. Consequently, in order to obtain an acoustic prediction technique which is applicable to both ideally expanded and non-ideally expanded jets, the aerodynamic model must include both two-dimensional effects and viscous mixing effects. During the present contract reporting period, we have developed such an aerodynamic model. The details of this analysis are given in the following sections.

1. DESCRIPTION OF THE AERODYNAMIC MODEL

Exhaust nozzles of most contemporary gas turbine engines generally operate near their ideal expansion ratios. In view of this, General Electric's initial efforts at the prediction of the sound field of a supersonic jet relied on an aerodynamic analysis which included only the effects of turbulent mixing. Specifically, this aerodynamic model was of the viscous, boundary layer type described above. The computerized version of this analysis is referred to as the JETMIX computer program. This computer program solves the time-averaged turbulent boundary layer equations using boundary conditions which are appropriate for free jets. The turbulent Reynold's stresses are included by means of a turbulence model which is based on a turbulent kinetic energy concept. This turbulence model is based on those developed by Rotta⁽¹⁾, Glushko⁽²⁾ and Spalding⁽³⁾. Details of the turbulence model and the JETMIX computer program as well as extensive comparison of the predictions with experimental data are given in References 4 and 5.

Starting from this basic viscous analysis, we have extended our aerodynamic model to enable it to predict non-ideally expanded jet flow fields. This improved aerodynamic capability allows us to predict the effects of non-ideal expansion on the acoustic field of a supersonic jet. In particular, the analysis enables us to estimate the difference between the sound which is generated by an ideally-expanded jet from a convergent-divergent nozzle and a highly underexpanded jet of the same Mach number from a convergent nozzle.

The method which we have used to include the two-dimensional effects which occur in non-ideally expanded jets is based on dividing the jet into an inner region and an outer region as shown in Figure 3. The outer region of the jet contains that part of the jet in which the effects of turbulent mixing are significant. Near the nozzle exit the outer region is composed of a narrow annular portion of the flow field on the outer edge of the jet; downstream of the exit plane, the thickness of the outer region increases until eventually it includes the entire jet. In our analysis, this outer region is computed by our original viscous, boundary layer (JETMIX) computer program. Now, whereas the outer region of the jet is dominated by the effects of viscous mixing, the inner region of the jet is dominated by the familiar Prandtl-Meyer expansions and shock waves which characterize two-dimensional supersonic flow fields. In order to include these effects in our aerodynamic model, a new computer program has been written to handle this inner region. This new program is called the

Supersonic Finite Difference (SSFD) computer program. Thus in the refined aerodynamic model, a supersonic jet is analyzed in two parts by two separate computer programs. The outer portion of the jet is analyzed by the viscous JETMIX analysis. The inner portion of the jet is computed by the two-dimensional SSFD analysis.

As indicated in Figure 3, these two separate parts of the flow field are matched along the sonic line. Thus the inner portion of the flow field is supersonic while the outer flow is subsonic. (In actuality some constant Mach number line which is slightly supersonic is chosen as the matching line rather than precisely the sonic line). However, it must be noted that the sonic line appears in the jet because viscous effects have reduced the Mach number of the formerly supersonic flow. This indicates that the outer edge of the supersonic region has experienced considerable viscous effects. Thus in order to include the two-dimensional effects in as large a region as possible, and in order to enforce as smooth a match as possible between the inner and outer solutions, the effects of the viscous mixing are included in the inner (SSFD) analysis as known "right-hand-side" terms. The magnitude of the "right-hand-side" terms is estimated from the viscous JETMIX computer program as indicated later. This matching technique allows the total pressure to vary continuously from the outer edge of the jet (where the flow is essentially stagnated) through the sonic line and all the way to the jet centerline (where the flow is supersonic). Then by matching the static pressure at the sonic line, we can be sure that all flow properties are continuous at the matching line.

2. DERIVATION OF THE EQUATIONS USED IN THE INNER REGION

As indicated above, the equations used in the inner region include the viscous effects as "right-hand-side" terms. In order to obtain the form of these "right hand side" terms, the equations for the inner region are obtained from the complete Navier-Stokes equations. An outline of the derivation follows.

The equations of motion for steady, compressible, viscous flow are

$$\nabla \cdot \rho \bar{v} = 0 \quad (1)$$

$$\rho (\bar{v} \cdot \nabla) \bar{v} + \nabla p = \nabla \cdot \bar{\tau} \quad (2)$$

$$\rho \bar{v} \cdot \nabla e = \bar{\tau} : \nabla \bar{v} - p \nabla \cdot \bar{v} - \nabla \cdot \bar{q} \quad (3)$$

Two vector identities which are useful are

$$\bar{v} \cdot (\bar{v} \cdot \nabla) \bar{v} = \bar{v} \cdot \nabla (v^2/2) \quad (4)$$

$$\bar{v} \cdot (\nabla \cdot \bar{\tau}) = \nabla \cdot (\bar{v} \cdot \bar{\tau}) - \bar{\tau} : \nabla \bar{v} \quad (5)$$

If we dot Equation (4) by the velocity vector, \bar{v} , and use identity (4), we obtain

$$\rho \bar{v} \cdot \nabla (v^2/2) + \bar{v} \cdot \nabla p = \bar{v} \cdot (\nabla \cdot \bar{\tau}) \quad (6)$$

Then, combining Equations (1) and (3) and using identity (5), the energy equation becomes

$$\rho \bar{v} \cdot \nabla h - \bar{v} \cdot \nabla p = \nabla \cdot (\bar{v} \cdot \bar{\tau}) - \bar{v} \cdot (\nabla \cdot \bar{\tau}) - \nabla \cdot \bar{q} \quad (7)$$

where we have also converted from internal energy to enthalpy. Then, adding Equations (6) and (7) gives

$$\rho \bar{v} \cdot \nabla h^0 = \nabla \cdot (\bar{v} \cdot \bar{\tau}) - \nabla \cdot \bar{q} \quad (8)$$

We now define the scalar function, Q , as

$$Q(x,y) = \rho \bar{v} \cdot \nabla h^{\circ} \quad (9)$$

and by Equation (8), we also have

$$Q(x,y) = \nabla \cdot (\bar{v} \cdot \bar{\tau}) - \nabla \cdot \bar{q} \quad (10)$$

If we now combine Equation (10) with Equation (7) and use the thermodynamic equation of state, the energy equation becomes

$$\rho T (\bar{v} \cdot \nabla S) = -\bar{v} \cdot (\nabla \cdot \bar{\tau}) + Q(x,y) \quad (11)$$

Finally, defining the scalar function, ϕ , as

$$\phi(x,y) = \bar{v} \cdot (\nabla \cdot \bar{\tau}) \quad (12)$$

we can write the entropy variation along a streamline as

$$\rho T \bar{v} \cdot \nabla S = -\phi(x,y) + Q(x,y) \quad (13)$$

Thus, the final version of the equations of motion (1), (2), and (3) can be re-written as

$$\nabla \cdot \rho \bar{v} = 0 \quad (14)$$

$$\rho (\bar{v} \cdot \nabla) \bar{v} + \nabla p = \bar{R} \quad (15)$$

$$\rho T \bar{v} \cdot \nabla S = -\bar{v} \cdot \bar{R} + Q(x,y) \quad (16)$$

where the vector \bar{R} is defined as

$$\bar{R} = \nabla \cdot \bar{\tau} \quad (17)$$

so that

$$\phi(x,y) = \bar{v} \cdot \bar{R} \quad (18)$$

These are the equations which are solved by the SSFD computer program. At present the function, $Q(x,y)$, is limited to the trivial function

$$Q(x,y) = 0 \quad (19)$$

This implies that only flow fields which have uniform total temperature throughout can be calculated. The extension of the computer program to include an arbitrary specification of the stagnation enthalpy is relatively simple. Note that the function, ψ , is not restricted; it can (in principle) be any function. When coupled to the JETMIX viscous analysis, the SSFD program automatically determines ϕ from the JETMIX - predicted entropy gain due to the turbulent stresses.

Equations (14), (15), (16) and (19) are solved numerically using a finite-difference algorithm developed by MacCormick⁽⁶⁾.

3. CALCULATION OF THE TURBULENCE FIELD

The previous paragraphs have described the model which is used to predict the velocity field in an off-design jet. However, before the acoustic characteristics of the jet can be determined, it is necessary to know something of the turbulence field in the jet. As indicated above, the turbulence model which is used in the JETMIX computer program is based on a turbulent kinetic energy approach. For ideally expanded jets, the magnitude of this turbulent kinetic energy has been used to evaluate the source terms in the classical Lighthill acoustic equations (5,7). Once these source terms are evaluated, the acoustic signature of the jet can be readily determined. Since this acoustic formulation is based on the local mean and fluctuating properties of the jet, it should also be directly applicable to non-ideally expanded jets. (This, of course, does not imply that the model would predict the same acoustic radiation from an ideally expanded jets, because both the mean velocity field and the turbulence field depend on the expansion ratio of the jet.) Thus, it remains to determine the turbulent kinetic energy in the non-ideally expanded jet.

The conservation of turbulent kinetic energy is governed by the balance between between the production, dissipation, convection, and diffusion of turbulence energy throughout the flow field. The form of the turbulent kinetic energy equation which is used in the JETMIX analysis is

$$\rho U \frac{\partial k}{\partial x} + \rho v \frac{\partial k}{\partial y} = \frac{1}{y} \frac{\partial}{\partial y} (C_1 \rho \mu_t y \frac{\partial k}{\partial y}) + \mu_t \frac{\partial u}{\partial y}^2 - \frac{C_2 \rho k^{3/2}}{L} \quad (20)$$

For clarity, the physical meaning of each of these terms is labeled. As used in the JETMIX analysis, this equation basically applies to ideally expanded jets. However, the local properties of the turbulence should not depend on whether or not the jet is ideally expanded. Consequently we take equation (20) as being applicable in non-ideally expanded jets also.

Although we use the same turbulence conservation equation in both ideally and non-ideally expanded jets, there is one flow phenomenon which affects the turbulence levels and which is unique to non-ideally expanded jets that is not included in the turbulence conservation equation (20). This phenomenon is the presence of shock waves in the flow field. These effects have been included in

our analysis by means of Ribner's Shock-Turbulence interaction theory (8,9).

Ribner's analysis starts by decomposing the turbulence field into an infinite number of elementary vorticity waves of all wavelengths and orientations. Then for any one of these elementary waves, he calculates the manner in which the vorticity of the wave is altered as it is convected through a normal shock wave. The results of his calculation show that the magnitude of the vorticity is increased as the wave goes through the shock. (Besides the increased vorticity, two new waves are generated, an entropy wave and an acoustic wave.) A summation over all wave numbers of the effects of the shock on each individual wave then yields an amplification factor for the turbulence as it is transmitted through the shock. Conversion from turbulence convected through a normal shock to turbulence convected through an oblique shock is made by a transformation of coordinates. Finally, it should be noted that although Ribner's analysis strictly applies only to straight shocks, it can also be applied to curved shocks (such as occur in supersonic jets) as long as the radius of curvature of the shock is significantly larger than the longest wavelength of the turbulence.

Figure 4 shows the amplification of turbulence by a shock in terms of the ratio of turbulent kinetic energy in front of and behind the shock. The turbulence amplification is plotted as a function of the ratio of the normal components of velocity in front of and behind the shock. As can be seen, the amplification is unity at a velocity ratio of unity (shock of vanishing strength) but quickly increases to a maximum of some 20% amplification for moderate shock strengths (normal component of incoming Mach number about 1.5).

In our computer model, the turbulent kinetic energy is monitored at each point in space by means of equation (20). The source term in this equation accounts only for the production of turbulence by the viscous shear forces. When a shock wave is encountered, the turbulence amplification is determined from Ribner's theory and the turbulent kinetic energy is increased locally by the amount of turbulence which is generated at the shock. The resulting turbulence energy profiles have a discontinuous jump across the shock. The magnitude of this jump is determined from Ribner's theory.

4. MATCHING BETWEEN THE INNER AND OUTER SOLUTIONS

As described above, the equations for the inner region require that the variations in entropy and stagnation enthalpy due to the turbulent shearing stresses be specified along each streamline before the solution is calculated. In the computational procedure, these variations are first estimated from a solution of the viscous boundary layer equations for the entire mass flow in the jet (i.e., both inner and outer flows). This viscous calculation also establishes the value of the stream function at which the flow becomes sonic, and hence the location of the boundary between the inner and the outer regions. Then, using the calculated entropy/enthalpy variations as a first approximation to their actual behavior, the velocity field in the inner region is re-calculated by means of the two-dimensional (inner) equations. (The velocity field in the outer region is left unchanged except for re-positioning the streamlines so that they match with the streamlines in the inner region.) In principle, this sets up an iterative process which could be continued by using the predicted pressure gradient as an impressed static pressure field for the outer equations. Thus upon convergence, the "exact" solution would be obtained (except that the viscous terms would be included only to the boundary layer approximation). Note that the iteration would proceed by assuming that a known static pressure field is impressed on the outer (boundary layer) equations. The boundary layer calculation then defines an entropy/enthalpy field which is impressed on the inner (two-dimensional "inviscid") equations which, in turn, re-define the static pressure field, and so forth. Nevertheless, for the problem at hand, it is assumed that the use of a constant pressure field in the boundary layer equations will give the entropy/enthalpy field to sufficient accuracy that an improved approximation need not be determined. The computational procedure is described schematically on Figure 5.

The boundary conditions along the sonic line complete the matching of the inner and outer solutions. The viscous solution assumes the static pressure is constant throughout the outer region and equal to the ambient. At the matching (sonic) line, the static pressure in the inner region is required to approach the ambient pressure. Thus by requiring the static pressure to be continuous across the sonic line, and by obtaining the entropy/enthalpy field for the entire jet from the outer solution, we are assured that all other flow and thermodynamic properties are continuous at the interface also.

Now since the entire total pressure field is obtained from the outer (viscous) solution, and since the static pressure is required to be continuous along the sonic line, then all other flow and thermodynamic properties will be continuous at the matching line also for the case of the cold jet. To achieve this complete matching of all properties in a hot jet case, the total temperature along each streamline would have to be superimposed on the inner solution (in addition to the total pressure). As mentioned above, the computer program does not currently have capability for variable total temperature, although all the necessary mathematical requirements have been worked out.

Finally it should be pointed out that the viscous boundary layer equations which are solved by the JETMIX computer program are parabolic in the axial coordinate, x , and that the solution can, therefore, be obtained by a matching process. A similar matching process can be used to solve the inner, two-dimensional equations because these equations are hyperbolic (so long as the flow remains supersonic). Consequently both the inner and outer solutions lend themselves to a matched, coupled calculation such as has been described.

5. SHOCK REFLECTION FROM AXIS OF SYMMETRY

As a shock wave in an axisymmetric flow field approaches the centerline, the shock becomes increasingly steeper. Because of this steepening, the axisymmetric equations will not allow the shock to reflect from the symmetry axis in a regular fashion. Instead, some sort of "strong" reflection must occur. As a result, a local pocket of subsonic flow appears behind the shock and any computational procedure which relies on the hyperbolic character of the equations becomes invalid and has to be terminated. However, experimental schlieren photographs show that this subsonic region is frequently small or even non-existent.⁽¹³⁾ Thus, although the reflection shows up as a nearly normal "Mach disc" or "Riemann wave" in some cases, an apparently regular reflection takes place in other cases when the shock is sufficiently weak, (even though the inviscid equations will not allow this). In order to provide a means for continuing the flow field calculation beyond the location at which the shock first reflects from the axis of symmetry, we have incorporated two approximate techniques for "calculating through" this presumably small, localized subsonic pocket. First, when the incoming shock is weak, a "regular" reflection procedure is used. However, for stronger incoming shocks, we switch

over to a "Mach disc" reflection procedure. Which of the two techniques is to be used must be determined by the problem at hand.

The "regular" reflection procedure utilizes a suggestion by Oswatitsch (14) that the axis of symmetry be "enlarged" near the shock impingement point so that the radial coordinate becomes small but still remains finite. The radial size of this "enlargement" is determined by the program depending on the local strength of the shock. (Stronger shocks require more "fattening" of the axis of symmetry.) It is emphasized that these "enlargements" generally encompass less than one half of one percent of the original mass flow so that they are scarcely detectable on a "blown up" plot of the shock locus.

The "Mach disc" reflection technique (which is considerably more complicated than the "regular" reflection procedure) involves the insertion of a triple point and the use of an iterative technique to determine its location. In this analysis, a triple point is inserted at a chosen location on the shock, and the oblique shock which is moving radially inward is forced to branch into a second outward-running shock and a normal shock which extends to the axis as shown in Figure 6. The normal shock represents the Mach disc. A slip line is also generated at the "lambda" intersection. Downstream of the Mach disc, this slip line serves as a boundary between the supersonic flow and the subsonic flow. The supersonic flow is handled by the standard SSFD algorithm, while the subsonic flow is analyzed by a one-dimensional approximation. The height of this one-dimensional channel at succeeding axial locations is determined by requiring the pressure to be balanced across the slip-stream, and by requiring the supersonic flow to be tangent to the slip line. This matching requirement causes the Mach number in the one-dimensional stream to vary as it flows downstream. The axial position of the Mach disc is then iteratively determined based on the behavior of the flow in this one-dimensional channel. The Mach disc is said to have been correctly positioned when the slip line forms a "throat" which re-accelerates the subsonic flow through sonic velocity in a smooth, continuous fashion. This Mach disc model is very similar to the ones used by Abbett (15), Averenkova, et al. (16) and (17). Comparisons between this Mach disc model and experimental results have shown reasonable agreement, but the iterative procedure is quite expensive (in terms of computer processing time) and tends to be unreliable.

Calculation of Jet Noise From Turbulent Kinetic Energy Field

As indicated above, once the turbulent kinetic energy is known, the acoustic radiation from an off-design jet can be computed directly as was done for ideally expanded jets in references I-5 and I-7. Note that this calculation automatically takes into account the indirect effect of the shock on the jet noise. That is, the local turbulence level is increased by the shock and so the local acoustic radiation is similarly increased by the presence of the shock.

Nevertheless, the presence of shock waves in a non-ideally expanded jet will not necessarily lead to a higher predicted level of noise (as compared to the corresponding ideally expanded jet) even though the shock wave acts to increase the turbulence (and hence the noise). The reason for this is that the corresponding change in the mean velocity field will also have an effect on the turbulence levels which could tend to off-set the generation of turbulence by the shocks.

In addition to this indirect effect of shocks on the jet noise, there is also a direct effect. In addition to generating additional turbulence, the shock also generates acoustic waves directly. These shock-generated acoustic waves are of two different natures; one subsonic and the other supersonic.

Those waves which are subsonic in nature decay exponentially with distance behind the shock, and so can be neglected in the far field. The supersonic waves propagate to infinity (as plane waves) and so are not negligible in the far field. The proportion of subsonic and supersonic waves depends on the Mach number of the incoming flow and on the particular (vectorial) Fourier component of the incoming turbulence.

As an estimate of the magnitude of the acoustic intensity which is generated by a shock-turbulence interaction, the shock-generated noise for a sonic jet which was under-expanded by the ratio $P_{jet}/P_{amb} = 2$ has been calculated. For this jet (in which the strength and location of the shock was determined by means of the SSFD computer program) the acoustic intensity of the noise generated by the first cell of the shock (shock wave running from the near the outer boundary of the jet in towards the axis of symmetry,

and then reflecting back to the outer edge) was 73 decibels, the reference level for the energy being 10^{-12} times the total flow energy in the jet, i.e.

$$\frac{\text{Shock Generated Acoustic Energy}}{\text{Shock Generated Acoustic Energy}} = 10 \log_{10} \frac{\rho u A_{\text{shock}} I_{\text{acoustic}}}{\rho u^3 A_{\text{jet}} \times 10^{-12}}$$

And the acoustic intensity, I_{AC} , is given in terms of the incoming turbulence intensity via Ribner's theory (10). These results indicate that the acoustic intensity generated by shock-turbulence interaction is small compared to the overall acoustic energy of a supersonic jet, but that it is sufficiently large to have a non-negligible effect on the acoustic signature of the jet. Finally, it should be noted that this calculation was made for a jet having an initial turbulence intensity of 10% at the jet exit.

In addition to this indirect effect on the jet noise, the shock also has a direct effect on the noise because of the acoustic waves which are produced by the shock turbulence interaction. This direct source of noise must be "added on" to the turbulence-produced noise in the jet. The magnitude of this shock-produced noise is also given by Ribner⁽¹⁰⁾.

Finally, it should be noted that the acoustic radiation which is predicted by this shock-turbulence interaction model is broadband in nature. As is well-known, shock waves add both broadband noise and narrowband noise to the overall jet acoustic pattern^(11,12). The above theory does not include a mechanism for estimating either the magnitude or the frequency of these narrowband (screech) tones.

6.0 RESULTS FOR SHOCK STRUCTURE COMPUTATIONS

Inviscid Calculations

Some typical predictions of the aerodynamic flow field are given in Figures 7 through 11. The results in these figures have been obtained from completely inviscid calculations. Figure 7 shows the predicted shock shape and outer boundary shape based on the inviscid calculation. The shock originates near the outer edge of the jet due to coalescing characteristics coming from the curved outer boundary. The shock moves radially inward and eventually reflects from the axis of symmetry and returns to the outer boundary. The "regular" reflection technique has been used in this case. Figures 8 and 9 show the composite result of a number of computations similar to that of Figure 7. In Figure 8 is plotted the distance from the nozzle exit to the point at which the shock first crosses the axis of symmetry as a function of pressure ratio, p_{jet}/p_{amb} . These results are for both "regular" and Mach disc reflection. Also shown on Figure 8 is a line representing the experimental data of Love⁽¹⁶⁾. The inviscid predictions agree quite well with the experimental results; however, this is to be expected since the viscous effects don't start to have significant effects on the shock shape until after it reflects from the axis and nears the outer boundary. Figure 9 is similar to Figure 8 except that it shows the height of the Mach disc as a function of pressure ratio. Again, Love's experimental data are shown for comparison. The predicted Mach disc heights are in only fair agreement with the experimentally observed values. Nevertheless, the qualitative agreement is sufficient to show that the Mach disc model can be used as an artifice to allow the two-dimensional supersonic flow calculation to proceed beyond the point where the shock hits the axis.

An overlay of the inviscid shock shape prediction of Figure 7 with a schlieren photograph taken under the experimental portion of this contact is shown as Figure 10. The agreement between the computed shock and the experimental shock is excellent except for two points. First of all, the computed shock starts considerably closer to the nozzle than does the experimental shock. However, the computed version of the shock represents a Mach number jump of only about 0.02 until very near the centerline. A shock this weak would not be expected to show up on a schlieren photograph. Secondly, the

predicted shock does not turn normal to the flow near the edge of the jet. This difference is due to the neglect of the viscous effects in the outer region of the jet. Some calculations which do include the effects of viscous mixing are shown in the next section.

Turbulent Flow Field Calculations

Figures 11 through 15 present the results of calculations based on the full coupled viscous - inviscid analysis. Figures 11, 12 and 13 show the effect of varying amounts of underexpansion on a jet plume. In all three figures, the total-to-ambient pressure ratio, $P_T/P_{amb} = 4.10$. The static-to-ambient ratio, P_J/P_{amb} , is, however, different in each figure. Figure 11 shows the radial variation of both the total pressure and the static pressure for the ideally expanded jet, $P_J/P_{amb} = 1.0$. Here, the pressure is constant (and equal to the ambient) throughout the entire jet. Consequently, both the complete inner-outer analysis and the purely viscous boundary layer analysis give identical results for this case. At the axial locations shown, $x/R = 1.90$ and 2.65 , the total pressure near the centerline of the jet has remained at its original upstream value indicating that the inviscid core is still present. Near the outer edge of the jet, the total pressure falls off quite rapidly due to mixing. This decrease continues until the total pressure approaches the static (ambient) pressure signifying that the velocity has dropped to zero.

A slightly underexpanded jet ($P_J/P_{amb} = 1.6$) is shown in Figure 12. This flow field contains a weak shock, which, at the axial location shown, $x/R = 2.65$, has just reflected from the axis of symmetry and is moving back toward the outer boundary. Because of the shock, there are now two sources of total pressure loss. Since the shock has already reflected from the axis of symmetry, the flow in the center of the jet has experienced a finite, shock-induced total pressure loss as shown by the smaller shaded region. Between this region and the outer mixing-loss region (also shown shaded) lies a portion of the gas which is unaffected by mixing and has been traversed by only a very weak shock so that its total pressure remains equal to its upstream value. The radial variation of the static pressure is no longer trivial in this case as it was in Figure 11. The pressure near the center is relatively high, then drops across the shock to a below-ambient value and finally asymptotically approaches the ambient value at the interface between the inner and outer regions.

The location of this interface as well as the location of the sonic point are also shown on Figure 12.

The last figure of this series represents a still larger degree of under-expansion than did Figure 12. Figure 13 corresponds to flow from a convergent nozzle with sonic velocity at the exit. The pressure ratio is $P_J/P_{amb} = 2.1$. This figure again shows radial variations of both total and static pressures at each of two axial stations, $x/R = 1.90$ and $x/R = 2.65$. The rate at which the mixing region spreads with distance from the nozzle exit can again be seen, as can the increasing total pressure loss due to shocks. Note the relatively large levels of static pressure variation even though the underexpansion is still mild. Finally, note that the viscous boundary layer analysis by itself would predict the same flow field for all three jets in Figures 12 and 13, (assuming the impressed pressure were taken as the ambient pressure in all cases). Also note that the considerable effect of the mixing-induced total pressure loss on the flow field would be ignored by pure inviscid analyses.

The last two figures show the predicted shock wave shapes for the jets of Figure 12 and 13. Figure 14 shows a comparison between the shock shape which is predicted by the complete inner-outer analysis and the shape predicted by a completely inviscid analysis. The inviscid calculation was made by specifying the entropy to be constant along all streamlines (except for shock losses). As Figure 14 shows, the two calculations give nearly identical shock shapes before and immediately after the reflection of the shock from the centerline. Indeed, the minor differences between the two calculations in this region is more due to small errors in calculation (stemming mostly from undesired interactions between the initial part of the mixing layer and the expansion fan at the nozzle lip) than from the physics of the problem. However, the sharply curved portion of the shock near the outer boundary is due to real effects. This sharp curvature comes about as the shock enters the strongly rotational flow region which has been created by the viscous mixing. As the shock traverses this mixing layer, the Mach number in front of the shock approaches unity so that even as the shock turns normal to the flow, its strength decreases until it eventually fades out.

Also shown in Figure 14 are the outer boundaries of the inviscid calculation (which is of course a streamline) and the "sonic" matching line ($M = 1.1$) which was used in the coupled analysis. Finally, the mixing region is shown by the shaded area.

Figure 15 presents a final comparison with experiment. This figure again shows the predictions of the coupled analysis (for a jet of pressure ratio, $P_J/P_{amb} = 2.1$), this time superimposed on a Schlieren photograph of a jet at the same conditions. As can be seen, the agreement is excellent. Note that the curved portion of the shock in the mixing region agrees quite well with the schlieren result, and that the predicted size of the "Mach disc" agrees with the photograph (although without the theoretical prediction superimposed, the photograph appears to show a regular reflection). Again, note that although the predicted shock starts much too close to the nozzle exit, it remains extremely weak until it nears the axis and so would not be expected to be visible on the Schlieren photograph. Finally Figure 15 shows that both the predicted and the experimental outer boundaries show a point of inflection at about the axial distance from the nozzle exit where the shock reflects from the centerline. This inflection in the outer boundary is caused by the displacement of the viscous mixing region by the inner inviscid core of the plume. At the exit plane, the inviscid flow turns outward through an expansion fan. Then the axisymmetric effects force this flow to again turn and approach the axis (see outer boundary shape of the inviscid calculations in Figure 7. The superposition of an ever-widening mixing region on these curved inviscid streamlines generates the inflection in the boundary.

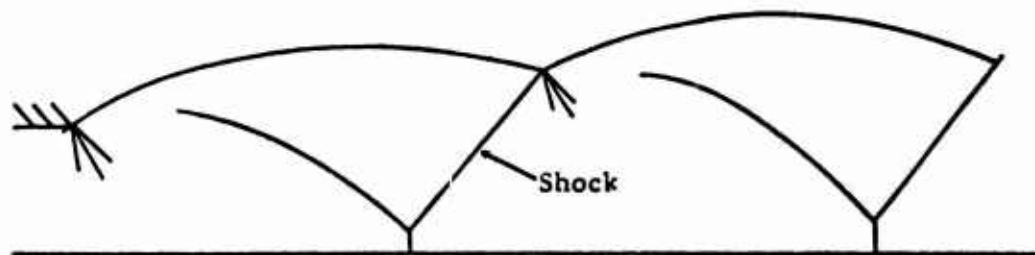


Figure 1 The Flowfield of an Inviscid Two-dimensional Supersonic Jet

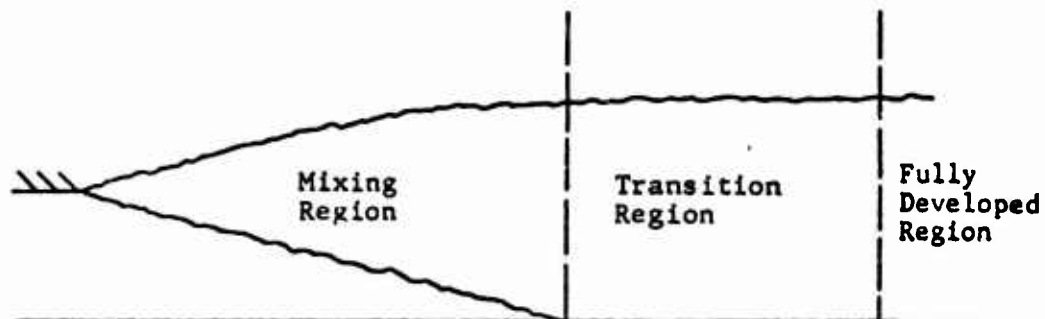


Figure 2 The Flowfield of an Ideally Expanded Viscous Jet

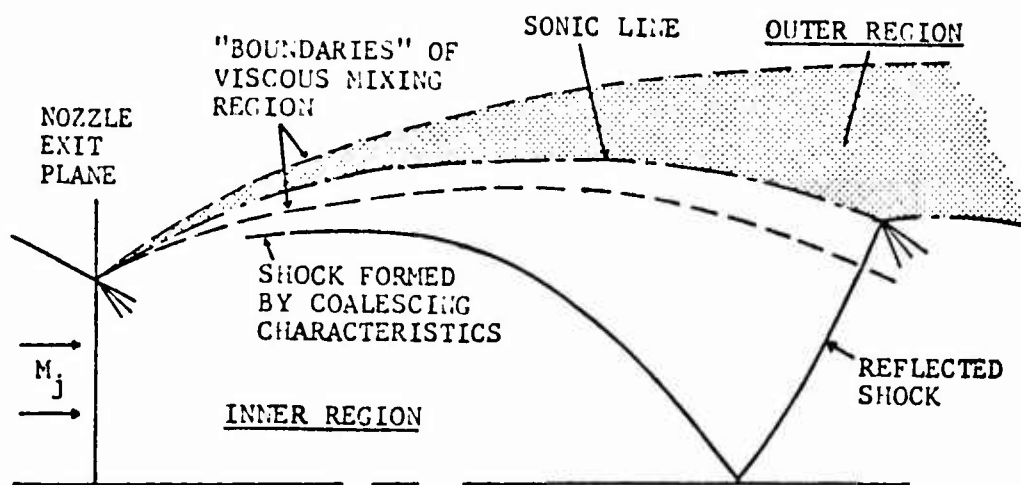


Figure 3 Subdivision of the Jet into Inner and Outer Regions
(Outer Region Shown Shaded)

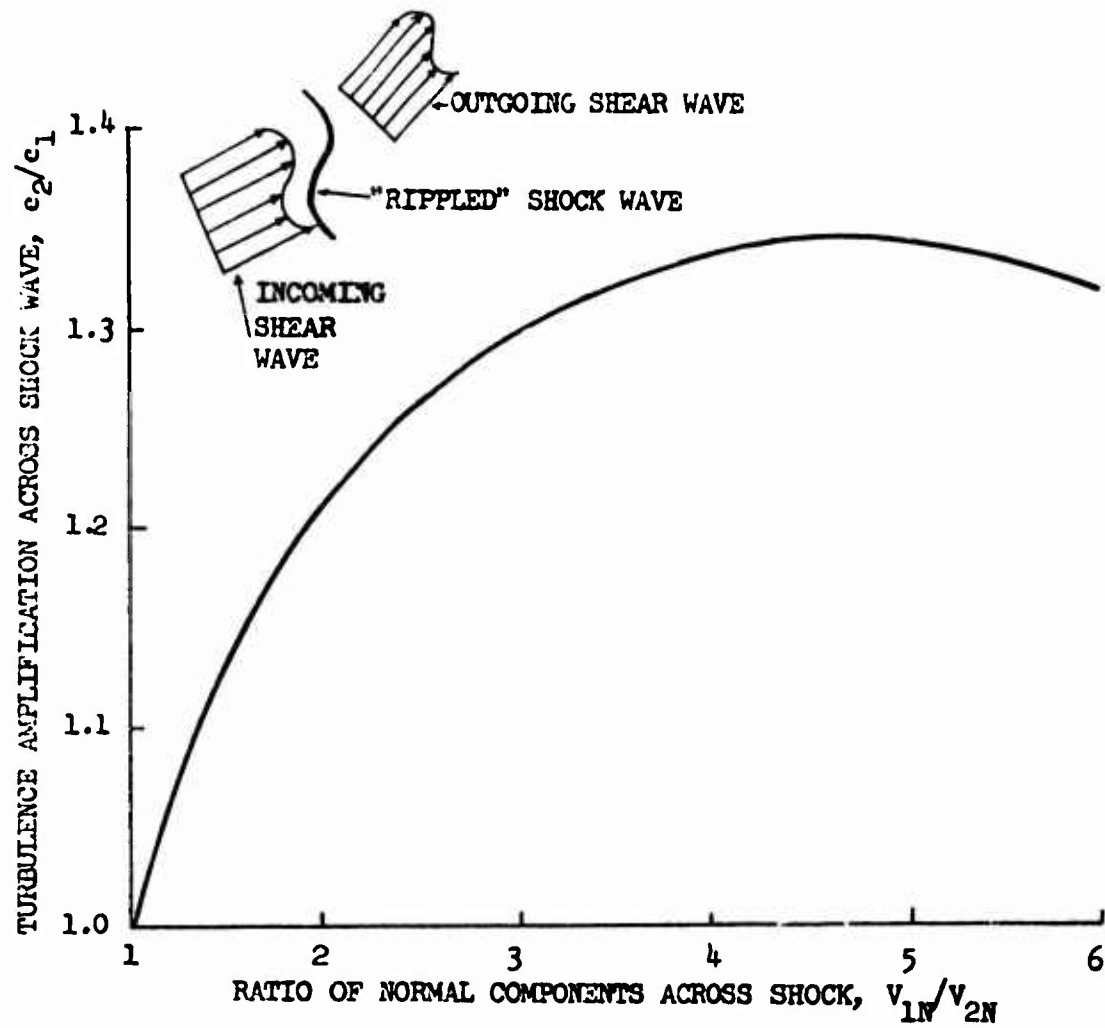


Figure 4 Amplification of Turbulence by a Shock Wave as Predicted by Ribner's Shock-Turbulence Theory

OUTLINE OF COMPLETE COMPUTATION SCHEME

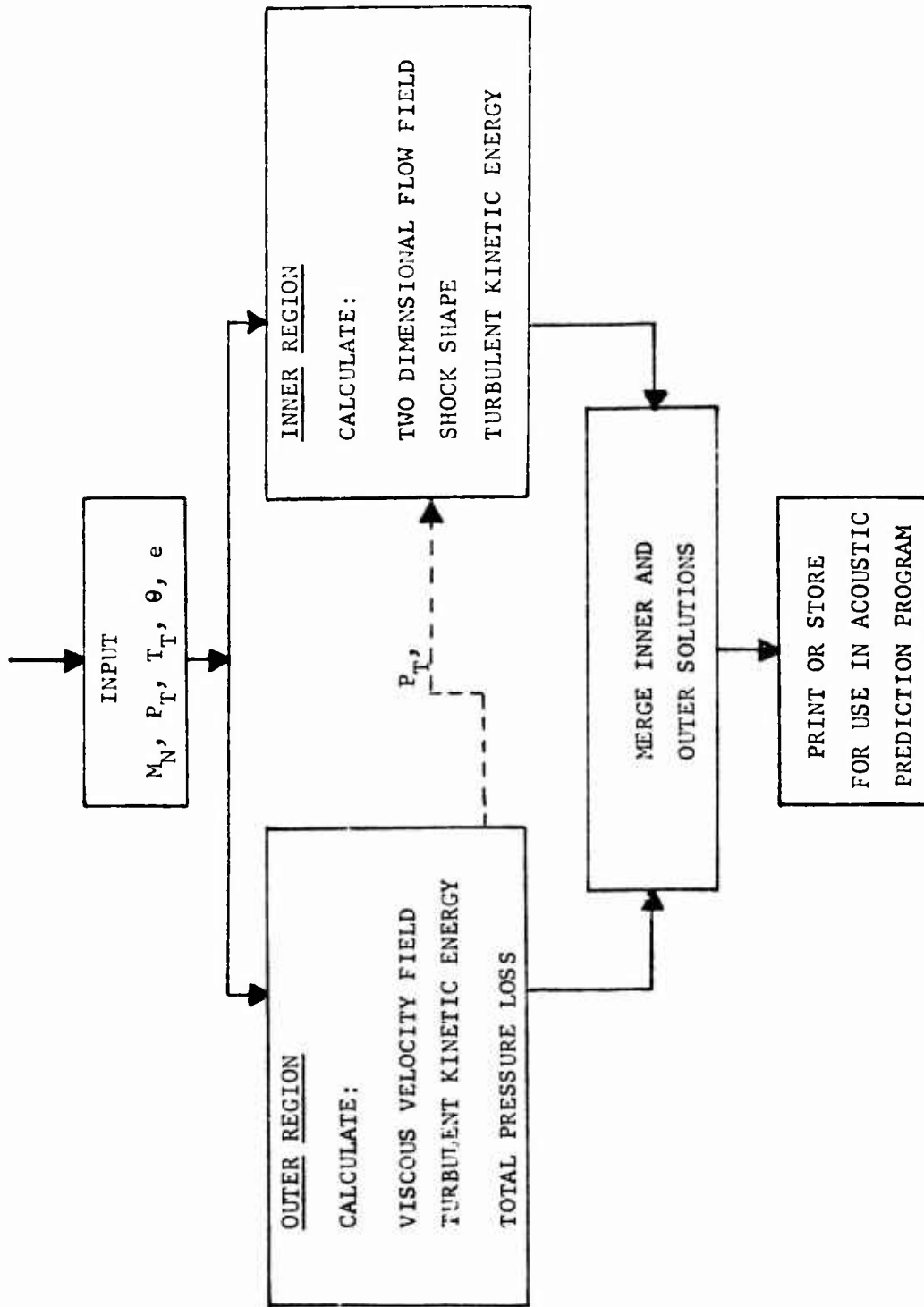


Figure 5 Outline of Complete Computational Procedure

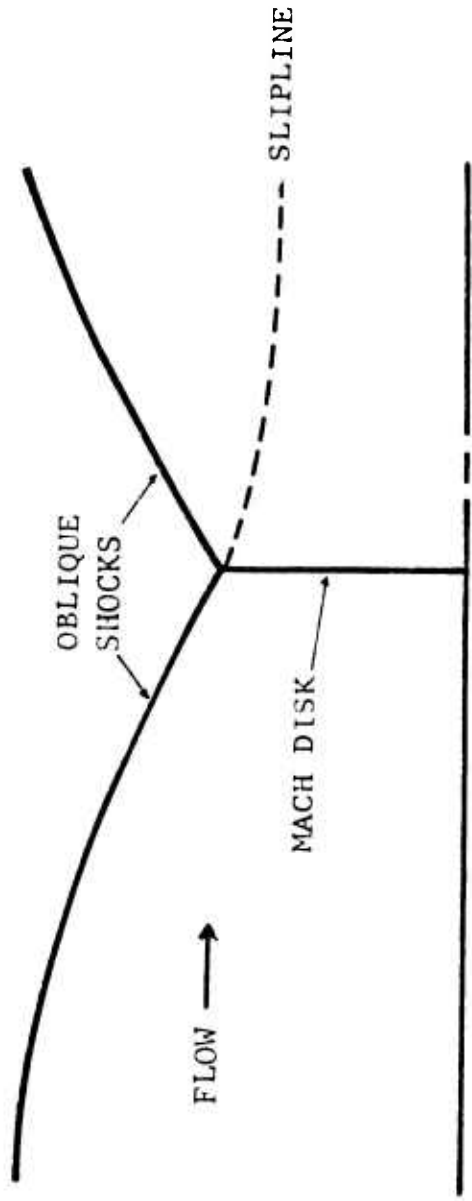


Figure 6 Mach Disk Model

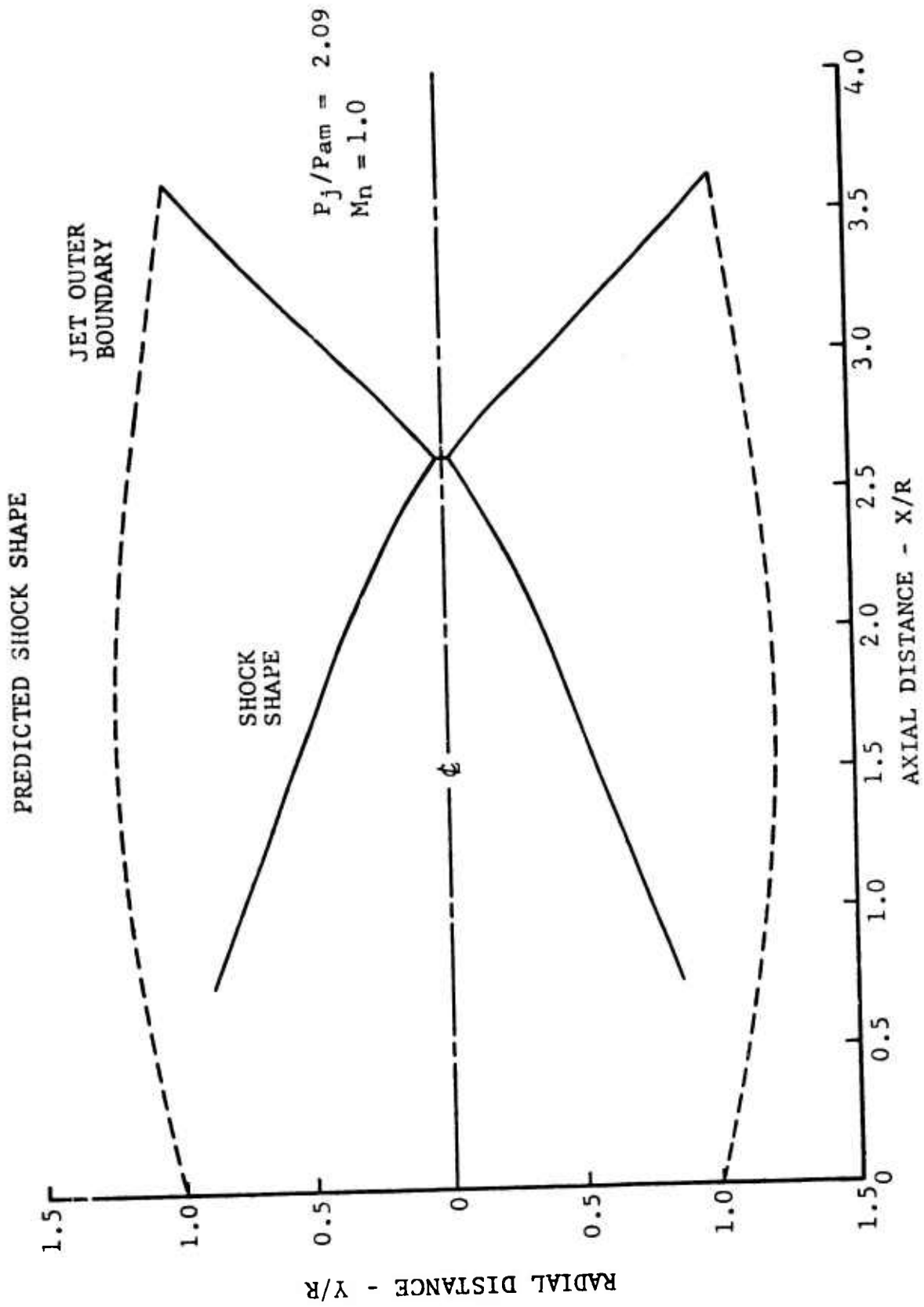


Figure 7 Predicted Shock Shape and Outer Boundary Shape --- Inviscid

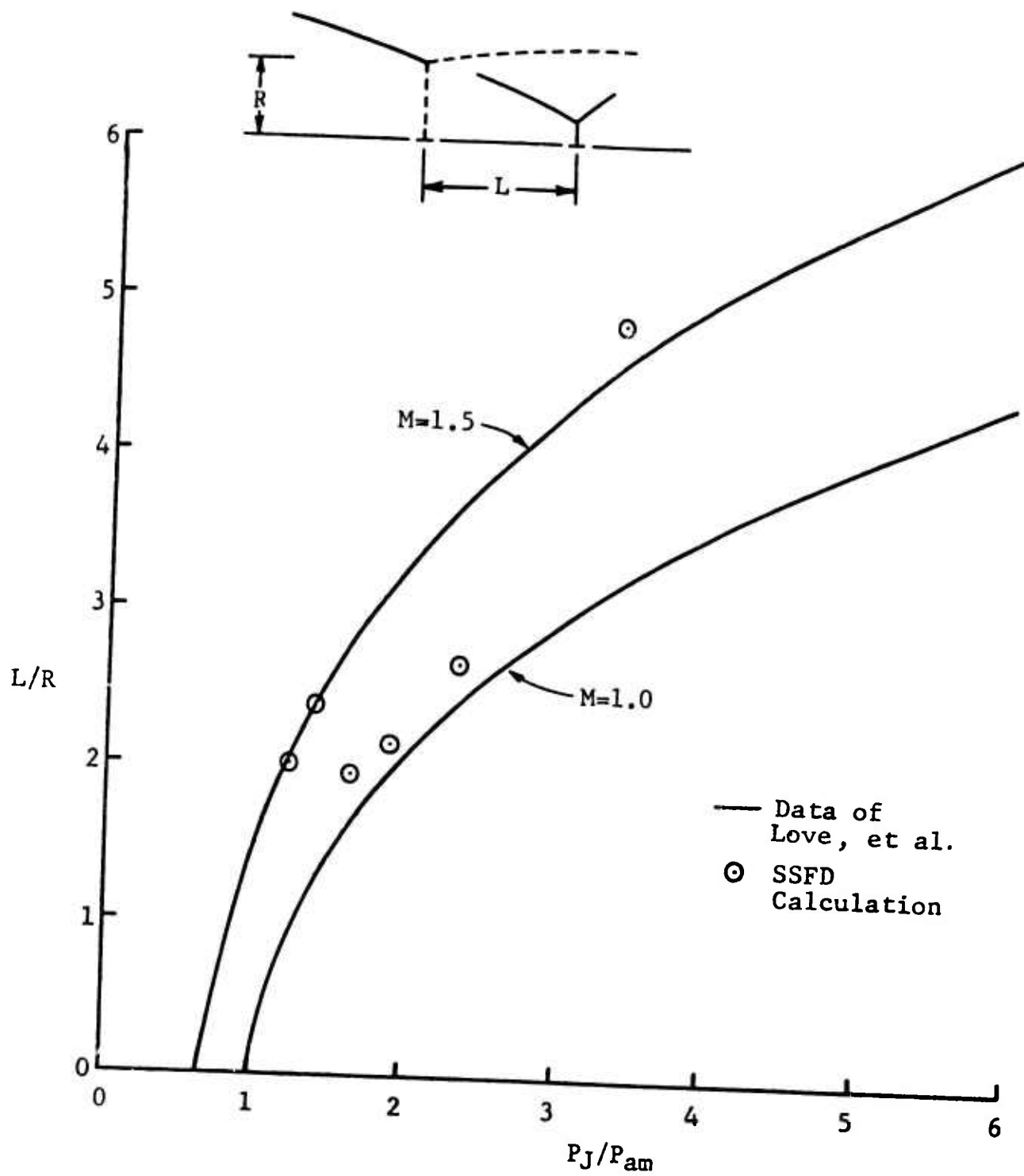


Figure 8 Intersection of Shock Shape with Axis of Symmetry

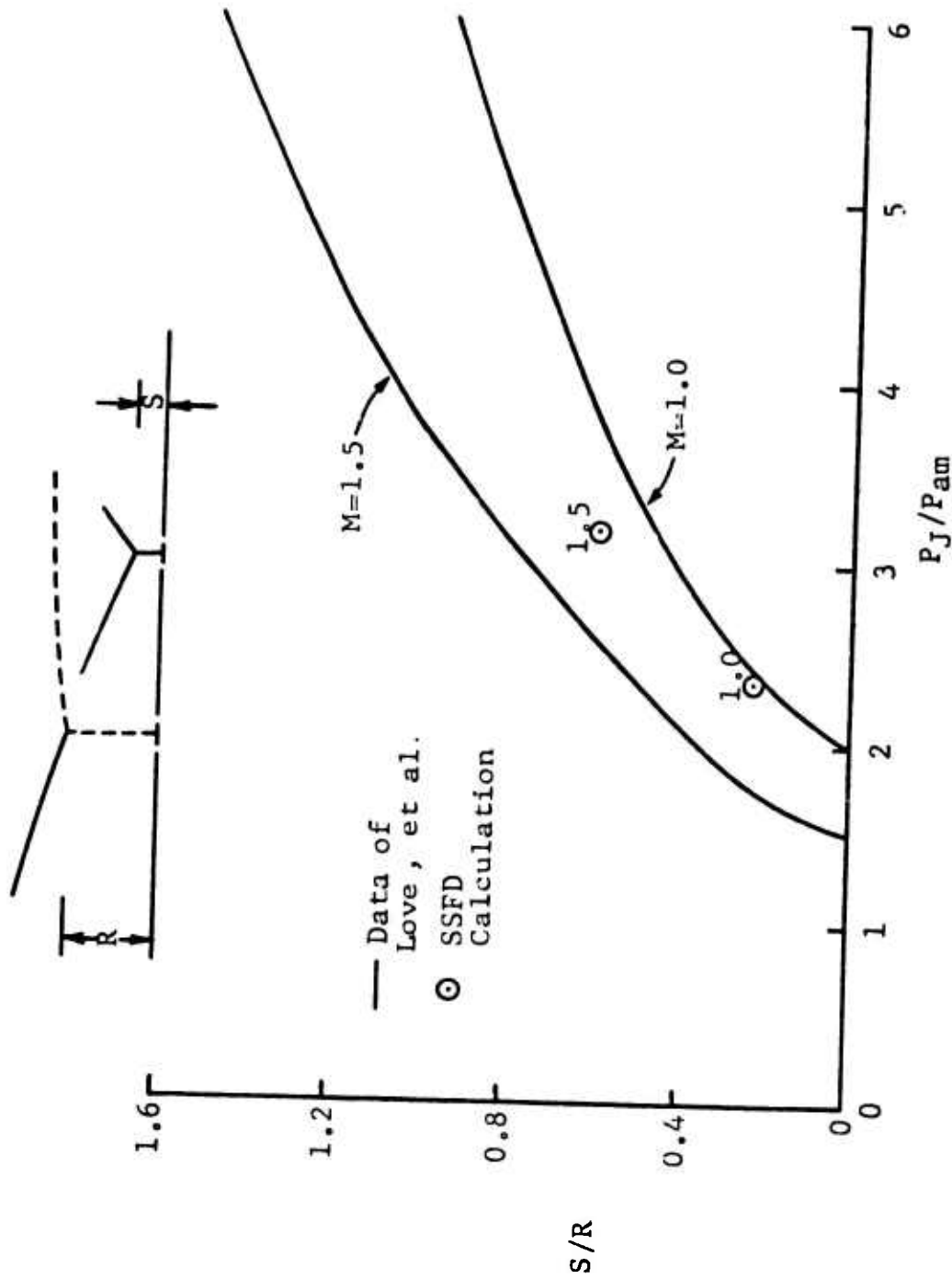


Figure 9 Height of Mach Disk

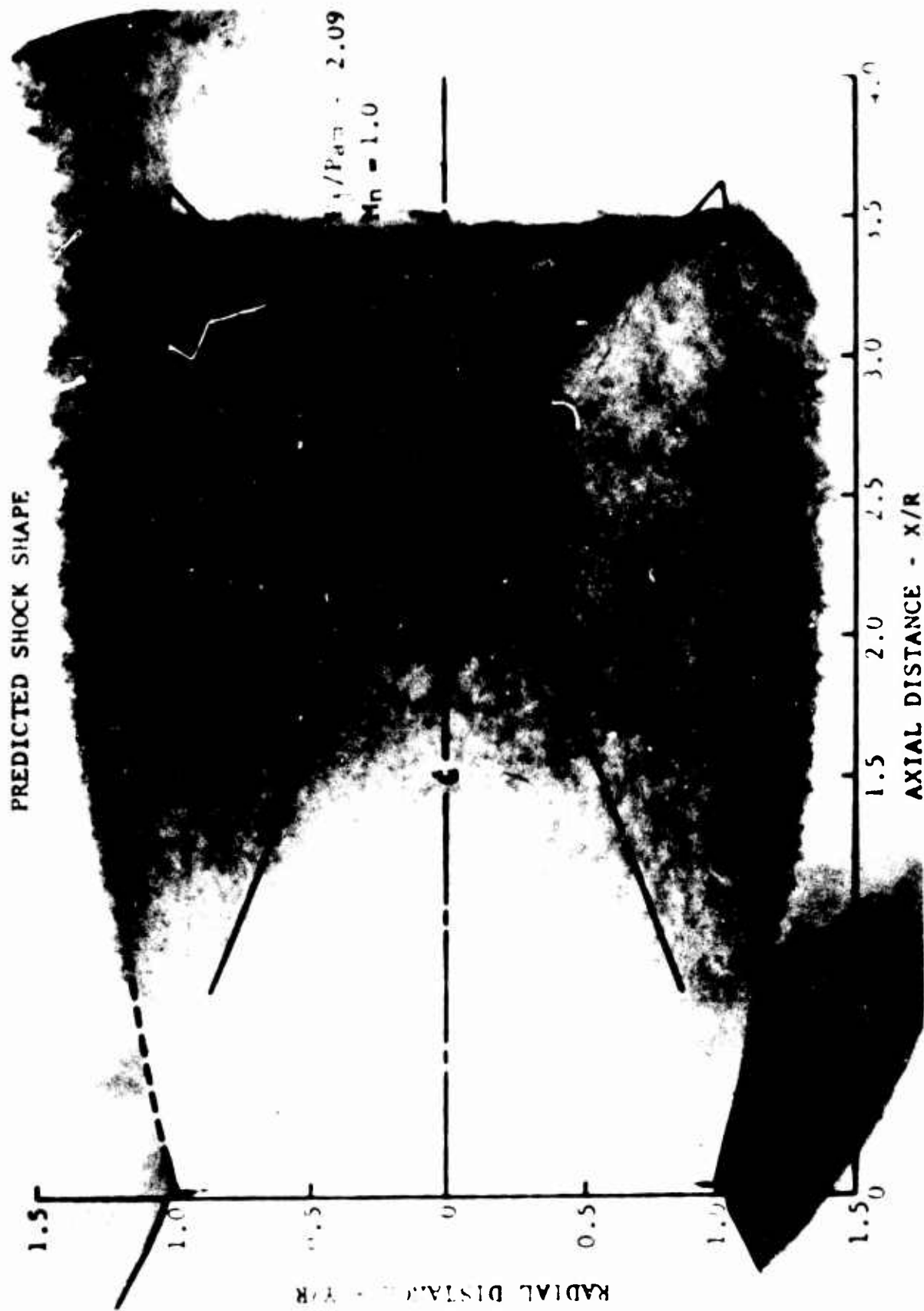


Figure 10 Shock Shape Prediction on Schlieren Photograph

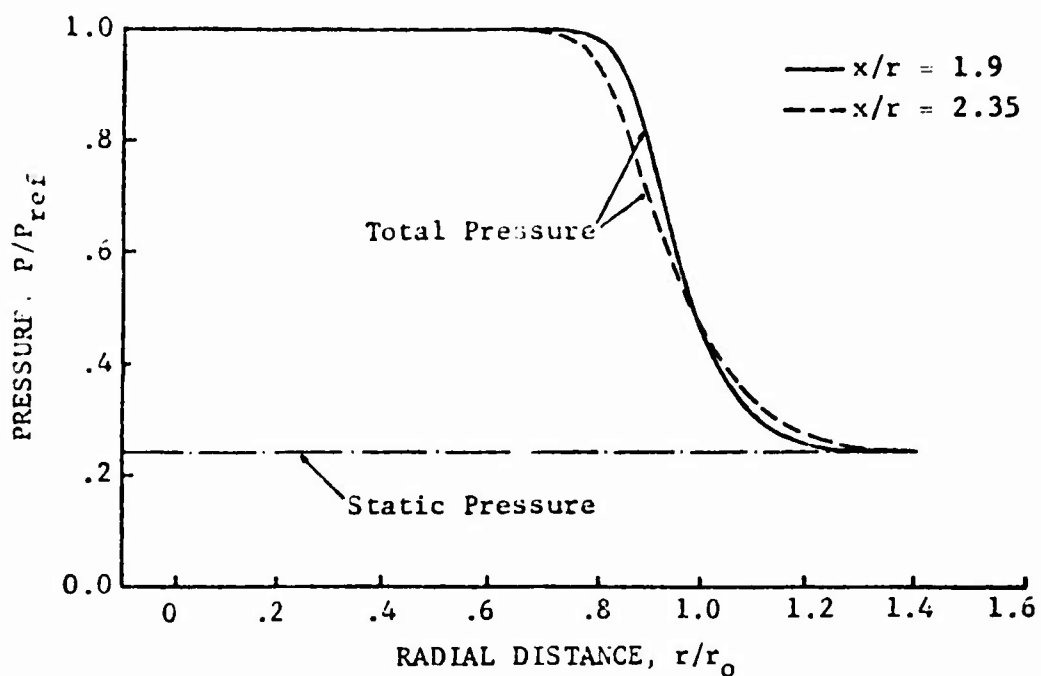


Figure 11 Cross-Stream Variation of Predicted Total Pressure and Static Pressure for Ideally Expanded Jet $M_{exit} = 1.60$, $P_{amb}/P_{Tref} = .242$

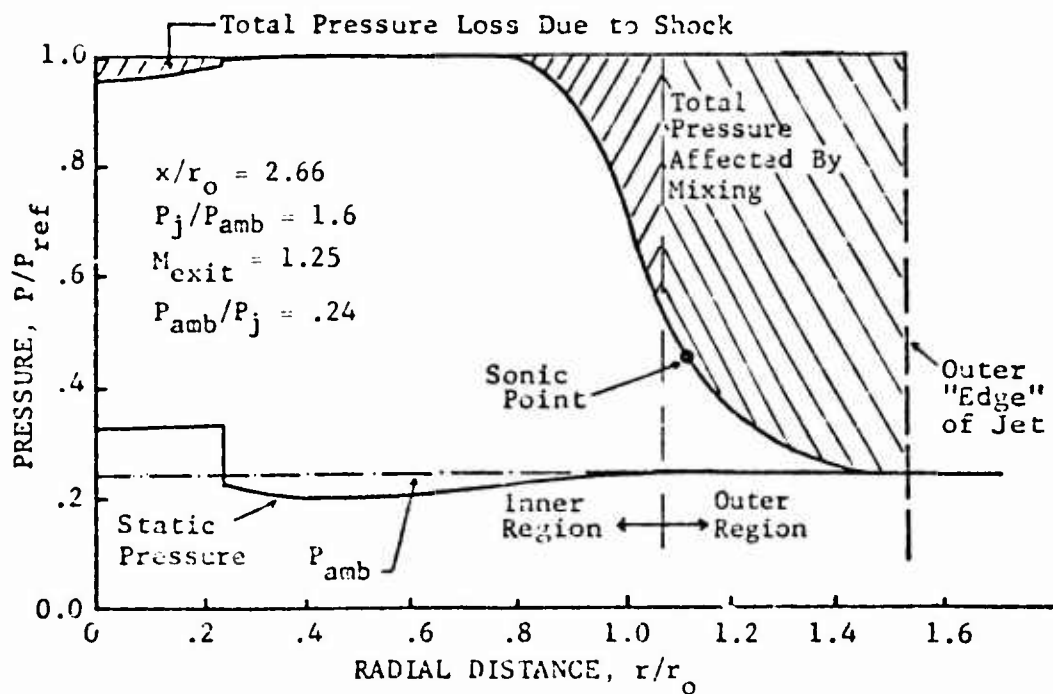


Figure 12 Cross-Stream Variation of Predicted Total Pressure and Static Pressure for Slightly Underexpanded Jet, Showing Total Pressure Loss Due to Both Shocks and Mixing. $M_{exit} = 1.25$, $P_{amb}/P_{Tref} = .242$

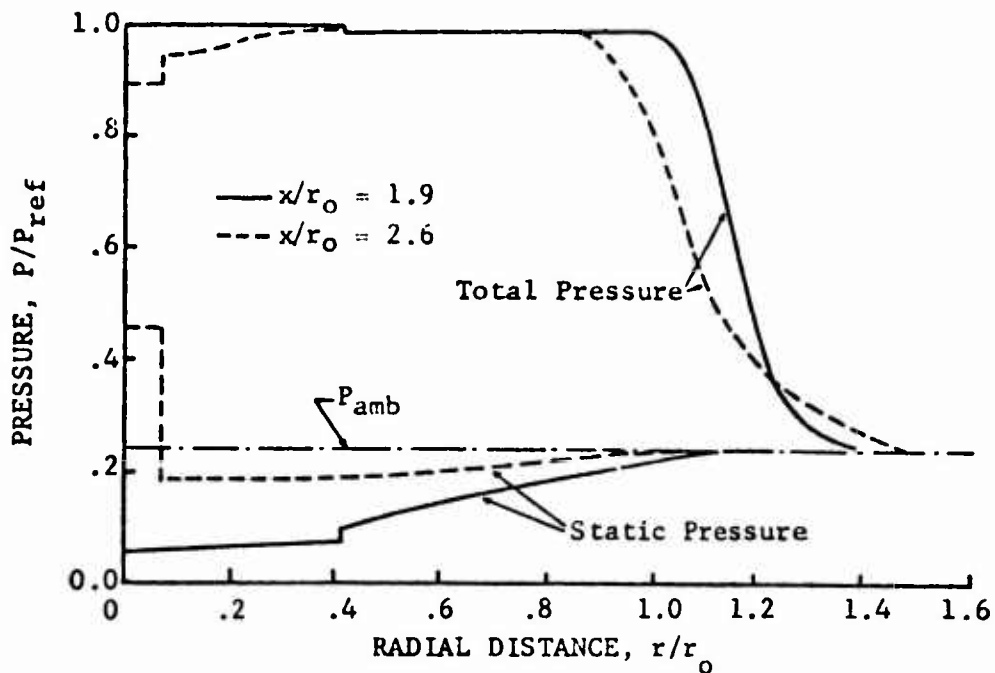


Figure 13 Cross-Stream Variation of Predicted Total Pressure and Static Pressure for Jet from Convergent Nozzle, Showing Total Pressure Loss Due to Both Shocks and Mixing. $M_{exit} = 1.0$, $P_{amb}/P_{Tref} = .242$

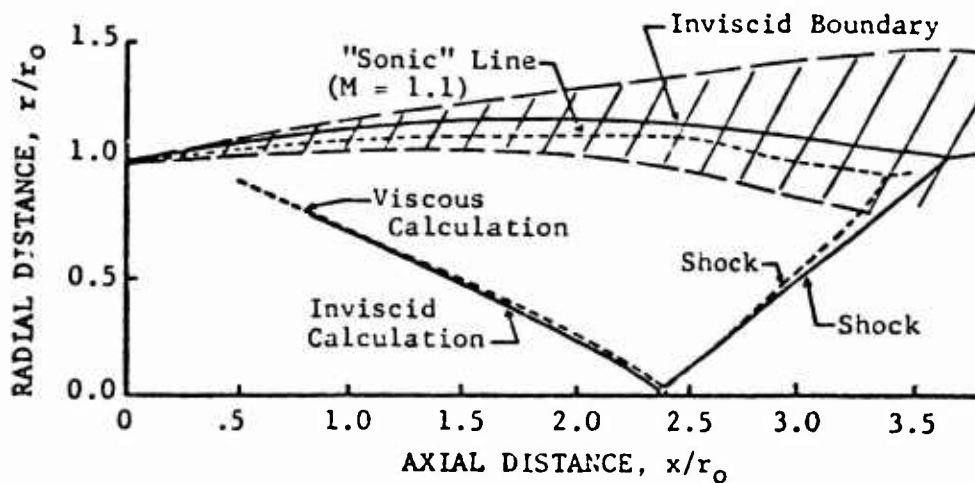


Figure 14 Comparison Between Predicted Shock Shapes Using Inviscid Prediction Technique and Coupled (Inner-Outer Analysis) Viscous Technique. Shaded Region Represents Flow Which Is Significantly Affected by Mixing. $M_{exit} = 1.25$, $P_{amb}/P_{Tref} = .242$

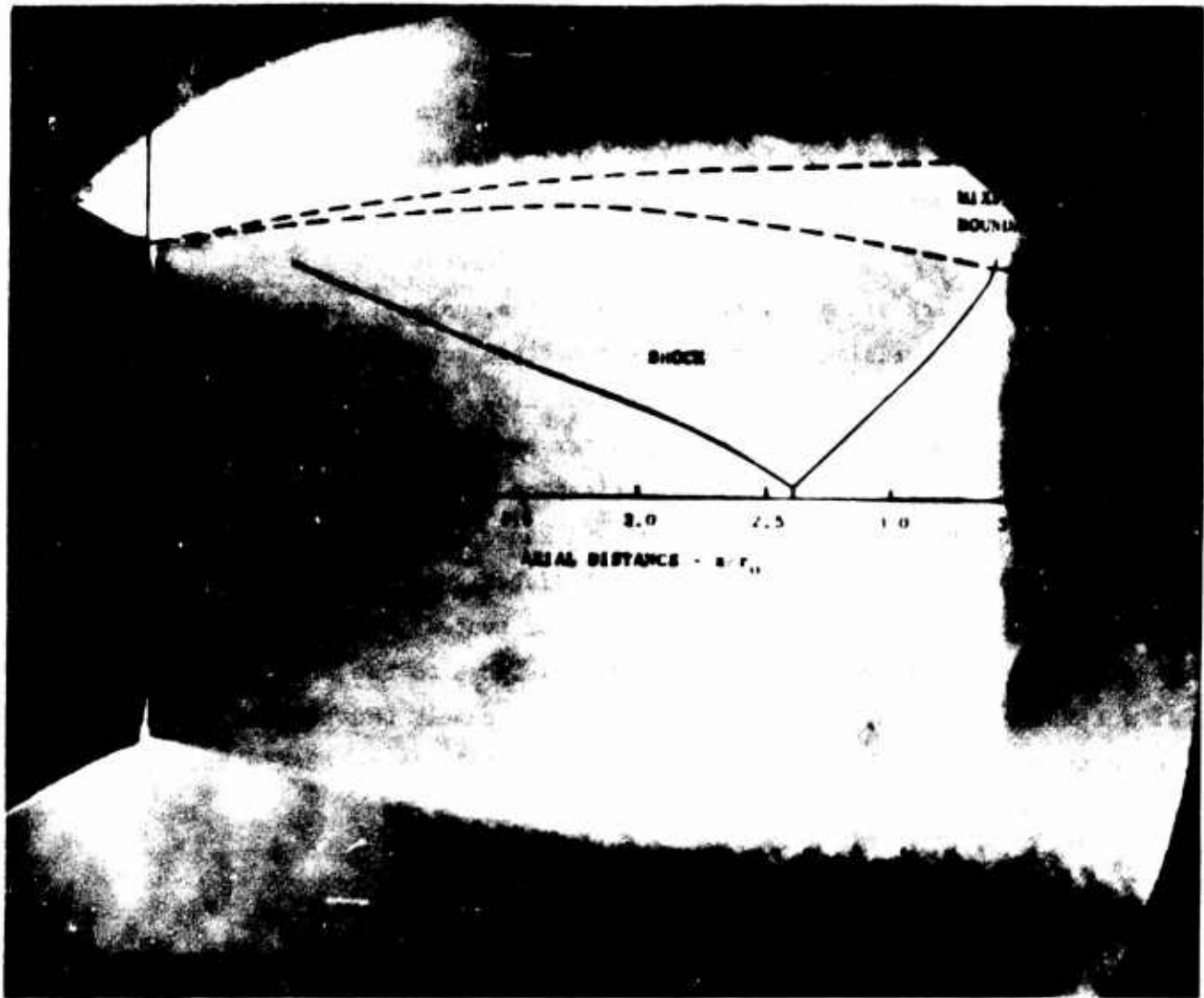


Figure 15 Comparison of the Theory Predicted Shock Structure and a Schlieren Photograph

II. THEORETICAL ACOUSTIC MODELS OF TURBULENT JETS

1. MOVING SOURCE MODELS FOR JET NOISE

R. Mani

The present section considers several problems of the sound power, power spectrum and directivity produced by moving acoustic sources shrouded by jet flows. The jets are assumed (for simplicity) to be characterized by a slug flow or top hat type mean velocity profiles in most cases. The sources are simple harmonic in their own frame of reference and are assumed to convect with the same velocity as the jet as well as at velocities of about 0.65 the jet velocity.

The studies are all motivated by one notion, namely, that Lighthill's original idea of ascribing jet noise to convected sources radiating freely to the ambient needs revision to allow for mean flow "shrouding" effects. The studies explain several experimentally observed features of jet noise such as the failure to exhibit convective amplification (particularly at high frequencies and shallow angles to the exhaust axis) and associated failure of peak frequencies in the power spectrum to shift linearly with jet velocity. Implications for the jet density exponent issue for heated jets are also considered. The study may be regarded as moving source solutions to the Phillips¹ equation for jet noise with a specific velocity profile, namely the top hat profile. The advantage of choice of a simple velocity profile is to obtain solutions valid for arbitrary frequencies.

1.1 First Model Problem (Figure 16)

Consider the problem of determining the sound field due to a fluctuating monopole point source translating at a uniform subsonic velocity M_c (where $M < 1$, M being the Mach number and c is the speed of sound). The source translates along the axis of a round jet whose velocity profile we assume to be a slug/flow velocity profile. Also, the jet velocity is taken equal to that of the source. The problem is illustrated in Figure 16. The monopole source is assumed to have a time dependence in its own frame of reference of $q_0 \cos(\omega_0 t)$. The mean jet density and temperature are assumed to be the same as that of the ambient.

Analytically, we wish to determine an acoustic velocity potential ϕ which satisfies in region I (outside the jet)

$$\nabla^2 \phi - \frac{1}{c^2} \phi_{tt} = 0 \quad (1)$$

and in region II (within the jet)

$$(1 - M^2) \phi_{xx} + \nabla_2^2 \phi - \frac{2M}{c} \phi_{xt} - \frac{\phi_{tt}}{c^2} = \frac{q_0}{\rho_0} \cos(\omega_0 t) \delta(x - Mct) \delta(y) \delta(z), \quad (2)$$

where ∇_2^2 stands for the Laplace operator in the $y - z$ plane. At the jet still-air interface, i.e., at $r = a$, we require (a) continuity of pressure, p , where

$$p = \rho_0 \phi_t, \quad \text{in region I,} \quad (3)$$

and

$$p = -\rho_0 (\phi_t + Mc \phi_x), \quad \text{in region II.} \quad (4)$$

and (b) continuity of radial acoustic particle displacement, say η , where

$$\phi_r = \eta_t, \quad \text{in region I,} \quad (5)$$

and

$$\phi_r = \eta_t + Mc \eta_x, \quad \text{in region II.} \quad (6)$$

An elegant procedure of solution suited to the above problem has been given by Morse and Ingard² and we follow closely their method of solution.

Let $\bar{\phi}$, \bar{p} , etc., denote the Fourier transforms with respect to time of the corresponding physical quantities. Thus

$$\bar{\phi} = \frac{1}{2\pi} \int_{-\infty}^{\infty} \phi e^{j\omega t} dt \quad j = \sqrt{-1} \quad (7)$$

and

$$\phi = \int_{-\infty}^{\infty} \bar{\phi} e^{-j\omega t} d\omega. \quad 35$$

Also, we write $\cos(\omega_0 t) = \frac{1}{2}[\exp(j\omega_0 t) + \exp(-j\omega_0 t)]$. The problem for the transforms is

$$\begin{aligned} \nabla^2 \bar{\phi} + k^2 \bar{\phi} &= 0, & \text{in region I,} & (1') \\ (1 - M^2) \bar{\phi}_{xx} + \nabla_z^2 \bar{\phi} + 2jkM \bar{\phi}_x + k^2 \bar{\phi} &= \frac{q_0 \delta(y) \delta(z)}{4\pi\rho_0 Mc} \end{aligned}$$

$$\times \left[\exp\left(\frac{j(k - k_0)x}{M}\right) + \exp\left(\frac{j(k + k_0)x}{M}\right) \right], \quad \text{in region II;} \quad (2')$$

$$\bar{p} = j\omega\rho_0 \bar{\phi}, \quad \text{in region I,} \quad (3')$$

$$\bar{p} = -\rho_0(-j\omega\bar{\phi} + Mc\bar{\phi}_x), \quad \text{in region II;} \quad (4')$$

$$\bar{\phi}_r = -j\omega\bar{\eta}, \quad \text{in region I,} \quad (5')$$

$$\bar{\phi}_r = -j\omega\bar{\eta} + Mc\bar{\eta}_x, \quad \text{in region II.} \quad (6')$$

Let $\bar{\phi} = \bar{\phi}^+ + \bar{\phi}^-$ and similarly for \bar{p} and $\bar{\eta}$ where $\bar{\phi}^+$ corresponds to the solution with the term $\exp\{j(k - k_0)x/M\}$ in equation (2') and $\bar{\phi}^-$ to the term involving $\exp\{j(k + k_0)x/M\}$. Note that $k = \omega/c$, $k_0 = \omega_0/c$, etc.

Consider in detail the problem for $\bar{\phi}^+$. Intuitively, it is clear that $\bar{\phi}^+$, \bar{p}^+ , $\bar{\eta}^+$ all have an x -dependence of the type $\exp\{j(k - k_0)x/M\}$. "Factoring" this dependence out, one is left with the following problem in the $y - z$ plane:

$$\nabla_z^2 \bar{\phi}^+ + k^{+2} \bar{\phi}^+ = 0, \quad \text{in region I;} \quad (8)$$

$$\nabla_2^2 \bar{\phi} + \kappa^{+2} \bar{\phi} = \frac{q_0 \delta(y) \delta(z)}{4\pi \rho_0 M c}, \quad \text{in region II;} \quad (9)$$

where

$$\kappa^{+2} = \left(\frac{1 - M^2}{M^2} \right) \left[\left(\frac{k_0}{1 - M} - k \right) \left(k - \frac{k_0}{1 + M} \right) \right] \quad (10)$$

and is ≥ 0 only if $k_0^+ \geq k \geq k_0^-$, where $k_0^+ = k_0 / (1 - M)$ and $k_0^- = k_0 / (1 + M)$

$$\kappa^{+2} = \frac{1}{M^2} \left[(\kappa_0^+ - k) (k - \kappa_0^-) \right], \quad (11)$$

where

$$\kappa_0^+ = k_0 (1 + M), \quad \kappa_0^- = k_0 (1 - M).$$

Also, let

$$\underline{\kappa}^{+2} = -\kappa^{+2} = \frac{1}{M^2} \left[(k - \kappa_0^+) (k - \kappa_0^-) \right]. \quad (12)$$

Note that

$$k_0^+ \geq \kappa_0^+ \geq k_0 \geq k_0^- \geq \kappa_0^-.$$

The fact that $\kappa^{+2} \geq 0$ only if $k_0^+ \geq k \geq k_0^-$ expresses the result that in the far field the moving source yields a frequency spectrum containing frequencies in the range $\omega_0 / (1 - M) \geq \omega \geq \omega_0 / (1 + M)$ which is what we expect from the Doppler shift formula. We restrict our attention to this range of k . The matching conditions for equations (8) and (9) are that, at $r = a$,

$$\bar{\phi}^+(r = a^+) = \frac{k_0}{k} \bar{\phi}^+(r = a^-) \quad (\text{pressure matching conditions}), \quad (13)$$

$$\tilde{\phi}_r^+(r = a^+) = \frac{k}{k_0} \tilde{\phi}_r^+(r = a^-) \quad (\text{transverse particle displacement matching condition}) \quad (14)$$

To solve equations (8), (9), (10), and (11) in the range $k_0^- < k < k_0^+$ and with restriction to outgoing waves at infinity, in the range $k_0^- \leq k \leq k_0^+$ we assume, for $\tilde{\phi}^+$ in regions I and II,

$$\text{in I:} \quad (15)$$

$$\tilde{\phi}^+ = A_I^+ H_0^{(1)}(\kappa^+ r) \exp \frac{j(k - k_0)x}{M},$$

$$\text{in II:} \quad (16)$$

$$\tilde{\phi}^+ = [A_{II}^+ J_0(\kappa^+ r) - \frac{j q_0 H_0^{(1)}(\kappa^+ r)}{16\pi \rho_0 M c}] \exp \frac{j(k - k_0)x}{M},$$

and if $\kappa_0^+ \leq k < k_0^+$, in region II,

$$\tilde{\phi}^+ = [A_{II}^+ I_0(\kappa^+ r) - \frac{q_0 K_0(\kappa^+ r)}{8\pi^2 \rho_0 M c}] \exp \frac{j(k - k_0)x}{M}. \quad (17)$$

(The form for $\tilde{\phi}^+$ in region I is independent of whether $k \geq \kappa_0^+ \leq \kappa_0^+$.)

Note that the change of sign κ^{+2} depending on whether $k \in [k_0(1-M), k_0(1+M)]$ is associated with the fact that if the jet in the present problem were of infinite radius (i.e., the moving fluid occupied all space) the Doppler shifted frequencies would range over $\omega_0(1-M)$ to $\omega_0(1+M)$. In other words, as is well known, there is a difference in the Doppler shift frequencies depending on whether the observer moves towards a source or whether the source moves towards the observer. This difference will be seen later to play a key role in suppressing convective amplification at high frequencies.

Equations (15) and (16) or (15) and (17) may now be readily solved for A_I^+ and A_{II}^- by using the matching conditions (13) and (14). Since we are interested in far field pressures far outside the jet, we only give the result for A_I^+ :

(a) if $k_0^- < k < k_0^+$,

$$A_I^+ = \frac{q_0 k k_0 \kappa^+ [Y_0(\kappa^+ a) J_1(\kappa^+ a) - Y_1(\kappa^+ a) J_0(\kappa^+ a)]}{16\pi\rho_0 M c [k^2 \kappa_0^{(1)}(k^+ a) J_1(\kappa^+ a) - k^+ k_0^2 J_0(\kappa^+ a) H_1^{(1)}(k^+ a)]}; \quad (18a)$$

(b) if $k_0^+ < k < k_0^-$,

$$A_I^+ = \frac{-q k \kappa^+ k_0 [K_0(\kappa^+ a) I_1(\kappa^+ a) + I_0(\kappa^+ a) K_1(\kappa^+ a)]}{8\pi^2 \rho_0 V [k^2 \kappa_0^+ I_1(\kappa^+ a) H_0^{(1)}(k^+ a) + k_0^2 k^+ I_0(\kappa^+ a) H_1^{(1)}(k^+ a)]}. \quad (18b)$$

Equation (18) essentially completes the formal solution to the problem. The far field pressure and the radial acoustic velocity may be computed by using $\tilde{p} = j\omega\rho_0 \tilde{\phi}$ and $\tilde{\phi}_r$. In this problem, every point on a cylindrical surface concentric with the jet experiences the same pressure time history. Morse and Ingard² have discussed thoroughly the problem of determining the power spectrum and total power radiated by the source and their concluding result is that the power spectral density extends over a frequency range $[\omega_0/(1+M)] < \omega < [\omega_0/(1-M)]$ and is given by

$$(16\pi\rho_0 M c \omega) |A_I^+|^2 = I(\omega). \quad (19)$$

The total power is given by

$$P = \int_{\omega_0/(1+M)}^{\omega_0/(1-M)} I(\omega) d\omega. \quad (20)$$

Actually Morse and Ingard² consider the case of a monopole point source convecting at M_c in free space, for which case

$$A_I^+ = \frac{-jq_0}{16\pi\rho_0Mc} \quad (21)$$

and hence

$$I(\omega) = \frac{q_0^2\omega}{16\pi\rho_0Mc} \quad \text{for } \frac{\omega_0}{1+M} \leq \omega \leq \frac{\omega_0}{1-M} \quad (22)$$

and the total power is

$$P = \frac{q_0^2\omega_0^2}{8\pi\rho_0(1-M^2)^2c} \quad (23)$$

Thus, in the case of a convected monopole, the convective amplification is as $(1-M^2)^{-2}$.

If we take the limit as $k_0 a \rightarrow 0$ of equation (18), we find that A_I^+ tends to (independent of whether $k > \kappa_0^+$ or $k < \kappa_0^+$)

$$A_I^+ \rightarrow \frac{-jq_0\omega}{16\pi\rho_0Mc\omega_0} \quad (24)$$

so that

$$I(\omega) = \frac{q_0^2\omega}{16\pi\rho_0Mc} \left(\frac{\omega}{\omega_0}\right)^2 \quad \text{for } \frac{\omega_0}{1+M} \leq \omega \leq \frac{\omega_0}{1-M} \quad (25)$$

and

$$P = \frac{q_0^2\omega_0^2(1+M^2)}{8\rho_0c\pi(1-M^2)^2} \quad (26)$$

In the general case, Λ_I^+ , $I(\omega)$ and P are given by equations (18a), (18b), (19) and (20), and specific results will be discussed in the following.

The total power emitted by such a source nondimensionalized by $[q_0^2 \omega_0^2 / 8\pi\rho_0 (1 - M^2)^2 c]$ and expressed in dB is plotted as a function of $(k_0 a)$ and M in Figure 17.

Shown by single points on the extreme right in Figure 17 are points given by $20 \log_{10} (1 - M^2)$, being the correction if there were no convective amplification at all corresponding to Csanady's³ suggestion. The portions of the curves corresponding to corrections > 0 dB indicate underestimates of convective amplification as estimated from a freely moving source model and conversely.

Clearly, such curves confirm the frequency dependent nature of convective amplification. The curves flatten as we move to the right and if we identify the point on each curve (for the different Mach numbers) at which the correction is within a decibel of the limit as $(k_0 a) \rightarrow \infty$, one deduces that beyond a source Strouhal number $[(2f_0 a)/Mc]$ of 0.5 there would be no significant convective amplification. Figure 15 of Lush's⁴ paper indicates lack of convective amplification beyond $[2f_0 a/Mc]$ of about 0.3.

Finally, we consider the implications with regard to Strouhal scaling of the results shown in Figure 17. As a starting point, in Figure 18 we show under the curve labelled $M = 0.3$, one-third octave intensities obtained by Lush⁴ in Figure 8 of his paper for a jet Mach number of 0.37 at 90° . This curve is chosen as a base line because at that low Mach number of 0.37 and location (90° to jet axis) we expect little convective amplification effects. The abscissae are shown in Strouhal numbers, $St = (2fa/Mc)$, and the ordinates are only relative decibel levels.

An intensity spectrum at 90° was chosen because, in addition to lack of convective amplification effects, the 90° location also provides a very good and clean measure of the intrinsic strength of the sources (their frequency distribution). This is because that location is largely characterized by "self noise". A basic assumption of the process used in deriving Figure 19 is that the frequency distribution of the "intrinsic source strengths" does follow Strouhal scaling with respect to velocity. This is, of course, excellently

borne out by Figure 8 of reference [4] where Lush shows that, at the 90° location, Strouhal scaling with respect to velocity was obtained. The basic argument of what follows is to point out that the radiative efficiency of the sources is frequency dependent and, being higher for the low frequencies than for the high frequencies, causes peak frequencies of the sound power spectrum to scale with velocity much slower than a first power (as is assumed in conventional Strouhal scaling). The particular low Mach number datum used to establish this result (taken in this case as the 90° intensity spectrum of Lush⁴) is not the main issue of this paper: a different datum would lead to the same qualitative conclusions. Ideally, perhaps, one would have to work out separately the "shear noise" and "self noise" portions of the power spectra.

The spreading of the source frequency due to the Doppler shift makes it a little difficult to apply Figure 17 directly. However, it can be shown that the Doppler spreading will be narrower than conventional moving source results would indicate (see Reference 5). Further, if we are interested in the sound power spectrum, it seems reasonable to apply Figure 17 to Figure 18 as follows. For each Strouhal number St , and Mach number M , determine a source frequency parameter $k_0 a = St \cdot \pi M$ and then determine the decibel correction from Figure 17. Starting with the curve labeled $M = 0.3$, such a frequency dependent correction procedure was applied to derive the curve labelled $M = 0.5$, $M = 0.7$ and $M = 0.9$ from the curve labelled $M = 0.3$. As expected, one observes a shift back of the peak frequency (in terms of the Strouhal numbers) at which the sound power spectrum peaks. The spectra are pretty flat as is typical of jet noise but an attempt was made to estimate the peak Strouhal number as a function of jet Mach number and the results are shown in Figure 19. Undoubtedly by a purely fortuitous coincidence, the curve in Figure 19 is fitted very well by a relation of the type $(St)_p = (0.21)/M$. Since the Strouhal number itself is given by $(f_p D/V)$, Figure II-5 suggests that the peak frequency in the sound power spectrum is independent of jet velocity being given (in the case of Figure 19 by $[(0.21)c/D]$). Such a tendency for the peak frequency to be independent of jet velocity has been noticed in several experiments.

The suggestion that emerges therefore is that the tenacious adherence of the total power to an eighth power law as well as the tendency of peak frequency of the power spectrum to be relatively insensitive to jet velocity are both manifestations of the same result indicated by Figure 17, namely the inhibition of convective amplification with increasing frequency and jet velocity.

1.2 Asymmetric Line of Source Convection

To illustrate the effect of lines of source convection different from the jet axis, we study the acoustic output of a line acoustic source convecting at the jet velocity in a plane, slug flow jet. The problem is two dimensional and, as indicated in Figure 20, the line source is allowed to convect at a distance σh from the jet centerline where h is the half width of the jet. We restrict σ to $0 \leq \sigma < 1$ to ensure that the source is always within the jet. The case of $\sigma = 0$ obviously corresponds to case of symmetric or centerline source convection.

The analytical problem corresponding to Figure 20 may be described in terms of the acoustic velocity potential ϕ as follows. We wish to determine ϕ such that in regions I, III (outside the jet), ϕ satisfies:

$$\nabla^2 \phi - \frac{1}{c^2} \phi_{tt} = 0 \dots \quad (27)$$

Inside the jet (in region II), it satisfies:

$$(1 - M^2) \phi_{xx} + \phi_{yy} - \frac{2M}{c^2} \phi_{xt} - \frac{\phi_{tt}}{c^2} = \frac{q_0}{\rho_0} \delta(x - Mct) \\ \times \delta(y - \sigma h) \cos(\omega_0 t) \dots \quad (28)$$

At both interfaces ($y = \pm h$) the acoustic pressures and transverse particle displacements must be continuous. Also in regions I and III only outgoing waves are permitted.

As in Subsection 1.1, the method of Fourier transforms will be applied since the problem is basically a transient problem.

Let $\tilde{\phi}$ be the Fourier Transform of ϕ , i.e.,

$$\tilde{\phi} = \frac{1}{2\pi} \int_{-\infty}^{\infty} \phi e^{j\omega t} dt \quad (j = \sqrt{-1})$$

where

$$\phi = \int_{-\infty}^{\infty} \tilde{\phi} e^{-j\omega t} d\omega$$

(29)

Also we write $\cos(\omega_0 t) = \frac{1}{2} [\exp(j\omega_0 t) + \exp(-j\omega_0 t)]$.

The problem for $\tilde{\phi}$ is:

$$v^2 \phi'' + k^2 \tilde{\phi} = 0 \text{ in regions I and III;} \quad (27')$$

$$\begin{aligned} (1 - M^2) \tilde{\phi}_{xx} + \tilde{\phi}_{yy} + 2jkM\tilde{\phi}_x + k^2 \tilde{\phi} \\ = \frac{q_0 \delta(y - \sigma h)}{4\pi \rho_0 Mc} \left\{ \exp\left(\frac{j(k - k_0)x}{M}\right) \right. \end{aligned}$$

$$\left. + \exp\left(\frac{j(k + k_0)x}{M}\right) \right\} \text{ in region II.} \quad (28')$$

The transforms \tilde{p} and $\tilde{\eta}$ of the acoustic pressure and transverse acoustic particle displacement are related to $\tilde{\phi}$ by:

$$\tilde{p} = j\omega\rho_0 \tilde{\phi} \text{ in I, III} \quad (30)$$

$$= -\rho_0 \{-j\omega \tilde{\phi} + Mc\tilde{\phi}_x\} \text{ in II}$$

$$\begin{aligned}\tilde{\phi}_y &= -j\omega\tilde{\eta} \text{ in I, III} \\ \tilde{\phi}_y &= -j\omega\tilde{\eta} + M\kappa\tilde{\eta}_x \text{ in II}\end{aligned}\quad (31)$$

Let $\tilde{\phi} = \tilde{\phi}^+ + \tilde{\phi}^-$ and similarly for \tilde{p} and $\tilde{\eta}$ where $\tilde{\phi}^+$ corresponds to the solution with the term $\exp\left\{\frac{j(k - k_0)x}{M}\right\}$ in (28') and $\tilde{\phi}^-$ to the term $\exp\left\{\frac{j(k + k_0)x}{M}\right\}$ in (28'). Note that $k = \omega/c_0$, $k_0 = \omega_0/c_0$, etc. Consider in detail the problem for $\tilde{\phi}^+$. Intuitively it is clear that $\tilde{\phi}^+$, $\tilde{\eta}^+$ and \tilde{p}^+ all have an x -dependence of type $\exp\{j(k - k_0)x/M\}$. "Factoring" this dependence out, one is left with the following one-dimensional problem for $\tilde{\phi}^+$:

$$\frac{d^2\tilde{\phi}^+}{dy^2} + \kappa^{+2}\tilde{\phi}^+ = 0 \text{ in I, III} \quad (32)$$

and

$$\frac{d^2\tilde{\phi}^+}{dy^2} + \kappa^{+2}\tilde{\phi}^+ = \frac{q_0 \delta(y - \sigma h)}{4\pi\rho_0 Mc} \text{ in II} \quad (33)$$

where

$$\kappa^{+2} = \frac{(1 - M^2)}{M^2} \left\{ \left(\frac{k_0}{1 - M} - k \right) \left(k - \frac{k_0}{1 + M} \right) \right\} \quad (34)$$

and is ≥ 0 only if $k_0^+ \geq k \geq k_0^-$, where $k_0^+ = k_0/(1 - M)$ and $k_0^- = k_0/(1 + M)$.

$$\kappa^{+2} = \frac{1}{M^2} \left\{ (\kappa_0^+ - k) (k - \kappa_0^-) \right\} \quad (35)$$

where $\kappa_0^+ = k_0(1 + M)$ and $\kappa_0^- = k_0(1 - M)$. Also, let

$$\underline{\kappa}^{+2} = -\kappa^{+2} = \frac{1}{M^2} \left[(k - \kappa_0^+) (k - \kappa_0^-) \right] \quad (36)$$

Note that $k_0^+ \geq k_0^+ \geq k_0 \geq k_0^- \geq k_0^-$. The fact that $k+2 \geq 0$ only if $k_0^+ \geq k \geq k_0^-$ expresses the result that in the far field the moving source yields a frequency spectrum containing frequencies in the range $\omega_0/(1-M) \geq \omega \geq \omega_0/(1+M)$ which is what we expect from the Doppler shift formula. We restrict our attention to this range of k . The matching conditions for equations (32, 33) are:

$$\begin{aligned} \bar{\phi}^+ \{y = \pm h \text{ outside jet}\} \\ = \frac{k_0}{k} \bar{\phi}^+ \{y = \pm h \text{ inside jet}\} \dots \end{aligned} \quad (37)$$

and

$$\begin{aligned} \frac{d\bar{\phi}^+}{dy} \{y = \pm h \text{ outside jet}\} \\ = \frac{k}{k_0} \frac{d\bar{\phi}^+}{dy} \{y = \pm h \text{ inside jet}\} \dots \end{aligned} \quad (38)$$

To solve (32), (33) in the range $k_0^- \leq k \leq k_0^+$ subject to the matching conditions (37), (38) is actually a somewhat more tedious problem than the problem studied in Section 1.1. Assume for $\bar{\phi}^+$ the following forms in regions I, II and III:

$$\bar{\phi}^+ = A \exp\left\{\frac{j(k - k_0)x}{M}\right\} \exp[jk^+(y - h)] \dots \quad (39)$$

In region II if $k_0^- \leq k \leq k_0^+$:

$$\begin{aligned} \bar{\phi}^+ = \{B \sin[\kappa^+(y - h)] - \frac{j \alpha_0 \exp[j \kappa^+ |y - \sigma h|]}{8\pi \rho_0 M c \kappa^+} \\ + C \sin[\kappa^+(y + h)] \exp\left[\frac{j(k - k_0)x}{M}\right] \dots \end{aligned} \quad (40)$$

on the other hand if $\kappa_0^+ \leq k \leq \kappa_0^+$:

$$\begin{aligned} \tilde{\phi}^+ = & \{ B \sinh[\underline{\kappa}^+(y - h)] - \frac{q_0 \exp[-\underline{\kappa}^+|y - \sigma h|]}{8\pi \rho_0 M c \underline{\kappa}^+} \\ & + C \sinh[\underline{\kappa}^+(y + h)] \} \exp\left[\frac{j(k - k_0)x}{M}\right] \end{aligned} \quad (40b)$$

In region II:

$$\tilde{\phi}^+ = D \exp\left[\frac{j(k - k_0)x}{M}\right] \exp[-j k^+(y + h)]. \quad (41)$$

Evaluating $\tilde{\phi}^+$ and $\frac{d\tilde{\phi}^+}{dy}$ in regions I, II and III and applying the matching conditions (37, 38) yields a set of four simultaneous equations for A, B, C, D. Solving for them yields (for A, D): if $k_0^- \leq k \leq \kappa_0^+$:

$$\begin{aligned} (A, D) = & \left\{ \frac{k k_0 \cos(\kappa^+ \sigma h)}{[k^2 \kappa^+ \sin(\kappa^+ h) + j k_0^2 k^+ \cos(\kappa^+ h)]} \right. \\ & \left. \pm \frac{k k_0 \sin(\kappa^+ \sigma h)}{[k^2 \kappa^+ \cos(\kappa^+ h) - j k_0^2 k^+ \sin(\kappa^+ h)]} \right\} \frac{q_0}{8\pi \rho_0 M c} \end{aligned} \quad (42)$$

(plus sign goes with D, minus sign with A).

and if $\kappa_0^+ \leq k \leq \kappa_0^+$:

$$A, D) = \frac{-q_0}{8\pi \rho_0 Mc} \left\{ \frac{k k_0 \cosh(\underline{\kappa}^+ \sigma h)}{[k^2 \underline{\kappa}^+ \sinh(\underline{\kappa}^+ h) - j k^+ k_0^2 \cosh(\underline{\kappa}^+ h)]} \right. \\ \left. \pm \frac{\sinh(\underline{\kappa}^+ \sigma h) k k_0}{[k^2 \underline{\kappa}^+ \cosh(\underline{\kappa}^+ h) - j k^+ k_0^2 \sinh(\underline{\kappa}^+ h)]} \right\} \quad (43)$$

The power radiated across two planes shown dotted in Figure 20 may be obtained from the solutions (42, 43) by integrating the power spectral density which is:

$$4\pi \rho_0 V k^+ \omega [|\dot{A}|^2 + |\dot{D}|^2] \quad (44)$$

((44) may be derived by a calculation very similar to that outlined in Reference 3) over a frequency range $\omega_0 (1 + M)^{-1} \leq \omega \leq \omega_0 (1 - M)^{-1}$. If there were no jet at all, one would determine the acoustic field by solving for

$$\frac{d^2 \tilde{\phi}^+}{dy^2} + k^{+2} \tilde{\phi}^+ = \frac{q_0}{8\pi \rho_0 V} \delta(y) \dots \quad (45)$$

the solution to which is:

$$\tilde{\phi}^+ = \frac{-j q_0 \exp[j k^+ |y|]}{8\pi \rho_0 V k^+} \quad (46)$$

The power in this case is:

$$\frac{q_0^2}{8\pi \rho_0 V} \int_{\frac{\omega_0}{1+M}}^{\frac{\omega_0}{1-M}} \frac{\omega d\omega}{k^+} = \frac{q_0^2 \omega_0}{8\rho_0 (1-M^2)^{3/2}} \quad (47)$$

Thus the convection amplification factor for line velocity sources is $(1-M^2)^{-3/2}$. (The corresponding result for point velocity sources is, of course, $(1-M^2)^{-2}$.) In the limit as $k_0 h \rightarrow 0$, (42) and (43) give

$$A \text{ or } D = \frac{-j q_0 k}{8\pi \rho_0 k^+ k_0} \quad (48)$$

As in Section 1.1, the moving source in a jet of limitingly small thickness does not reduce to a freely moving source and one finds that the convection amplification factor for a line displacement source (following the terminology of Morfey and Tanna⁶ is $(1 + \frac{3}{2} M^2) (1 - M^2)^{-7/2}$, i.e., stronger than the freely moving line source (or line velocity source) by a factor $(1 + \frac{3}{2} M^2) (1 - M^2)^{-2}$. (The corresponding factor for point sources is $(1 + M^2) (1 - M^2)^{-2}$).

More general calculations require incorporation of (42) or (43) in (44) and an integration over the frequency range $\omega_0(1+M)^{-1} \leq \omega \leq \omega_0(1-M)^{-1}$ to obtain the total power. Such calculations have been carried out for M ranging from 0.5 to 0.9, $(k_0 h)$ ranging from 0.01 to 1.0 and σ from 0 to 0.99. In all cases (results are shown in Figure 21, the total power is normalized by (47), i.e., by $[q_0^2 \omega_0 / 8\rho_0 (1 - M^2)^{3/2}]$. The interest in Figure 21 is really in how much the results in the range $0 < \sigma < 1$ deviate from the $\sigma = 0$ results (case of centerline source convection). As is observed from Figure 21, the results for total power are essentially unaffected by the exact location of the line of source convection so long as it is within the jet. This result, while deduced for a plane problem, lends confidence to the notion that the results of Section 1.1 will have a wider range of applicability than just to sources convecting along the jet centerline. The results of Figure 21 are physically tantamount to the observation that it is the "total extent" of shrouding to which the moving source is exposed which determines its radiative efficiency.

1.3 Effect of Finite Shear on Model Problem Studies in Section 1.1

In a recent study Eversman⁷ has indicated an interesting procedure (in connection with lined duct propagation problems) by which, in case the transition from the mean velocity to the ambient value of zero velocity occurs in a shear layer of thickness δ (the slug flow model assumes this transition to take place in a shear layer of zero thickness), calculations correct to order (δ/λ) or (δ/a) (λ = wavelength of sound, a = jet radius) may be carried out. This section will briefly summarize the application of Eversman's approach to the model problem of Section 1.1. To set the stage of how Eversman's method needs to be adapted for the current study, the application to the problem of Section 1.1 is prefaced by an application to the Ribner-Miles^{8,9} problem of reflection of plane, acoustic waves by a velocity discontinuity.

In terms of Figure 22, the problem is to determine the reflection coefficient of a plane, simple harmonic wave by a shear layer of thickness δ across which the velocity changes from a value $M_0 c$ to zero.

Eversman used the terminology of inner and outer expansions to develop his method, but (in hindsight!) his approach can be illustrated without recourse to such terminology as under. In general, the governing equation for the linear, inviscid propagation of sound in a parallel sheared flow involves a third order differential equation but, in terms of Figure 22, if interest is restricted to pressure waves of type $P(y)\exp[j(kKx - \omega t)]$ where $k = \frac{\omega}{c}$ (this class of waves is all that is involved in the Ribner-Miles problem), we may show that $P(y)$ is governed by:

$$\frac{d}{dy} \left\{ \frac{1}{(1 - M(y)K)^2} \frac{dP}{dy} \right\} = \left\{ \frac{K^2}{(1 - M(y)K)^2} - 1 \right\} k^2 P \quad (49)$$

Now integrate (49) from $y = 0$ to $y = \delta$ to obtain first:

$$\left[\frac{1}{(1 - M_0 K)^2} \frac{dP}{dy} \right]_{y = \delta} = \left[\frac{dP}{dy} \right]_{y = 0} + \quad (50)$$

$$k^2 \int_0^{\delta} \left\{ \frac{K^2}{(1 - M(y)K)^2} - 1 \right\} P(y) dy$$

As it stands (50) is just an integro-differential version of (49) but (anticipating a step to follow in (52) by integrating (22) twice) to zeroth order in (δ/λ) $P(y) = P(0)$ or $P(\delta)$ so long as $0 \leq y \leq \delta$. Correct to order (δ/λ) then we may assert that:

$$\frac{1}{(1 - M_0 K)^2} \left(\frac{dP}{dy} \right)_{y = \delta} = \left(\frac{dP}{dy} \right)_{y = 0} + k^2 [P(0) \text{ or } P(\delta)] I_1 \quad (51)$$

where

$$I_1 = \int_0^{\delta} \left\{ \frac{K^2}{[1 - M(y)K]^2} - 1 \right\} dy$$

By integrating (50) twice, again to order (δ/λ) , one finds that:

$$P(y = \delta) = P(y = 0) + \left(\frac{dP}{dy} \right)_{y = 0} I_2 \quad (52)$$

where

$$I_2 = \int_0^{\delta} (1 - M(y)K)^2 dy$$

It is rather important to observe that in (52) we may substitute (if we choose) $\left(\frac{dP}{dy}\right)_{y=0}$ by $\left(\frac{dP}{dy}\right)_{y=\delta} \frac{1}{(1 - M_0 K)^2}$ and not by $\left(\frac{dP}{dy}\right)_{y=\delta}$. In other

words to zeroth order in (δ/λ) , the quantities conserved across the shear layer are $P(y)$ and $\frac{1}{(1 - M(y)K)^2} \frac{dP}{dy}$. As Eversman has pointed out, conservation of

$\frac{1}{(1 - M(y)K)^2} \frac{dP}{dy}$ amounts to continuity of acoustic particle displacement.

In case of the Ribner-Miles problem of Figure II-7, $K = [\cos\phi / (1 + M_0 \cos\phi)]$ and the angle of emission θ is given by $\cos^{-1}(K)$. Assume for $M(y)$ a profile of type $M_0 \sin(\frac{\pi y}{2\delta})$ for $0 \leq y \leq \delta$. Then we may show that

$$I_1 = \delta \left[\frac{2K^2}{\pi(1 - M_0^2 K^2)} \left\{ M_0 K + \frac{2}{\sqrt{1 - M_0^2 K^2}} \left[\tan^{-1} \sqrt{\frac{1 - M_0 K}{1 + M_0 K}} + \tan^{-1} \left(\frac{M_0 K}{\sqrt{1 - M_0^2 K^2}} \right) \right] \right\} - 1 \right] \quad (53)$$

and

$$I_2 = \delta \left\{ 1 + \frac{M_0^2 K^2}{2} - 4 \frac{M_0 K}{\pi} \right\} \quad (54)$$

These results now suffice to determine a reflection coefficient R defined as follows. The incident pressure wave is denoted by $\exp[j\{ \frac{k(x \cos\phi - (y - \delta) \sin\phi)}{1 + M \cos\phi} \} - \omega t]$. R depends on ϕ , M_0 and (δ/λ) where $\lambda = [2\pi/k]$. The case $(\delta/\lambda) = 0$ corresponds to the case calculated by Ribner-Miles^{8,9}.

Some calculations of $|R|$ and $\arg(R)$ are tabulated in Appendix II-1 for $M_0 = 0.5, 0.7$ and 0.9 , for $0 \leq \phi \leq 0.18$. (The value of 0.18 corresponds to $(k\delta) \approx 1$ and it was felt that the $0(\delta/\lambda)$ calculation would not be meaningful

for $(k\delta) \gg 1$). The tabulation in Appendix II-1 shows that in most cases $|R|$ decreases with increasing (δ/λ) in accord with the physical expectation that the reflection coefficient should be weaker for a profile with continuous shear as compared to the case of a step function change in velocity. In five of the thirty cases tabulated (marked by an arrow in Appendix II-1), $|R|$ records an increase with increasing (δ/λ) . Evidently these correspond to cases of some unusual constructive interference of waves reflected continuously from the shear layer. This conjecture is supported by the observation that $\arg(R)$ in these cases exhibits an unusual trend (with increasing (δ/λ)) being either the reverse of the usual trend of variation of $\arg(R)$ with (δ/λ) or exhibiting unusually large changes of $\arg(R)$.

Adaptation of a procedure similar to the above to the cylindrical shear flow geometry of Figure 23 yields the following matching conditions between $p, \frac{dp}{dr}$ at $r = (a - \delta)$ and $p, \frac{dp}{dr}$ at $r = a$.

$$\left(\frac{dp}{dr}\right)_{r=a} = \frac{(1 - \frac{\delta}{a})}{(1 - M_0 K)^2} \left(\frac{dp}{dr}\right)_{r=(a-\delta)} + k^2 p(r = (a - \delta) \text{ or } r = a) I_3 \quad (55)$$

and

$$p(r = a) = p(r = a - \delta) + \left(\frac{dp}{dr}\right)_{r=(a-\delta)} \frac{I_4}{(1 - M_0 K)^2} \quad (56)$$

where

$$I_3 = \int_{a-\delta}^a \frac{K^2 dr}{(1 - M(r)K)^2} - \delta \quad (57)$$

and

$$I_4 = \int_{a-\delta}^{\bar{a}} (1 - M(r)K)^2 \bar{c}r \quad (58)$$

The integrals I_3 , I_4 are again evaluated assuming a half sine profile for the transition from M_0 to the ambient as sketched in Figure 23. The calculations of Section 1.1 were revised using (55), (56) in place of the p , η matching employed therein. In Figures 24 and 25, calculations for the total power normalized by that of the freely moving source are shown for $(k_0 a)$ in the range 0.01 to 1, and (δ/a) in the range 0 to 0.2. (The case $\delta/a = 0$ corresponds to the previous calculation of Section 1.1). As can be seen there is a small (1-2 dB) effect on the total power results.

1.4 Jet Density Exponent Issue for Noise of Heated Subsonic Jets

The subject matter of the present section is the question of how the sound power of a jet of constant exit velocity would vary as the jet exit density is varied. Changes in jet exit density would inevitably be accomplished in a real experiment by changes in speed of sound (temperature) of the jet so that both effects must be considered simultaneously. The point of view advanced at the end of the section is that experimentally observed results in this area seem to admit of an explanation based how the radiative efficiency of moving acoustic sources is affected by the shrouding effect of a jet flow whose velocity, temperature and density differ from those of the ambient. This change of efficiency is calculated with the aid of a simple model problem as follows. We determine the acoustic power output of a convected monopole source, simple harmonic in its own frame of reference, moving along the axis of a slug flow, round jet whose velocity is taken to be the same as that of the source. The jet is doubly infinite and the source is assumed to be of infinite lifetime. The jet density and temperature are allowed to be different from that of the ambient though the specific heat ratio of the jet fluid is assumed to be the same as that of the ambient. The requirement of equality of the static pressure inside and outside the jet then calls for a certain restraint

on how the jet density and temperature must vary. For a specific value of jet exit velocity, the variation of acoustic power with the ratio of jet density to the ambient density along with a simple assumption on how the source strength would vary with jet density is employed to theoretically deduce the "jet density exponent" for jets which are subsonic with respect to the ambient speed of sound. The jet density exponent is found to depend both on the jet Mach number and even more strongly on a source frequency parameter. The theoretical results are compared to some experimental studies of this problem. Encouraging agreement is obtained both for the detailed observed effects on the power spectrum and the exponent for the overall power.

The model problem is sketched in Figure 26. We wish to determine the sound field due to a fluctuating monopole point source translating at a uniform subsonic velocity U (where $U < c_o$, c_o being the speed of sound of the ambient). The source translates along the axis of a round jet whose velocity profile we assume to be a slug flow velocity profile. Also the jet velocity is taken equal to that of the source. The source is assumed to have a time dependence in its own frame of reference of $q_o \cos(\omega_o t)$. The mean jet density and speed of sound are taken as ρ_1, c_1 while those of the ambient are denoted by ρ_o, c_o . Now the static pressure inside the jet is given by $p = \rho_1 c_1^2 / \gamma_1$ and similarly of the ambient by $\rho_o c_o^2 / \gamma_o$. Since the static pressures inside and outside the jet must be equal, if we assume that $\gamma_1 = \gamma_o$ (a reasonable assumption for the heated jet situation but less valid if foreign gases such as Freon, etc., are used for the jet fluid), then we must have $\rho_1 c_1^2 = \rho_o c_o^2$ to balance the static pressures. This implies a coupling between the density ratio and speed of sound ratio (i.e. $(\rho_1 / \rho_o) = (c_1 / c_o)^{-2}$) which is always employed in the current study.

Analytically we wish to determine an acoustic velocity potential ϕ which satisfies in region I of Figure 26 (outside the jet)

$$\nabla^2 \phi - \frac{1}{c_o^2} \phi_{tt} = 0 \quad (59)$$

and in region II (inside the jet) of Figure 26

$$\begin{aligned}
 (1 - M_1^2) \phi_{xx} + \nabla_2^2 \phi - 2 \frac{M_1}{c_1} \phi_{xL} - \frac{\dot{\phi}_{Lt}}{c_1^2} \\
 = \frac{q}{\rho_0} \cos(\omega_0 t) \delta(x - Ut) \delta(y) \delta(z)
 \end{aligned}
 \tag{60}$$

where $M_1 = U/c_1$ and ∇_2^2 stands for the Laplace operator in the y-z plane. We assume that $\rho_1 \leq \rho_0$ (in view of the interest in heated jets) so that $c_1 \geq c_0$ and hence if $U < c_0$ then U is also $< c_1$. This means that $M_1 < 1$. At the jet-still air interface (i.e. at $L = a$), we require:

a) Continuity of acoustic pressure p , where

$$p = -\rho_0 \phi_t \text{ in region I,} \tag{61}$$

$$p = -\rho_1 \{\phi_t + U \phi_x\} \text{ in region II.} \tag{62}$$

b) Continuity of the radial acoustic particle displacement, say η , so that:

$$\phi_r = \eta_t \text{ in region I,} \tag{63}$$

$$\text{and } \phi_r = (\eta_t + U \eta_x) \text{ in region II.} \tag{64}$$

Outside the jet, i.e. in region II, the velocity potential ϕ is also subject to a radiation condition which states that only outgoing waves be emitted by the moving source.

Before proceeding further, it is necessary to discuss the implications of employing a slug flow or top hat velocity profile which is known to be unstable when excited by certain wave number-frequency combinations of longitudinally traveling waves. The general procedure for examining the

instability issue (e.g. Batchelor and Gill¹⁰ consider the incompressible case) is to consider the unforced jet eigenvalue problem. In other words, a solution of type $R(r) \exp[j(kx - \omega t)]$ is assumed for ϕ whence, in the absence of any source term driving the systems, specifying real ω determines k as a function of ω (spatial stability analysis) or alternatively specifying real k determines ω as a function of k (temporal stability analysis). The imaginary parts of k or ω respectively determine the regimes of instability. In the present problem a source of type $\cos(\omega_0 t) \delta(x - Ut)$ imposes a rather specific type of traveling wave disturbance on the jet column. By Fourier decomposition of the source excitation, the traveling waves turn out to be of type $\exp[j[(\omega \mp \omega_0) \frac{x}{U} - \omega t]]$ with real ω . Thus formal consideration of the infinite lifetime source problem yields simple traveling wave excitation of the jet column which produces either a propagating or a decaying sound field outside the jet depending on whether the wave speed parallel to the jet axis which is $|\omega(1 \mp \frac{\omega_0}{\omega})^{-1}|$ exceeds c_0 or not. This then leads to the obvious result that effective acoustic power is produced in the far field over a frequency range $\frac{\omega_0}{1 + M_0} \leq \omega \leq \frac{\omega_0}{1 - M_0}$ where $M_0 = U/c_0$ (Morse and Ingard² as predicted by the Doppler shift formula).

It seems likely, however, that if one sought the solution to the problem as the limit of an initial value problem, i.e. assumed a source strength of type $\delta(y) \delta(z) \cos(\omega_0 t) \delta(x - Ut) H(t - t_0)$ where $H(t)$ is the unit step function and then studies the limit of the solution as $t_0 \rightarrow -\infty$, one would find that the "starting up" process of the source triggers the Kelvin-Helmholtz instability at the jet still air interface. (If the source is assumed switched on only at the time $t = t_0$, it would be required that $\phi \equiv 0$ (or constant) for $t \leq t_0$.) To ensure this requires that in the Fourier integral representation of ϕ the path of integration in the ω -plane be specified in a certain manner. Presumably, then, in deforming that path of integration on to the real axis of ω ($-\infty < \omega < \infty$), unstable pole contributions corresponding to the excitation of the instability modes would be picked up in addition to the contribution from integration over the real ω -axis which alone is discussed herein.

This aspect of the problem, while undoubtedly a difficulty with the slug flow profile or indeed any mean flow velocity profile that is inflectional, is ignored in the present study based on the following physical argument. Practical jets (at sufficiently high Reynolds numbers) do represent a stable flow situation though characterized by high turbulence levels (the rms turbulence level can often be as high as 15% of the jet velocity). The real jet flow then represents a flow with a distribution of mean velocity and turbulence levels which is manifestly stable to source excitations of the type that lead to jet noise. The high turbulence level in the jet itself could be a stabilizing agent by a mechanism of eddy viscosity as has been noted by several previous studies of turbulent shear flows. For example, Landahl¹¹ surmised that even for turbulent boundary layers (generally characterized by lower turbulence levels than a jet flow) the eddy viscosity seemed about 80 times as effective as the molecular viscosity. Similarly Bishop¹², et al., specifically suggested, with respect to high speed jets, the substantial lowering of the effective jet Reynolds number due to the eddy viscosity. The justification for the use of a slug flow velocity profile then rests on the fact in attempting to infer the effect of the more complicated mean velocity profile of the pure jet on the radiative efficiency of a moving source, one may exploit the relatively low frequency nature of jet noise sources to argue that the precise nature of the true velocity profile need not be retained. Since we know that the true jet flow is stable and it is understood that the slug flow profile is only employed as an analytical artifice to conveniently assess the shrouding effect of the flow on the radiative efficiency of the source, we may then reject the unstable excitation of the slug flow profile owing to the start up process of the source (which appears in the rigorous analytical solution of (59) and (60) when a proper initial value problem is posed) as not germane to the real physical problem. In what follows then we will deal only with the stable and bounded solution to (59) and (60) subject to the matching conditions of (61) - (64) assuming a source of infinite lifetime. The problem posed by (59) and (60) is a transient one and the required bounded solution may be obtained by formally applying the Fourier integral method taking ω real. A similar difficulty arises, of course, in the calculations of Section 1.1 through the arguments for ignoring the stability issue were not spelled out in as much detail as above. From a fluid mechanics rather than a mathematical

point of view the case for both the present calculations as well as those of the earlier study (Section 1.1) must perhaps be judged on the degree to which the results are in accord with physically observed features of jet noise.

The analysis that follows parallels closely that of Section 1.1 and is given below mainly for completeness and to clearly delineate the new elements that arise due to ρ_1, c_1 not being equal to ρ_0, c_0 .

Let $\tilde{\phi}, p$, etc., denote the Fourier transforms with respect to time of the corresponding physical quantities. Thus

$$\tilde{\phi} = \frac{1}{2\pi} \int_{-\infty}^{\infty} \phi e^{j\omega t} dt, \quad j = \sqrt{-1} \quad (65)$$

and

$$\phi = \int_{-\infty}^{\infty} \tilde{\phi} e^{-j\omega t} d\omega.$$

Also, we write $\cos(\omega_0 t) = \frac{1}{2}[\exp(j\omega_0 t) + \exp(-j\omega_0 t)]$. The problem for the transforms is

$$\nabla^2 \tilde{\phi} + k_0^2 \tilde{\phi} = 0, \quad (k_0 = \omega/c_0) \quad \text{in region I,} \quad (59')$$

$$(1 - k_1^2) \tilde{\phi}_{xx} + \nabla_2^2 \tilde{\phi} + 2jk_1 M_1 \tilde{\phi}_x + k_1^2 \tilde{\phi} = \frac{q_0 \delta(y) \delta(z)}{4\pi \rho_1 U}$$

$$\times \left[\exp\left(\frac{j(\omega - \omega_0)x}{U}\right) + \exp\left(\frac{j(\omega + \omega_0)x}{U}\right) \right], \quad \text{in region II; } (60')$$

where $k_1 = \omega/c_1$ and $M_1 = U/c_1$

$$\bar{p} = j\omega\rho_0\bar{\phi}, \quad \text{in region I,} \quad (61')$$

$$\bar{p} = -\rho_1(-j\omega\bar{\phi} + U\bar{\phi}_x), \quad \text{in region II.} \quad (62')$$

$$\bar{\phi}_r = -j\omega\bar{\eta}, \quad \text{in region I,} \quad (63')$$

$$\bar{\phi}_r = -j\omega\bar{\eta} + U\bar{\eta}_x, \quad \text{in region II.} \quad (64')$$

Let $\bar{\phi} = \bar{\phi}^+ + \bar{\phi}^-$ and similarly for \bar{p} and $\bar{\eta}$ where $\bar{\phi}^+$ corresponds to the solution with the term $\exp\{j(\omega - \omega_0)x/U\}$ in equation (60') and $\bar{\phi}^-$ to the term involving $\exp\{j(\omega + \omega_0)x/U\}$.

Consider in detail the problem for $\bar{\phi}^+$. Intuitively, it is clear that $\bar{\phi}^+$, \bar{p}^+ , $\bar{\eta}^+$ all have an x -dependence of the type $\exp\{j(\omega - \omega_0)x/U\}$. "Factoring" this dependence out, one is left with the following problem in the y - z plane:

$$\nabla_2^2 \bar{\phi}^+ + \kappa^{+2} \bar{\phi}^+ = 0, \quad \text{in region I;} \quad (65)$$

$$\nabla_2^2 \bar{\phi}^+ + \kappa^{+2} \bar{\phi}^+ = \frac{q_0 \delta(y) \delta(z)}{4\pi\rho_0 U}, \quad \text{in region II;} \quad (66)$$

where

$$\kappa^{+2} = \left(\frac{1 - M_0^2}{M_0^2} \right) \left[\left(\frac{\omega_0/c_0}{1 - M_0} - k_0 \right) \left(k_0 - \frac{\omega_0/c_0}{1 + M_0} \right) \right] \quad (67)$$

and is ≥ 0 only if $\frac{\omega_0}{1 - M_0} \geq \omega \geq \frac{\omega_0}{1 + M_0}$.

$$\kappa^{+2} = \frac{1}{M_1^2} \left\{ \left(\frac{\omega_0}{c_1} (1 + M_1) - k_1 \right) \left(k_1 - \frac{\omega_0}{c_1} (1 - M_1) \right) \right\}, \quad (68)$$

Also let

$$\underline{\kappa}^{+2} = -\kappa^{+2} = \frac{1}{M_1^2} \left(\left[\kappa_1 - \frac{\omega_0}{c_1} (1 + M_1) \right] \left[\kappa_1 - \frac{\omega_0}{c_1} (1 - M_1) \right] \right) \quad (69)$$

We restrict our attention to the frequency range $\frac{\omega_0}{1 - M_0} \geq \omega \geq \frac{\omega_0}{1 + M_0}$. The matching conditions for equations (68) and (66) are that, at $r = a$,

$$\tilde{\phi}^+(r = a^+) = \frac{\rho_1 \omega_0}{\rho_0 \omega} \tilde{\phi}^+(r = a^-) \quad (\text{pressure matching condition}). \quad (70)$$

$$\tilde{\phi}_r^+(r = a^+) = \frac{\omega}{\omega_0} \tilde{\phi}_r^+(r = a^-) \quad (\text{transverse particle displacement matching condition}). \quad (71)$$

To solve equations (65), (66), (67), and (68) in the range $\frac{\omega_0}{1 + M_0} < \omega < \frac{\omega_0}{1 - M_0}$ and with restriction to outgoing waves at infinity, in the range we assume, for $\tilde{\phi}^+$ in regions I and II,

$$\text{in I: } \tilde{\phi}^+ = \lambda_I^+ H_0^{(1)}(\kappa^+ r) \exp \frac{j(\omega - \omega_0)x}{U}, \quad (72)$$

$$\text{in II: } \tilde{\phi}^+ = \left[\lambda_{II}^+ J_0(\kappa^+ r) - \frac{j q_0 \Pi_0^{(1)}(\kappa^+ r)}{16\pi \rho_1 U} \right] \exp \frac{j(\omega - \omega_0)x}{U}, \quad (73)$$

$$\text{if } \omega \in [\omega_0(1 - M_1), \omega_0(1 + M_1)]$$

Otherwise in region II,

$$\tilde{\phi}^+ = [A_{II}^+ I_0(\underline{\kappa}^+ r) - \frac{q_0 K_0(\underline{\kappa}^+ r)}{8\pi^2 \rho_1 U}] \exp \frac{j(\omega - \omega_0)x}{U} \quad (74)$$

Equations (72) and (73) or (72) and (74) may now be readily solved for A_I^+ and A_{II}^- by using the matching conditions (70) and (71). Since we are interested in far field pressures far outside the jet, we only give the result for A_I^+ :

(a)

if $\omega \in [\omega_0(1 - M_1), \omega_0(1 + M_1)]$,

$$A_I^+ = \frac{q_0 \kappa^+ [Y_0(\kappa^+ a) J_1(\kappa^+ a) - Y_1(\kappa^+ a) J_0(\kappa^+ a)]}{16\pi \rho_0 \left[\frac{\omega}{\omega_0} \kappa^+ H_0^{(1)}(\kappa^+ a) J_1(\kappa^+ a) - \kappa^+ \frac{\rho_1}{\rho_0} \left(\frac{\omega_0}{\omega}\right) J_0(\kappa^+ a) H_1^{(1)}(\kappa^+ a) \right] U} \quad (75a)$$

(b) otherwise,

$$A_I^+ = \frac{-q_0 \underline{\kappa}^+ [K_0(\underline{\kappa}^+ a) I_1(\underline{\kappa}^+ a) + I_0(\underline{\kappa}^+ a) K_1(\underline{\kappa}^+ a)]}{8\pi^2 \rho_0 U \left[\frac{\omega}{\omega_0} \underline{\kappa}^+ I_1(\underline{\kappa}^+ a) H_0^{(1)}(\underline{\kappa}^+ a) + \frac{\rho_1}{\rho_0} \frac{\omega_0}{\omega} \kappa^+ I_0(\underline{\kappa}^+ a) H_1^{(1)}(\underline{\kappa}^+ a) \right]} \quad (75b)$$

Equation (75) essentially completes the formal solution to the problem. The far field pressure and the radial acoustic velocity may be computed by using $\tilde{p} = j\omega \rho_0 \tilde{\phi}$ and $\tilde{\phi}_r$. In this problem, every point on a cylindrical surface concentric with the jet experiences the same pressure time history. Morse and

Ingard² have discussed thoroughly the problem of determining the power spectrum and total power radiated by the source and their concluding result is that the power spectral density extends over a frequency range $[\omega_0/(1 + M_0)] < \omega < [\omega_0/(1 - M_0)]$ and is given by

$$(16\pi\rho_0 U\omega) |\Delta_I^+|^2 = I(\omega) \quad (76)$$

The total power is given by

$$P = \int_{\omega_0/(1 + M_0)}^{\omega_0/(1 - M_0)} I(\omega) d\omega \quad (77)$$

1.5 Computed Results and Inferences

The power calculated in (77) is nondimensionalized first by the power of a freely moving source which is $q_0^2 \omega_0^2 / 8\pi \rho_0 c_0 (1 - M_0^2)^2$. Fixing M_0 and $(\omega_0 a / \pi U)$, the nondimensional power (say P') against $\log(\rho_1 / \rho_0)$ by a least squares fit an exponent n' is determined for each M_0 and $(\omega_0 a / \pi U)$. $(\omega_0 a / \pi U)$ may be termed a source Strouhal number (e.g. as in Lush (1971)). Now the source strength q_0 itself will vary linearly with jet density whether one uses the quadrupole model of Lighthill¹³ or the fluid dilatation model of Ribner¹⁴. Since p' itself varies as $\rho_1^{n'}$ and P' is the power normalized by q_0^2 , with $q_0 \sim \rho_1$ one would then expect the actual power to vary with density ρ_1 as with an exponent $(n' + 2) = n$.

This theoretically deduced exponent n is plotted in Figures 27, 28 and 29 for $M_0 = 0.5, 0.7$ and 0.9 and a range of source Strouhal numbers in range 0.1 to 1.0. For source Strouhal numbers in excess of 1, owing to the high frequencies involved the slug flow model would be less adequate.

If we take the limit of 75(a) or (b) at very low frequencies one can readily show that the index n would be expected on the basis of this model to tend to zero. In general, then, for subsonic Mach numbers, the present model predicts that $n \rightarrow 0$ as the frequency parameter approaches zero, and it's then negative for a range of frequencies and finally starts increasing monotonically with frequency. It is not possible to analytically extract a high frequency

limit from 75(a) and (b) but if one used the argument that at high frequencies the source output is determined only by its own immediate ambient, the exponent should depend on how $(q_0^2/\rho_1 c_1)$ varies with ρ_1 and since $q_0 \sim \rho_1$, and $c_1 \sim \rho_1^{-1/2}$, for a monopole source model, the exponent would tend to 1.5 at high frequencies. The intrinsic source distributions generating jet noise do exhibit Strouhal scaling with respect to velocity (this is confirmed either by in-jet measurements or by looking at the 90° point far field data where convective-refractive effects are absent) so that high speeds do go with high true source frequencies and vice versa. In Figure 32, the exponents for $M_0 = 0.5, 0.7,$ and 0.9 are shown as a function of a true frequency parameter $(\omega_0/a c_0)$. There is a general trend to exponents of value zero as $(\omega_0 a/c_0) \rightarrow 0$, followed by a region of negative exponents and a tendency for n to attain values of 1.5 for high values of $(\omega_0 a/c_0)$ almost independent of jet Mach number. In view of the Strouhal scaling with respect to velocity exhibited by the source distributions, one would expect (in terms of Figure 32) the higher jet velocities to go with higher values of $(\omega_0 a/c_0)$. ($\omega_0 a/c_0$ is (πM_0) times the source Strouhal number). In other words Figure 32 indicates that even in terms of jet velocities one would expect a changing exponent (say for the total power) starting off at zero at the lowest velocities, then being negative and then finally increasing monotonically with velocity. The present calculations are of course limited to subsonic jet velocities.

In Figure 31, we show first the empirical result obtained for the exponent n for the total power obtained by Hoch¹⁵, et al. As indicated earlier, Hoch, et al., find that n is a junction of jet Mach number. In order to compare the present analysis with the data of Hoch, et al., it is necessary to estimate source Strouhal numbers representative of the total power. Based on jet noise at low Mach numbers (wherein refractive, shrouding and Doppler shift effects should be negligible), it was felt that a source Strouhal number somewhere between 0.3 and 0.6 would represent a "typical" source Strouhal number for assessing an exponent for the total power. Shown in Figure 31 for M_0 in range 0.5 to 0.95 are results for n of the present study for source Strouhal numbers of both 0.3 and 0.6. Except at the lowest Mach number of 0.5, the predicted values of the exponent for source Strouhal numbers of 0.3 and 0.6 bracket the experimental values of Hoch, et al. quite well.

It appears from the present study that the differences in noise between a heated and a cold jet do admit largely of an acoustic explanation being attributable to the effect on the radiative efficiency of a moving source due to the mismatch of velocity, density and temperature within and outside the jet. The fact that Figure 30 taken from Hoch, et al., is in accord with Figures 27-29 appears to be the most impressive evidence of this for it is difficult to conceive of other explanations based on entropy fluctuations, jet mixing, etc., that would explain the tendency of heating to raise the low frequency end of the power spectrum while depressing the high frequency end.

As noted earlier, extensions to higher order multipoles and to sources of finite lifetime are undoubtedly needed but the least the present study may be said to achieve is to indicate the profitability of pursuing such analyses.

1.6 Directivity of Subsonic Jet Noise

In the last Subsection, we will calculate the directivity of a fluctuating, simple harmonic point source embedded in a slug flow, cold round jet with the source convecting along the jet axis at a velocity different from the jet velocity. It is required that the convection velocities of the source or eddy be subsonic. In the calculations of directivity to be shown later the eddy convection velocity is always assumed to be 0.65 times the jet velocity.

Initially, we start with the case of a moving source of time dependence $e^{j\omega_o t}$ in a stationary medium. The objective is to calculate its directivity as opposed to its power spectrum. Since interest is in directivity rather than a power spectrum it is obvious that rather than a transform in time one in space needs to be employed.

The velocity potential $\phi(x,r,t)$ satisfies (cf. Figure 33):

$$\begin{aligned} \phi_{xx} + \frac{1}{r} \frac{\partial}{\partial r} \left(r \frac{\partial \phi}{\partial r} \right) - \frac{1}{c^2} \phi_{tt} \\ = \frac{q_o}{\rho_o} e^{j\omega_o t} \delta(x - Mct) \delta(y) \delta(z) \end{aligned} \quad (78)$$

As noted earlier, at the lower Mach numbers (and associated low true frequencies), the present analysis predicts the exponent to tend to zero. This result is apparently at variance with the SNECMA-NGTE study of Hoch, et al. There are two points to note in this regard:

1) The present study needs extension to higher order multipoles as well as to sources convecting at velocities different from (less than) the jet speed. So also the extension to finite source lifetimes is also needed. It is not clear how much these extensions will alter the theoretical predictions of the exponent.

2) It is in the lower velocity range that isolation of the jet density exponent associated with pure jet noise becomes most difficult from an experimental point of view. This is because of the ever present danger of internal noise sources termed "parasitic" noise by Hoch, et al.) such as valve noise, combustion noise, etc. One can easily show that the effect of such a combustion noise source will be to lower the effective index from its value for pure jet noise in an experimental situation. In Hoch¹⁵, et al., it is pointed out that the NGTE group worked in the low velocity end while the SNECMA group worked at the high velocity end. Hoch, et al., have cited the good agreement between the results of the two groups in the region of overlap of velocities as one indication of the internal cleanliness of their facility. However Hoch, et al., do point out that the region of overlap extends from $M_0 = 0.6$ on up so that "pure jet noise is being measured, at least, above jet velocities of 200 m/s" ($M_0 = 0.6$). We may note that an earlier experimental study by Rollin¹⁶ did conclude that the density exponent was zero.

Finally, in Figure 30, we show the detailed effects on the power spectrum due to heating observed by Hoch, et al., at two velocities corresponding to $M_0 = 0.6$ and $M_0 = 1.2$. It is observed that they find that heating increases the low frequency portions of the spectrum while depressing the higher frequencies. This is fully in accord with Figures 27-29 wherein (as indicated) indices greater than zero correspond to portions of the frequency spectrum lowered upon heating and indices less than zero to portions raised by heating.

Now let

$$\phi = \frac{1}{2\pi} \int_{-\infty}^{\infty} \phi e^{j\alpha x} dx \quad (79)$$

so that

$$\phi = \int_{-\infty}^{\infty} \phi e^{-j\alpha x} dx \quad (80)$$

Then

$$\begin{aligned} \frac{1}{r} \frac{\partial}{\partial r} \left(r \frac{\partial \phi}{\partial r} \right) - \alpha^2 \phi - \frac{1}{c^2} \frac{\partial^2 \phi}{\partial t^2} \\ = \frac{q_0}{2\pi\rho_0} e^{j\omega_0 t} e^{j\alpha V t} \delta(y) \delta(z) \end{aligned} \quad (81)$$

where $Mc = V$.

Clearly ϕ depends on time as $\exp\{j(\omega_0 + \alpha V)t\}$. Thus the radial dependence of ϕ is to be determined from:

$$\begin{aligned} \frac{1}{r} \frac{d}{dr} \left(r \frac{d\phi}{dr} \right) + (1 - M^2) \left(\frac{k_0}{1 - M} - \alpha \right) \left(\alpha + \frac{k_0}{1 + M} \right) \phi \\ = \frac{q_0}{2\pi\rho_0} \delta(y) \delta(z) \end{aligned} \quad (82)$$

$$\text{Let } \alpha^+ = (1 - M^2)^{1/2} \left\{ \left(\frac{k_0}{1 - M} - \alpha \right) \left(\alpha + \frac{k_0}{1 + M} \right) \right\}^{1/2} \quad (83)$$

Note α^+ is real only if

$$\frac{-k_0}{1 + M} \leq \alpha \leq \frac{k_0}{1 - M} \quad (84)$$

and we will restrict attention to this range of α . Then ϕ satisfies,

$$\frac{1}{r} \frac{d}{dr} \left(r \frac{d\phi}{dr} \right) + \alpha^{+2} \phi = \frac{q_0}{2\pi\rho_0} \delta(y) \delta(z) \quad (85)$$

Solution for ϕ corresponding to outgoing waves is

$$\frac{j q_0}{8\pi\rho_0} H_0^{(2)}(\alpha^+ r) \quad (86)$$

(assuming that $\omega_0 > 0$). Thus

$$\phi = \frac{j q_0 e^{j\omega_0 t}}{8\pi\rho_0} \int_{-\infty}^{\infty} H_0^{(2)}(\alpha^+ r) e^{-j\alpha(x - vt)} d\alpha \quad (87)$$

Let (Figure 33) $r = R' \sin \theta'$, and $(x - vt) = R' \cos \theta'$. For large R' and $\theta' \neq 0, \pi$, r will also be large and ϕ will be

$$\phi \sim \frac{e^{j\pi/4} j q_0 e^{j\omega_0 t}}{8\pi\rho_0} \sqrt{2/\pi r} \int_{-\infty}^{\infty} \frac{e^{-j\alpha^+ r} e^{-j\alpha(x - vt)}}{\sqrt{\alpha^+}} d\alpha \quad (88)$$

The exponential terms depending on α inside the integral may be written as:

$\exp[jR' h(\alpha)]$ where

$$h(\alpha) = - [\alpha^+ \sin \theta' + \alpha \cos \theta'] \dots \quad (89)$$

and the integral for ϕ may be written as:

$$\phi = \frac{e^{(j \cdot \pi/4)} j a_0 e^{j\omega_0 t}}{8\pi\rho_0} \sqrt{2/\pi r} \int_{-\infty}^{\infty} \frac{e^{jR'h(\alpha)} d\alpha}{\sqrt{\alpha^2}} \dots \quad (90)$$

Let α_0 denote the value of α for which $h(\alpha)$ is stationary, i.e. $h'(\alpha) = 0$. Then by the method of stationary phase (cf. e.g. A. Erdélyi, "Asymptotic Expansions," p. 51), for large R' ,

$$\phi = \frac{C \exp[j R' h(\alpha_0) + j \frac{\pi}{4}]}{\sqrt{\alpha^2(\alpha_0)}} \left[\frac{2\pi}{R' h''(\alpha_0)} \right]^{1/2} \dots \quad (91)$$

(this form assumes that α_0 is a minimum of $h(\alpha)$, i.e. that $h''(\alpha_0) > 0$) where C is just

$$\frac{e^{j \pi/4} j a_0 e^{j\omega_0 t}}{8\pi\rho_0} \sqrt{2/\pi r} \dots \quad (92)$$

$$h(\alpha) = - [\alpha^+ \sin\theta' + \alpha \cos\theta'] \dots \quad (93)$$

is stationary when

$$\frac{d\alpha^+}{d\alpha} \sin(\theta') + \cos\theta' = 0 \text{ or when}$$

$$(1 - M^2) \left\{ \left(\frac{k_0}{1 - M} - \alpha \right) - \alpha - \frac{k_0}{1 + M} \right\} \sin\theta' + 2\alpha^+ \cos\theta' = 0 \quad (94)$$

or $\{2M k_o - 2\alpha (1 - M^2)\} \sin\theta' + 2\alpha^+ \cos\theta' = 0$. Let $\beta = k_o + \alpha M$. Then

$$(M\beta - \alpha) \sin\theta' = -\cos\theta' \sqrt{\beta^2 - \alpha^2} \quad (95)$$

After some painful algebra we find that

$$z_o = \frac{\cos\theta' [\sqrt{1 - M^2} \sin^2\theta' + M \sin^2\theta'] k_o}{\sqrt{1 - M^2} \sin^2\theta' \{\sqrt{1 - M^2} \sin^2\theta' - M \cos\theta\}} \quad (96)$$

θ' , R' denote (in Figure 33) the angle from line of source motion and distance from source location of the far field point at current time. Denote by θ , R these same quantities measured from the source location at the time that the radiation reaching the observer at current time was emitted. θ , R are shown in Figure 33. Straightforward kinematics leads to:

$$\tan(\theta') = \frac{\sin\theta}{\cos\theta - M} \quad (97)$$

$$\text{or } \sin(\theta') = \frac{\sin\theta}{\sqrt{1 + M^2 - 2M \cos\theta}} \quad (98)$$

$$\text{and } \cos(\theta') = \frac{(\cos\theta - M)}{\sqrt{1 + M^2 - 2M \cos\theta}} \quad (99)$$

In terms of θ ,

$$a_o = \frac{k_o \cos\theta}{(1 - M \cos\theta)} \quad (100)$$

A tedious calculation of $h''(a_o)$ from (93) shows that,

$$+ h''(a_o) = \frac{(1 - M \cos\theta)^3}{k_o \sqrt{1 + M^2 - 2M \cos\theta} \sin^2\theta} \quad (101)$$

confirming that $h''(\alpha_0) > 0$ (for $0 \leq \theta \leq \pi$). Also corresponding to (100)

$$\alpha^+(\alpha_0) = \frac{k_0 \sin\theta}{(1 - M \cos\theta)} \quad (102)$$

$$\alpha_0 M + k_0 = \frac{k_0}{(1 - M \cos\theta)} \quad (103)$$

$$h(\alpha_0) = \frac{-k_0 \cos(\theta - \theta')}{(1 - M \cos\theta)} \quad (104)$$

Since $p = -\rho_0 \frac{\partial \phi}{\partial t}$, from (87) we may deduce that,

$$p = \frac{q_0 e^{j\omega_0 t}}{8\pi\rho_0} \int_{-\infty}^{\infty} (\omega_0 + \alpha V) H_0^{(2)}(\alpha^+ r) e^{-j\alpha(x - Vt)} d\alpha \quad (105)$$

The point of stationary phase for p is clearly the same as for ϕ and hence in the far field p may be approximated by

$$p \sim \frac{j q_0 e^{j\omega_0 t} e^{-jk_0 R}}{4\pi R (1 - M \cos\theta)^2} \quad (106)$$

This result is in complete accord with the far field part of equation (11.2.15) of Morse and Ingard's "Theoretical Acoustics" (p. 724).

1.6.1 Extension to a Slug Flow, Cold Jet (Figure 34)

In this case, in region I, the transform $\phi(r, t)$ satisfies:

$$\begin{aligned} \frac{1}{r} \frac{\partial}{\partial r} \left(r \frac{\partial \phi}{\partial r} \right) - \alpha^2 (1 - M^2) \phi + 2j M \frac{\alpha}{c} \frac{\partial \phi}{\partial t} - \frac{1}{c^2} \frac{\partial^2 \phi}{\partial t^2} \\ = \frac{q_0}{2\pi\rho_0} e^{j\omega_0 t} e^{j\alpha V c t} \delta(y) \delta(z) \end{aligned} \quad (107)$$

where $V_c = c M_c =$ source convection velocity (M_c is the source convection Mach number)

and in region II:

$$\frac{1}{r} \frac{\partial}{\partial r} \left(r \frac{\partial \phi}{\partial r} \right) - \alpha^2 \phi - \frac{\partial^2 \phi}{c^2 \partial t^2} = 0 \quad (108)$$

(107) can be rewritten as:

$$\begin{aligned} \frac{1}{r} \frac{\partial}{\partial r} \left(r \frac{\partial \phi}{\partial r} \right) + \{ [k_0 - \alpha(M - M_c)]^2 - \alpha^2 \} \phi \\ = \frac{q_0}{2\pi\rho_0} \delta(y) \delta(z) \end{aligned} \quad (109)$$

for $0 \leq r < a$.

For $r > a$, (109) can be rewritten as:

$$\frac{1}{r} \frac{\partial}{\partial r} \left(r \frac{\partial \phi}{\partial r} \right) + [(k_0 + \alpha M_c)^2 - \alpha^2] \phi = 0 \text{ for } r > a \quad (110)$$

As before interest is only in range of α such that,

$$-\frac{k_0}{1 + M_c} \leq \alpha \leq \frac{k_0}{1 - M_c}$$

The solution of (109) for $\frac{-k_0}{1 + M_c} \leq \alpha \leq k_0/(1 - M_c + M)$ will be assumed of form

$$\left\{ \frac{j q_0}{8\pi\rho_0} H_0^{(2)}(\underline{a}^+ r) + A_I J_0(\underline{a}^+ r) \right\} \text{ where } \underline{a}^+ = \sqrt{[k_0 - \alpha(M - M_c)]^2 - \alpha^2}$$

For $k_0/(1 - M_c + M) \leq \alpha \leq \frac{k_0}{(1 - M_c)}$, the solution is assumed of form

$$\left\{ \frac{-q_0}{4\pi^2 \rho_0} K_0(\underline{\alpha}^+ r) + A_{II} I_0(\underline{\alpha}^+ r) \right\} \text{ where } \underline{\alpha}^+ = \sqrt{\alpha^2 - [k_0 - \alpha(M - M_c)]^2}.$$

The solution to (110) will be (for $\frac{-k_0}{(1 + M_c)} \leq \alpha \leq \frac{k_0}{(1 - M_c)}$) of form $A_{II} H_0^{(2)}(\underline{\alpha}^+ r)$ where

$$\alpha^+ = \{(\alpha M_c + k_0)^2 - \alpha^2\}^{1/2}.$$

Matching conditions at $r = a$ of radial particle displacement and of acoustic pressure will yield:

$$\left[1 - \alpha \left(\frac{M - M_c}{k_0}\right)\right] \phi(r \rightarrow a_-) = \left[1 + \frac{\alpha M_c}{k_0}\right] \phi(r \rightarrow a^+) \dots \quad (111)$$

and

$$\left(\frac{\partial \phi}{\partial r}\right)_{r \rightarrow a_-} = \frac{\left[1 - \frac{\alpha(M - M_c)}{k_0}\right]}{\left(1 + \frac{\alpha M_c}{k_0}\right)} \left(\frac{\partial \phi}{\partial r}\right)_{r \rightarrow a^+} \dots \quad (112)$$

Equations (111) and (112) suffice to determine A_I and A_{II} .

Solution for A_I and A_{II}

Consider first the case where $\frac{-k_0}{1 + M_c} \leq \alpha \leq k_0/(1 - M_c + M)$. Then the matching conditions (111) and (112) give:

$$\left(1 + \frac{\alpha M_c}{k_0}\right) A_{II} H_0^{(2)}(\underline{\alpha}^+ a) - A_I J_0(\underline{\alpha}^+ a) \left(1 - \frac{\alpha(M - M_c)}{k_0}\right)$$

$$\begin{aligned}
&= \frac{j q_0}{8\pi \rho_0} H_0^{(2)}(\underline{\alpha}^+ a) \left(1 - \frac{\alpha(M - M_c)}{k_0}\right) \\
A_{II} &= \frac{H_1^{(2)}(\underline{\alpha}^+ a)}{\left(1 + \frac{\alpha M_c}{k_0}\right)} - \underline{\alpha}^+ J_1(\underline{\alpha}^+ a) A_I / \left(1 - \frac{\alpha(M - M_c)}{k_0}\right)
\end{aligned}$$

(113a)

$$= \frac{j \underline{\alpha}^+ H_1^{(2)}(\underline{\alpha}^+ a) q_0}{8\pi \rho_0 \left(1 - \frac{\alpha(M - M_c)}{k_0}\right)}$$

(113b)

The solution to (113a, b) for A_{II} is:

$$\begin{aligned}
A_{II}(\alpha) &= \frac{q_0}{4\pi^2 \rho_0 \left\{ \left(1 + \frac{\alpha M_c}{k_0}\right) H_0^{(2)}(\underline{\alpha}^+ a) J_1(\underline{\alpha}^+ a) \underline{\alpha}^+ a / \left(1 - \frac{\alpha(M - M_c)}{k_0}\right) \right.} \\
&\quad \left. \frac{\alpha^+ a J_0(\underline{\alpha}^+ a) H_1^{(2)}(\underline{\alpha}^+ a) \left(1 - \frac{\alpha(M - M_c)}{k_0}\right)}{\left(1 + \frac{\alpha M_c}{k_0}\right)} \right\}}
\end{aligned}$$

(114)

Now consider $k_0/(1 - M_c + M) \leq \alpha \leq k_0/(1 - M_c)$. The matching conditions (111), (112) yield:

$$\begin{aligned}
 & \left(1 + \frac{\alpha M}{k_0 c}\right) A_{II} H_0^{(2)}(\underline{a}^+ a) - A_I I_0(\underline{a}^+ a) \left(1 - \frac{\alpha(M - M_c)}{k_0}\right) \\
 &= \frac{-q_0}{4\pi^2 \rho_0} K_0(\underline{a}^+ a) \left(1 - \frac{\alpha(M - M_c)}{k_0}\right)
 \end{aligned}$$

(115a)

and

$$\begin{aligned}
 & \frac{\alpha^+ H_1^{(2)}(\underline{a}^+ a)}{\left(1 + \frac{\alpha M}{k_0 c}\right)} + \underline{a}^+ I_1(\underline{a}^+ a) / \left(1 - \frac{\alpha(M - M_c)}{k_0}\right) \\
 &= \frac{-q_0 \underline{a}^+}{4\pi^2 \rho_0} K_1(\underline{a}^+ a) / \left(1 - \frac{\alpha(M - M_c)}{k_0}\right)
 \end{aligned}$$

(115b)

The solution for A_{II} of (115a) and (115b) is:

$$\begin{aligned}
 A_{II} &= \frac{-q_0}{4\pi^2 \rho_0 \left(1 - \frac{\alpha M}{k_0 c}\right) \underline{a}^+ a I_1(\underline{a}^+ a) H_0^{(2)}(\underline{a}^+ a) / \left(1 - \frac{\alpha(M - M_c)}{k_0}\right)} \\
 &+ \frac{(\underline{a}^+ a) H_1^{(2)}(\underline{a}^+ a) I_0(\underline{a}^+ a) \left(1 - \frac{\alpha(M - M_c)}{k_0}\right)}{\left(1 + \frac{\alpha M}{k_0 c}\right)}
 \end{aligned} \tag{116}$$

Equations (114) and (116) give the complete solution to $A_{II}(\alpha)$ for $\frac{-k_0}{(1+M_c)} \leq \alpha \leq \frac{k_0}{(1-M_c)}$. The following limits are to be noted. As α tends to $-k_0/(1+M_c)$ or $k_0/(1-M_c)$, α^+ tends to zero and it turns out that $A_{II}(\alpha)$ also tends to zero (as $1/\log(\epsilon)$ as ϵ tends to zero). Also as α tends to $k_0/(1+M-M_c)$ α^+ and α^- tend to zero and A_{II} tend to:

$$\frac{-q_0(1+M)}{4\pi^2 \rho_0 (\alpha^+ a) H_1^{(2)}(\alpha^+ a)} \quad (117)$$

where $\alpha^+ a = k_0 a \sqrt{M^2 + 2M}$ ($1+M = M_c$). For $r > a$ then, one has:

$$\phi = e^{j\omega_0 t} \int_{-\infty}^{\infty} A_{II}(\alpha) H_0^{(2)}(\alpha^+ r) e^{-j\alpha(x - v_c t)} d\alpha \dots \quad (118)$$

$$p = -\rho_0 \frac{\partial \phi}{\partial t} \quad (\text{for } r > a) =$$

$$-j e^{j\omega_0 t} \rho_0 \int_{-\infty}^{\infty} A_{II}(\alpha) H_0^{(2)}(\alpha^+ r) (\omega_0 + \alpha v_c) e^{-j\alpha(x - v_c t)} d\alpha \quad (119)$$

As before to get the far field, directivity is obtained by an asymptotic expansion of (119) by the method of stationary phase for large values of $[(x - v_c t)^2 + r^2]^{1/2}$. The point of stationary phase for the integral in (119) is clearly the same as for the integral of (105). Thus p is given in the far field by:

$$\frac{2 e^{j(\omega_0 t - k_0 R)} \omega_0 A_{II}(\alpha_0) \rho_0}{R(1 - M_c \cos\theta)^2} \quad (120)$$

where $\alpha_0 = k_0 \cos\theta / (1 - M_c \cos\theta)$.

The limit of $A_{II}(\alpha_0)$ as $(k_0 a)$ tends to zero (low frequency limit) is:

$$\frac{j q_0}{8\pi \rho_0 (1 - M_c \cos\theta)} \dots \quad (121)$$

so that the low frequency expression for the far field of a moving harmonic point source in a slug flow, cold, round subsonic jet is:

$$p = \frac{j q_0 \alpha_0 e^{j(\omega_0 t - k_0 R)}}{4\pi (1 - M_c \cos\theta)^2 R(1 - M_c \cos\theta)} \quad (122)$$

Contrast this with (106) wherein p is given by:

$$\frac{j q_0 \omega_0 e^{j(\omega_0 t - k_0 R)}}{4\pi R(1 - M_c \cos\theta)^2}$$

being the directivity of a freely moving point harmonic source (i.e. unencumbered by the presence of a shrouding jet flow).

The general case is given by (120) with $A_{II}(\alpha)$ given by (114), (116), and α_0 given by (100) (substituting M_c for M).

1.6.2 Results

In Figures 35-37, we show first results of the present calculations compared with data from Lush⁴. A range of source Strouhal numbers from 0.03 to 1.0 and a range of jet velocities from 124 m/s to 300 m/s (corresponding to jet Mach numbers from 0.366 to 0.878) was covered by Lush. In the theoretical predictions it is assumed that owing to the finite eddy life time as well as the measurements being several diameters away from the jet nozzle, the angle from the jet axis will correspond to the angle measured from the position of emission which appears in the theoretical results.

The predictions and data of Figure 35 agree fairly well. In Figures 36 and 37 however we notice that the plug flow model consistently overestimates the refractive effect especially at the higher source frequencies. For example the angle at which the peak radiation occurs is consistently overestimated by anywhere from 0 to 20° or so. If we make an allowance for this by one empirical adjustment whereby we force the peaks of the predicted and measured patterns to coincide, the present calculations turn out to be in rather good agreement with Lush's data. This is shown in Figures 38-40 wherein as indicated the theoretical predictions have been shifted or translated towards the jet axis by varying amounts (the amounts are shown) so that the peaks of the measured and predicted patterns coincide. Now except for one case of $M_j = 0.878$ and source Strouhal number = 1.0, there is extremely good agreement between predicted and measured directivity patterns. In the case of $M_j = 0.878$ and source Strouhal number = 1.0 the radiation aft of the peak angle is still nicely predicted but the refractive dip is again overestimated.

Thus, allowing for the fact that an overestimation of the peak angle of radiation occurs which can be corrected for empirically by adjusting (translation towards jet axis) the theoretically predicted directivity so that its peak coincides with the peak of the experimental pattern, the calculations of this last section succeed in explaining the directivity of cold, subsonic jet noise over five octaves of source Strouhal numbers (0.03 to 1.0) and velocities ranging from 124 m/s to 300 m/s.

2.0 AERODYNAMIC NOISE EMISSION FROM TURBULENT SHEAR LAYERS

S.P. Pao

In this section the Phillips-Pao convected wave equation is employed to study aerodynamic noise emission processes in subsonic and supersonic shear layers. Particular attention is directed toward applying the theory to study the effects of jet density on sound emission, the effects of refraction and convection, and how this theory can be incorporated into GE comprehensive aero-acoustic prediction methods.

The Phillips-Pao analysis is based on the convected wave equation first introduced by Phillips in 1960. The convected wave equation itself is derived through the basic principles of fluid mechanics, and it is a natural extension of the Lighthill equation of aerodynamic noise. The linearized version of the general equation has the form of a simple wave equation in Lagrangian coordinates. The right-hand side of this equation contains four terms: a turbulent quadrupole, shear flow and turbulence interaction, entropy fluctuations and viscous effects. If the flow field is free of shocks, the acoustic pressure fluctuation can be assumed to be decoupled from the entropy fluctuations. It is tacitly assumed in the analysis that all terms on the right-hand side of the wave equation are known quantities and the contributions of individual terms can be considered as independent of each other.

2.1 The Effects of Jet Density on Sound Emission

Many recent experimental investigations have reported on the variation of sound power and frequency characteristics with jet density. Of particular interest is that the sound power depends on jet density following a power law dependence different from the classical Lighthill theory ρ_j^2 dependency. The actual experimental index has been observed to change significantly with the convection Mach number. The main objective here is to set forth a model within the framework of the Phillips-Pao theory to account for such variation.

In the Phillips-Pao theory, the first order effects on convection, refraction, and their coupling are included in the formulation. Hence, the only empirical elements in the theory are the structure of turbulence and the mean flow

properties. In previous numerical work, it was found that the assumption of L_1 (the scale of the turbulence) and α (the eddy decay parameter) influences strongly the character of sound emission. In the present GE jet noise project, the range of jet velocity is within 200 m/s to 1000 m/s, or $0.6 < M_j < 3.0$. Experimental evidences indicated that the value of L_1 may vary from 0.4 to 2.0, and the value of α is somewhere between 0.3 and 0.6. However, there is little further information on the structure of turbulence. Hence, an empirical model is proposed. This model is based on three assumptions:

- (a) For M_j less than one, the spatial scale remains constant. The temporal scale is assumed to vary as a function of the local speed of sound. Since frequency of sound with a fixed wave length increases with the speed of sound, the time scale is expected to decrease with an increase of the local speed of sound. Analytically, this assumption is represented by

$$\alpha = \alpha_0 A^{0.75}, \text{ where } A^{-2} \equiv \rho_j / \rho_0 \text{ and } \alpha_0 = \text{constant}$$

The index of 0.75 is chosen empirically.

- (b) For M_j greater than one, the scale ratio is assumed to be a function of the local true Mach number. In the classical approach, the scale ratio is assumed to follow the convection Mach number.

This assumption can be expressed by the following relation:

$$\alpha = \alpha_0 A^{-1}$$

The above formula follows from a comparison between the classical and the modified concepts of the scale ratio:

$$\frac{L_1}{c_0 L_t} = \alpha_0 M_c \text{ (classical); } \frac{L_1}{c_0 L_t} = \frac{\alpha_0}{A} M_c \text{ (Modified)}$$

- (c) The spatial scale, L_1 , is directly proportional to the local speed of sound:

$$L_1 = L_1^* A$$

This assumption permits not only a precise modeling of the sound power variation with jet density, but also a correct shift in frequency spectrum as compared with results given in Reference 15.

The assumption in (a) and (b) can be represented by a single formula:

$$\alpha = \alpha_0 A^{0.75} \{a + b A^{1.75}\}^{-1}$$

where

$$a = 1-b; \quad b = M_j^4 \{2.5 + M_j^4\}^{-1}$$

The parameters a and b are chosen to represent the change of range in the convection Mach number. No other physical meaning is associated with the definition of these parameters.

Based on this empirical model of turbulence, sound emission calculations are made according to the analytical solutions of the Phillips-Pao theory. Twenty-four cases of typical jet noise radiation in the range of M_j from 0.6 to 2.0, and the range of density ratio from 1.0 to 4.0. It should be noted that the density ratio is represented in the Phillips-Pao theory by the speed of sound ratio. For a perfectly expanded jet, these two quantities are related via a simple formula:

$$\rho_j / \rho_0 = A^{-2}$$

In these calculations, $\alpha_0 = 0.55$ and $L_1^* = 0.72$ which are consistent with the current accepted values for these parameters. Only one typical slice of the jet near the end of the potential core is used in the numerical work. This slice of jet is further subdivided into nine annular segments. Noise radiation from each segment is calculated separately, and the resultant sound power and intensity levels are summed to obtain the overall noise radiation from the jet. From experiences of previous numerical modeling of the noise radiation from an entire exhaust flow (Reference 17), the total sound power of the entire jet is contributed mainly from the transition region of the jet. Furthermore, the noise radiation characteristics in the initial region of the jet is analytically similar to the typical slice as chosen above. In most cases, this typical slice can represent approximately 70% of the sound power from the entire jet. Since a large number of cases are now considered, this simplified approach leads to a tremendous saving in terms of computer time.

The computed sound power is given in Figure 41. In this figure, only relative decibel values are given. The value of M_j is chosen to be 0.6, 0.8, 1.0, 1.25, 1.50, and 2.0. The speed of sound ratio A is chosen to be 1.0, 1.26, 1.59, and 2.0. These values of A correspond to density ratios of 1.0, 0.63, 0.395, and 0.25, respectively. Since the results in Reference 15 are given on logarithmic scales, the above value of density ratio are chosen for convenience. In the SNECMA-NGTE¹⁵ report, the sound power for supersonic jets are normalized according to the throat area. The sound power dependence on M_j is slightly different from the velocity dependence laws which normalizes the sound power according to the jet exit diameter. Figure 42 illustrates how this prediction compares with recent GE measurements. The exponential index for the density dependence can be obtained directly from Figure 41 by measuring the slopes of the curves. The results are given in Figure 43. The agreement of the empirical modeling with the SNECMA-NGTE and GE results are very close. It is also very interesting to note that the predicted trends of the power index in the high M_j range are also similar to the experimental results.

A normalized sound power curve has also been obtained from the numerical results. Figure 44 shows that the normalized sound power follows M_j at a rate which is slightly above U_j -law in the high velocity range. This increase in velocity dependence is caused partially by the normalization with respect to the nozzle throat area.

In a high velocity jet, the frequency characteristics is controlled mainly by the spatial scale of the turbulence. This is in direct contrast with low speed jet noise where the temporal scale of turbulence controls the frequency. In the present model, the spatial scale is assumed to increase with A . Therefore, the entire noise spectrum will shift to lower frequencies as the temperature of the jet increases. This is exactly the trend as observed in the SNECMA-NGTE experiments. Hence, with the present assumptions concerning the turbulence structure, the numerical results can represent accurately the sound power and the frequency characteristics of jet noise over a wide range of jet velocity and density.

2.2 The Effects of Refraction and Convection

In the Phillips theory, the effects of refraction and convection are closely coupled. In addition, the aerodynamical coupling between the sound source and the mean flow created an internal attenuation effect which is not detected in the classical theory of aerodynamic noise. These effects are best demonstrated by one of the solutions of the Phillips-Pao theory:

$$\frac{d^2 \psi^*(y)}{dy^2} = \frac{3\sqrt{2} \pi^{3/2} \gamma^2 v_0^4 M_c^4 M_c^4 \alpha^4}{r^2 A^2 L_1} \cdot \frac{q_\infty}{q_0} \cdot \frac{F(b)}{F(0)} \cos^4 \theta \left\{ (1 - M_c \cos \theta)^2 + \alpha^2 M_c^2 \cos^2 \theta \right\}^{-5/2}$$

This equation is applicable for noise radiation in the downstream directions, where the turbulence volume as responsible for noise emission is located below a transition point. In the above equation, the attenuation factor is represented by the function $F(b)/F(0)$. The definitions of $F(b)$ and its argument b can be found in Reference 18. The genuine refraction effect is given by the ratio q_∞/q_0 . The convection factor is different from its classical form. Although some refraction effect is represented by q_∞/q_0 , the coupling of convection and refraction is so strong such that the evaluation of the pure refraction factor alone becomes an academic exercise. In the present study, the effect of convection-refraction coupling is evaluated as a single quantity. If the attenuation factor is removed from the above equation, the remainder of the equation is equivalent to the classical result. Two special cases are investigated. The convection Mach number is chosen to be 1.0 and 2.0, while the speed of sound ratio is 1.0. Results from the Phillips-Pao theory are compared with the Lighthill theory. The results of the numerical calculations are given in Figures 45 and 46. In the Mach number range of interest to the present study, the coupled effects of convection and refraction reduce the sound emission intensity in the downstream direction by a significant amount. As a consequence of these interactions, the peak noise direction is moved outward to the 45° to 60° area. The effect of attenuation reduces further the total sound power in the directions close to the jet axis. The net effect of refraction and convection can be obtained by comparing the directivities of the Lighthill theory and the Phillips-Pao calculation without the attenuation

effect. The results are given in Figures 47 and 48. The effect of attenuation is also given on these figures. In the downstream directions, the effect of refraction-convection is comparable with the attenuation effect. However, there is no attenuation effect in the transverse and upstream directions. The coupled effects of refraction and convection generally increase the noise intensity in the upstream direction. At 90° from the jet axis, the predictions of the Lighthill theory and the Phillips-Pao theory are identical.

It should be noted that the classical convection effect is completely nullified by its coupling with refraction in upstream directions. This can be seen clearly in the governing solution in this region:

$$\overline{\phi\phi^*}(y) = \frac{3\sqrt{2}\pi^{3/2} \gamma^2 v_o^4 M_c^4 \alpha^4}{r^2 A^2 L_1} \cdot \frac{q_\infty}{q_o} \cdot \frac{A}{(1-M_c \cos\theta)} \{A^2 + \alpha^2 M_c^2\}^{-5/2}$$

The commonly recognized convection factor is reduced to a constant:

$$C^5 = \{A^2 + \alpha^2 M_c^2\}^{-5/2}$$

Hence, the directivity in the upstream direction is determined entirely by the refraction factor and a Doppler shift factor, as indicated in the above formula. As a consequence of this change of mechanism, the predicted directivity pattern follows apparently a $\{(1-M_c \cos\theta)^2 + \alpha^2 M_c^2\}^{-3/2}$ law.

Based on these studies of refraction and convection, there are several possible experimental approaches which can serve to verify the Phillips-Pao theory:

- (a) The attenuation effect is restricted to the downstream direction. The amount of attenuation is a function of frequency. The magnitude of attenuation as measured in dB is directly proportional to frequency. The integrated attenuation effect over the entire spectrum is given by F(b) as previously shown. Hence, the difference in directivity for jet noise at different frequencies can be compared to the analytical predictions.

- (b) In upstream directions, the directivity pattern is determined entirely by refraction and Doppler effects. Hence, the upstream directivity appears to follow a $\{(1-M_c \cos\theta)^2 + \alpha^2 M_c^2\}^{-3/2}$ pattern instead of the classical $\{(1-M_c \cos\theta)^2 + \alpha^2 M_c^2\}^{-5/2}$. Hence, there should be no conflict between the experimental measurement and the theoretical predictions of the convection effects.
- (c) In the theory, the correspondence between the source and the sound field is precisely defined. Hence correlation measurements between the two should be an effective way to verify the theoretical model.

2.3 Phillips-Pao Model for Detailed Predictions

The purpose here as well as in most of the theory development in this program is to formulate the theories in a fashion applicable for incorporation into General Electric's comprehensive aero-acoustic predictive schemes. To compute the sound pressure spectra via the Phillips-Pao theory the following sound pressure spectrum equations are necessary:

$$(S_0) \quad \frac{\overline{p^2}}{p_o^2}(r, \omega) = \frac{\pi v_o^4 M^8 \tilde{L}_t}{32 r^2 A^6 L_1} \frac{q_\infty}{q_o} \frac{(\omega_o \tilde{L}_1)^4}{(1-M_c \cos\theta)} \times \\ \exp \left[-\frac{1}{8} \{ (k_o \tilde{L}_1)^2 + (\omega_o \tilde{L}_t)^2 \} \right]$$

$$(S1)_a \quad \frac{\overline{p^2}}{p_o^2}(r, \omega) = \frac{\pi^2 v_o^4 M^8 \tilde{L}_t A_i^2(o) \tan\theta}{8 r^2 A^2 L_1^{4/3} \Omega^{1/3}} \frac{(\omega_o \tilde{L}_1 \cos\theta)^{13/3}}{(1-M_c \cos\theta)^{16/3}} \times \\ \exp \left[-\frac{1}{8} \{ (k_1 \tilde{L}_1)^2 + (\omega_o \tilde{L}_t)^2 \} \right]$$

$$(S1)_b \quad \frac{\overline{p^2}}{p_o^2}(r, \omega) = \frac{\pi^2 v_o^4 M^8 \tilde{L}_t}{32 r^2 A^2 L_1} \frac{q_\infty}{q_o} e^{-2Q} \frac{(\omega_o \tilde{L}_1 \cos\theta)^4}{(1-M_c \cos\theta)^5} \times \\ \exp \left[-\frac{1}{8} \{ (k_1 \tilde{L}_1)^2 + (\omega_o \tilde{L}_t)^2 \} \right]$$

where

$$\tilde{L}_t = \frac{L_1 U}{u_j \alpha b}$$

$$\omega_o = 2\pi S_t (1 - M_c \cos\theta)$$

$$k_1 = -M\omega \cos\theta$$

$$k_o = -\omega_o M/A$$

The characteristic Strouhal number of self noise and shear noise for each volume of turbulence may be computed via the following expressions:

For self noise

$$St = \frac{1}{4\pi a^2} \left\{ -d + \sqrt{d^2 + 8a^2} \right\}$$

For shear-noise

$$St = \frac{1}{4\pi a^2} \left\{ -d + \sqrt{d^2 + 4a^2} \right\}$$

where

$$a^2 = 1/8 \{ (1 - M_c \cos\theta)^2 + \alpha^2 M_c^2 \cos^2\theta \} L_t^2$$

$$d = MW(r, \theta) \cos\theta$$

$$M = u_t / a_o$$

Preliminary checks of this model have been performed and a complete check-out of the method is underway. However, some results can be shown. Comparisons of Pao's model with two hot supersonic jet measurements have been run. The comparisons are made at the important 90° location. At this location the effects of convection amplification and refraction are minimal and this location

is a base location for any initial comparison of exact theories. Figure 49 shows a theory data comparison of OASPL for cases of $M_j = 1.095$ and 1.464 . Figure 50 shows a set of SPL spectra comparisons for these two cases as well. For the case where $M_j = 1.095$, close agreement between data and computation is observed. However, the comparison is rather poor for $M_j = 1.464$. The difference in SPL is more than 5 dB for a significant portion of the spectrum, whereas the computed spectrum does not demonstrate the correct trend for the SPL variation as a function of frequency. It is important to point here that the theoretical results as stated at the beginning of this section describes the noise radiation from a single correlated volume of turbulence. The structure of turbulence is assumed to be Gaussian and isotropic in a moving frame of reference. For noise radiation from a complete jet exhaust flow, the observed sound field is a collection of contributions from many individual source volume elements. A vastly complex synthesis is involved in building a noise calculation model such as the GE Aero Acoustic prediction methods. In addition, a more realistic model of turbulence (vs. Gaussian and isotropic) may be required for spectral predictions. The development of this model is currently performed by the engineering staff at GE, and undoubtedly it will continue to receive great attention so that this predictive method will be checked out completely.

3. THE QUESTION OF CONVECTION AND REFRACTION COUPLING
IN JET NOISE TURBULENT MIXING THEORIES

H.S. Ribner

Lighthill's theory of jet noise employs a nonconvected wave equation forced by a certain source term. In its exact form this term accounts fully for the co-moving fluid, including convection and refraction effects. In practice it is necessary to hold the density factor constant in the source term, and this has the effect of suppressing the refraction effect and throwing some doubt on values of the convection effect. Alternate formulations via convected wave equations such as are discussed in Section 1 and 2 above are gaining interest. An attempt is made in this section to bring some coherence into the subject.

In addition, some supporters of the convected wave approach have asserted that convection and refraction effects are intimately related and must be dealt with jointly in the solution of the convected wave equation. On the other hand, the position taken here is that convection and refraction can be obtained as separable multiplicative factors. In the present work an analysis is carried out to indicate the degree of separation of these two effects that can be obtained.

3.1 Does the Lighthill Equation Account for Refraction? Yes and No

Lighthill's wave equation for an inviscid nonheatconducting fluid may be written:

$$\frac{1}{c_o^2} \frac{\partial^2 p}{\partial t^2} - \nabla^2 p = \frac{\partial^2 \rho v_i v_j}{\partial x_i \partial x_j} + \frac{1}{c_o^2} \frac{\partial^2}{\partial t^2} (p - c_o^2 \rho) \quad (1)$$

On expanding the right-hand side, with use of the equation of continuity, etc:

$$\frac{1}{c_o^2} \frac{\partial^2 p}{\partial t^2} - \nabla^2 p = \frac{1}{c_o^2} \frac{\partial^2 p}{\partial t^2} - \frac{1}{c^2} \frac{D^2 p}{Dt^2} + \rho \frac{\partial v_i}{\partial x_j} \frac{\partial v_j}{\partial x_i} + \frac{\gamma}{\rho} \frac{De}{Dt}^2 - \frac{1}{\rho} \frac{\partial p}{\partial x_i} \frac{\partial \rho}{\partial x_i}$$

Shifting terms from the RHS to the LHS yields a convected wave equation

$$\frac{1}{c^2} \frac{D^2 p}{Dt^2} - \nabla^2 p - \text{"extra terms"} = \rho \frac{\partial v_i}{\partial x_j} \frac{\partial v_j}{\partial x_i} \quad (2)$$

by virtue of the convective operator $\frac{D}{Dt}$.

Thus density derivatives in the expansion of Lighthill's source term, the RHS of (1), lead to a convected wave equation, hence to prediction of refraction effects (cf. work of e.g. Schubert) arising from the jet velocity gradients.

In the normal application of Lighthill's equation (1) the density ρ is taken constant on the RHS. This has the effect of eliminating the additional terms which led to the convected wave equation (2); that is, setting $\rho =$ constant in effect suppresses the refraction effect

3.2 Separation of Convection and Refraction Effects by Use of Green's Function

We can restore the missing refraction effect by solving (2) instead of (1). Solution of (1) by the method of Ribner yields the mean square pressure as a product of a "basic directivity" times a "convection factor". The basic solution of (2) yields a Green's function for a stationary monopole point source. This is then manipulated to yield a "basic directivity" times a "convection factor" - which are the same as for equation (1) - multiplied by a "refraction factor". The latter is developed from the Green's function according to the following procedure.

We, in effect, extract a single frequency ω by taking Fourier transforms of both sides of (2). Then we inject a stationary harmonic point source into the flow at \underline{y} by replacing the RHS by $4\pi \delta(\underline{y}-\underline{x})$. The sound pressure $p(\underline{x})$ is the Green's function

$$\tilde{g}_c(\underline{x}|\underline{y};\omega) \quad (3)$$

which may be obtained by calculation (cf. Schubert) or by the experimental injected point source technique (cf. Stvars et al). The refraction effect is embodied in \tilde{g}_c as it varies with the direction of the observer vector \underline{x} .

The solution of the narrow band convected wave equation (Fourier transform of (2)) is then

$$\tilde{p}_c(\underline{x}, \omega) = \frac{1}{4\pi} \int \tilde{g}_c ; \left\{ \begin{array}{l} \text{source strength at } \underline{y} \\ \text{(narrow band)} \end{array} \right\} d^3 y \quad (4)$$

The source strength is the F.T. of the RHS of (2); however, equivalent results can be obtained with the Proudman-Lighthill source strength in narrow band,

$$\text{F.T. } \frac{\bar{\rho}}{c_o} \frac{\partial^2 v_x}{\partial t^2} \quad (5)$$

with ρ approximated by $\bar{\rho}$ (in this case the refraction is not suppressed).

On squaring (4) and manipulating the results according to established procedures for random functions, there results

$$\phi_c(\underline{x}, \omega) = \frac{1}{16\pi^2} \iint \tilde{g}_c(\underline{x}|\underline{y}'; \omega) \phi_q(\underline{y}', \underline{y}''; \omega) d^3 \underline{y}' d^3 \underline{y}'' \quad (6)$$

where ϕ_q is a two-point cross-spectral density of the source-strength $\frac{\bar{\rho}}{c_o} \frac{\partial^2 v_x}{\partial t^2}$.
Let

$$\underline{y} = \frac{\underline{y}' + \underline{y}''}{2} \quad \text{and} \quad \xi = \underline{y}'' - \underline{y}' \quad (7)$$

Then $d^3 \underline{y}' d^3 \underline{y}'' \rightarrow d^3 \xi d^3 \underline{y}$ in (6). If now, we specialize the LHS to apply to a unit volume at \underline{y} , rather than the entire jet, the integral over $d^3 \underline{y}$ may be dropped, and there results

$$\phi_c(\underline{x}|\underline{y}; \omega) = \frac{1}{16\pi^2} \int \tilde{g}_c \tilde{g}_c^* \phi_q(\underline{\xi}, \underline{y}; \omega) d^3 \xi \quad \text{at } \underline{y} \quad (8)$$

\tilde{g}_c and \tilde{g}_c^* are evaluated to a sufficient approximation at \underline{y}_0 , rather than \underline{y}' , \underline{y}'' respectively. This approximation reflects the known insensitivity of the Green's function to source position which was found experimentally.

In the far field \tilde{g}_c will decay like $1/X$ and will have a directional factor and a phase:

$$\text{Green's Function } \tilde{g}_c \approx \frac{F(\theta, \gamma, \omega)}{x} e^{i\psi} \quad (9)$$

Thus (8) will have the form

$$\text{Spectral Density } \phi_c(\underline{x}|\underline{y}; \omega) = \frac{F^2(\theta, \omega)}{16\pi^2 x^2} \int \phi_q(\xi, \underline{y}, \omega) e^{i\Delta\psi(\tau^*, \theta, \underline{y}, \omega)} d^3\xi \quad (10)$$

where $\tau^* = \underline{\xi} \cdot \underline{X}/C_0 X$, and a weak dependence on azimuth angle γ is neglected in F and in ψ .

The corresponding result of solving the ordinary nonconvected wave equation of Lighthill has the form

$$\text{Spectral Density } \phi_o(\underline{x}|\underline{y}; \omega) = \frac{1}{16\pi^2 x^2} \int \phi_q(\xi, \underline{y}, \omega) e^{i\omega\tau^*} d^3\xi \quad (11)$$

phase factor

Equations (10) and (11) are narrow band directivities of the jet noise emitted from unit volume at y . For the case of the Lighthill derived format, (11), was, in effect, postulated as the Fourier transform of a Gaussian 2-point correlation function in earlier work of Ribner and of Ffowcs Williams. (Ribner used a "moving" correlation function in a stationary frame, as required in the present formulation. Ffowcs Williams used a correlation function that appeared stationary in a frame moving with the jet flow). Both approaches gave identical results upon carrying out the integration in (11). The results, when normalized to unity at $\theta = 90^\circ$ take the form

$$\frac{\phi_o(\theta, \omega)}{\phi_o(90^\circ, \omega')} = \frac{C^{-4}(\theta)}{C^{-4}(90)} \quad \begin{array}{l} \text{Convection Factor} \\ \text{(Narrowband)} \end{array} \quad (12)$$

where

$$C(\theta) = [(1 - M_c \cos\theta) + \alpha^2 M_c^2]^{1/2}; \text{ Doppler Factor}$$

$$\omega C(\theta) = \omega' C(90^\circ) = \text{Source frequency} \quad (13)$$

$$\omega = \text{observed frequency}$$

(Although $(1-Mc \cos \theta)^{-1}$ is the true Doppler shift of frequency owing to source motion, the constituent frequencies of jet noise behave as if there were an effective Doppler shift C^{-1} between source frequencies and observed frequencies. The reasons are fully explained in Ribner (1960), (1962), (1963), etc.)

The corresponding broad band correction factor was obtained as $C^{-5}(\theta)/C^{-5}(90^\circ)$ by Ffowcs Williams and by Ribner.

The corresponding ratio of narrow band directivities resulting from the corrected wave equation is derived from equation (10). It is convenient to multiply and divide by $C^{-4}(\theta)/C^{-4}(90^\circ)$.

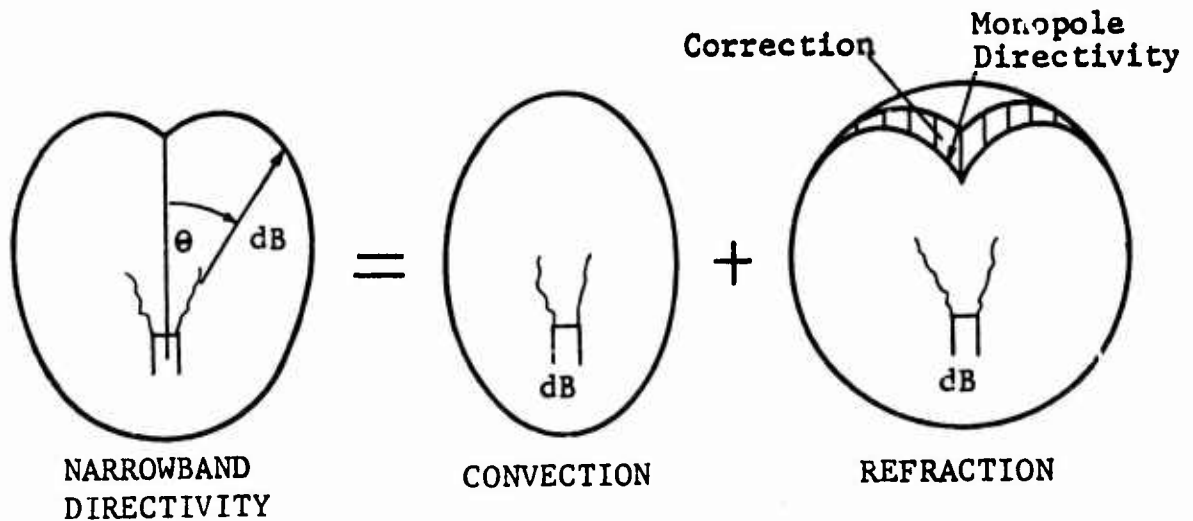


Figure 51

(Somewhat elliptic "Basic Directivity" is overlooked in this analysis).

Thus the net effect of replacing the Lighthill equation by the convected wave equation is to multiply (or to add on a dB basis) the Lighthill-based convection factor C^{-4} by a refraction factor. The refraction factor consists of a dominant part $F^2(\theta, \omega)$, which is the (amplitude)² of the Green's function, and a correction (integral). The $F^2(\theta, \omega)$ is simply the directivity that could be (and has been) observed by injecting a monopole pure tone point source into the jet. The correction - it is thought (cf. MacGregor, Ribner, Law (1973) - accounts for the difference between the refraction experienced by a spherical initial pattern (monopole pattern) and that which would be experienced by the nonspherical pattern labelled "Convection" in the sketch.

APPENDIX II-1

(E-01, E-02 and E-03 denote 10^{-1} , 10^{-2} and 10^{-3})

$$M_0 = 0.50$$

$$\phi \text{ (degrees)} = 10.0 \quad \theta \text{ (degrees)} = 48.7$$

δ/λ	$ R $	$\arg(R)$ (degrees)
0.	4.871E-01	180.00
0.05	4.856E-01	178.35
0.10	4.813E-01	176.80
0.18	4.702E-01	174.76

$$\phi \text{ (degrees)} = 20.0 \quad \theta \text{ (degrees)} = 50.3$$

δ/λ	$ R $	$\arg(R)$ (degrees)
0.	2.094E-01	180.00
0.05	2.081E-01	177.18
0.10	2.048E-01	174.59
0.18	1.964E-01	171.28

$$\phi \text{ (degrees)} = 30.0 \quad \theta \text{ (degrees)} = 52.8$$

δ/λ	$ R $	$\arg(R)$ (degrees)
0.	5.301E-02	180.00
0.05	5.299E-02	179.82
0.10	5.291E-02	179.66
0.18	5.274E-02	179.50

$$\phi \text{ (degrees)} = 40.0 \quad \theta \text{ (degrees)} = 56.4$$

δ/λ	$ R $	$\arg(R)$ (degrees)
0.	3.276E-02	0.
0.05	3.253E-02	-19.09
0.10	3.191E-02	-37.13
0.18	3.056E-02	-62.16

$$\phi \text{ (degrees)} = 50.0 \quad \theta \text{ (degrees)} = 60.9$$

δ/λ	$ R $	$\arg(R)$ (degrees)
0.	7.346E-02	0.
0.05	7.191E-02	-15.38
0.10	6.784E-02	-29.73
0.18	5.912E-02	-49.21

$M_0 = 0.50$ (Cont.)

ϕ (degrees) = 60.0 θ (degrees) = 66.4

<u>δ/λ</u>	<u>R</u>	<u>arg(R) (degrees)</u>
0.	8.305E-02	0.
0.05	8.081E-02	-16.64
0.10	7.510E-02	-31.87
0.18	6.360E-02	-51.80

ϕ (degrees) = 70.0 θ (degrees) = 73.0

<u>δ/λ</u>	<u>R</u>	<u>arg(R) (degrees)</u>
0.	7.001E-02	0.
0.05	6.772E-02	-18.52
0.10	6.208E-02	-35.18
0.18	5.143E-02	-56.36

ϕ (degrees) = 80.0 θ (degrees) = 80.0

<u>δ/λ</u>	<u>R</u>	<u>arg(R) (degrees)</u>
0.	4.042E-02	0.
0.05	3.888E-02	-20.51
0.10	3.521E-02	-38.67
0.18	2.869E-02	-61.20

ϕ (degrees) = 100.0 θ (degrees) = 101.0

<u>δ/λ</u>	<u>R</u>	<u>arg(R) (degrees)</u>
0.	4.383E-02	180.00
0.05	4.186E-02	156.21
0.10	3.738E-02	135.56
0.18	3.010E-02	110.67

ϕ (degrees) = 120.0 θ (degrees) = 131.8

<u>δ/λ</u>	<u>R</u>	<u>arg(R) (degrees)</u>
0.	6.871E-02	180.00
0.05	6.573E-02	157.55
0.10	5.887E-02	137.97
0.18	4.737E-02	114.19

$$M_0 = 0.70$$

$$\phi \text{ (degrees)} = 10.0 \quad \theta \text{ (degrees)} = 54.3$$

δ/λ	$ R $	$\arg(R)$ (degrees)
0.	4.695E-01	180.00
0.05	4.686E-01	179.20
0.10	4.664E-01	179.47
0.18	4.606E-01	177.56

$$\phi \text{ (degrees)} = 20.0 \quad \theta \text{ (degrees)} = 55.5$$

δ/λ	$ R $	$\arg(R)$ (degrees)
0.	1.847E-01	180.00
0.05	1.844E-01	179.50
0.10	1.838E-01	179.06
0.18	1.823E-01	178.54

$$\phi \text{ (degrees)} = 30.0 \quad \theta \text{ (degrees)} = 57.4$$

δ/λ	$ R $	$\arg(R)$ (degrees)
0.	2.376E-02	180.00
0.05	2.626E-02	-162.57
0.10	3.206E-02	-152.96
0.18	4.238E-02	-149.48

$$\phi \text{ (degrees)} = 40.0 \quad \theta \text{ (degrees)} = 60.1$$

δ/λ	$ R $	$\arg(R)$ (degrees)
0.	6.508E-02	0.
0.05	6.431E-02	-16.25
0.10	6.224E-02	-31.72
0.18	5.757E-02	-53.63

$$\phi \text{ (degrees)} = 50.0 \quad \theta \text{ (degrees)} = 63.7$$

δ/λ	$ R $	$\arg(R)$ (degrees)
0.	1.068E-01	0.
0.05	1.047E-01	-14.48
0.10	9.901E-02	-28.03
0.18	8.663E-02	-46.53

$$M_0 = 0.70 \text{ (Cont.)}$$

$$\phi \text{ (degrees)} = 60.0 \quad \theta \text{ (degrees)} = 68.3$$

δ/λ	$ R $	$\arg(R)$ (degrees)
0.	1.145E-01	0.
0.05	1.116E-01	-15.71
0.10	1.041E-01	-30.16
0.18	8.871E-02	-49.20

$$\phi \text{ (degrees)} = 70.0 \quad \theta \text{ (degrees)} = 74.0$$

δ/λ	$ R $	$\arg(R)$ (degrees)
0.	9.573E-02	0.
0.05	9.276E-02	-17.68
0.10	8.536E-02	-33.66
0.18	7.107E-02	-54.10

$$\phi \text{ (degrees)} = 80.0 \quad \theta \text{ (degrees)} = 81.1$$

δ/λ	$ R $	$\arg(R)$ (degrees)
0.	5.571E-02	0.
0.05	5.366E-02	-19.96
0.10	4.871E-02	-37.69
0.18	3.980E-02	-59.80

$$\phi \text{ (degrees)} = 100.0 \quad \theta \text{ (degrees)} = 101.4$$

δ/λ	$ R $	$\arg(R)$ (degrees)
0.	6.241E-02	180.00
0.05	5.949E-02	155.41
0.10	5.295E-02	134.19
0.18	4.256E-02	108.78

$$\phi \text{ (degrees)} = 120.0 \quad \theta \text{ (degrees)} = 140.3$$

δ/λ	$ R $	$\arg(R)$ (degrees)
0.	6.328E-02	180.00
0.05	5.986E-02	160.17
0.10	5.219E-02	143.77
0.18	3.987E-02	125.81

$$M_0 = 0.90$$

$$\phi \text{ (degrees)} = 10.0 \quad \theta \text{ (degrees)} = 58.5$$

	δ/λ	$ R $	$\arg(R)$ (degrees)
	0.	4.450E-01	180.00
←	0.05	4.451E-01	-179.94
←	0.10	4.453E-01	-179.89
	0.18	4.457E-01	-179.83

$$\phi \text{ (degrees)} = 20.0 \quad \theta \text{ (degrees)} = 59.4$$

	δ/λ	$ R $	$\arg(R)$ (degrees)
	0.	1.538E-01	180.00
←	0.05	1.549E-01	-177.62
←	0.10	1.578E-01	-175.60
	0.18	1.647E-01	-173.58

$$\phi \text{ (degrees)} = 30.0 \quad \theta \text{ (degrees)} = 60.9$$

	δ/λ	$ R $	$\arg(R)$ (degrees)
	0.	9.151E-03	0.
←	0.05	1.669E-02	-66.50
←	0.10	2.839E-02	-90.24
	0.18	4.482E-02	-110.31

$$\phi \text{ (degrees)} = 40.0 \quad \theta \text{ (degrees)} = 63.0$$

	δ/λ	$ R $	$\arg(R)$ (degrees)
	0.	9.845E-02	0.
	0.05	9.716E-02	-14.67
	0.10	9.367E-02	-28.67
	0.18	8.561E-02	-48.61

$$\phi \text{ (degrees)} = 50.0 \quad \theta \text{ (degrees)} = 66.0$$

	δ/λ	$ R $	$\arg(R)$ (degrees)
	0.	1.394E-01	0.
	0.05	1.367E-01	-13.66
	0.10	1.297E-01	-26.48
	0.18	1.139E-01	-44.05

$M_0 = 0.90$ (Cont.)

ϕ (degrees) = 60.0 θ (degrees) = 69.8

δ/λ	$ R $	$\arg(R)$ (degrees)
0.	1.445E-01	0.
0.05	1.410E-01	-14.89
0.10	1.321E-01	-28.62
0.18	1.131E-01	-46.84

ϕ (degrees) = 70.0 θ (degrees) = 74.8

δ/λ	$ R $	$\arg(R)$ (degrees)
0.	1.202E-01	0.
0.05	1.167E-01	-16.91
0.10	1.077E-01	-32.26
0.18	9.016E-02	-52.02

ϕ (degrees) = 80.0 θ (degrees) = 81.4

δ/λ	$ R $	$\arg(R)$ (degrees)
0.	7.054E-02	0.
0.05	6.801E-02	-19.44
0.10	6.189E-02	-36.77
0.18	5.071E-02	-58.46

ϕ (degrees) = 100.0 θ (degrees) = 101.9

δ/λ	$ R $	$\arg(R)$ (degrees)
0.	8.162E-02	180.00
0.05	7.766E-02	154.56
0.10	6.889E-02	132.72
0.18	5.528E-02	106.79

ϕ (degrees) = 120.0 θ (degrees) = 155.4

δ/λ	$ R $	$\arg(R)$ (degrees)
0.	6.688E-02	0.
0.05	7.670E-02	-56.16
0.10	9.255E-02	-92.04
0.18	1.085E-01	-122.42

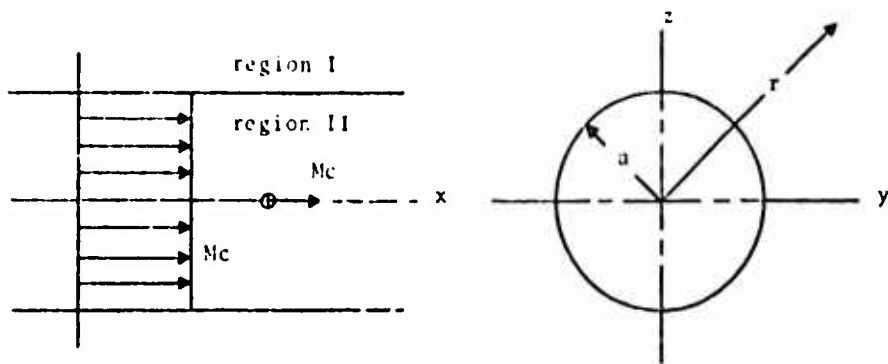


Figure 16 First Model Problem

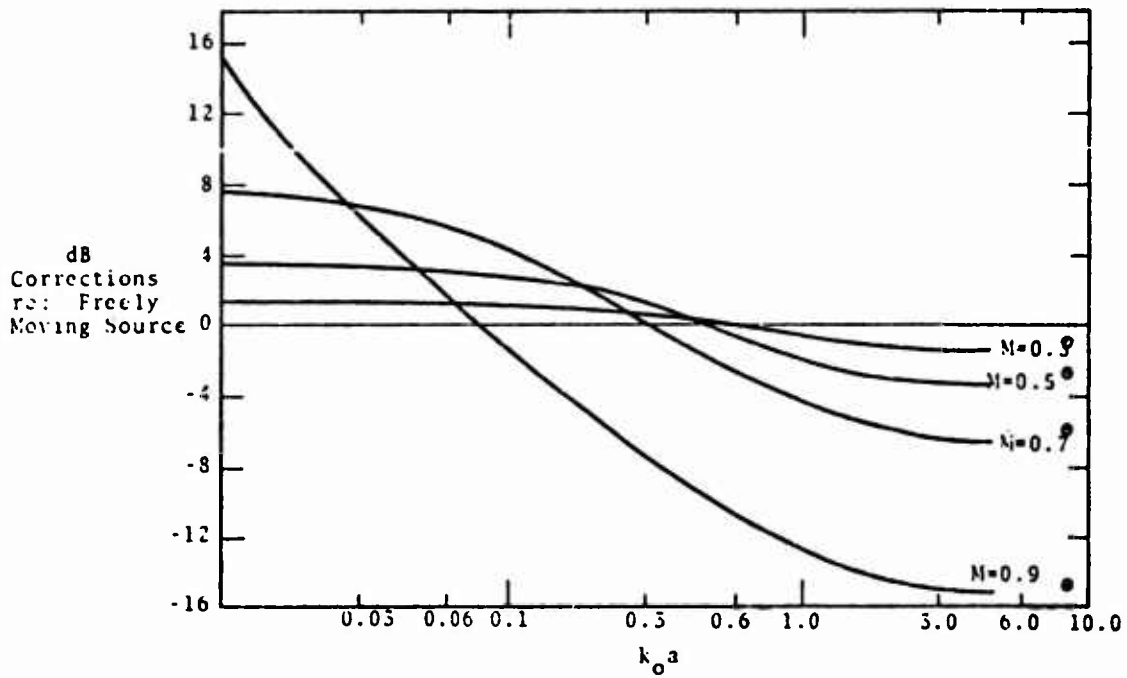


Figure 17 Convective Amplification as a Function of M and $k_0 a$

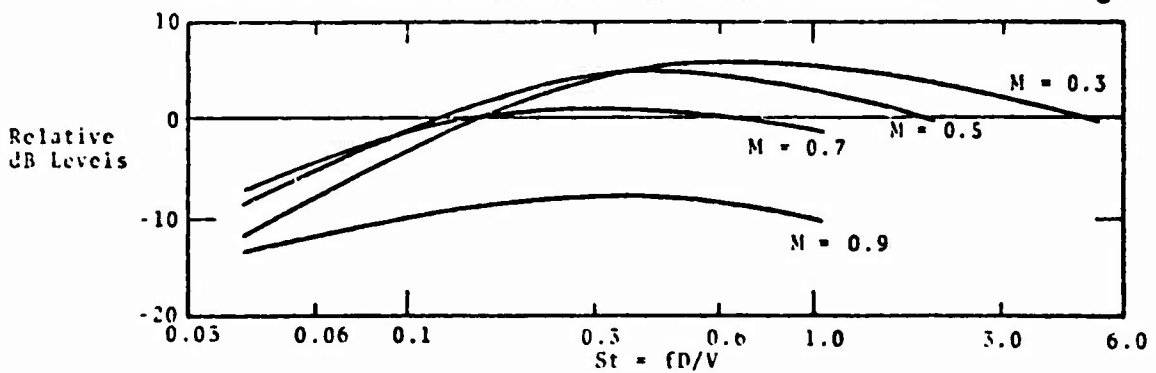


Figure 18 Implications for Strouhal Scaling

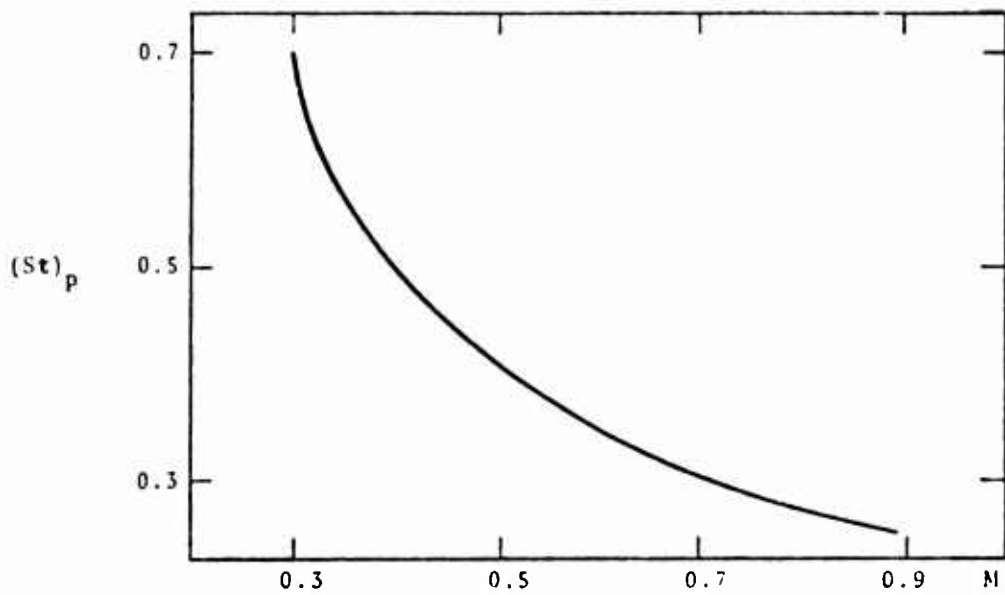


Figure 19 Peak Strouhal Number as a Function of Jet Mach Number

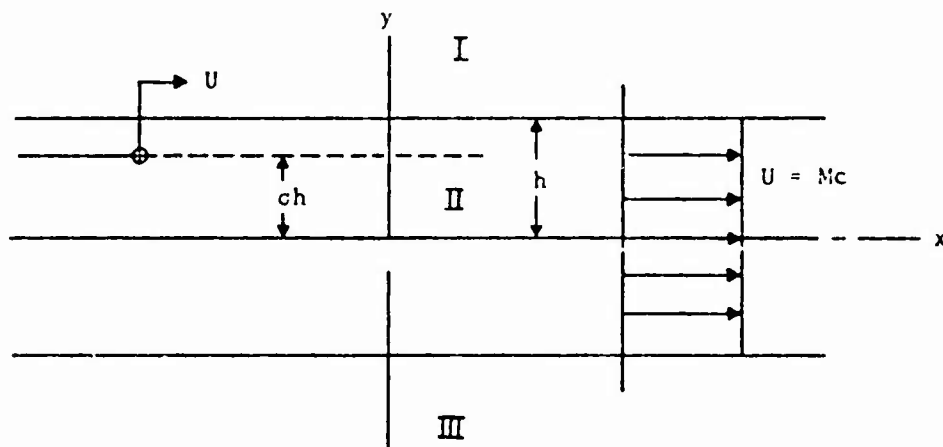


Figure 20 Second Model Problem

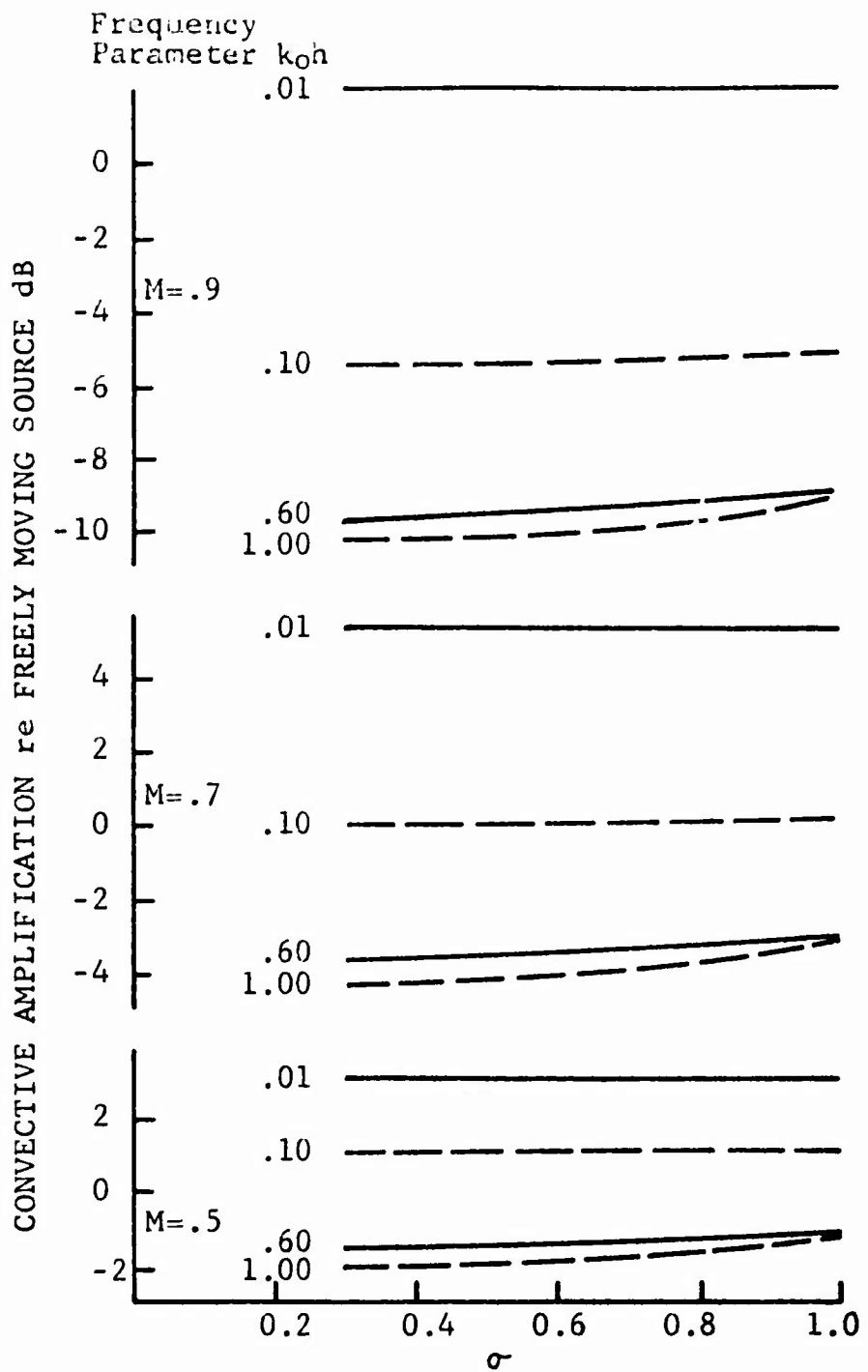


Figure 21 Results of Second Model Problem

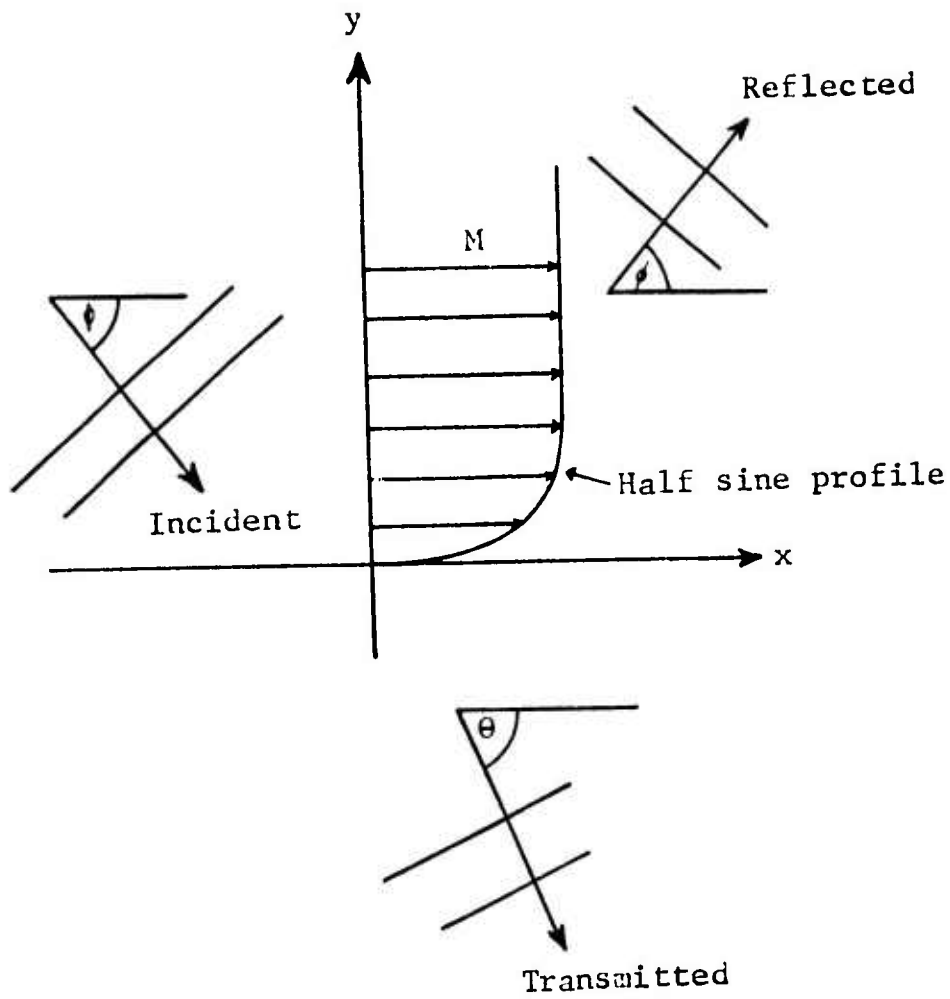


Figure 22 Application to Ribner-Miles Problem

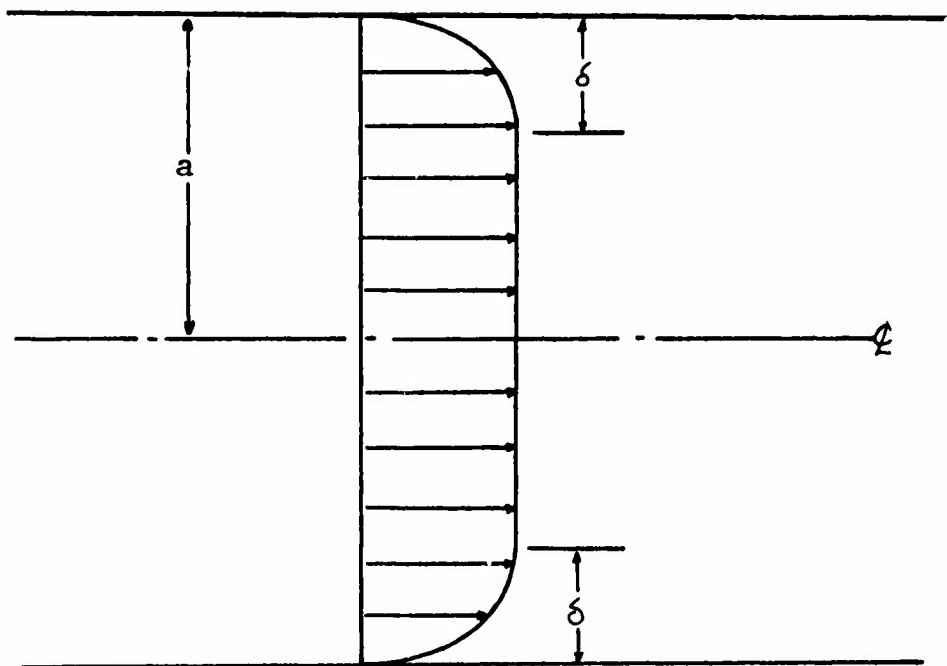


Figure 23 Application to Problem of Reference 1

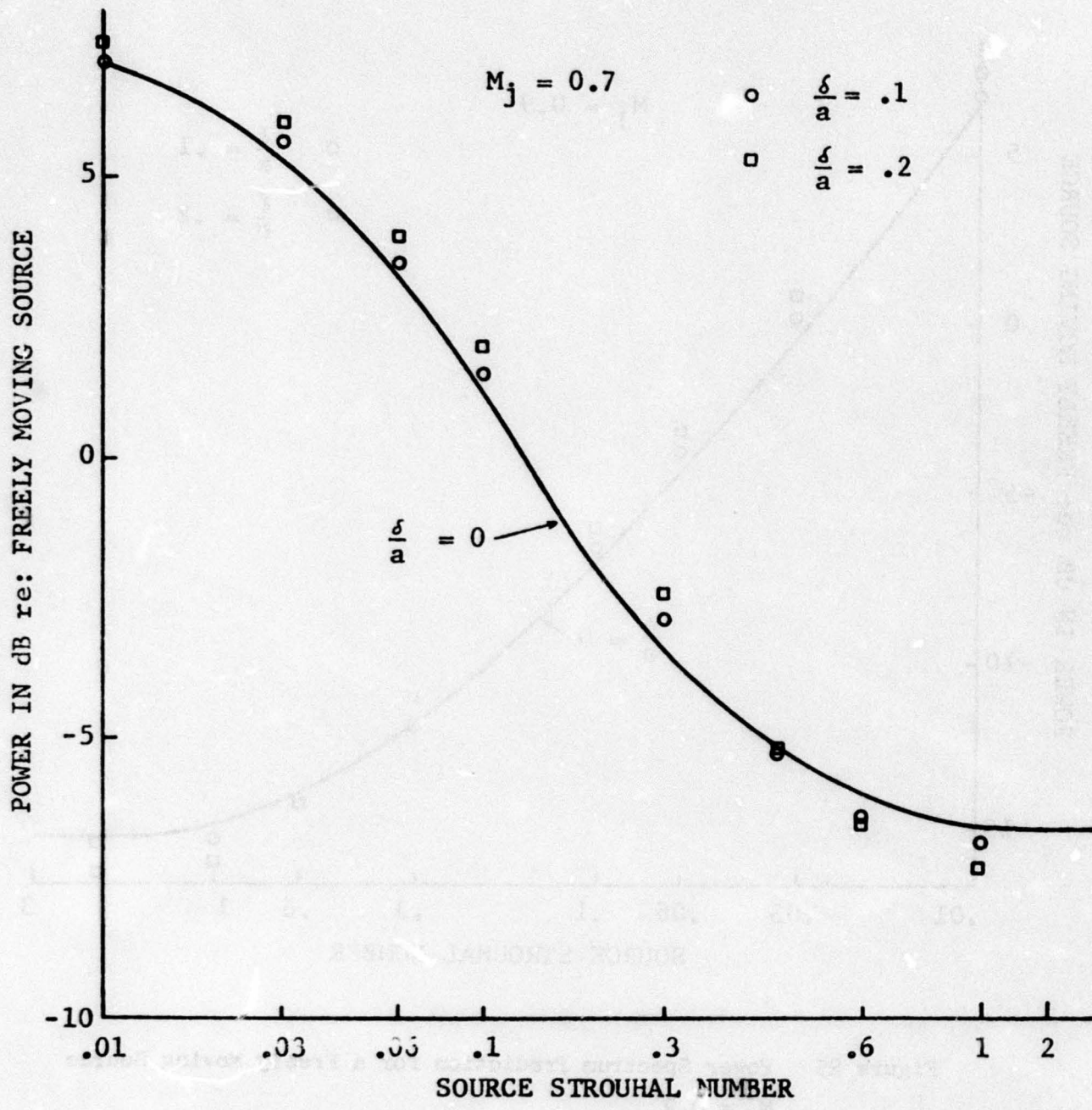


Figure 24 Power Spectrum Prediction for a Freely Moving Source
 $M_j = 0.7$

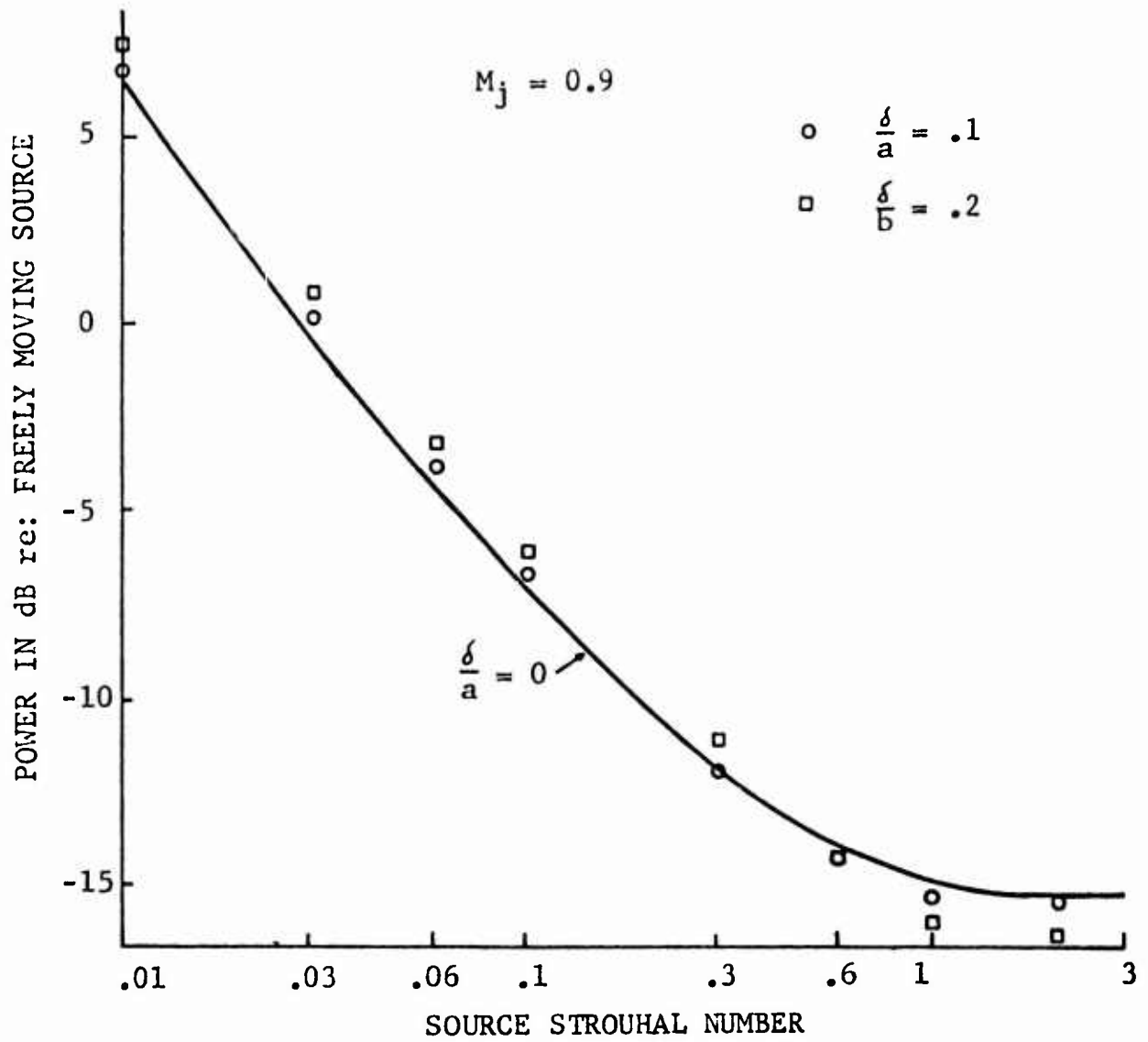


Figure 25 Power Spectrum Prediction for a Freely Moving Source
 $M_j = 0.9$

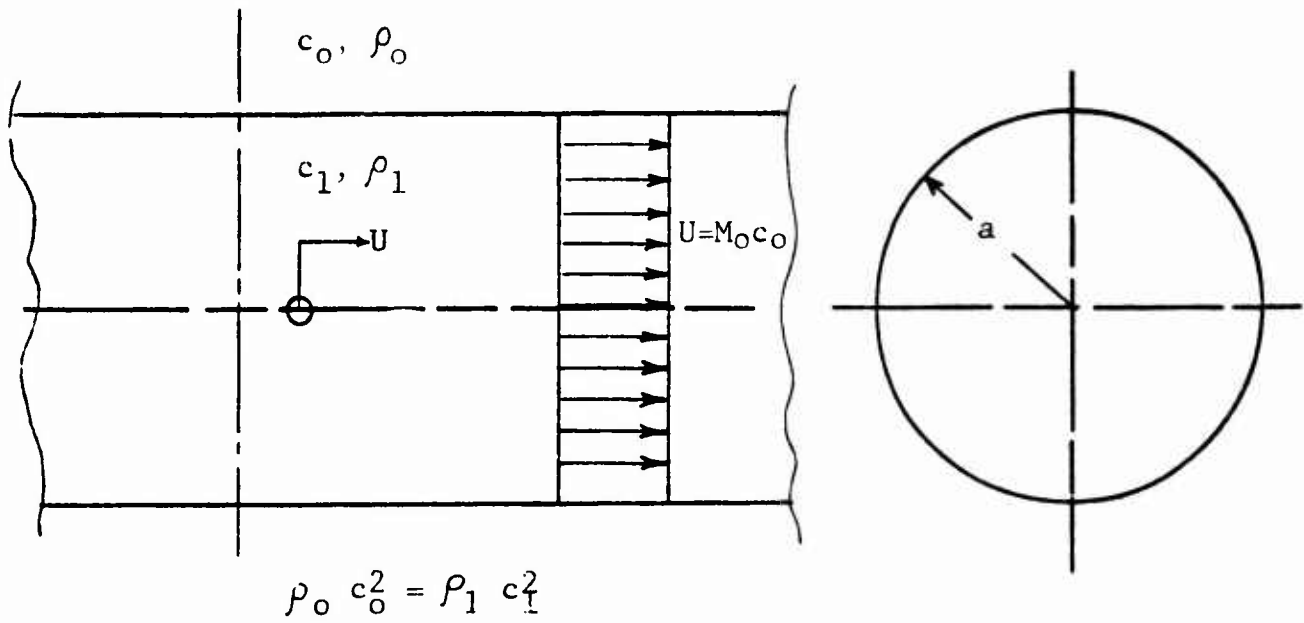


Figure 26 Third Model Problem

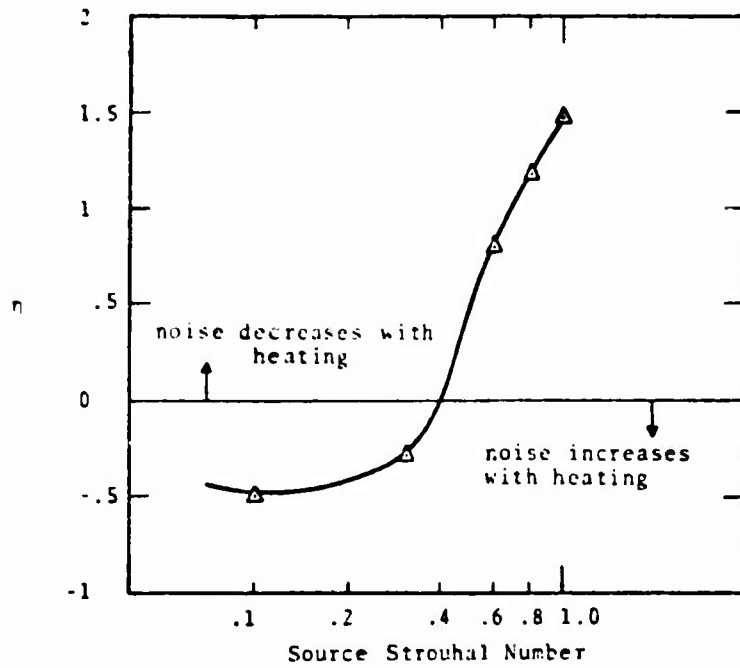


Figure 27 η as a Function of $(St)_0$ for $M_0 = 0.5$

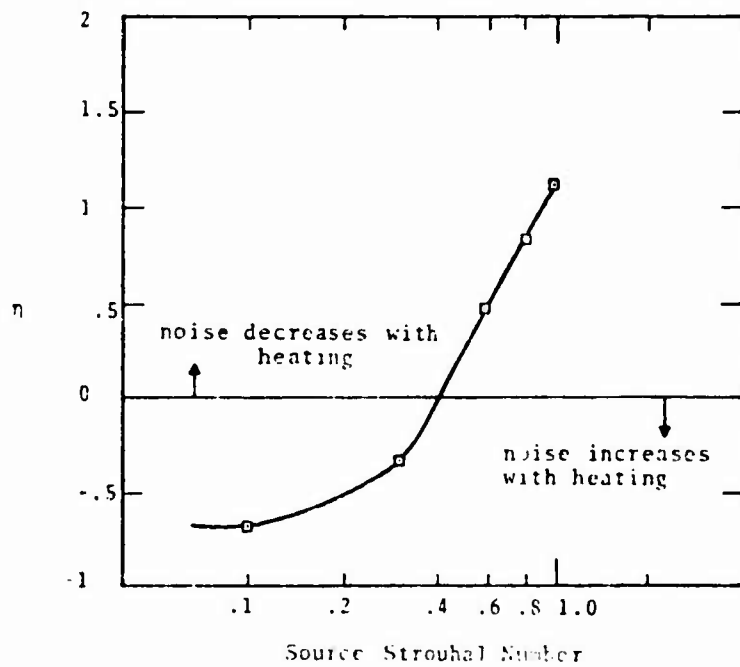


Figure 28 η as a Function of $(St)_0$ for $M_0 = 0.7$

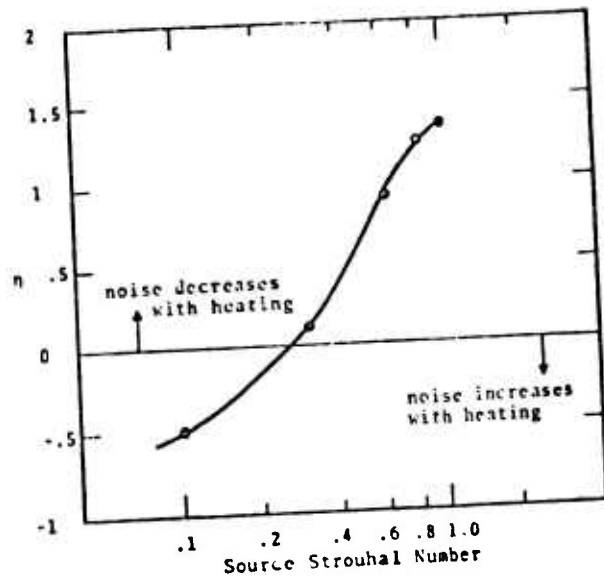


Figure 29 η as a Function of $(St)_0$ for $M_0 = 0.9$

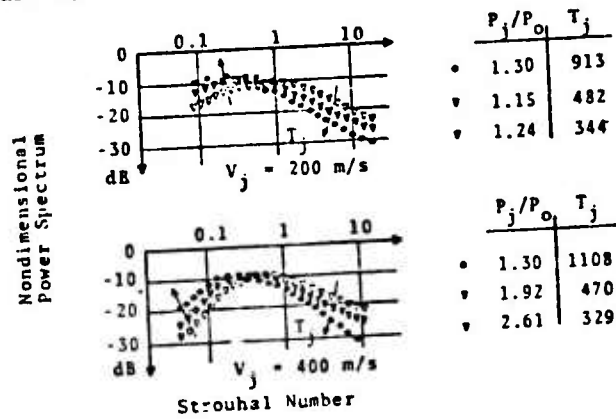


Figure 30 Normalized Power Spectra (Figure 19 of Reference 15)

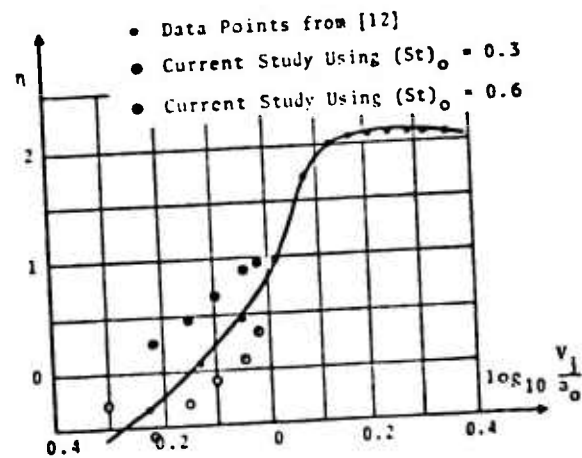


Figure 31 Jet Density Exponent (Figure 17 of Reference 15)

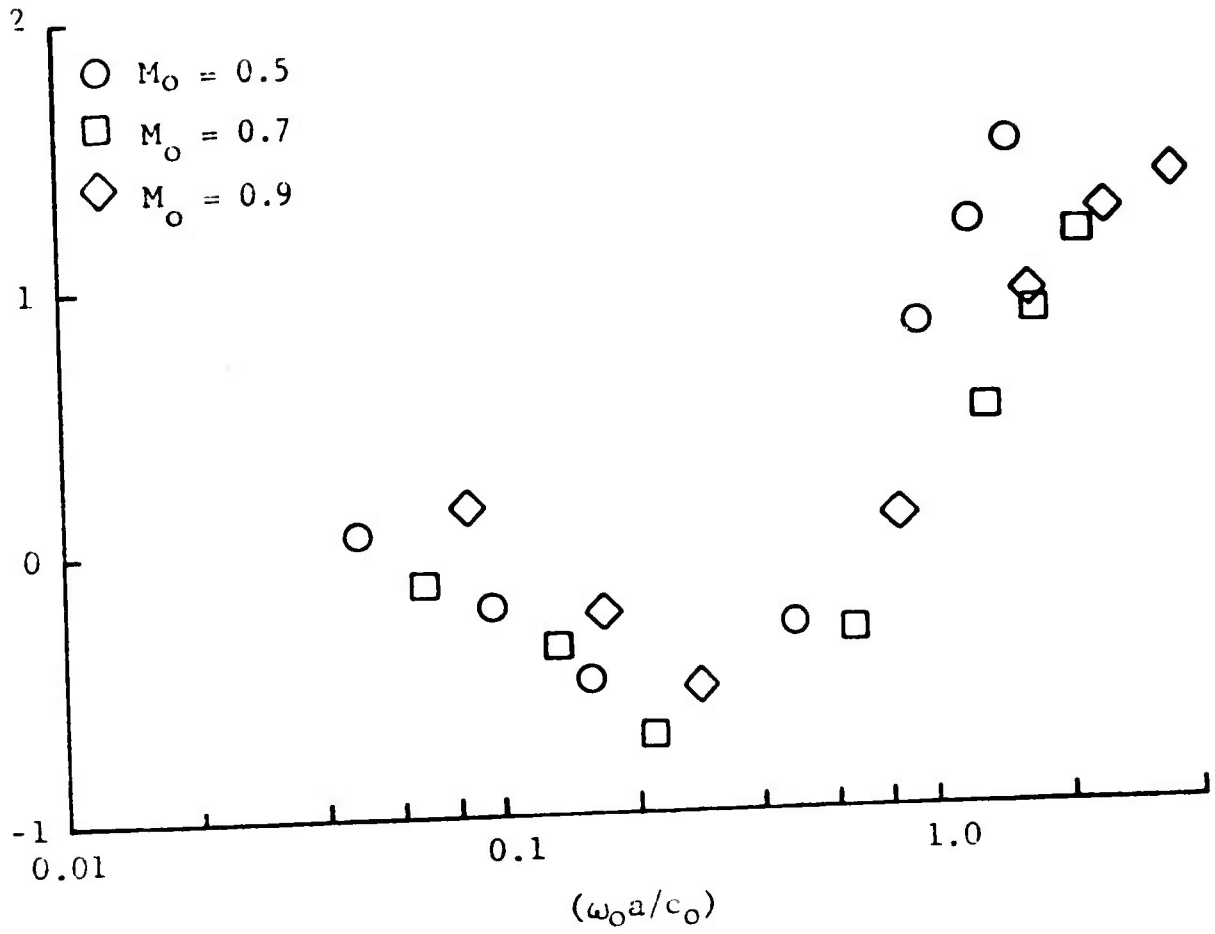


Figure 32 η as a Function of $(\omega_0 a / c_0)$ for Various M_0

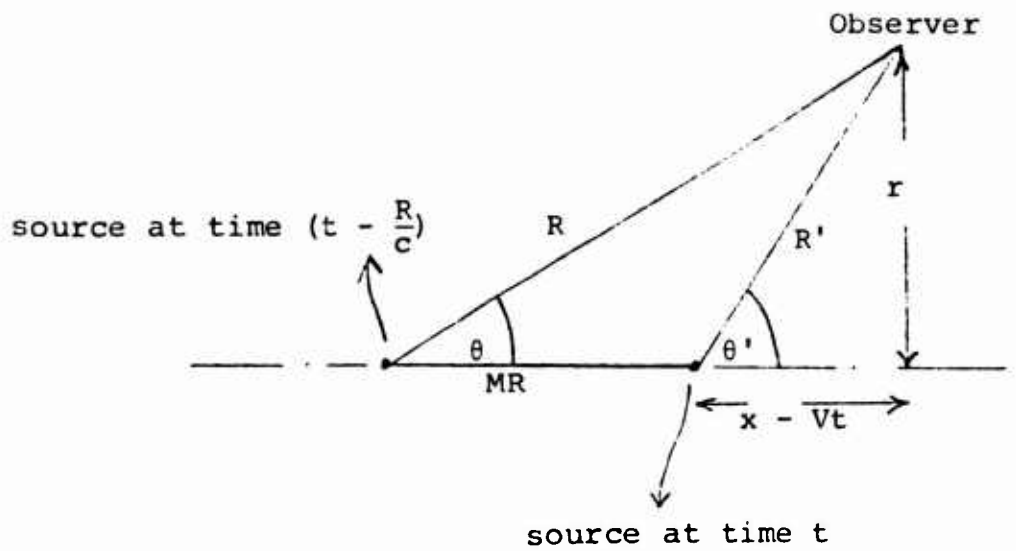
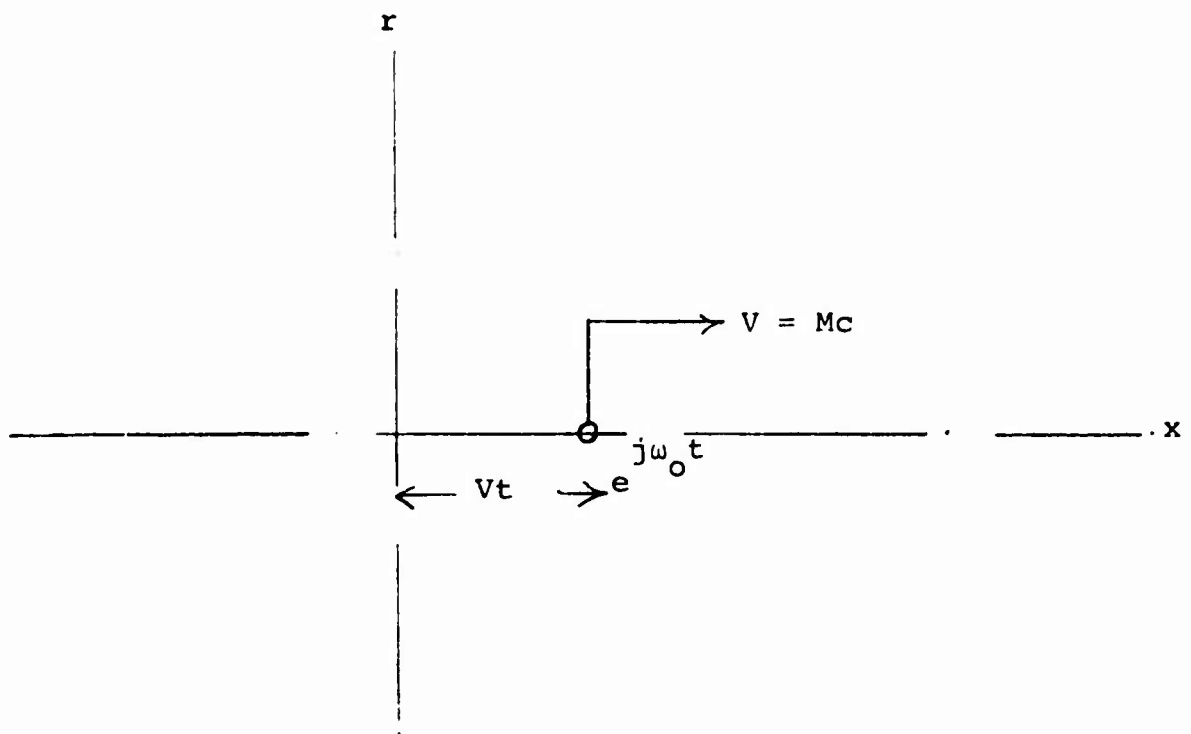


Figure 33 Schematic of a Moving Source

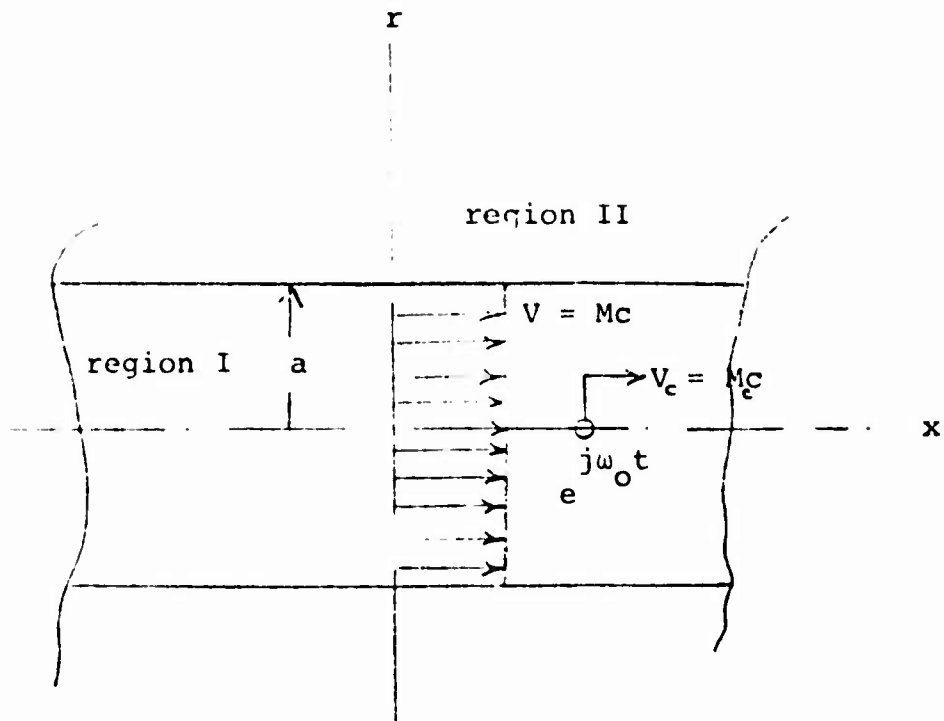


Figure 34 Schematic of Moving Source with Finite Lifetime

$$M_j = 0.366$$

SOURCE STROUHAL
NUMBER

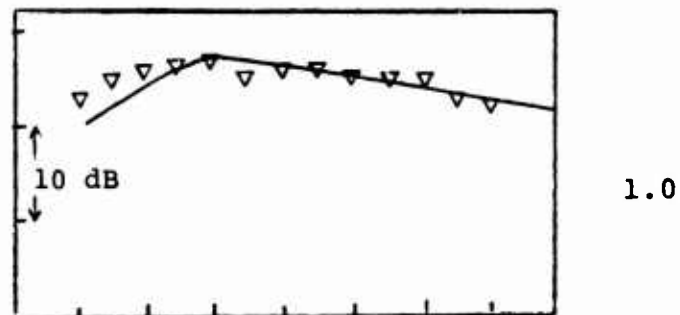
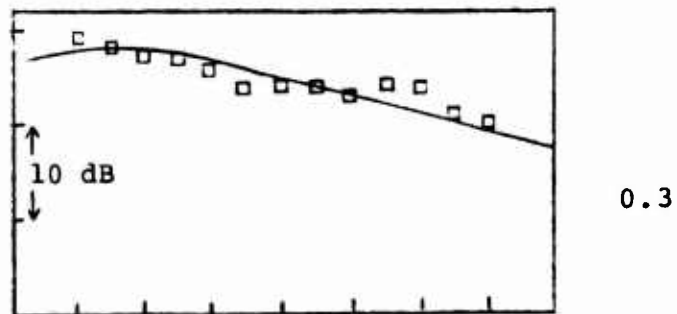
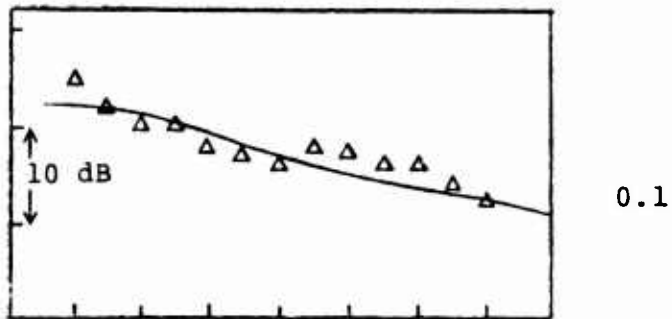
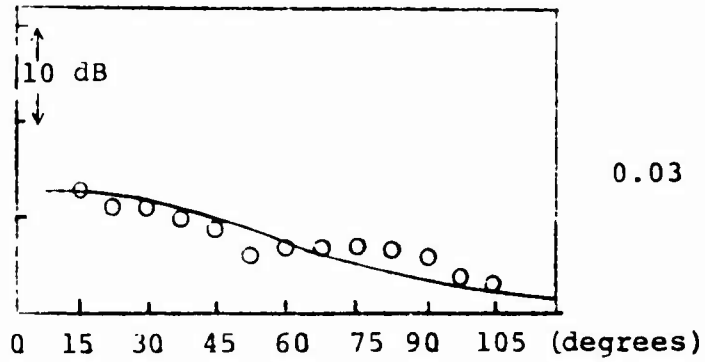
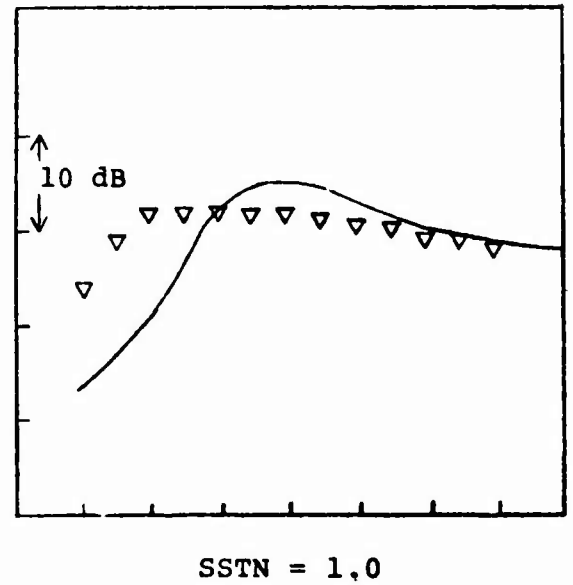
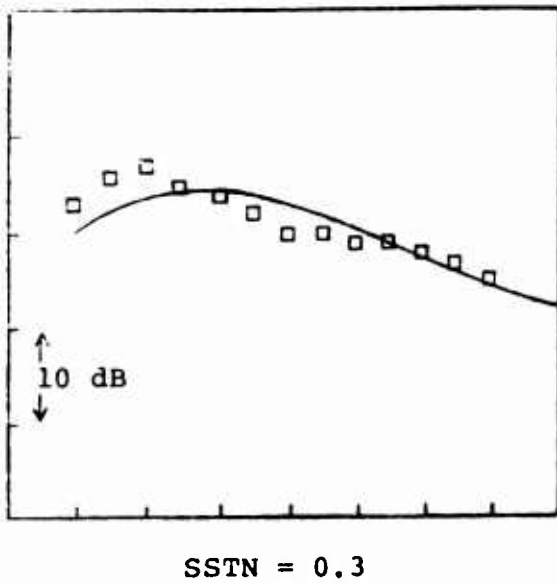
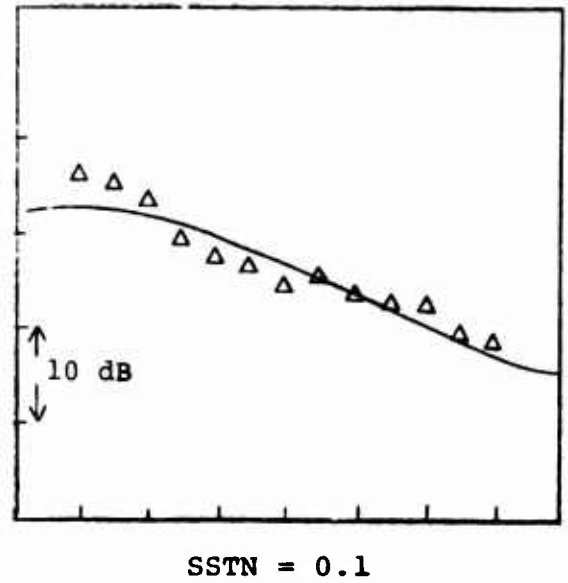
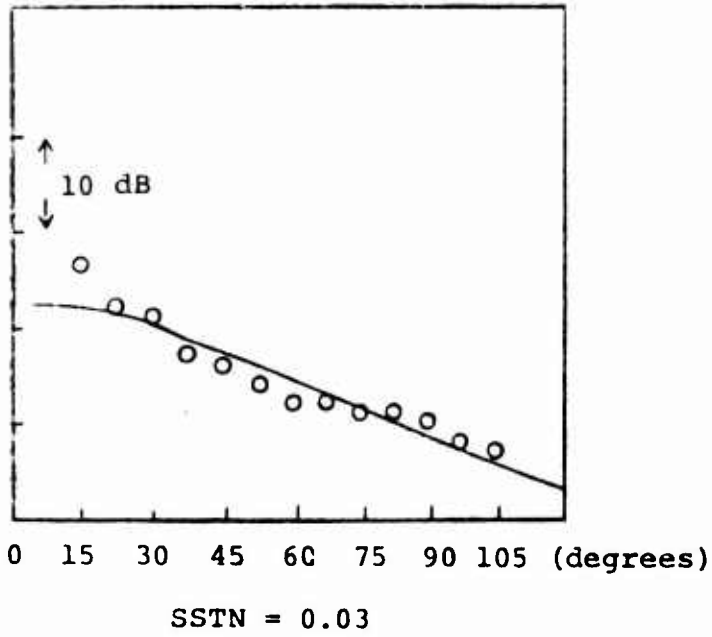


Figure 35 Directivity Predictions for a Freely Moving Point Source ($M_j = .366$)

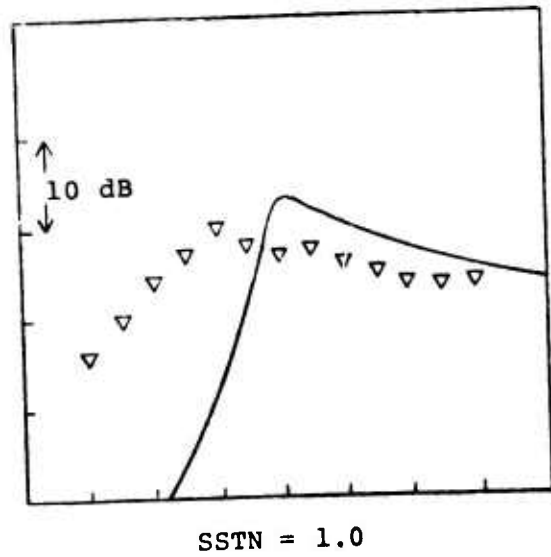
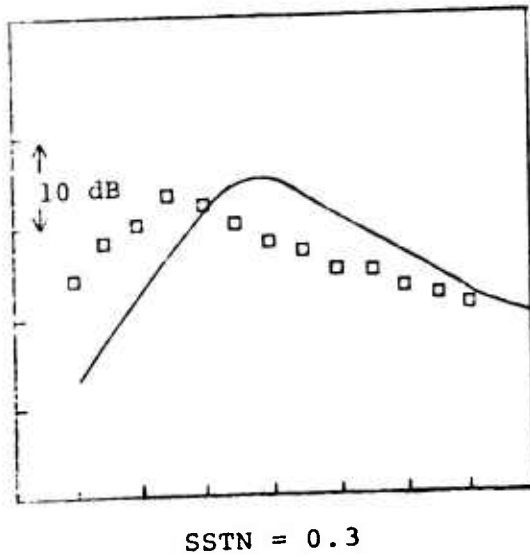
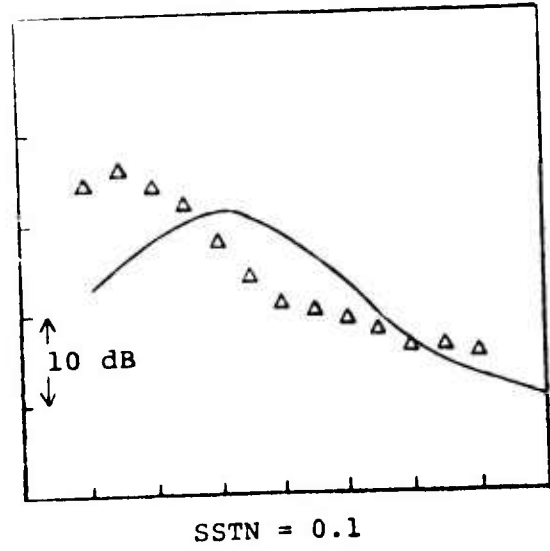
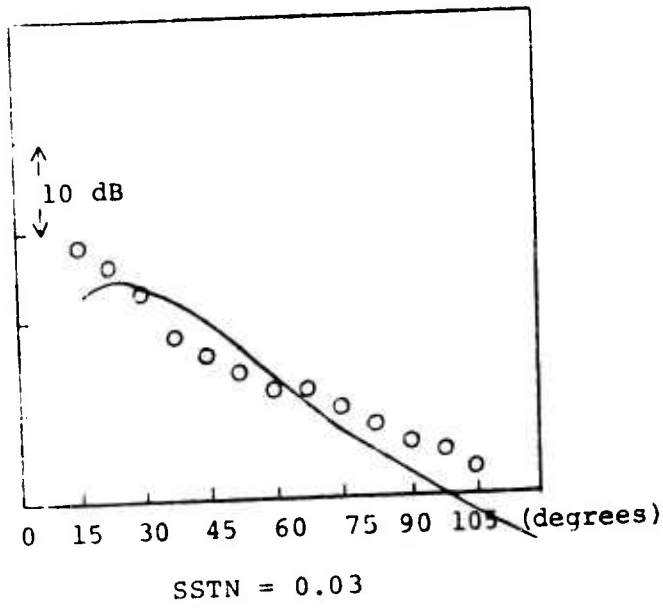
$$M_j = 0.57$$



SSTN = Source Strouhal Number

Figure 36 Directivity Predictions for a Freely Moving Point Source ($M_j = .57$)

$$M_j = 0.878$$

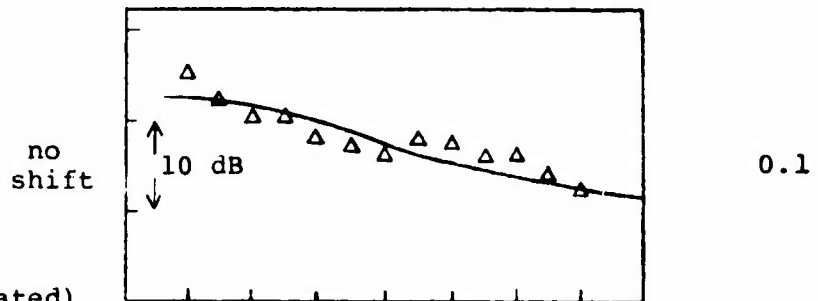
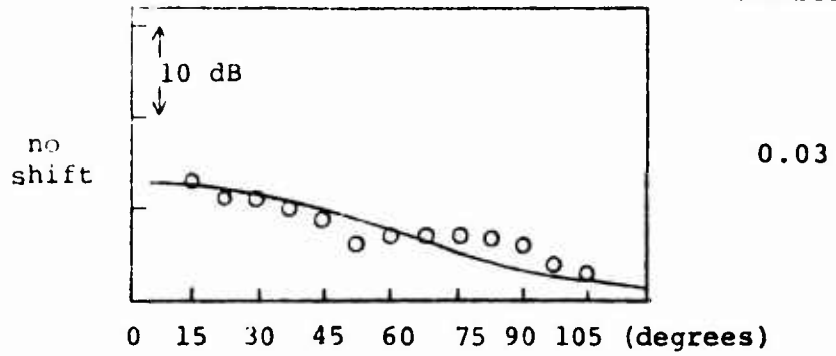


SSTN = Source Strouhal Number

Figure 37 Directivity Predictions for a Freely Moving Point Source ($M_j = .878$)

$$M_j = 0.366$$

Source Strouhal
Number



Theoretical
prediction
shifted (translated)
towards jet axis by
amount shown.

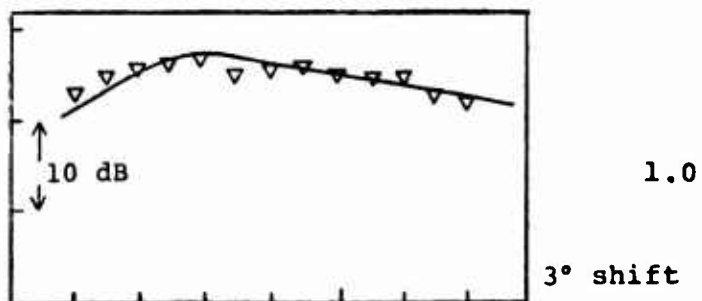
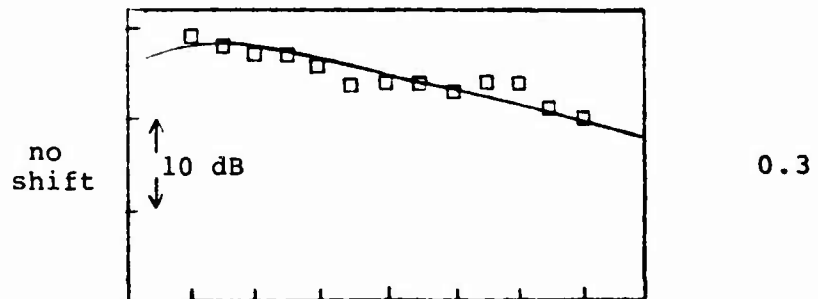
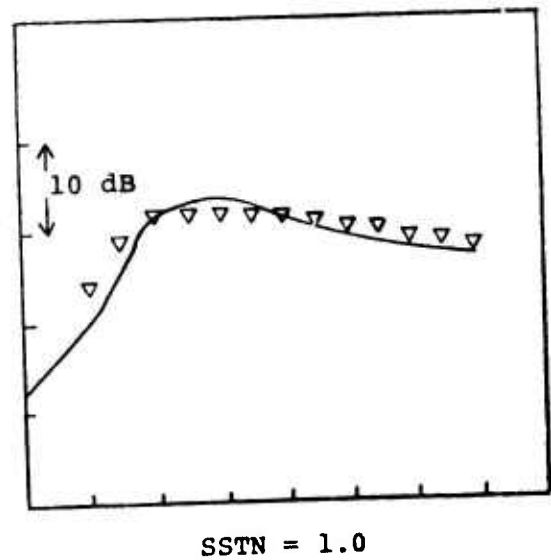
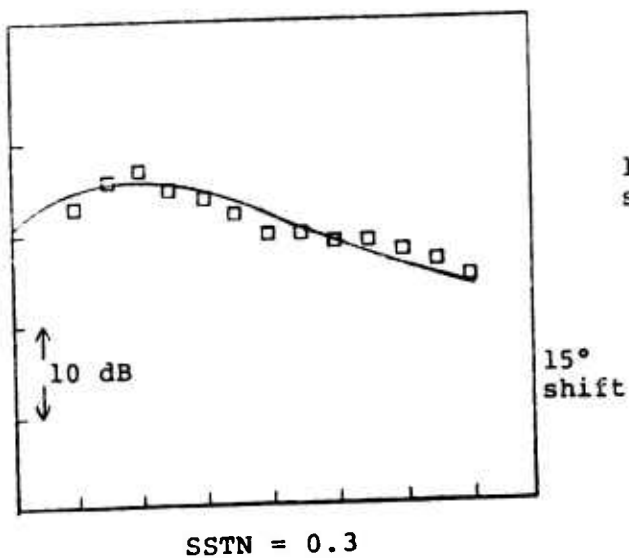
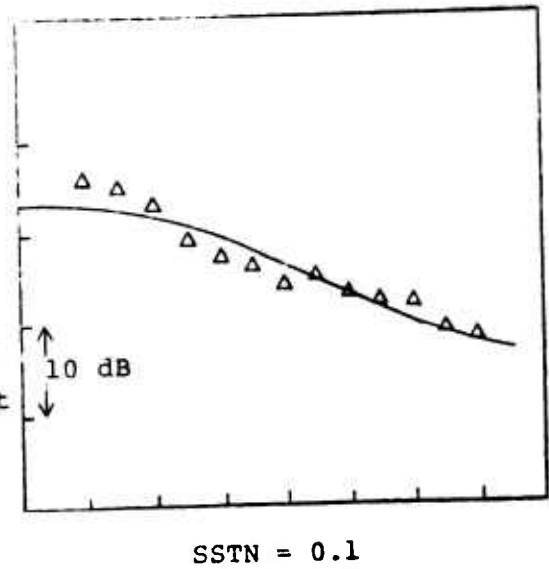
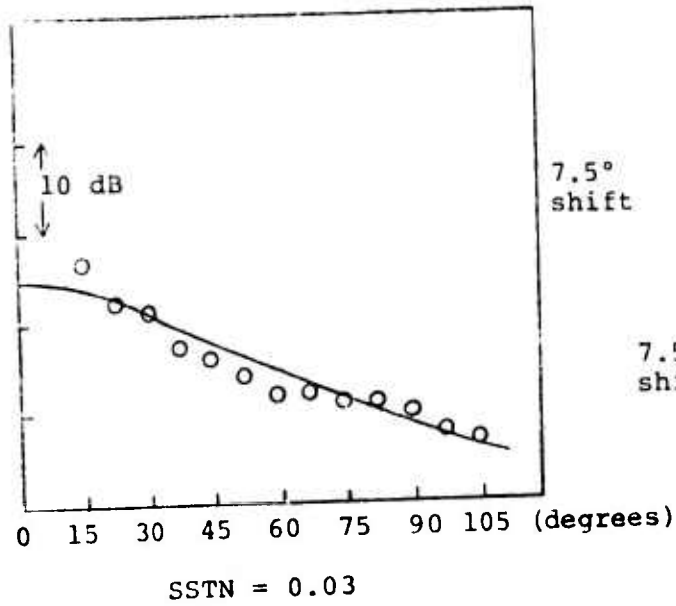


Figure 38 Directivity Predictions for a Freely Moving Point Source ($M_j = .366$)

$$M_j = 0.57$$

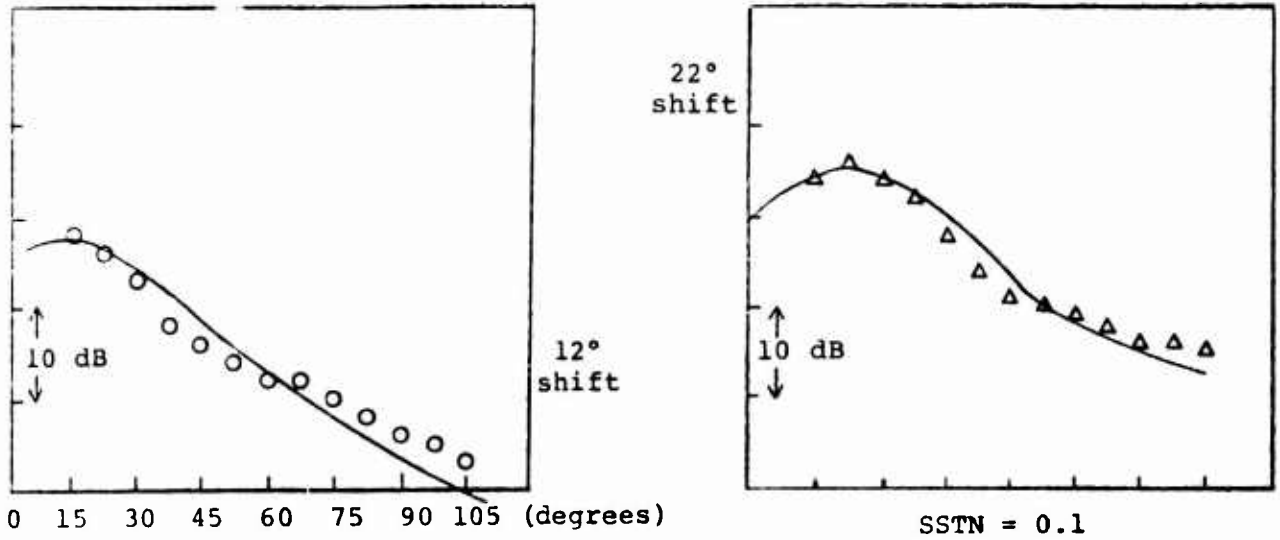


SSTN = Source Strouhal Number

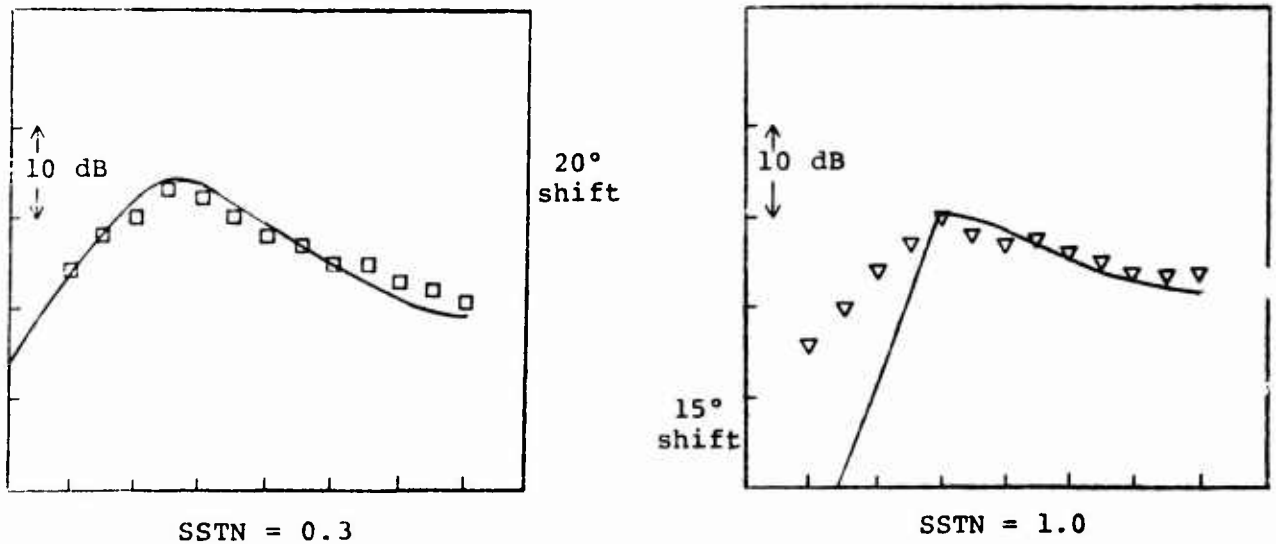
Theoretical prediction shifted (translated) towards jet axis by amount shown.

Figure 39 Directivity Predictions for a Freely Moving Point Source ($M_j = .57$)

$$M_j = 0.878$$



Theoretical prediction shifted (translated) towards jet axis by amount shown.



SSTN = Source Strouhal Number

Figure 40 Directivity Predictions for a Freely Moving Point Source ($M_j = .878$)

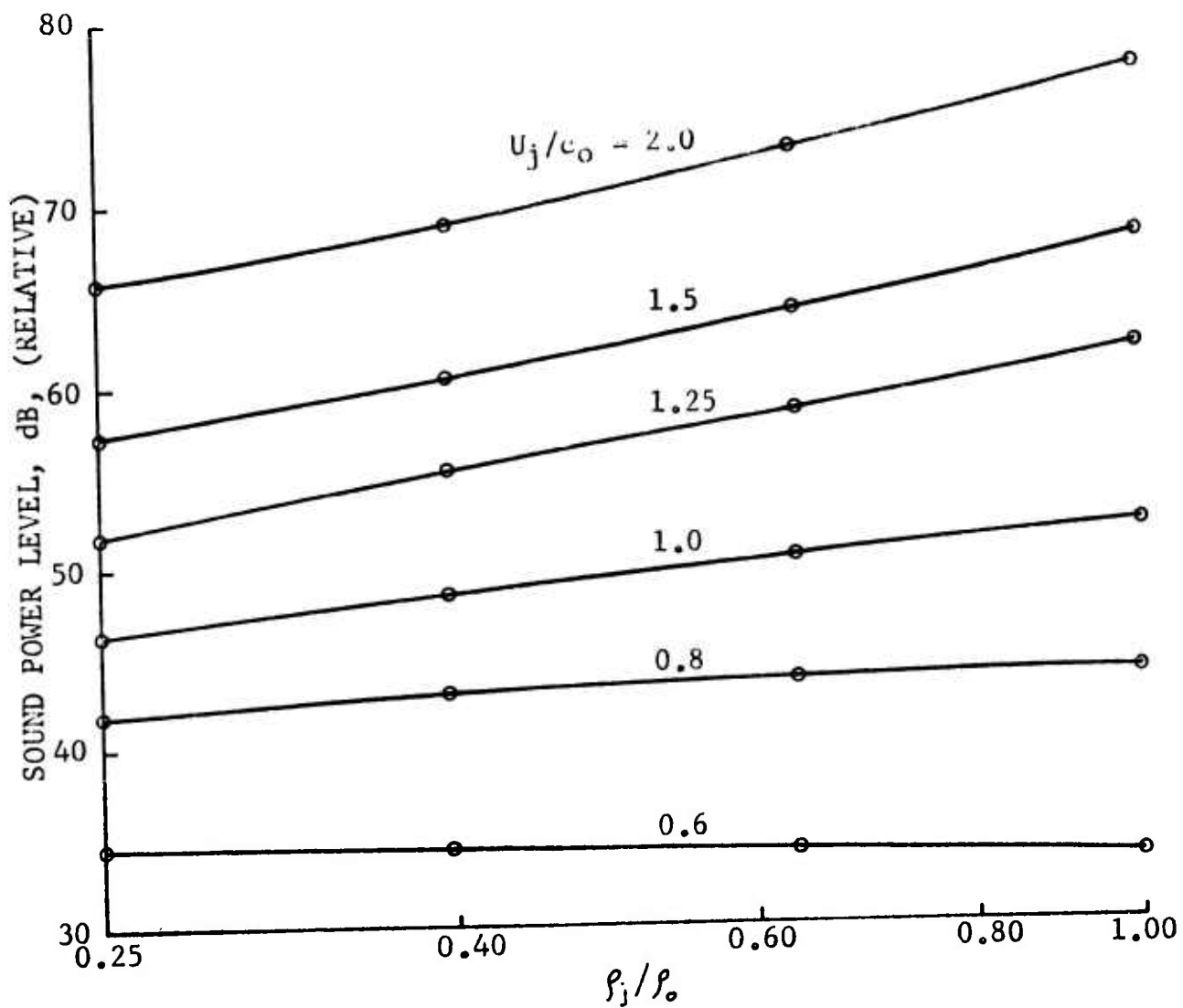


Figure 41 Dependence of Sound Power on Jet Density Ratio

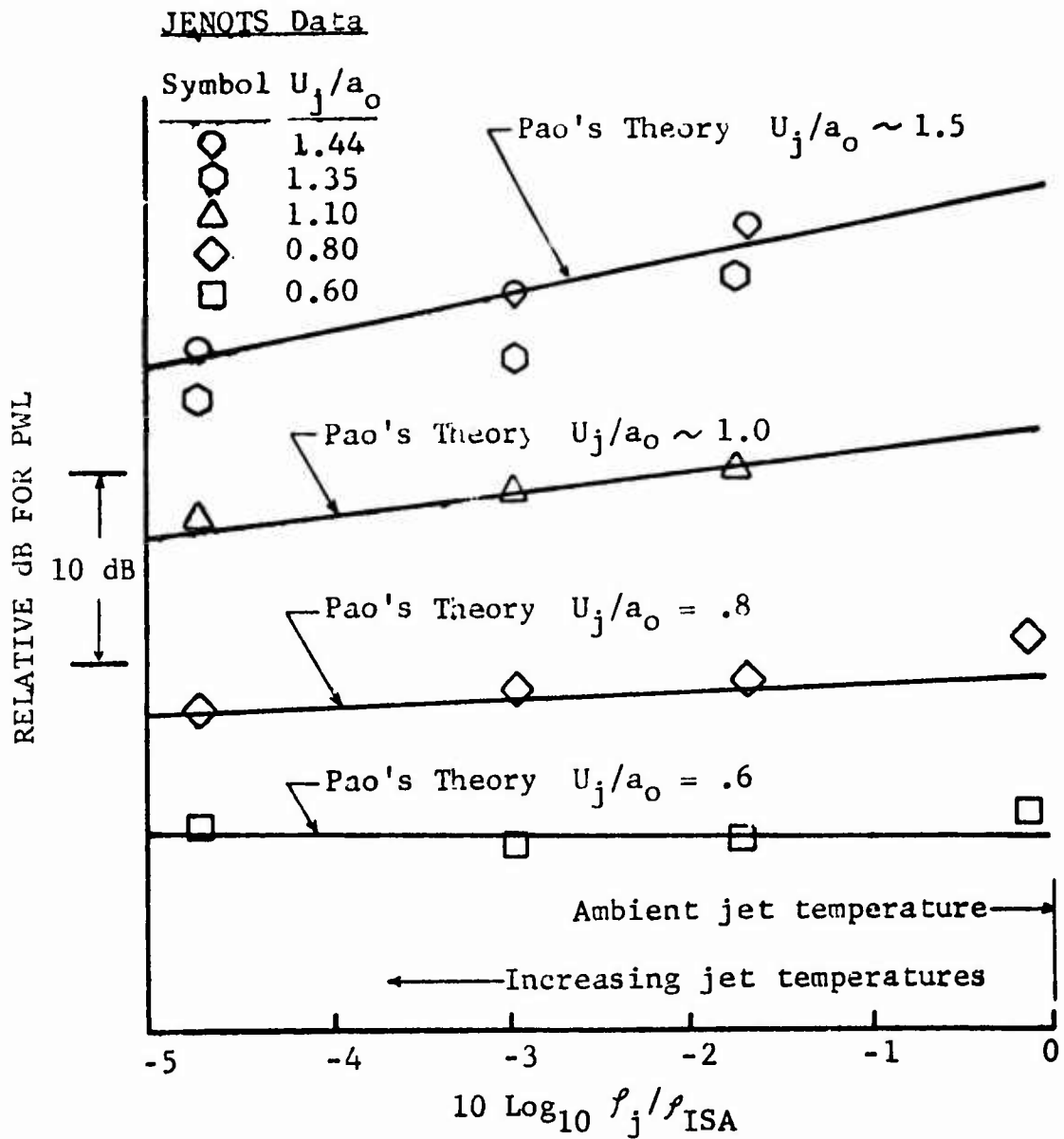


Figure 42 Theory -- Data Comparison of Sound Power as a Function of Density Ratio and Exit Convection Mach Number

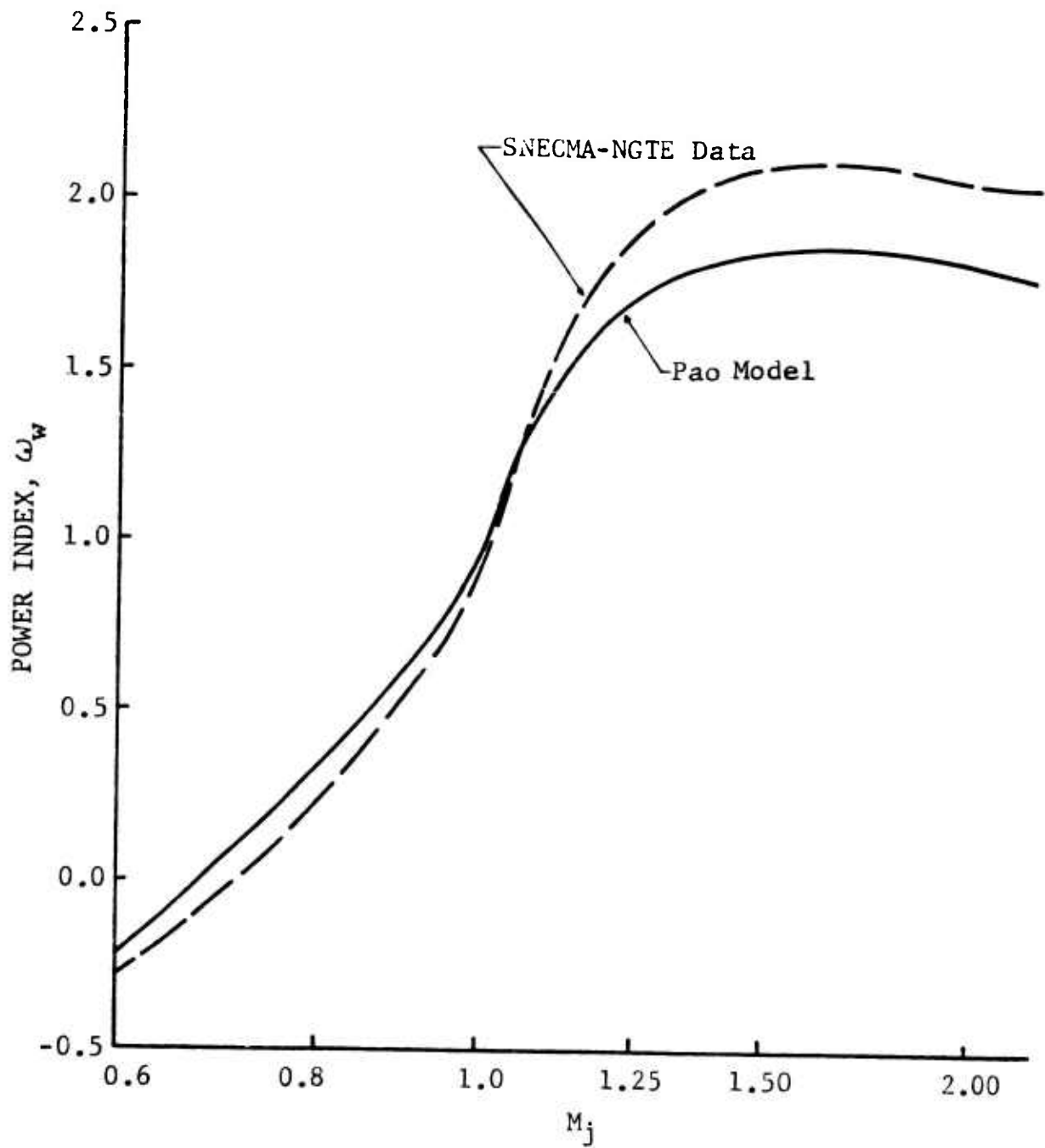


Figure 43 The Density Power Index at Various Levels of M_j

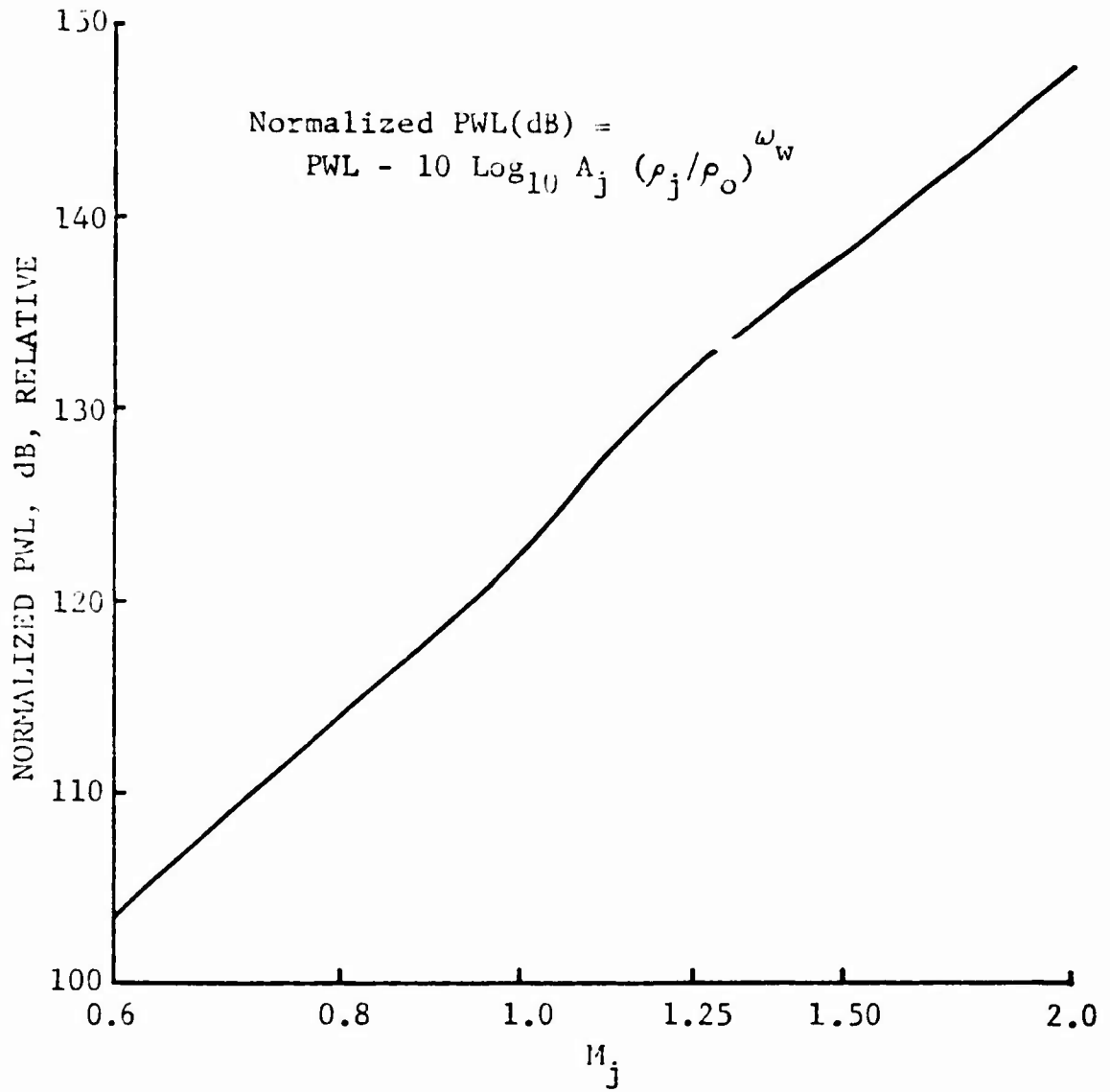


Figure 44 The Generalized Sound Power Correlation

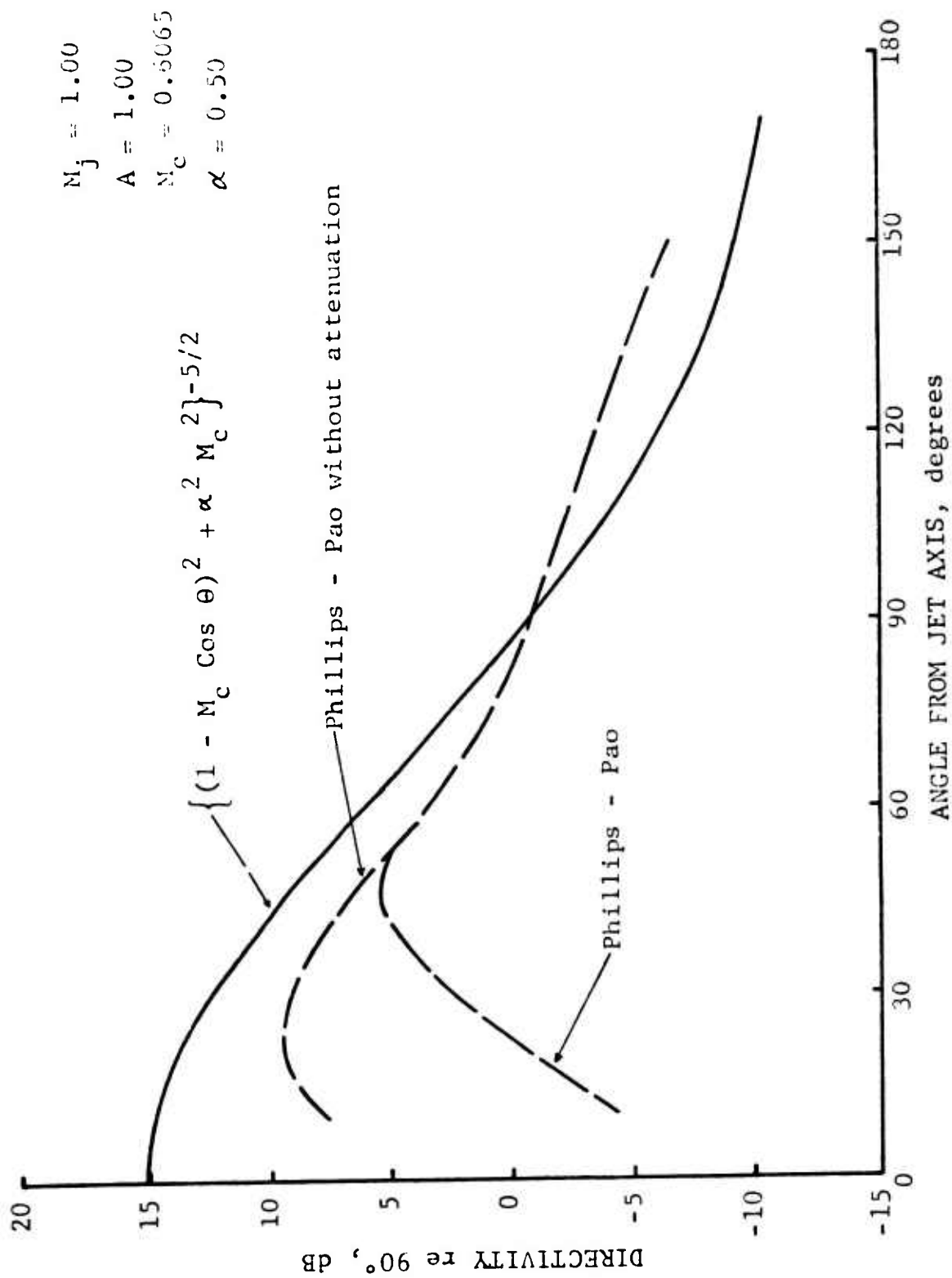


Figure 45 Directivity Pattern for a Typical Slice of Jet with $M_j = 1.0$

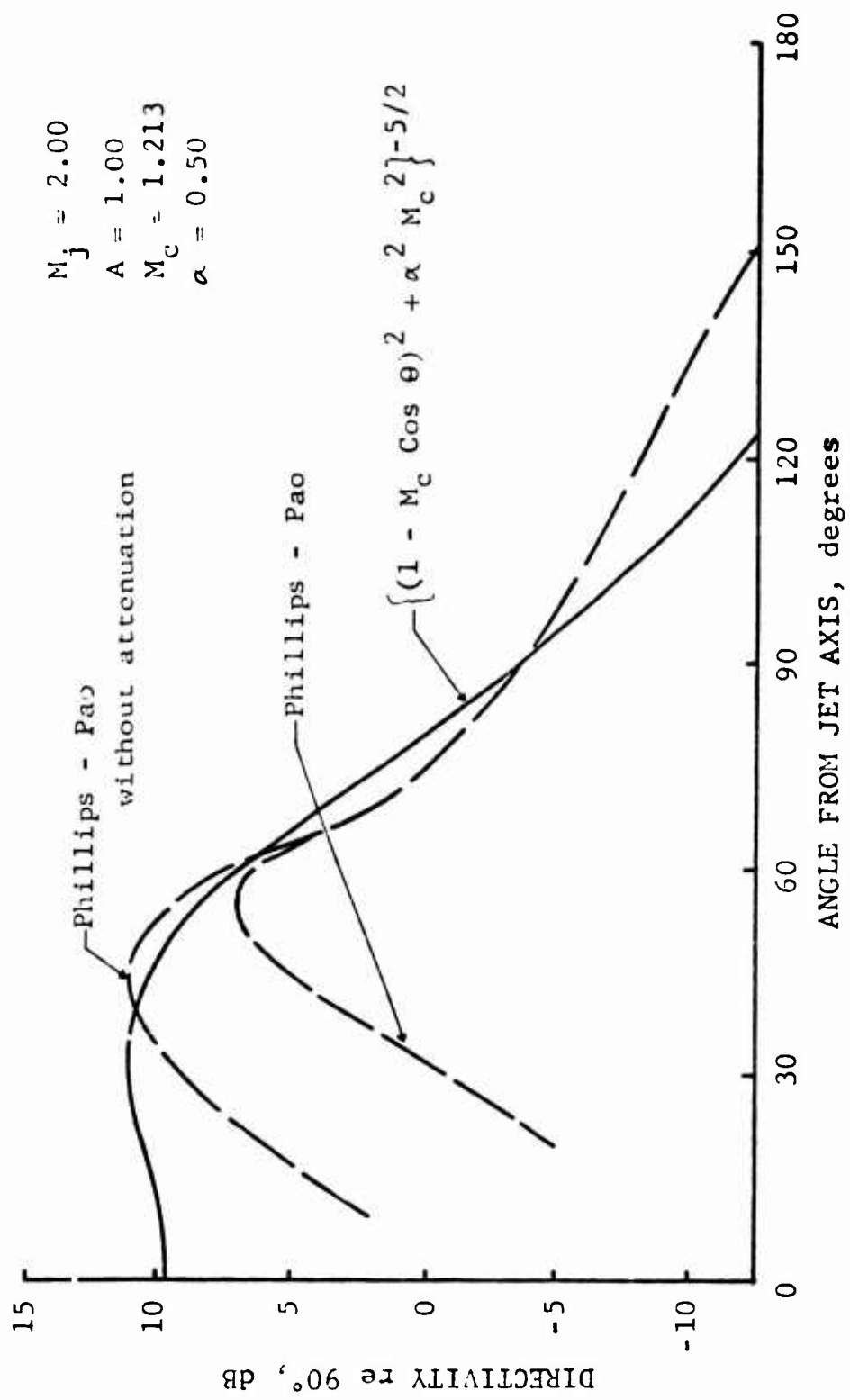


Figure 46 Directivity Pattern for a Typical Slice of Jet with $M_j = 2.0$

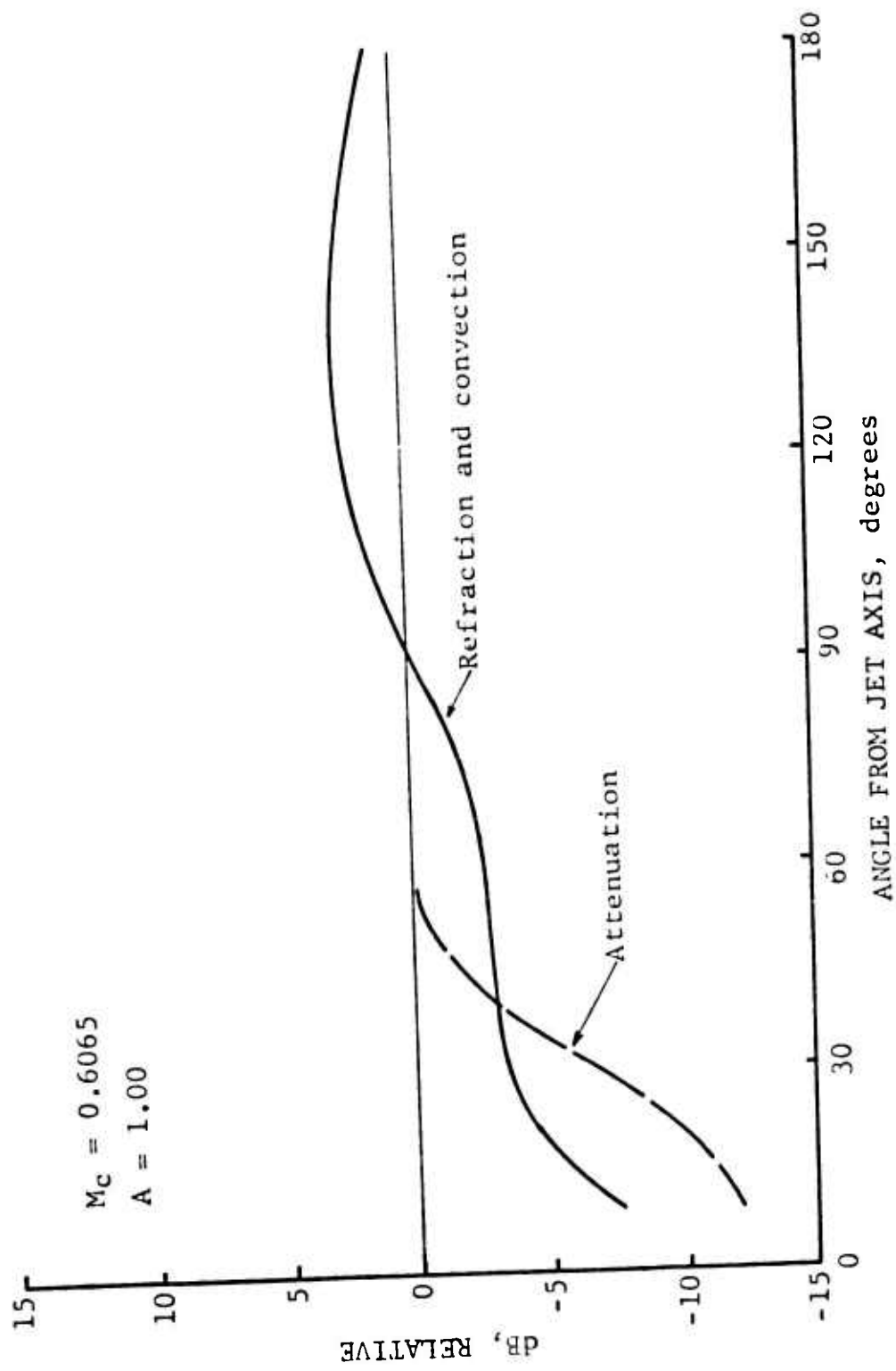


Figure 47 Effects of Attenuation and the Coupled Effects of Convection and Refraction ($M_j = 1.0$)

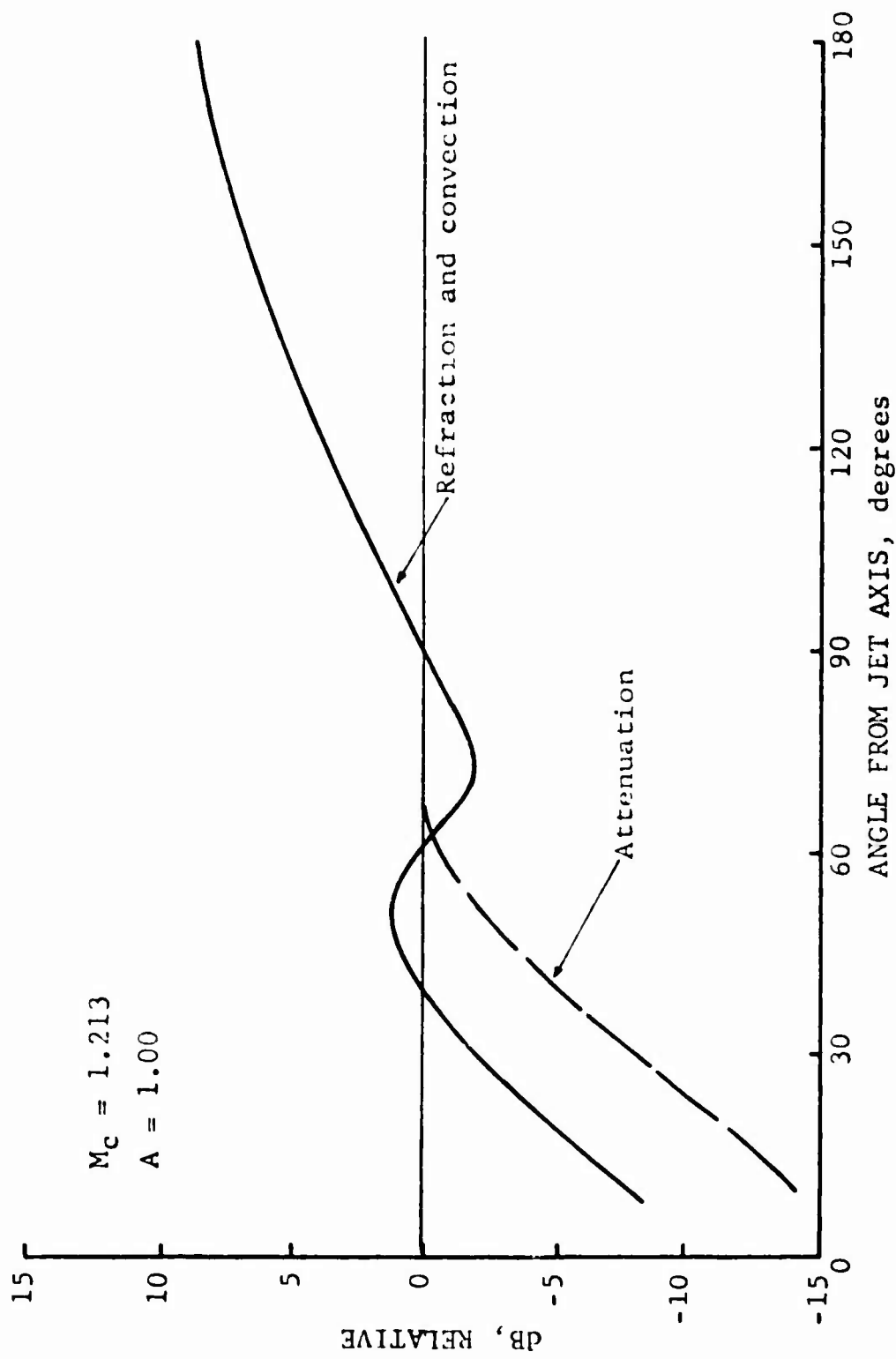


Figure 48 Effects of Attenuation and the Coupled Effects of Convection and Refraction ($M_j = 2.0$)

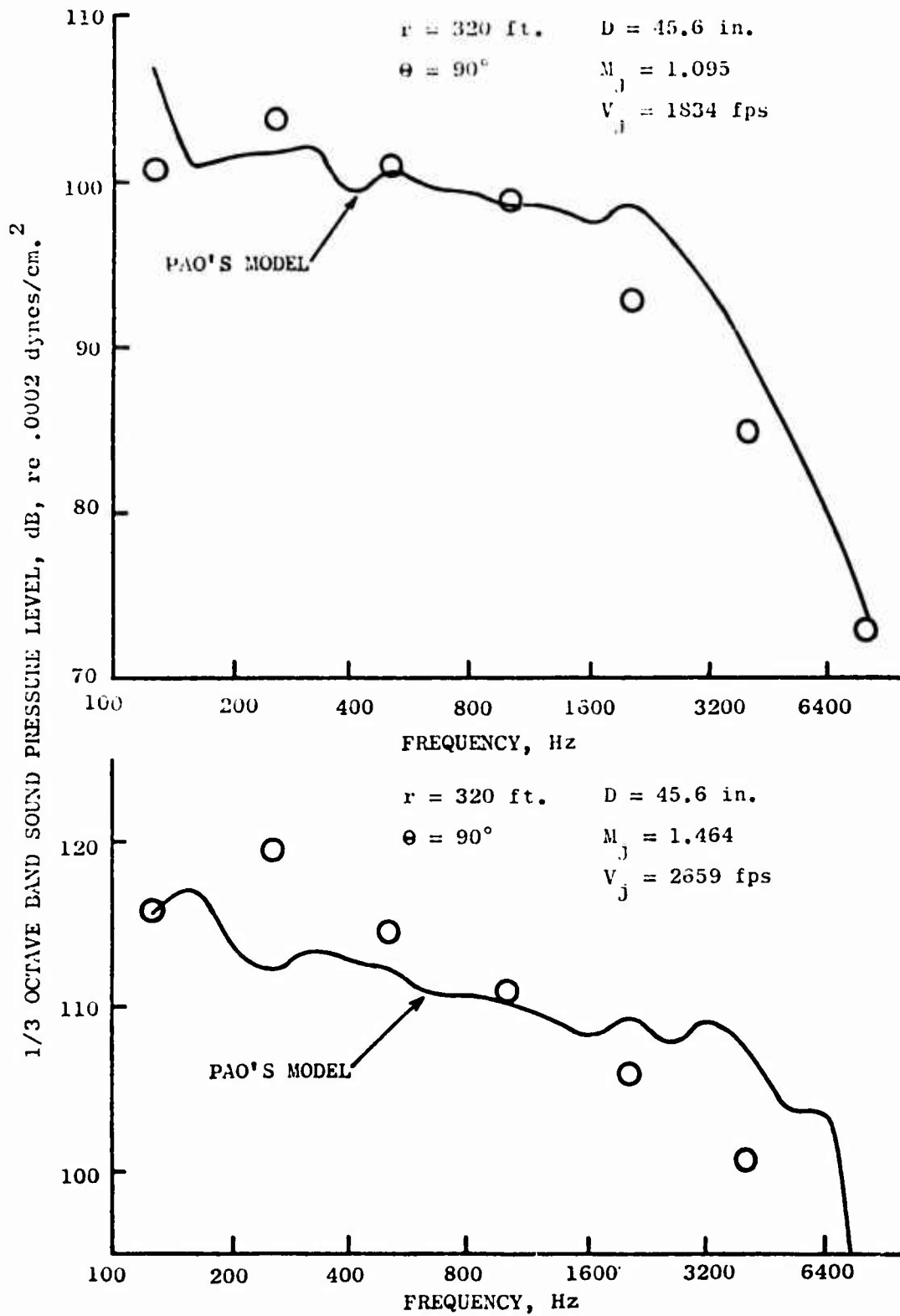


Figure 49 Comparison of Theoretical Results and Experimental Data

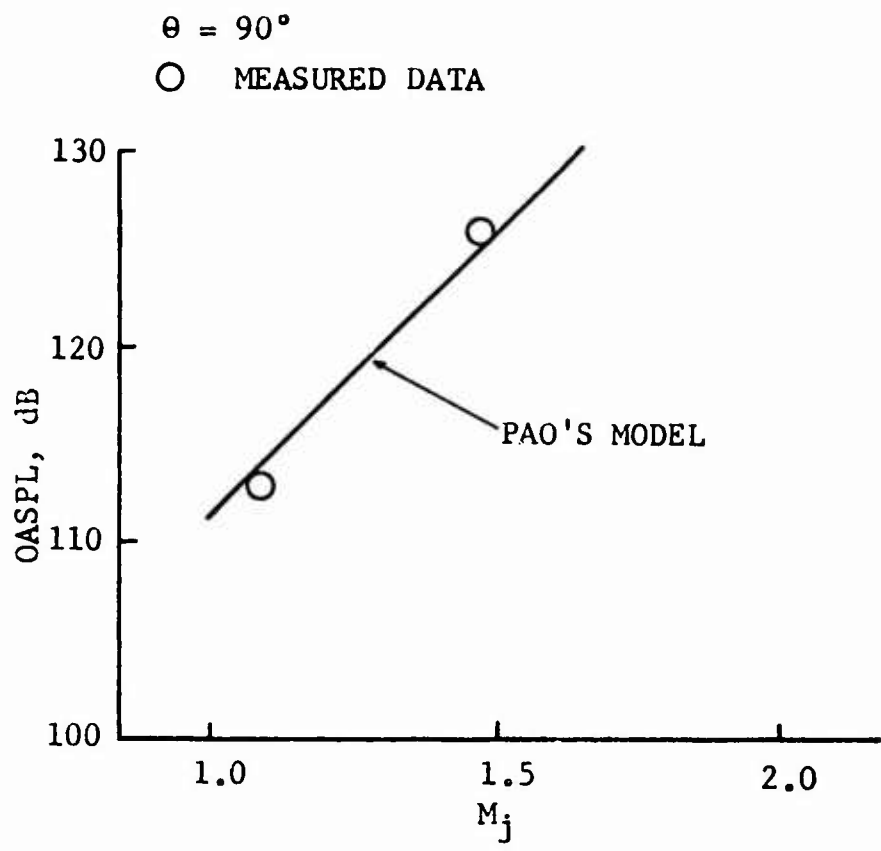


Figure 50 Comparison of Theoretical Results and Experimental Data

III. EXPERIMENTAL INVESTIGATION OF HEATED SUPERSONIC JET ACOUSTIC CHARACTERISTICS

P.R. Knott, K.R. Bilwakesh, J. Brausch

In order to augment and provide the theoretical aero and acoustic efforts with a body of experimental acoustic results at extended temperature ranges, a series of detailed far-field and near-field acoustic parametric studies were performed. Additionally a series of photographic studies was also performed for further documentation of the exhaust plume characteristics. In the paragraphs which follow some of the preliminary results of these experiments will be reported.

1.0 FAR-FIELD ACOUSTIC EXPERIMENTS

1.1 Experimental Apparatus, Test Set-up and Conditions

The experiments were carried out at General Electric's jet engine noise outdoor test site (JENOTS). Sixteen far-field microphones at a height of 15.93 ft from the ground were used on a forty foot arc, at ten degree increments starting from an angle of 20° with respect to the jet axis. Ten near-field microphones were used to obtain representative near-field acoustic characteristics (Section 2 will discuss more about additional near field tests performed). Figures 52 and 53 schematically show the far-field and near field microphone locations. The nozzle centerline height was 55-inches. The first 25 foot radius of the test site is concrete, and the rest is large crushed gravel.

Acoustic measurements were taken with 1/4-inch Bruel and Kjaer condenser microphones (4135). The signals were recorded on a twenty-eight channel tape recorder (80 KH flat response with appropriate corrections), and the microphone were calibrated with a piston phone and oscillator calibrations before each test.

1.2 Nozzles Tested

Two basic nozzle configurations were tested. One nozzle was a convergent - divergent (C/D) conical nozzle designed for parallel shock free flow at $M_j \approx 1.5$ for stagnation temperature operation between 1500° R and 2500° R.

The second nozzle was a convergent conical thin lip nozzle with a 1/2 inch thick lip adapter. The C/D nozzle design was performed using a method of characteristics computer program with corrections for boundary layer displacement. Both nozzles were water cooled and designed to withstand continuous and non-continuous testing at gas stream temperatures of 3200° R at internal total pressures to ambient pressure ratios of 4.0. The C/D nozzle had static pressure instrumentation provided for measuring wall static pressures along the divergent section of the nozzle and near the exit plane of the nozzle. The conical nozzle had an exit diameter of 4.3 inches. The C/D nozzle had a 4.3 inch throat diameter. Figures 54 and 55 are photographs of the nozzles.

1.3 Experimental Conditions

The experimental test conditions were so designed as to examine the velocity and temperature dependence of high velocity and high temperature jets. Table I shows the number of test points and flow conditions taken for the C/D nozzle. Tables 2 and 3 show the flow conditions tested for the conical thin lip and thick lip nozzles. Table 4 shows the flow conditions tested for shock free jet exhaust operation at elevated test conditions. The range of conditions are seen to be from 1000 fps to 3000 fps each for stagnation temperatures ranging from 1000° R to 3000° R.

1.4 Preliminary Results

1.4.1 Effect of Temperature on Jet Noise

The work of Hoch¹ et al. first illustrated the influence of exhaust temperature on the acoustic characteristic of jet noise. Following their example, except for an extended range of conditions, Figures 56 and 57 illustrate the effects of temperature on overall power level. Shown are results for constant acoustic Mach numbers ranging from .6 to 2.7 for a wide range of jet densities. Clearly shown is the decrease in acoustic power with increasing jet temperature while keeping jet velocity constant (the results at $M_0 = .6$ show an opposite effect). Also shown is the deviation of density power law dependency from the classical ρ^2 law of Lighthill. The solid lines drawn through the curves and based on Pao's theory are discussed in Section II-2.

TABLE 1

C/D NOZZLE - FLOW CONDITIONS - ACOUSTIC TEST - Tt/Vj MATRIX

Rdg No	TPS Pt No	Pt8/Po	Tt8-°R	Vj-fps
1	1	1.366	1081	1057
2	2	2.045	1067	1553
3	3	2.691	1061	1795
4	4	3.862	1052	2046
5	5	4.513	1062	2153
6	6	1.228	1484	1011
7	7	1.595	1469	1494
8	8	2.417	1490	2020
9	9	3.029	1479	2227
10	10	4.143	1474	2476
11	11	4.516	1475	2538
12	16	4.757	1934	2947
13	15	2.816	1904	2453
14	14	1.891	1921	1976
15	13	1.411	1925	1478
16	12	1.156	1925	970
1	17	1.120	2362	954
2	18	1.302	2308	1423
3	19	1.633	2329	1925
4	20	2.234	2302	2407
5	21	3.268	2330	2879
6	27	2.643	2949	2968
7	26	1.929	2889	2458
8	25	1.518	2857	1975
9	24	1.313	2882	1718
10	23	1.254	2846	1468
11	22	1.105	2885	987

TABLE 2

CONE, THIN LIP - FLOW CONDITIONS - ACOUSTIC TEST - T_t/V_j
MATRIX + SHOCK FREE DESIGN LINE OF C/D NOZZLE

Rdg No	TPS Pt No	Pt8/Po	Tt8-°R	Vj-fps
1	22	1.109	2815	995
2	23	1.243	3270	1543
3	24	1.368	3355	1865
4	25	1.500	3316	2098
5	26	1.949	3271	2634
6	27	1.654	3276	3134
7	21	3.263	2576	3024
8	20	2.231	2339	2424
9	19	1.639	2398	1960
10	18	1.288	2375	1416
11	17	1.126	2343	969
12	19	3.829	1417	2369
13	20	3.890	1591	2522
14	21	3.954	1755	2663
15	22	3.990	1946	2812
16	23	4.017	2150	2961
17	24	4.020	2309	3070
18	16	4.797	1853	2892
19	15	2.818	1850	2418
20	9	3.075	1409	2187
21	10	4.120	1435	2438
22	3	2.706	1018	1762
23	8	2.426	1444	1992
24	4	3.888	1003	2003
1	1	1.347	1033	1010
2	2	2.060	1019	1525
3	7	1.661	1441	1539
4	6	1.222	1436	983
5	13	1.393	1908	1445
6	12	1.150	1883	942
7	24	1.373	3000	1774
8	25	1.488	2925	1967
9	27	2.657	2947	2973
10	15	2.792	1876	2426
11	14	1.891	1908	1969
12	7	4.512	1453	2519
13	5	4.510	1018	2108

TABLE 3

CONE, THICK LIP - FLOW CONDITIONS - ACOUSTIC TEST - SHOCK FREE DESIGN LINE

Rdg No	TPS Pt No	Pt8/Po	Tt8-°R	Vj/fps
4	19	3.876	1411	2373
5	20	3.916	1624	2554
6	21	3.977	1766	2676
7	22	4.010	1946	2816
8	23	4.035	2129	2951
9	24	4.047	2347	3102
14	19	3.863	1447	2401
15	20	3.903	1633	2558
16	21	3.947	1805	2699
17	22	4.014	1979	2841
18	23	4.019	2179	2982

TABLE 4

C/D NOZZLE - FLOW CONDITIONS - ACOUSTIC TEST - SHOCK FREE DESIGN LINE

Rdg No	TPS Pt No	Pt8/Po	Tt8-°R	Vj-fps
12	19	3.837	1415	2369
13	20	3.925	1575	2517
14	21	3.967	1752	2664
15	22	4.022	1927	2805
1	22	4.022	1927	2950
2	23	4.031	2129	2950
3	24	4.065	2326	3092

Figure 58 illustrates the density dependence of peak OASPL for ideal exhaust speeds of 1000 fps to 3000 fps over a wide range of jet densities. At these angles, shock wave noise is usually negligible and the influence of the jet density on acoustic radiation indicates that these influences correspond to the jet's turbulent mixing. The results shown here indicate a somewhat lesser exponent dependence than observed by Reference 1; however, the limited results of recent Boeing² work seem to be in closer agreement with the data presented here. For the same range of flow conditions, Figure 59 shows a study of the influence of jet density on jet noise at $\theta = 90^\circ$. The results shown are for subsonic as well as supersonic jet exhaust Mach numbers. At super-critical pressure ratios, the noise levels may contain shock noise influence as well as turbulent mixing noise characteristics. These results as well as the velocity dependent nature of the jet at other angles will be studied further during the course of the program.

1.4.2 Velocity Dependence of Jet Noise

Preliminary results are shown only. The full analysis of these results and how they compare with theory predictions will come later. Figure 60 illustrates the velocity dependent nature of overall power level. The results shown were normalized with respect to their density power law dependence. A velocity eighth power law dependence is shown as a reference line in this figure. Further results illustrating the velocity dependence of high temperature model scale jets are shown in Figures 61 through 68. These figures show the velocity dependence of 1/3 octave band sound pressure for a wide range of Strouhal numbers: .1, .3, 1., 3., 5.0, and 10.0. Figures 61, 62 and 63 are figures of the velocity dependence at $\theta_{jet} = 150^\circ$ at $T_T = 2000^\circ R$, $2500^\circ R$ and $3000^\circ R$. Figures 64, 65 and 66 are for θ_{jet} at 90° at $T_T = 2000^\circ R$, $2500^\circ R$, and $3000^\circ R$. Figures 67 and 68 illustrate the velocity dependences per frequency band for $\theta_{jet} = 40^\circ$ for $T_T = 2000^\circ R$ and $2500^\circ R$.

1.4.3 Temperature Influences on Jet Directivity

In subsections 1.4.1 and 1.4.2 results of the parametric acoustic test results illustrated the velocity and temperature dependent nature of heated

($T_8 = 1000^\circ \text{ R} \rightarrow 3000^\circ \text{ R}$) air jets over a velocity range of 1000 fps \rightarrow 3000 fps. Figures 69 and 70 illustrate the temperature effect on a jet's one-third octave band directivity pattern for source Strouhal number of 1.0. Figures 71 and 72 show a similar directivity pattern at a constant frequency of 3150 Hz (close to a Strouhal number of 1.0 based on the observed acoustic frequency).

For the data at a jet speed of 1000 fps (Figures 69 and 71) increase in temperature is seen to move the peak of noise to larger jet angles as well as to decrease the acoustic radiated at the small jet angles. The character of the directivity pattern is seen to be very similar when the results are plotted based on source Strouhal number or observed Strouhal number. For the jet nozzle at an ideal jet speed of 2500 fps (Figures 70 and 72) the peak noise stays constant at 50° to the jet axis. At the larger jet angles the lower temperature tests show a substantial increase in noise over the higher temperature jets. These increases may be primarily due to increased shock noise effects. Further data reduction of test results at different Strouhal numbers will be pursued in future studies on this program.

2.0 NEAR FIELD ACOUSTIC EXPERIMENTS

2.1 Experimental Apparatus, Test Set-up, Conditions, Results

Tests were conducted to obtain detailed near field maps (simultaneously with far field measurements) for shock-free and shocked-flow hot jets for source location studies. The 4.3" throat-diameter C/D nozzle and the 4.3" exit dia. thin lip conical nozzle were used respectively for the shock-free and shocked flow conditions.

Simultaneous with the near field acoustic measurement a far field microphone array consisting of eight B&K 4136 microphones at a height of 15.93 feet from the ground on a 40-ft. arc at angles of 20° , 30° , 40° , 50° , 60° , 70° , 80° and 90° to the jet axis were also taken. The near field microphone array consisted of ten microphones (B&K 4136) mounted along a line parallel to the jet axis on a stand, which in turn was mounted on a tracked cart capable of being traversed in a direction perpendicular to the jet axis. The setup is shown in Figure 73 and 74. This system made possible obtaining near field data at fifty microphone locations, as shown in Figure 75.

The test conditions were primarily chosen to repeat the shock-free cases of the C/D nozzle for which Schlieren pictures and acoustic far field data had been taken as described in Section 1.0. These detailed near field tests covered a velocity range of 2400-3100 ft. per second, and in a total temperature range of 1400-2500° R. The same total temperature and total pressure ratio conditions were then specified for the thin-lip conical nozzle. A correlation of the acoustic data with the aerodynamic data can thus be expected to aid in the source location efforts. In addition, a subsonic ($M_j = 0.8$) and an $M_j = 1$ condition were prescribed for the conical nozzle, and an $M_j = 1$ point for the C/D nozzle. Table 5 summarizes the principal test conditions.

Detailed analysis is continuing on the data obtained from these near field acoustic measurements. Plots of variation of overall sound pressure level with axial distance at fixed radial distances from the jet axis are being made for both the conical and the C/D nozzle at various operating conditions. Such plots should be expected to identify zones of increased acoustic output corresponding to localized sources. In addition, at supersonic Mach numbers, comparison plots between a conical and a shock-free C/D nozzle can be expected to shed light on the influence of shocks.

Sample plots of OASPL vs. $\frac{X}{D}$ (X = axial distance from exit plane) at different radial locations are shown in Figures 76 through 78 for the conical nozzle and -28 and -29 for the C/D nozzle. Figures 76 through 78 correspond to a constant temperature (1500° R) and increasing velocity thus showing also the influence of velocity at constant temperature on the acoustic output. The increase in OASPL with X/D within the limits of X/D shown appears to show the effect of the increasing turbulence zone.

The influence of shock waves on the acoustic output may be seen from Figures 81 in which OASPL vs. $\frac{X}{D}$ has been plotted at different radial locations for both the conical and the C/D nozzles at $M_{ideal} = 1.55$ at the same temperature. These results show that

$$\Delta dB = OASPL_{conical} - OASPL_{CD}$$

is considerable, close to the nozzle exit plane (small $\frac{X}{D}$) and drops off at higher $\frac{X}{D}$ values.

In order to examine this phenomenon more closely, one-third octave band spectra of SPL are described in Figures 82(a) through 82(j) corresponding to the ten axial positions of the microphones at radial location $\frac{Y}{D} = 4$. These spectra correspond to $T_{T_8} = 2000^\circ \text{ R}$, $M \approx 1.55$ and $V_j \text{ ideal} \approx 2800 \text{ fps}$, that is, the same conditions represented in Figure 81. It is seen that at the closer microphones, there is a distinctly higher broad band content above 1000 Hz for the conical nozzle as compared to the C-D nozzle, but as you move downstream these effects are minimized.

One method of noise source location is to study the detailed near field radiation field. To do this contour plots of OASPL are being obtained for selected test conditions. In addition, contour plots of SPL at chosen 1/3 octave band frequencies are also being generated from the data measured at each near field microphone locations.

An example contour plot of OASPL in the near-field region for a shock free flow is shown in Figure 83 for a jet velocity of 3100 ft/sec and jet total temperature of 2400° R . Comparisons of results are shown here as well as others, and examination of the Schlieren data for corresponding test runs obtained earlier is also in progress and will be reported at a later date.

3.0 PHOTOGRAPHIC & SOME SHOCK NOISE EXPERIMENTS

3.1 Photographic Results

In addition to the acoustic tests discussed above a series of Schlieren still and high speed movie pictures were taken to further document the exhaust plume characteristics. Figures 84 through 88 are photographs of the Schlieren still and high speed movie systems used for photographic work recently completed at JENOTS. Figure 84 shows a complete setup for the Schlieren system. Figures 85 and 86 show closeups of the Schlieren still and high speed movie systems. Figures 87 and 88 show the Schlieren light source systems for the still and high speed systems.

Figures 54 and 55 are photographs of the C/D nozzle and the conical thick and thin lip nozzles for which Schlieren and high speed Schlieren movies were taken. Figures 89 through 96 show typical still Schlierens of the C/D nozzle and the conical thick and thin lip nozzles operating at high temperature

and velocity conditions. Figure 89 shows the C/D nozzle operating at shock free conditions. Figure 90 and 91 show the conical thin lip nozzle plume. Figure 90 shows the immediate vicinity of the nozzle exit, while Figure 91 shows the jet plume up to the second shock bottle. Figures 92 and 92 show the exhaust plume of the conical thick lip nozzle at the same operating conditions as shown for the C/D and the conical thin lip nozzles. Figures 94, 95, and 96 show spark Schlieren (previous photos were with a continuous light source) photos of the C/D and conical thick and thin lip nozzles. The C/D nozzle is operating at shock free conditions. A radiation pattern emanating from the nozzle lip is clearly visible. The frequency of acoustic radiation for these waves are however around 100,000 Hz, and are not considered to be of acoustic significance, but may be indicators of jet instability.

3.2 Preliminary Shock Noise Results for Thin and Thick Lip Nozzles

Narrowband farfield SPL spectral comparisons of the convergent-divergent shock free jet with the conical thin lip and thick lip nozzles operating at flow conditions of 1400° F and 2500 fps are shown in Figure 97, 98 and 99 for jet angles of 30°, 130° and 140° respectively. At near peak jet noise angles the narrow band noise levels for the three nozzles are nearly identical. At the larger jet angles the conical thin and thick lip nozzles show a shock screech well above the shock free C/D nozzle noise. Increased levels of broad band noise at frequencies higher than the screen tone are also observed. The thick lip nozzle is seen to enhance shock screech over the thin lip nozzle (~6 dB at the 130° location) as well as the over all broad band noise (~5 dB over the frequency range of 1.5 KHz to 5.0 KHz). Of particular interest here is the increased broad band noise due to shock waves. Future work efforts will be carried on to study this behavior in conjunction with the shocked aero acoustic models discussed in Section I.

TABLE 5 Test Conditions for Detailed Near Field Tests

4.3" Exit Diameter Thin Lip Conical Nozzle

M_{ideal}	$T_{T8} \text{ } ^\circ R$	$V_j, \text{ fps}$	$\frac{P_{T8}}{P_{amb.}}$
0.8	1500	1450	1.54
1.0	1500	1750	1.86
1.55	1450	2400	3.88
1.55	2000	2800	3.88
1.55	2400	3100	3.88

4.3" Throat Diameter C-D Nozzle

1.0	1400	1680	1.86
1.55	1400	2400	3.88
1.55	1950	2800	3.86
1.55	2400	3100	3.86

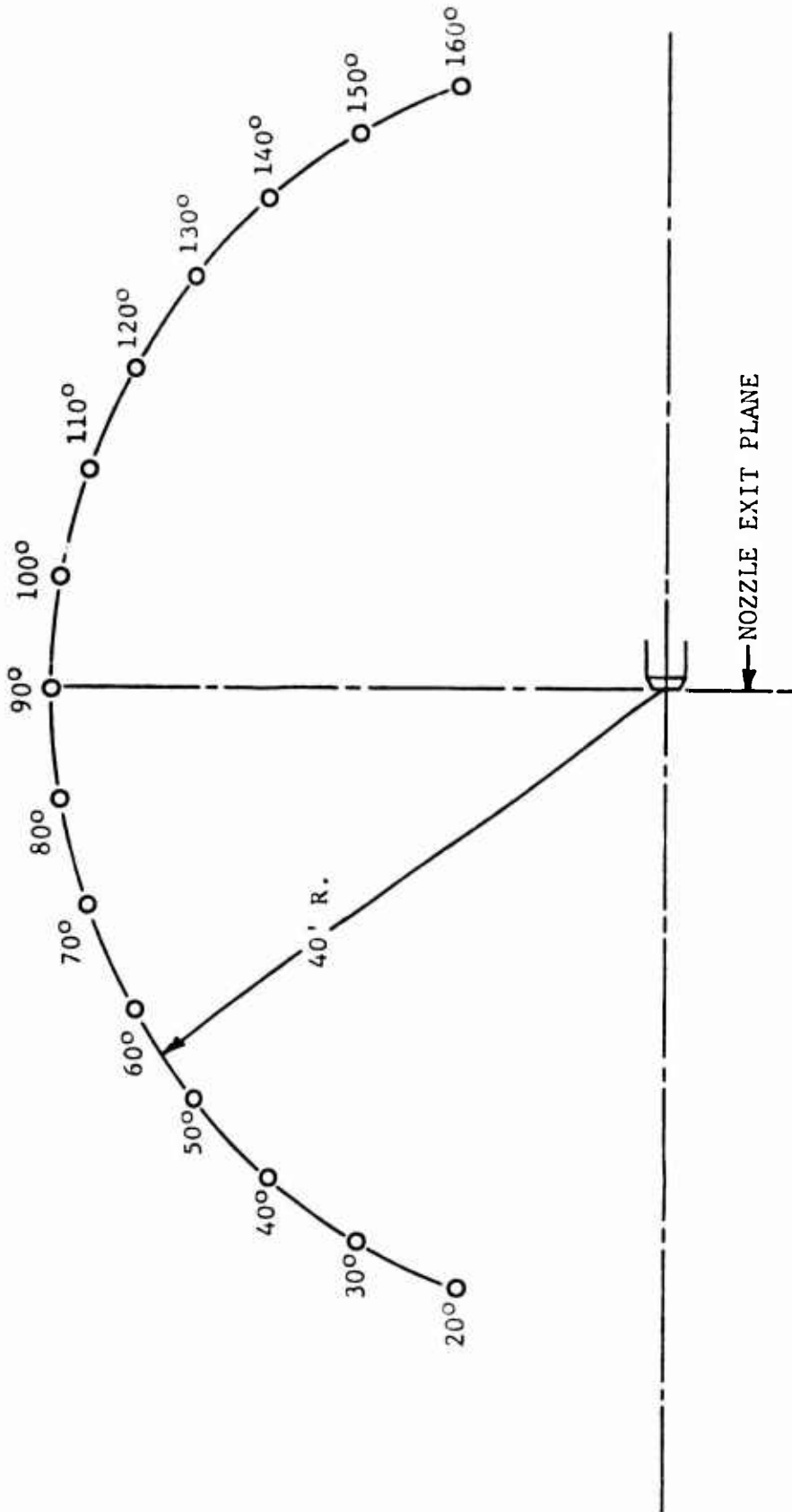


Figure 52 Acoustic Far-Field Measuring Stations

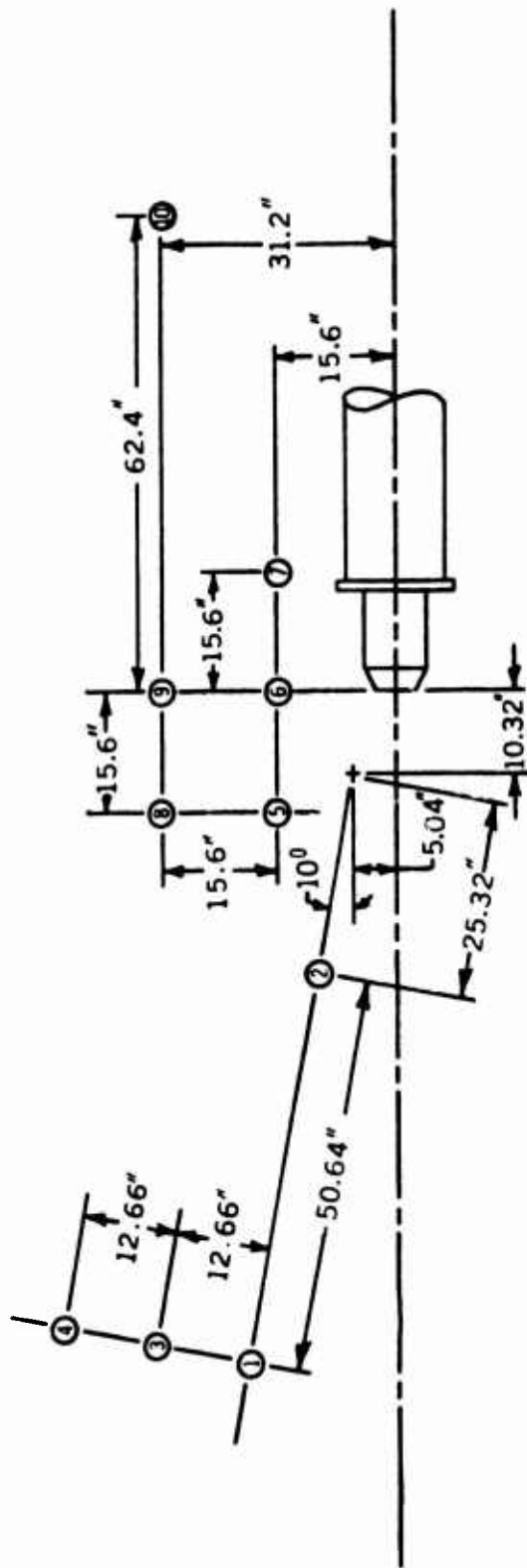


Figure 53 Acoustic Near-Field Measuring Stations

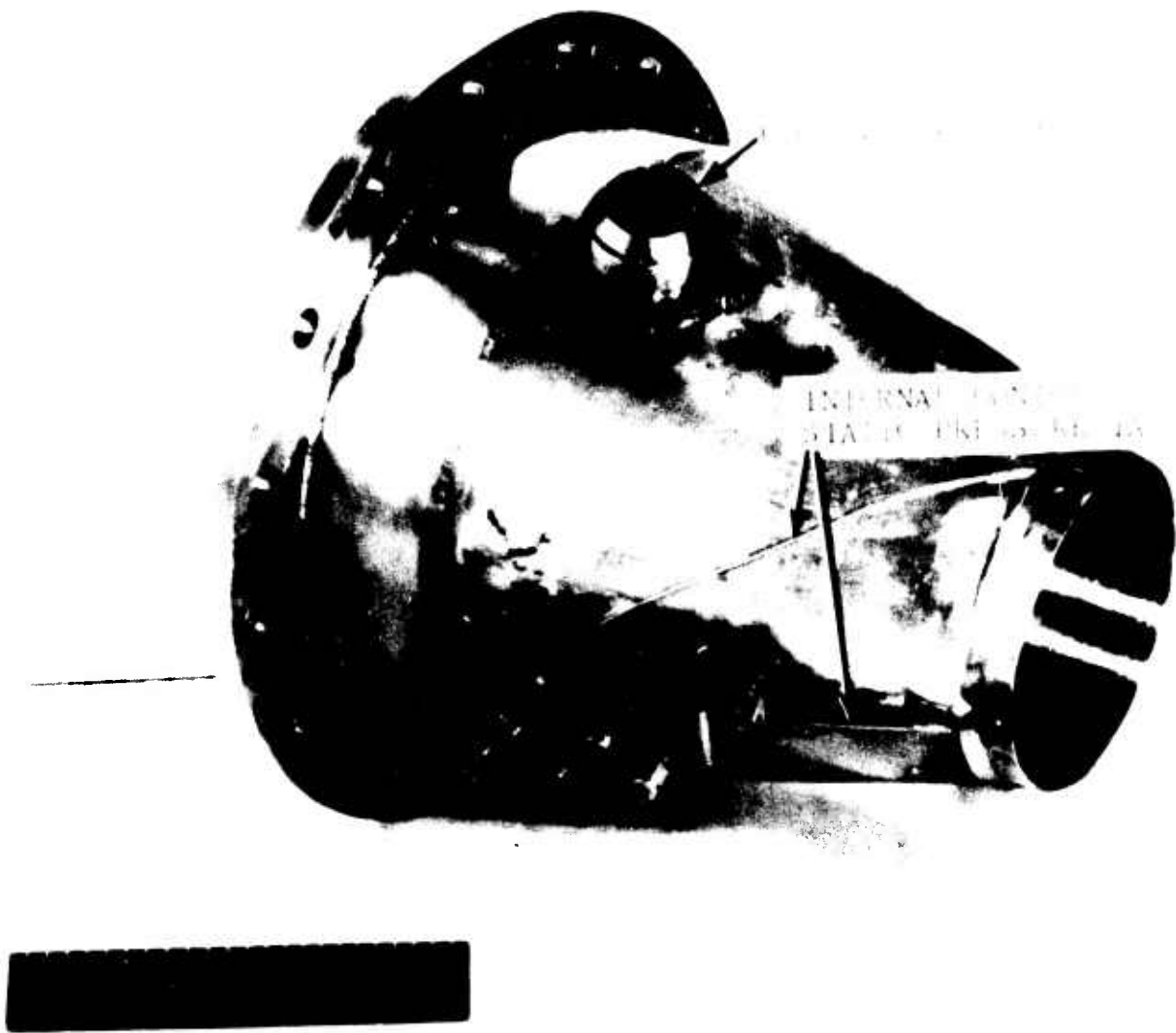


Figure 54 4.3 In. Throat Diameter Water-Cooled Parallel Flow
Convergent/Divergent Nozzle

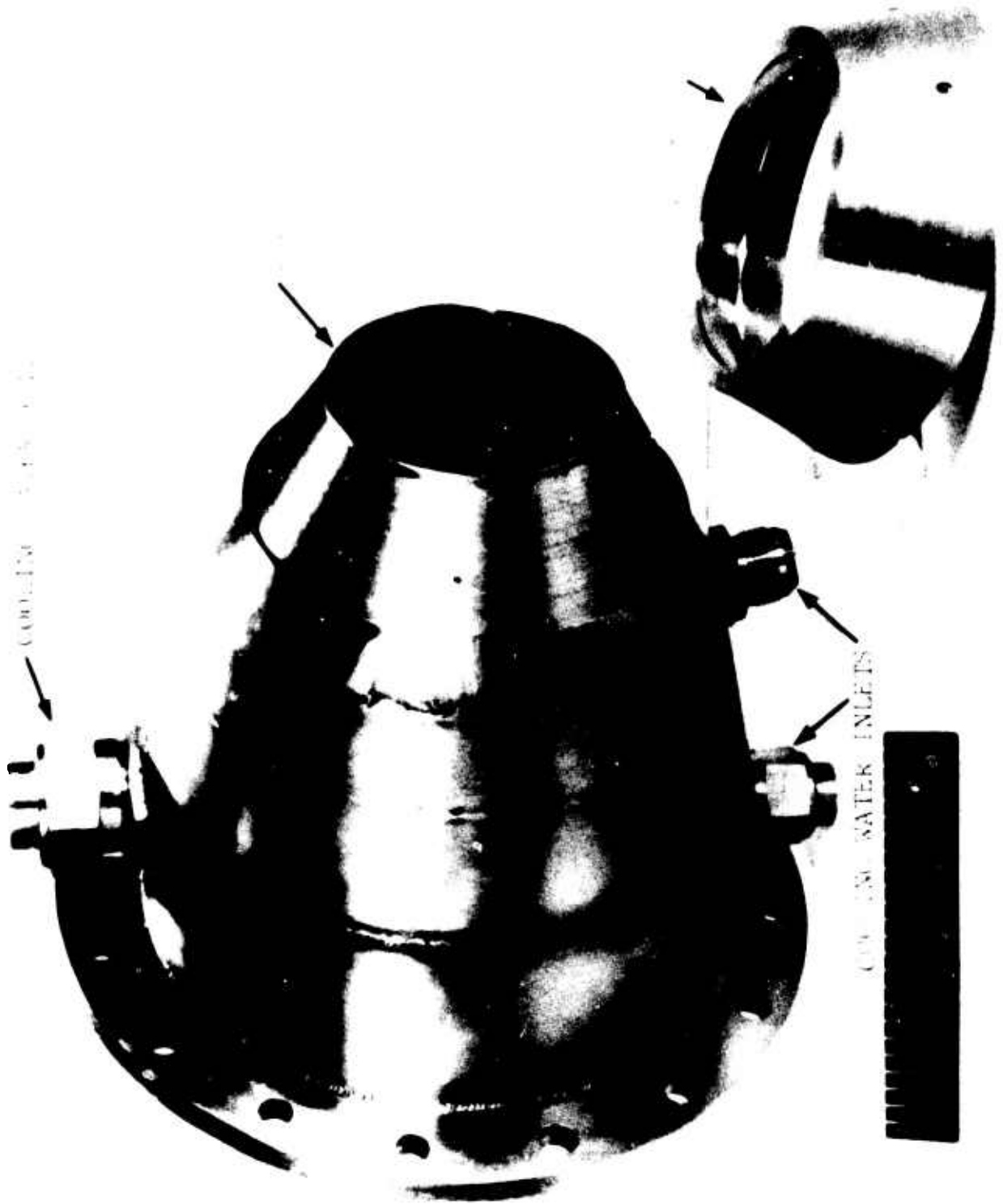


Figure 55 4.3 In. Exit Diameter Water-Cooled Conical Convergent Nozzle

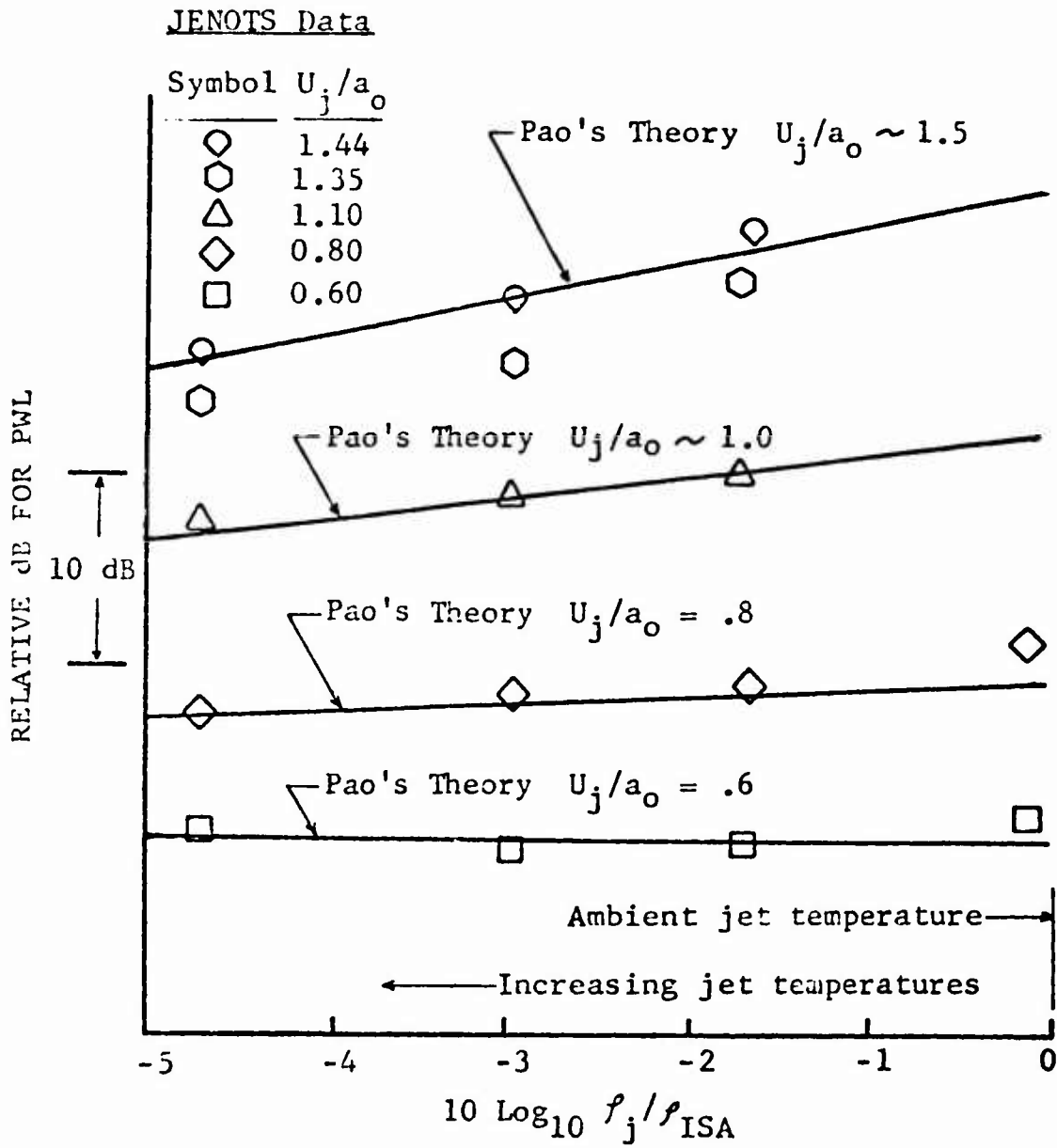


Figure 56 Theory -- Data Comparison of Sound Power as a Function of Density Ratio and Exit Convection Mach Number

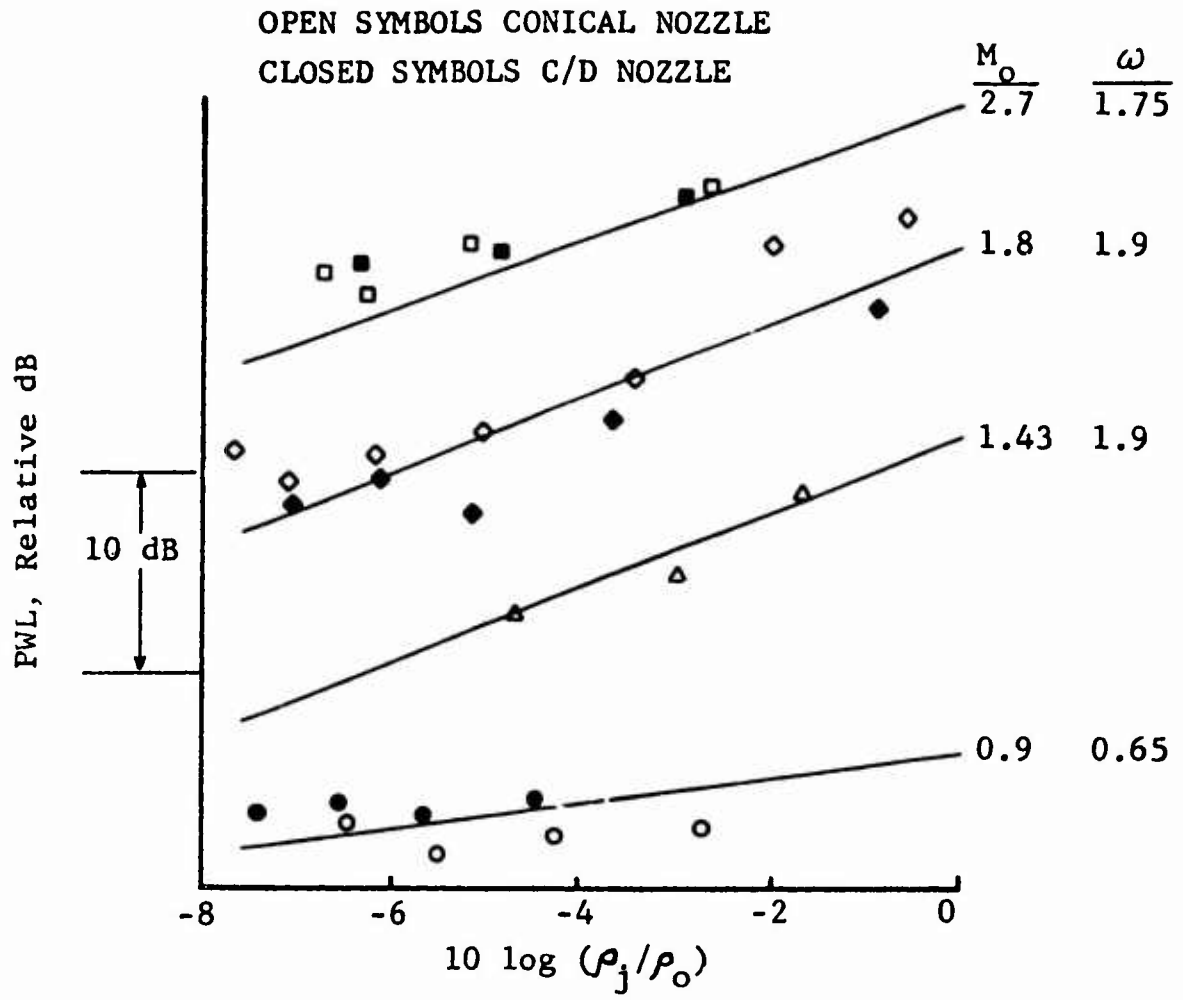


Figure 57 Effect of Temperature on OAPWL

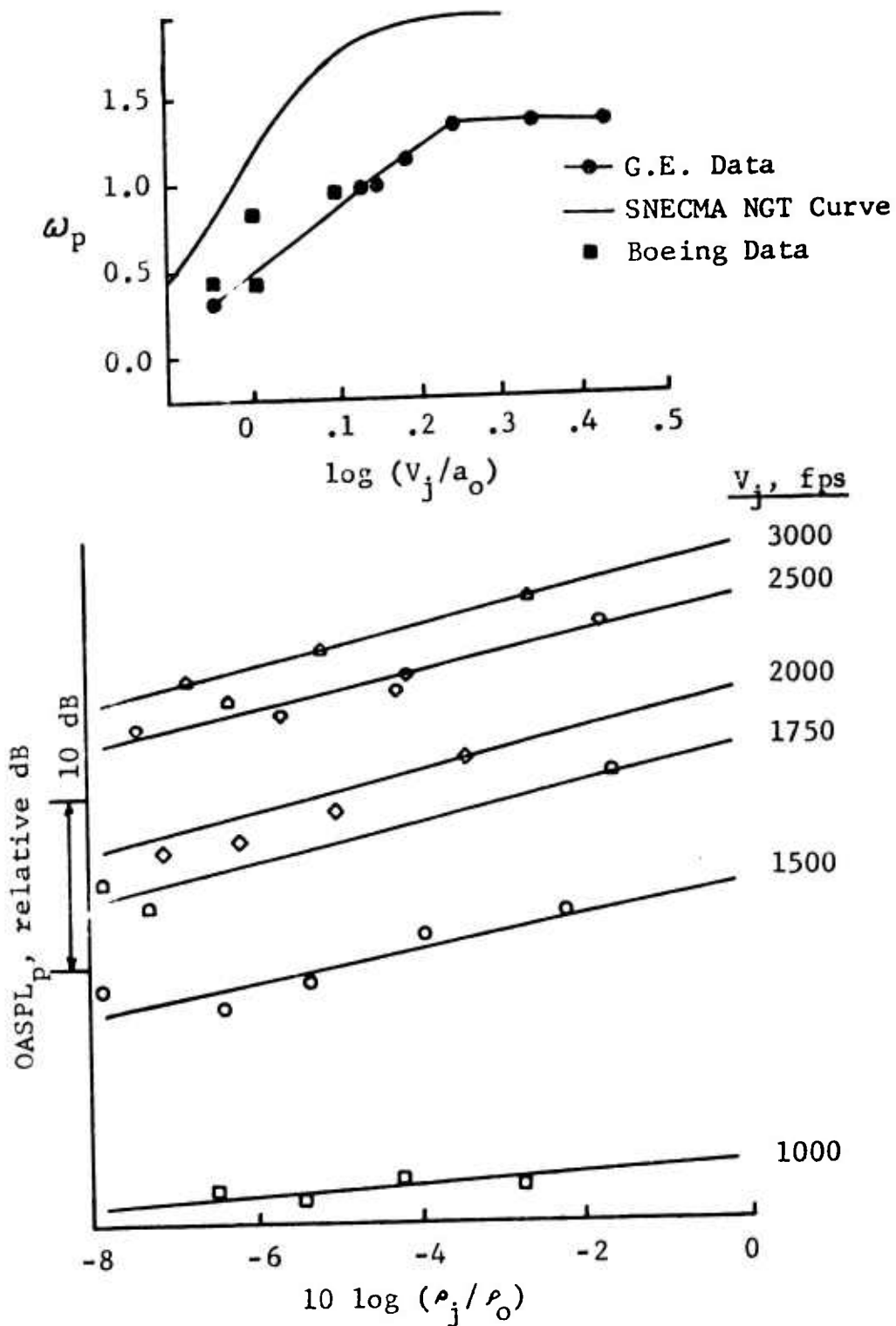


Figure 58 Effect of Jet Density on Peak OASPL

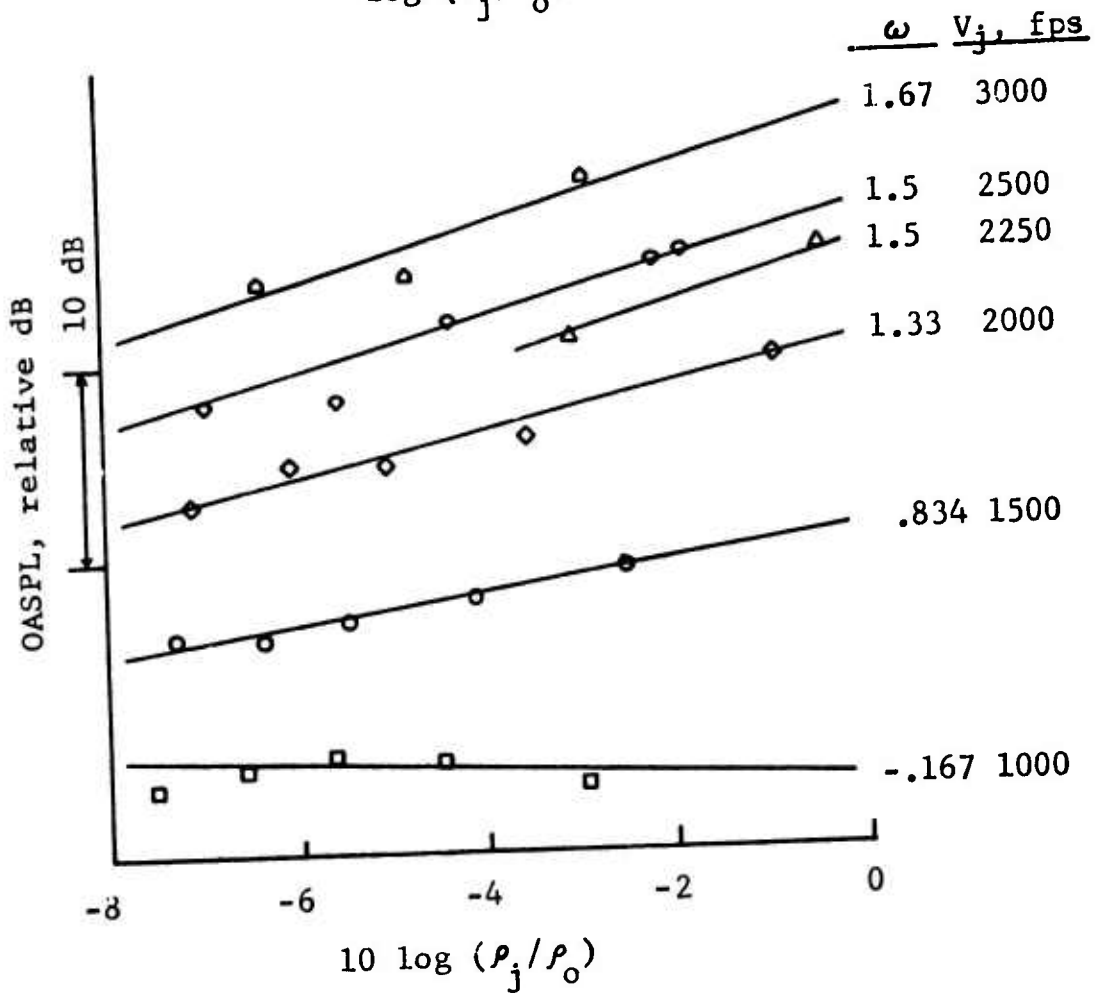
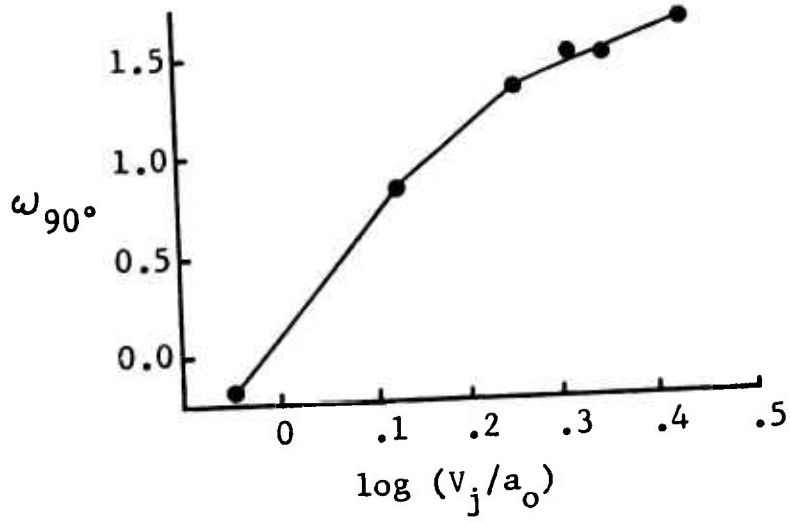


Figure 59 Effect of Jet Density on Jet Noise at Theta = 90°

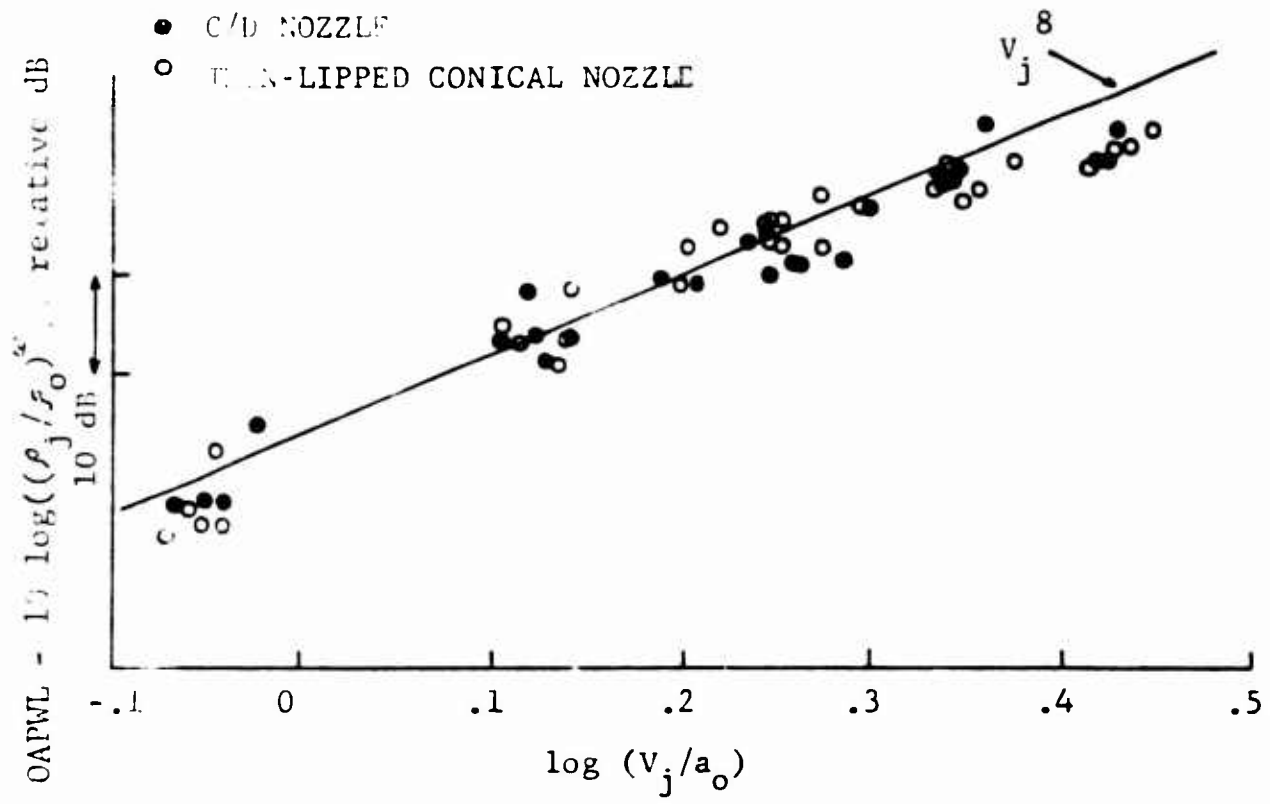


Figure 60 Velocity Dependence of Overall Power Level

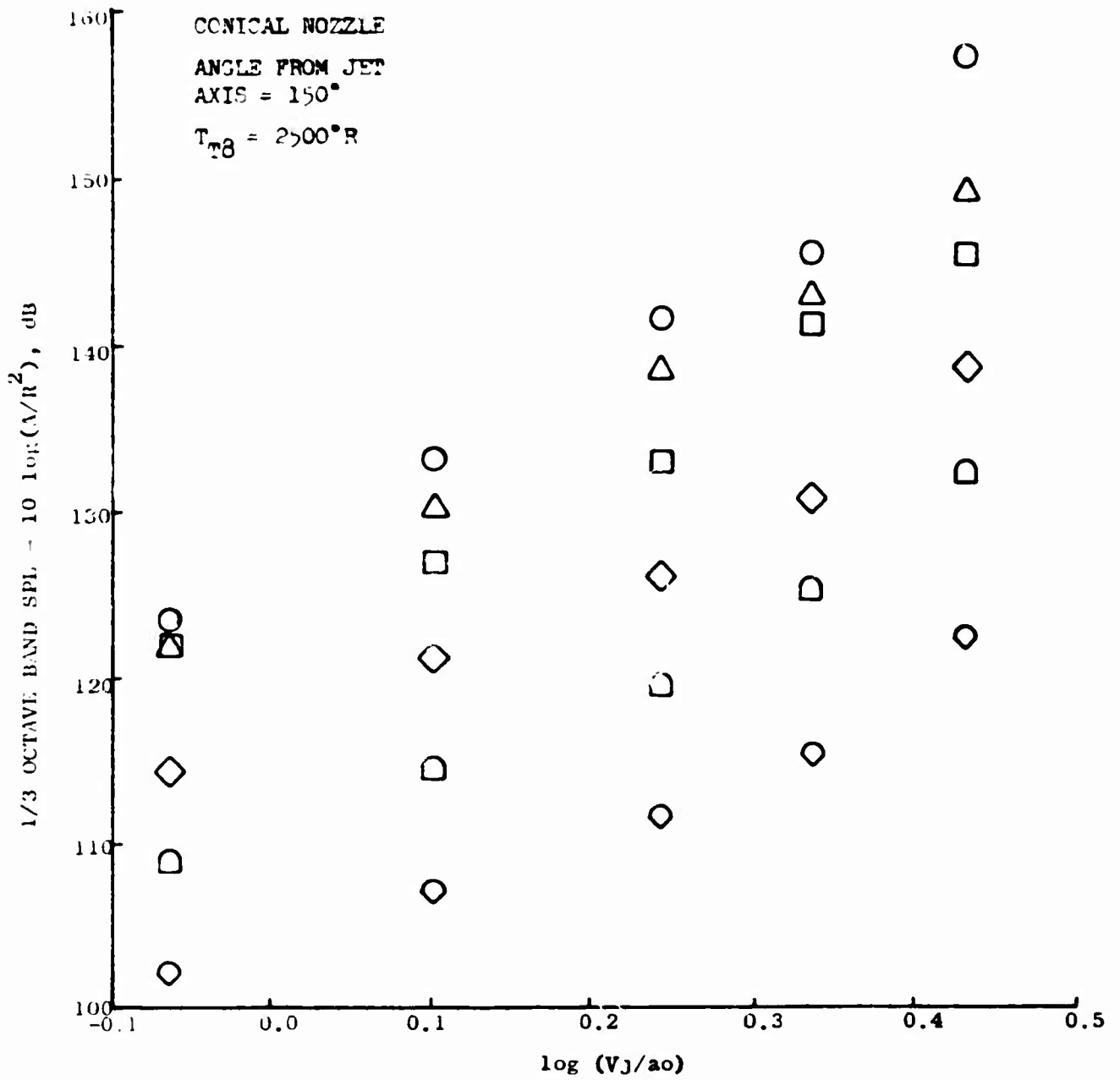


Figure 61 Velocity Dependence of 1/3 Octave Band SPL
 at Source Strouhal Numbers from 0.1 to 10.0

<u>SYMBOL</u>	<u>fD/V</u>
□	0.1
○	0.3
△	1.0
◇	3.0
◻	5.0
◊	10.0

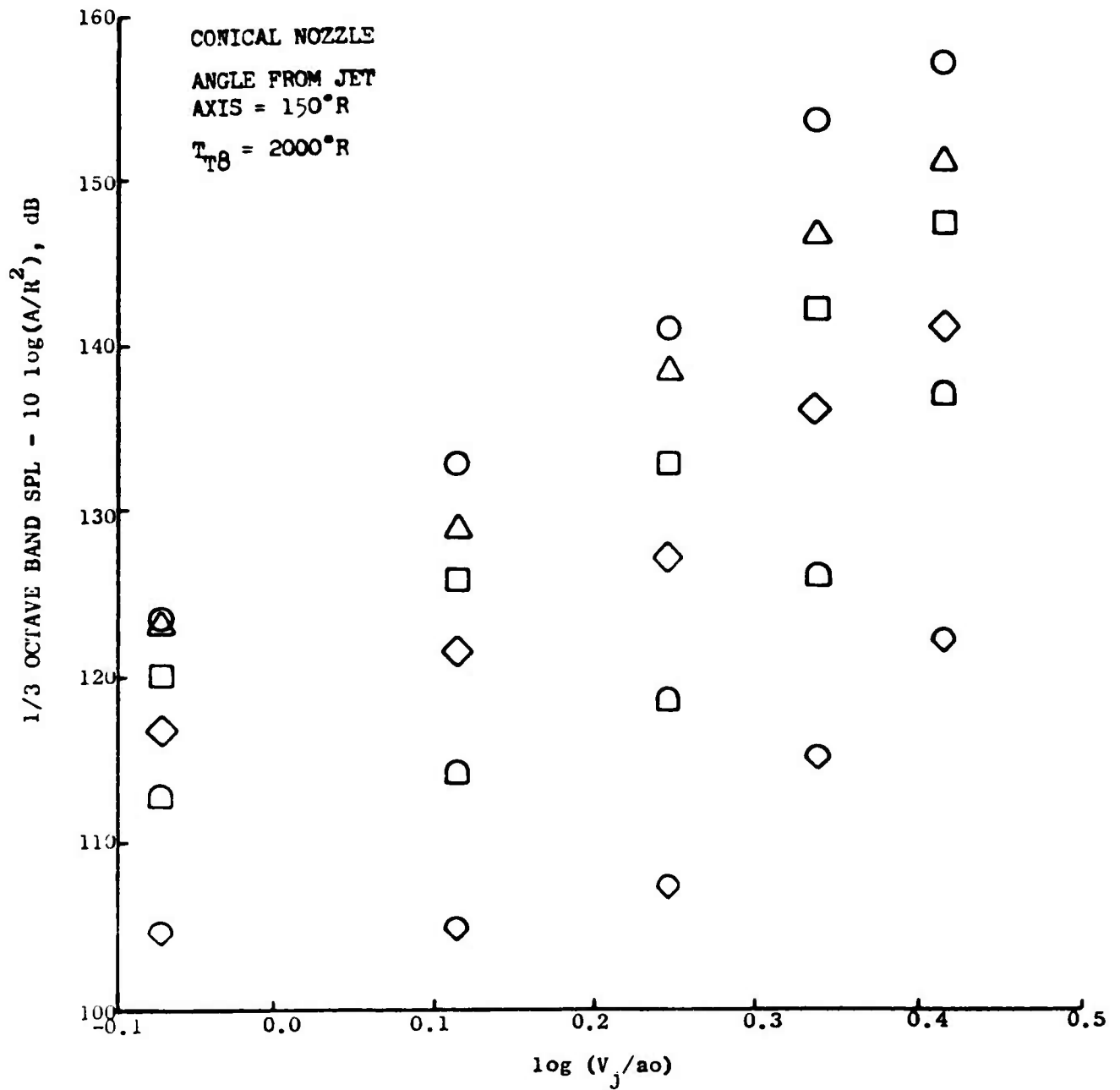


Figure 62 Velocity Dependence of 1/3 Octave Band SPL
 at Source Strouhal Numbers from 0.1 to 10.0

<u>SYMBOL</u>	<u>fd/V</u>
□	0.1
○	0.3
△	1.0
◇	3.0
◻	5.0
○	10.0

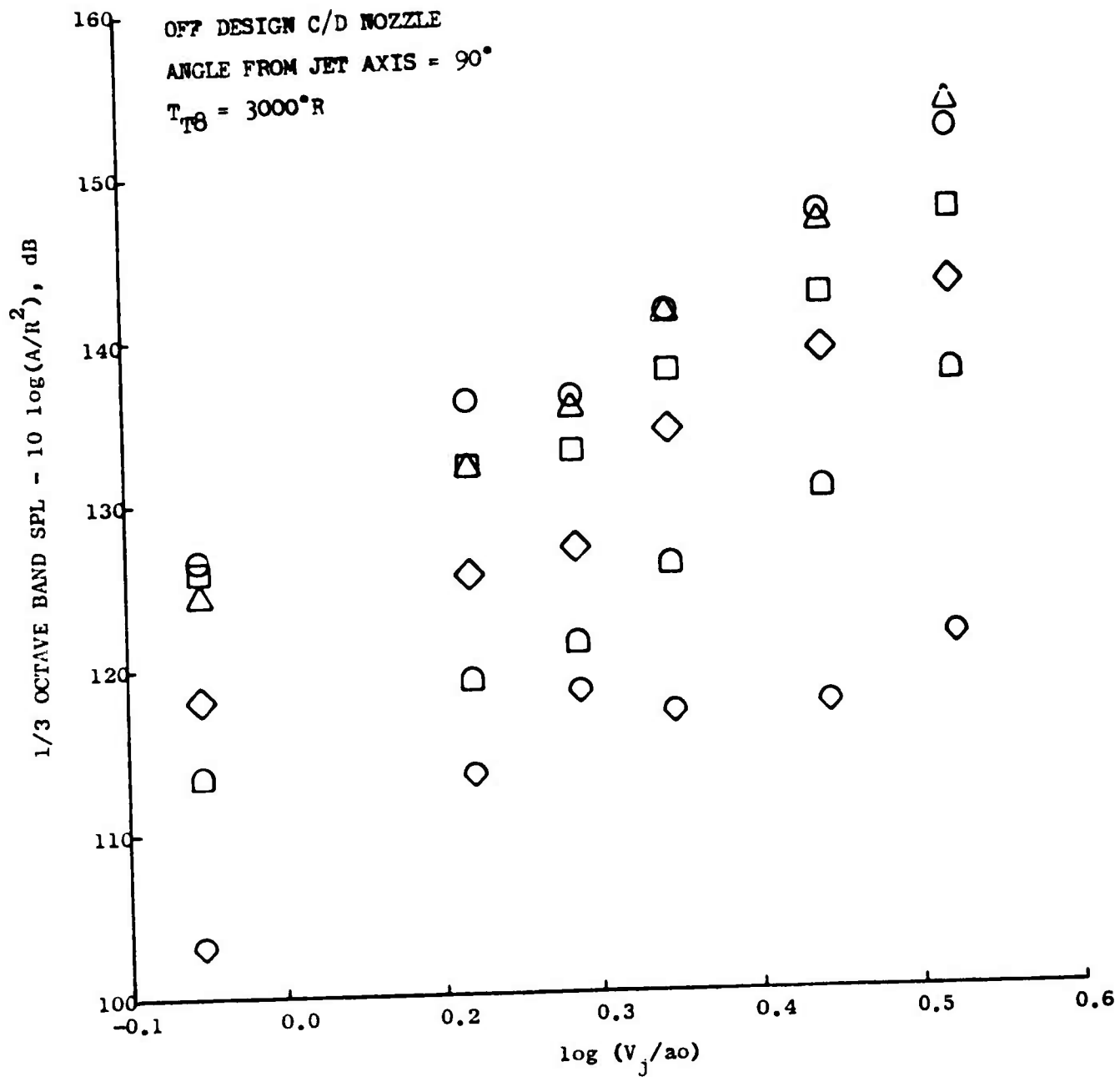


Figure 63 Velocity Dependence of 1/3 Octave Band SPL
 at Source Strouhal Numbers from 0.1 to 10.0

SYMBOL	fD/V
□	0.1
○	0.3
△	1.0
◇	3.0
◻	5.0
◊	10.0

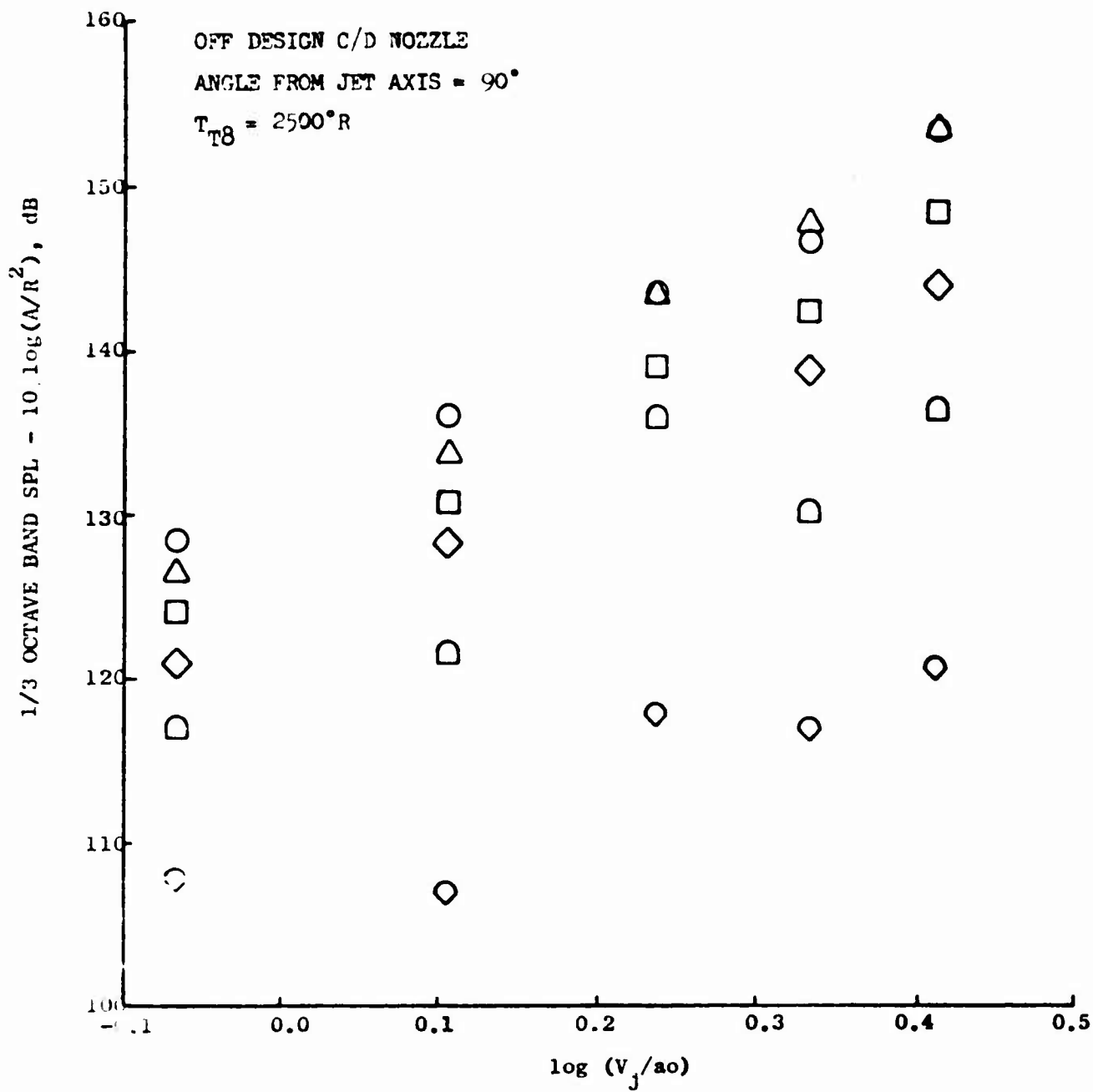


Figure 64 Velocity Dependence of 1/3 Octave Band SPL at Source Strouhal Numbers from 0.1 to 10.0

<u>SYMBOL</u>	<u>fD/V</u>
□	0.1
○	0.3
△	1.0
◇	3.0
◻	5.0
◊	10.0

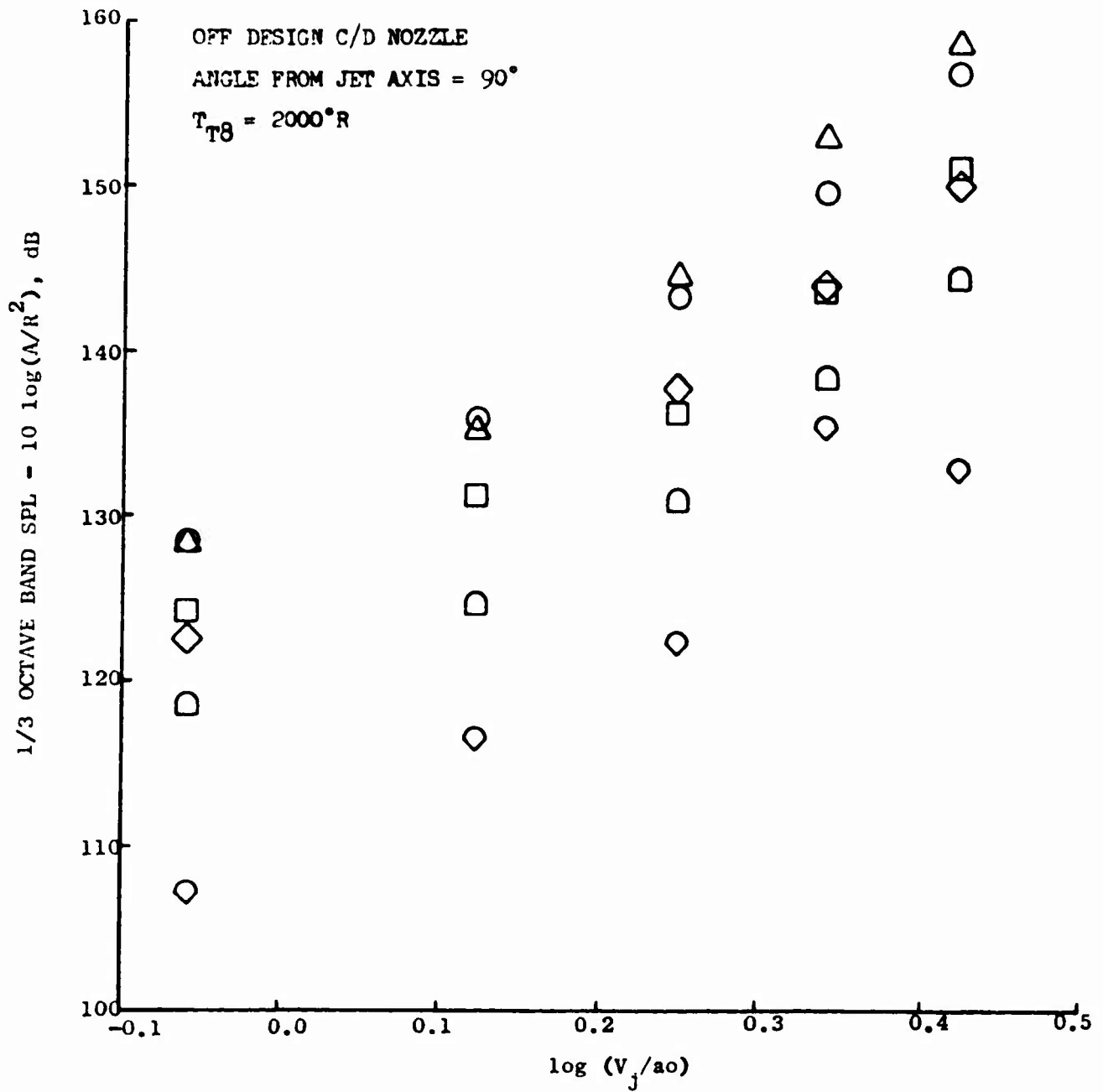


Figure 65 Velocity Dependence of 1/3 Octave Band SPL at Source Strouhal Numbers from 0.1 to 10.0

SYMBOL	fD/V
□	0.1
○	0.3
△	1.0
◇	3.0
◻	5.0
◊	10.0

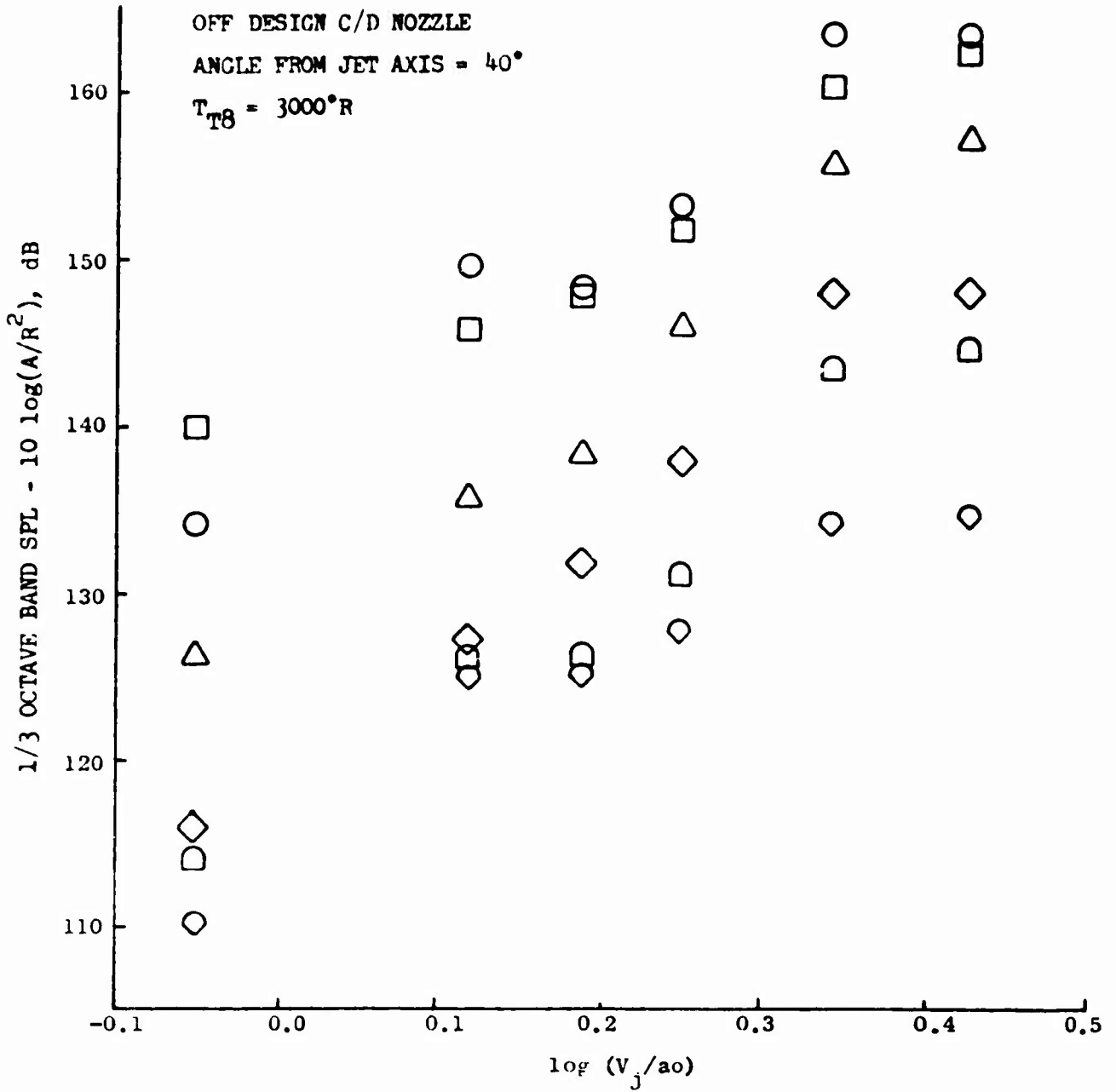


Figure 66 Velocity Dependence of 1/3 Octave Band SPL at Source Strouhal Numbers from 0.1 to 10.0

<u>SYMBOL</u>	<u>fD/V</u>
□	0.1
○	0.3
△	1.0
◇	3.0
◻	5.0
◊	10.0

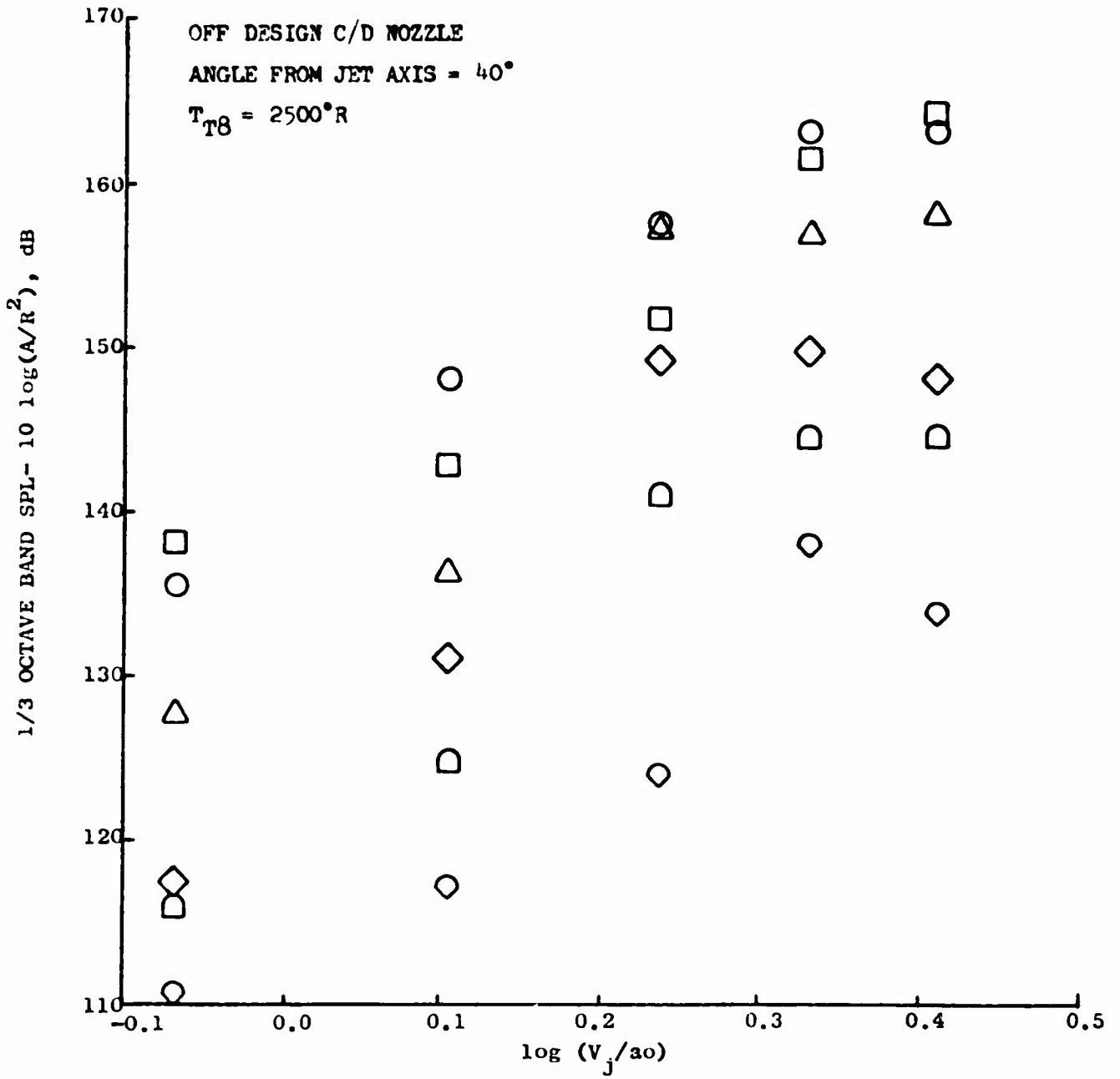


Figure 67 Velocity Dependence of 1/3 Octave Band SPL at Source Strouhal Numbers from 0.1 to 10.0

<u>SYMBOL</u>	<u>fD/V</u>
□	0.1
○	0.3
△	1.0
◇	3.0
◻	5.0
◊	10.0

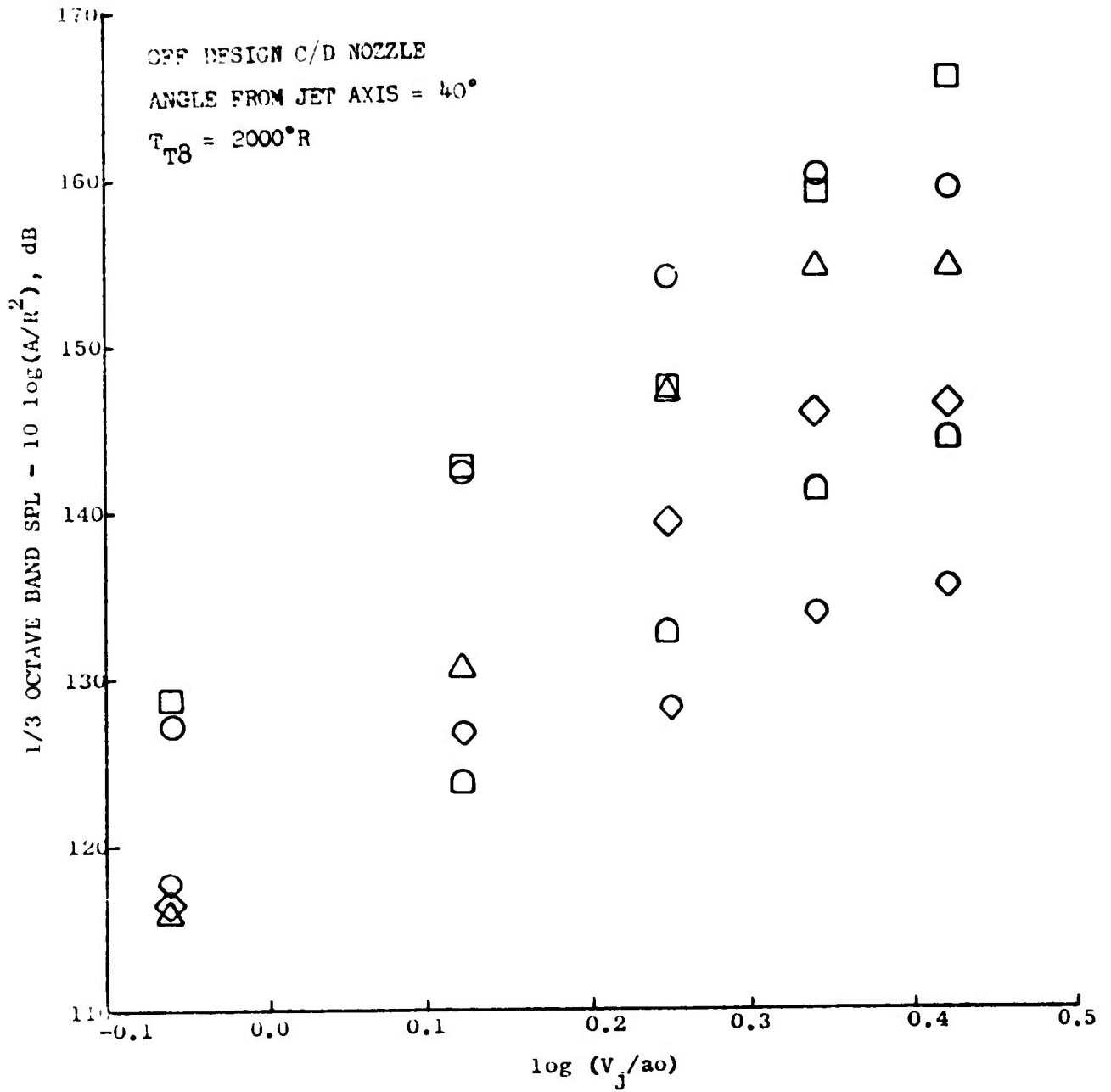


Figure 68 Velocity Dependence of 1/3 Octave Band SPL at Source Strouhal Numbers from 0.1 to 10.0

SYMBOL	fD/V
□	0.1
○	0.3
△	1.0
◇	3.0
◻	5.0
◊	10.0

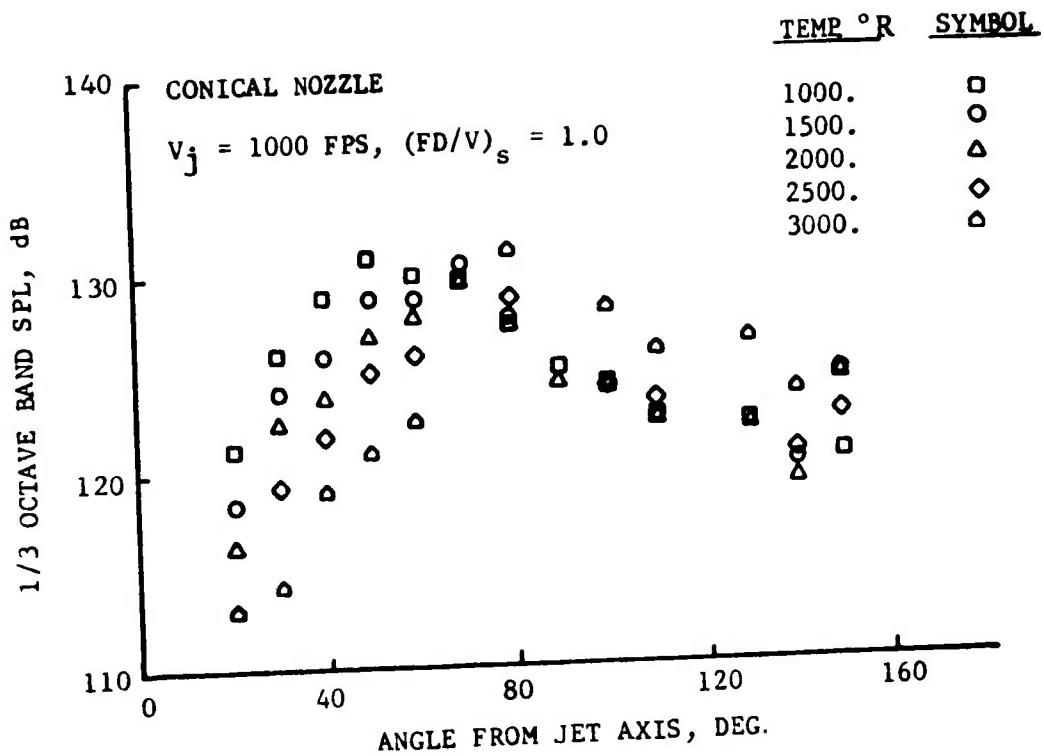


Figure 69 Effect of Jet Temperature on 1/3 Octave Band Directivity Pattern at a Constant Source Strouhal Number of 1.0

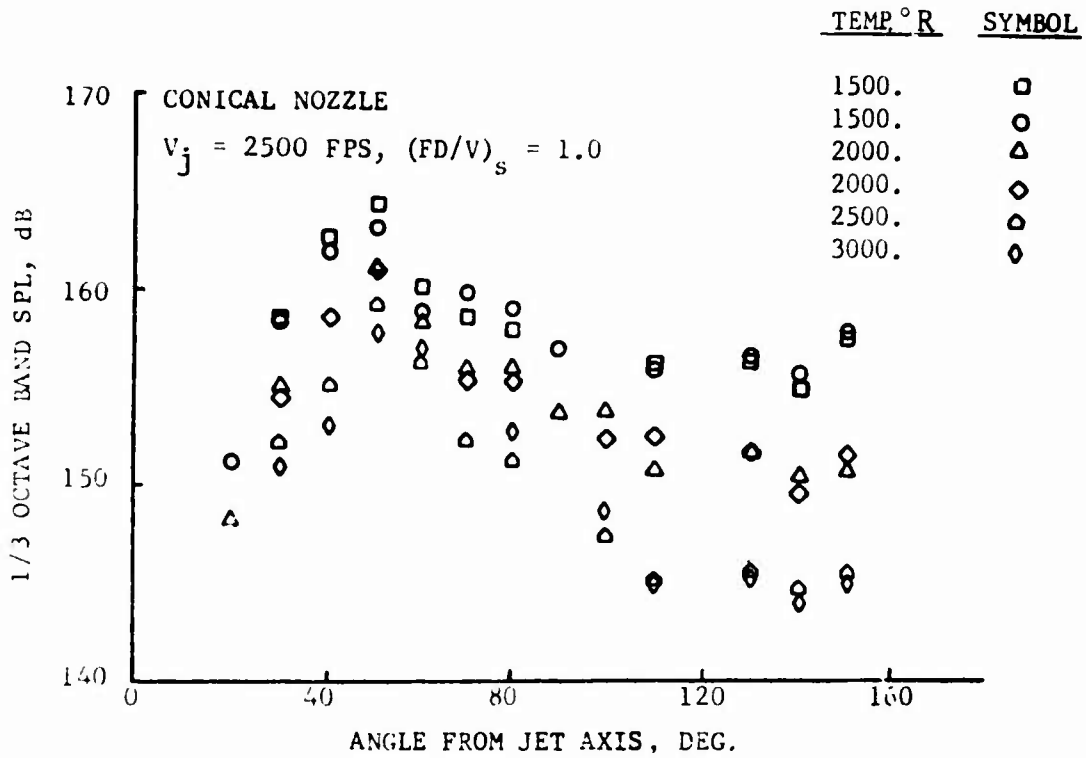


Figure 70 Effect of Jet Temperature on 1/3 Octave Band Directivity Pattern at a Constant Source Strouhal Number of 1.0

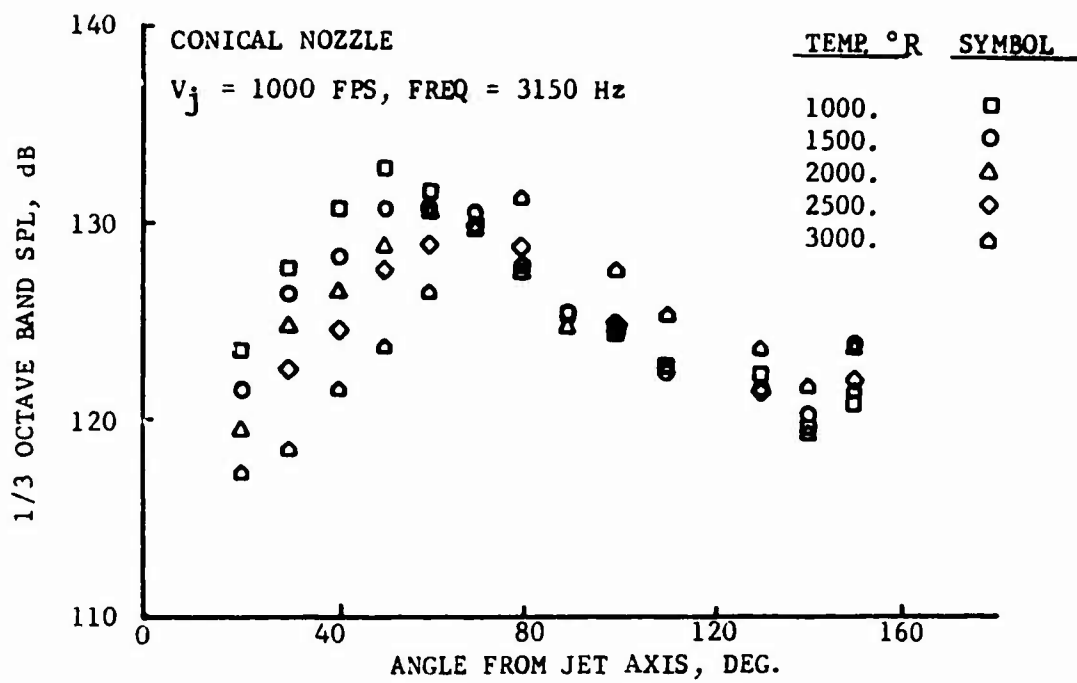


Figure 71 Effect of Jet Temperature on 1/3 Octave Band Directivity Pattern at a Constant Source Strouhal Number of 1.0

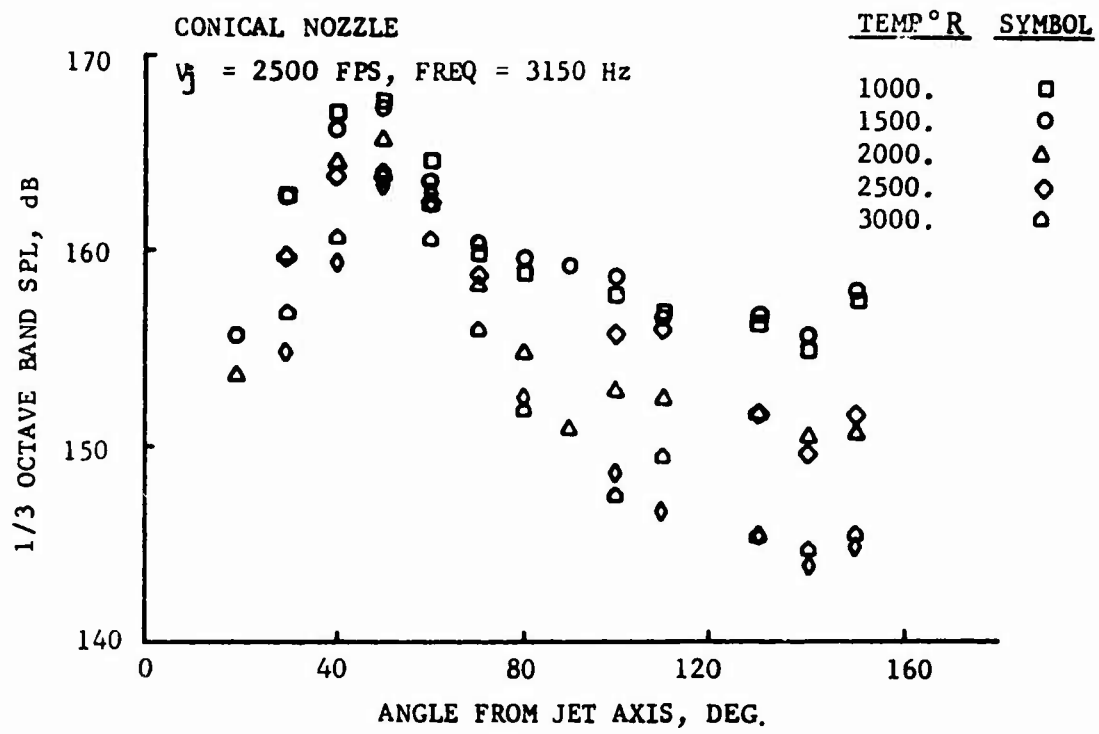


Figure 72 Effect of Jet Temperature on 1/3 Octave Band Directivity Pattern at a Constant Source Strouhal Number of 1.0

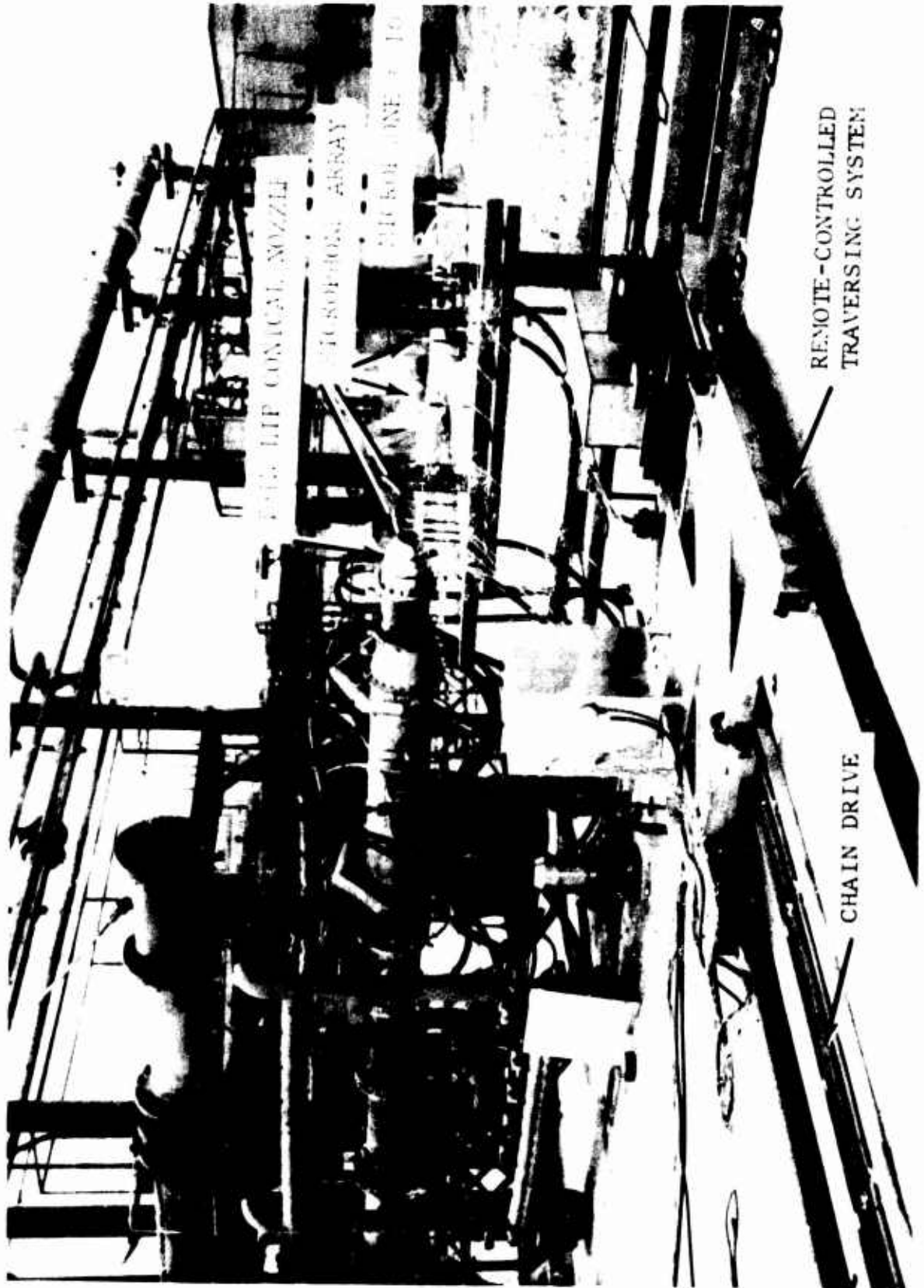


Figure 73 View of the Near-Field Microphone Array and Traversing Mechanism

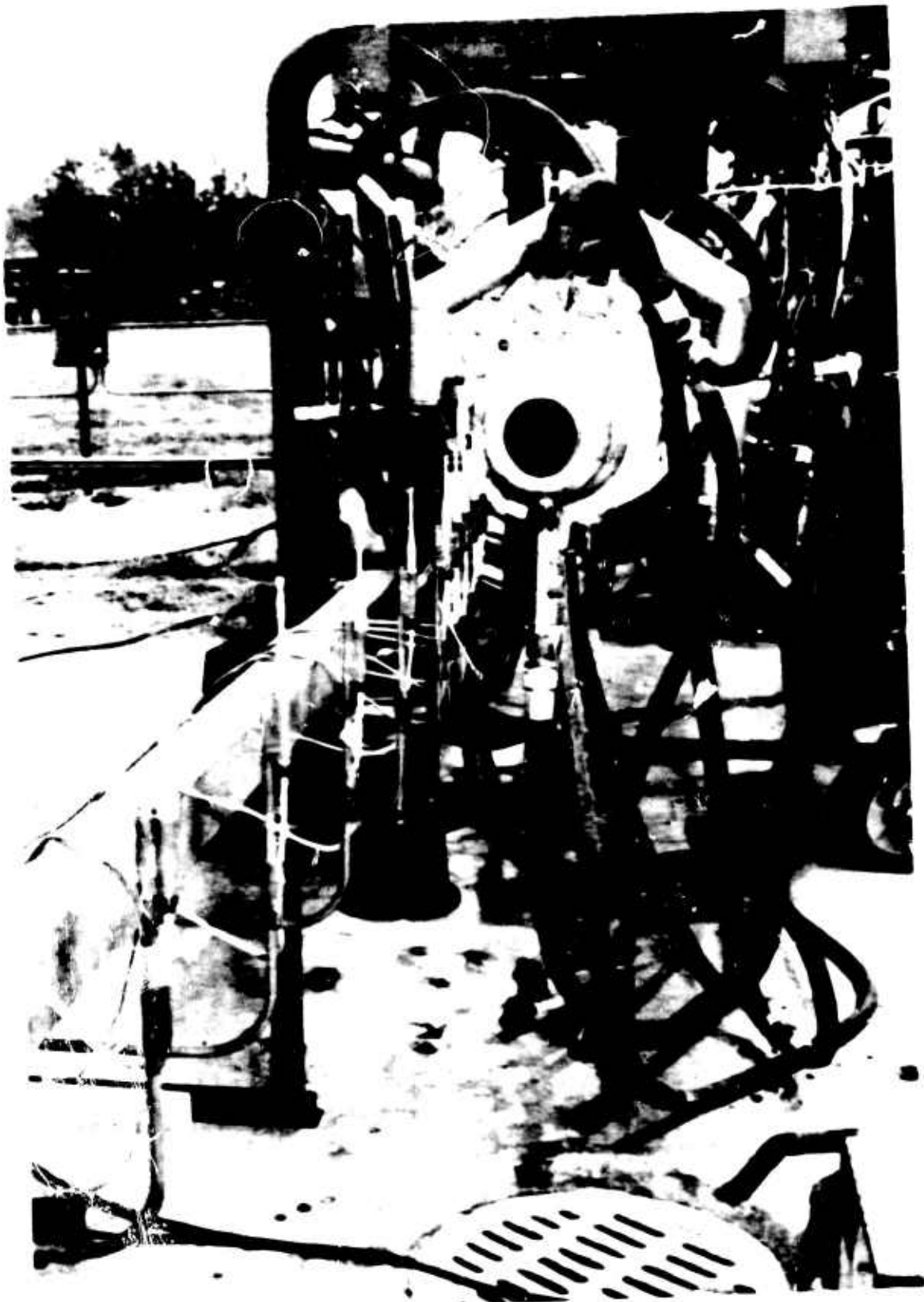


Figure 74 Close-Up View of the Near-Field Microphone Array

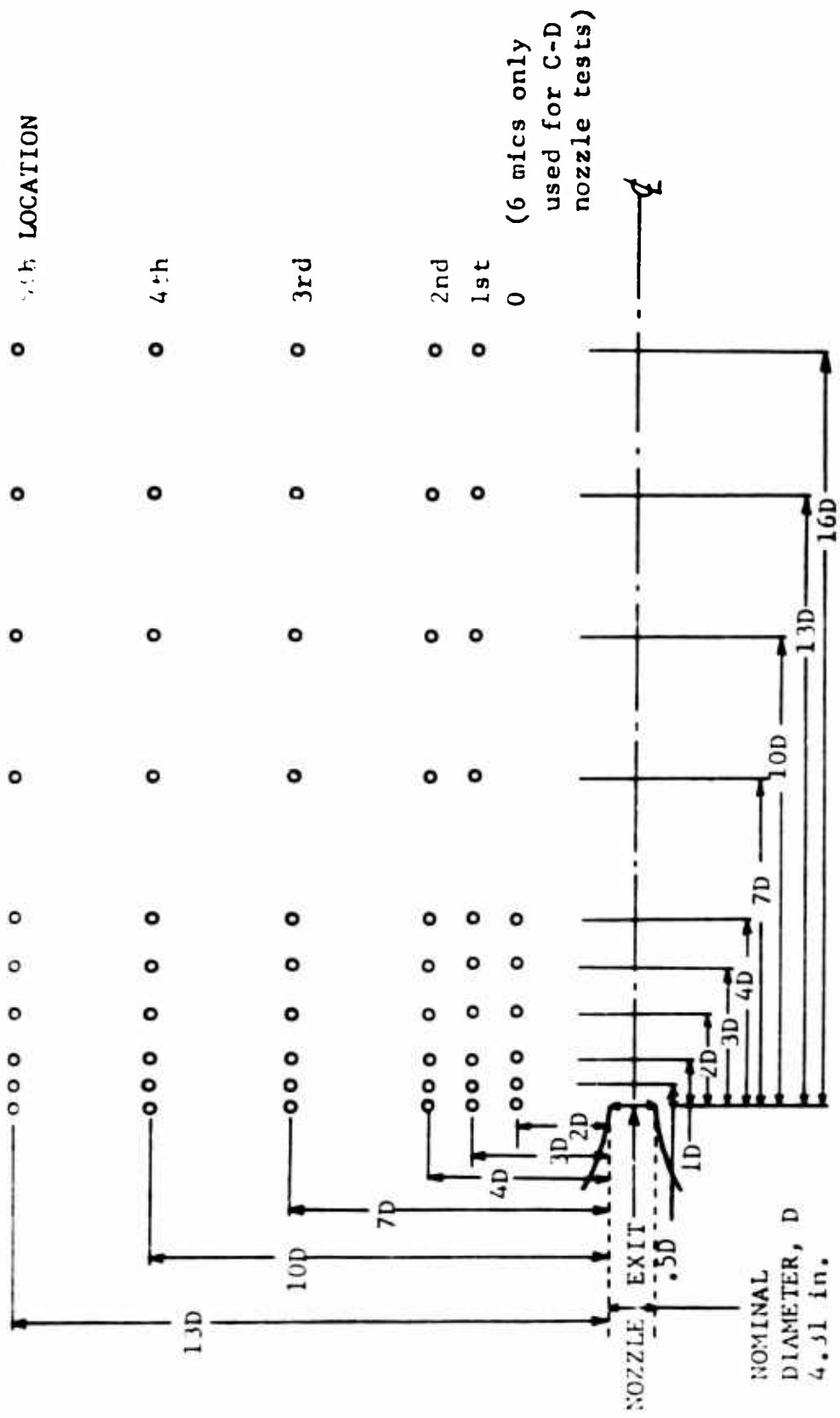


Figure 75 Microphone Array for Detailed Near-Field Acoustic Data

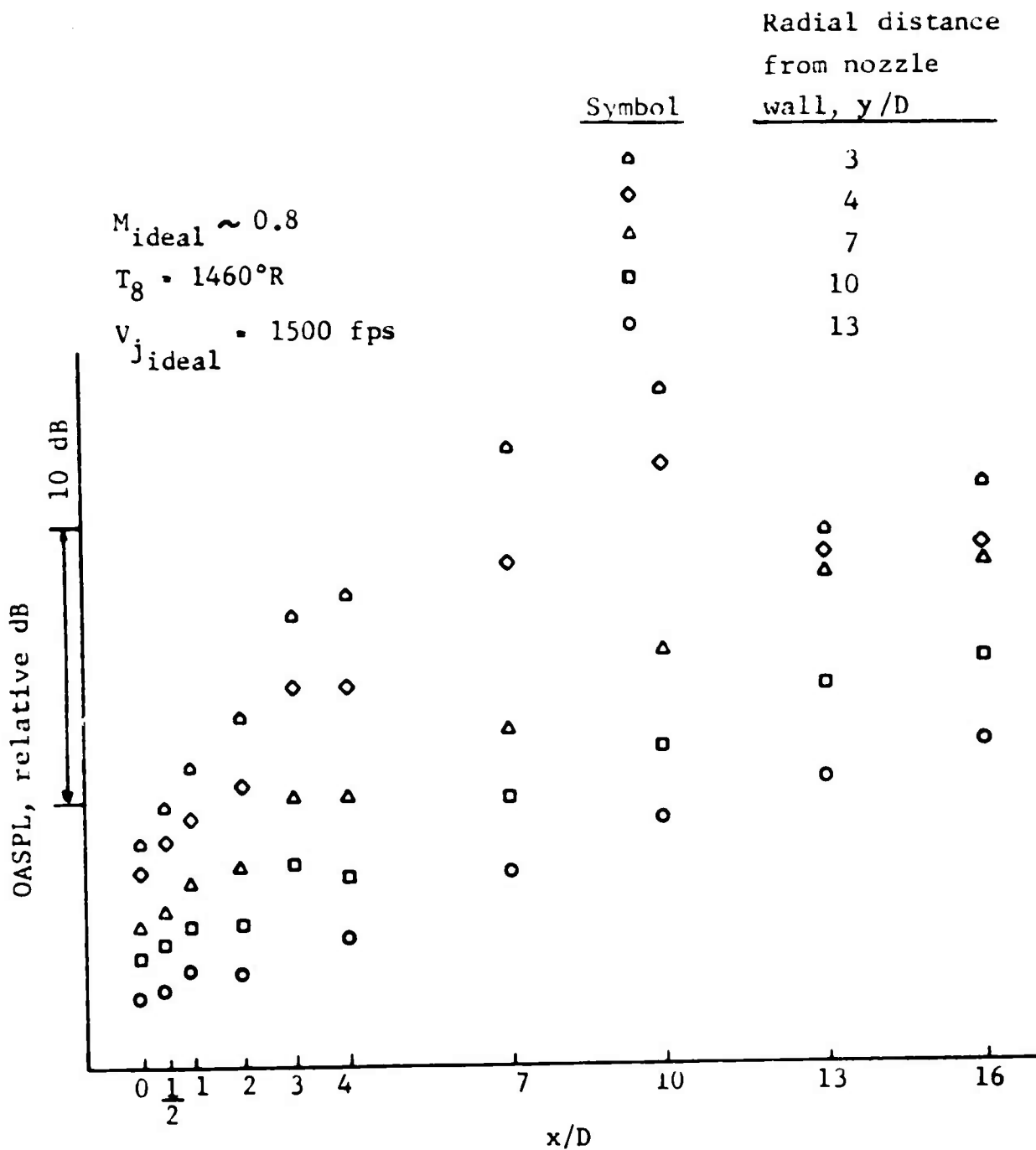


Figure 76 Variation of OASPL with Axial Distance from Nozzle Exit Plane at Different Radial Locations (4.31 in. Diameter Conical Nozzle)

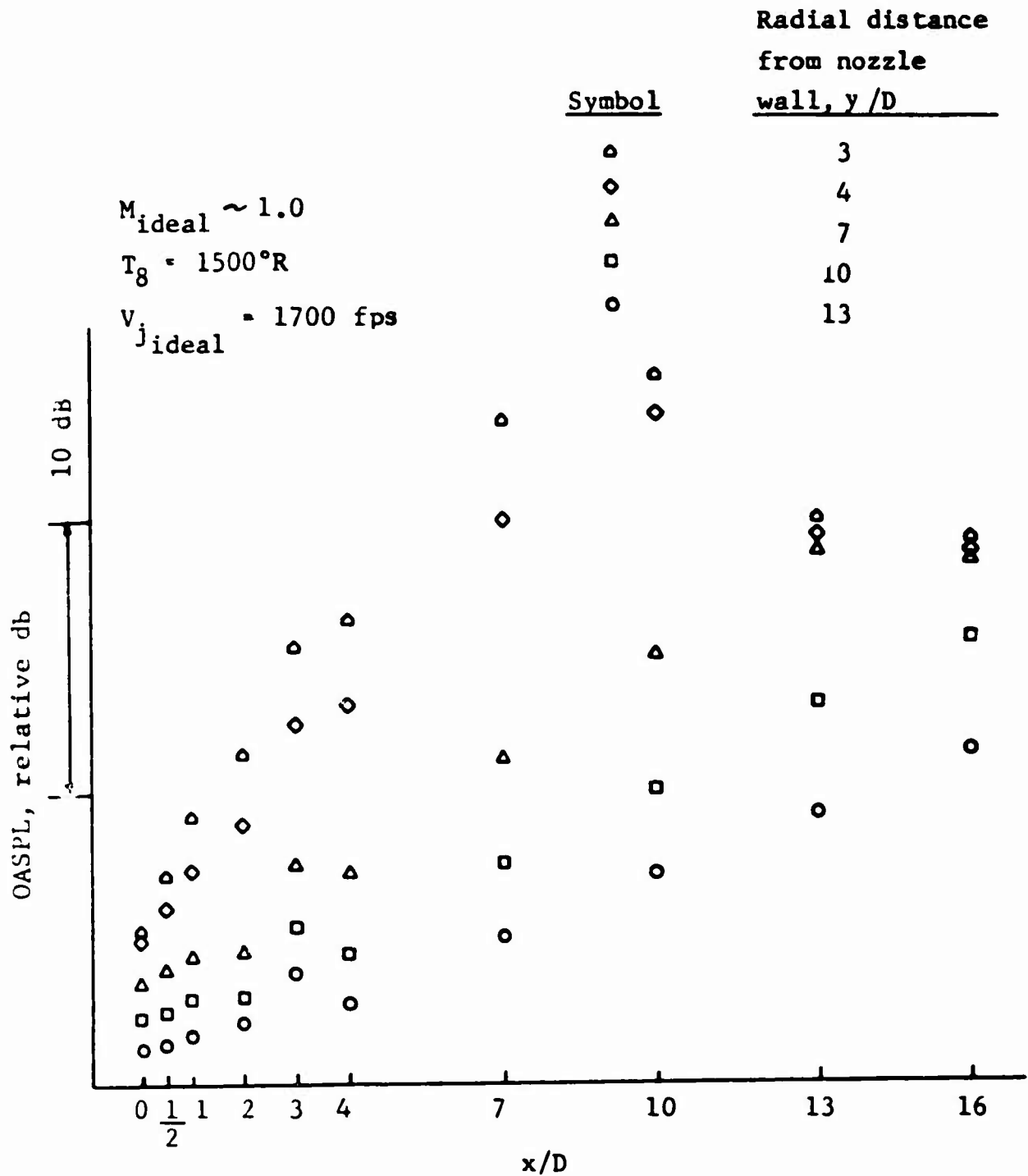


Figure 77 Variation of OASPL with Axial Distance from Nozzle Exit Plane at Different Radial Locations (4.31 in. Diameter Conical Nozzle)

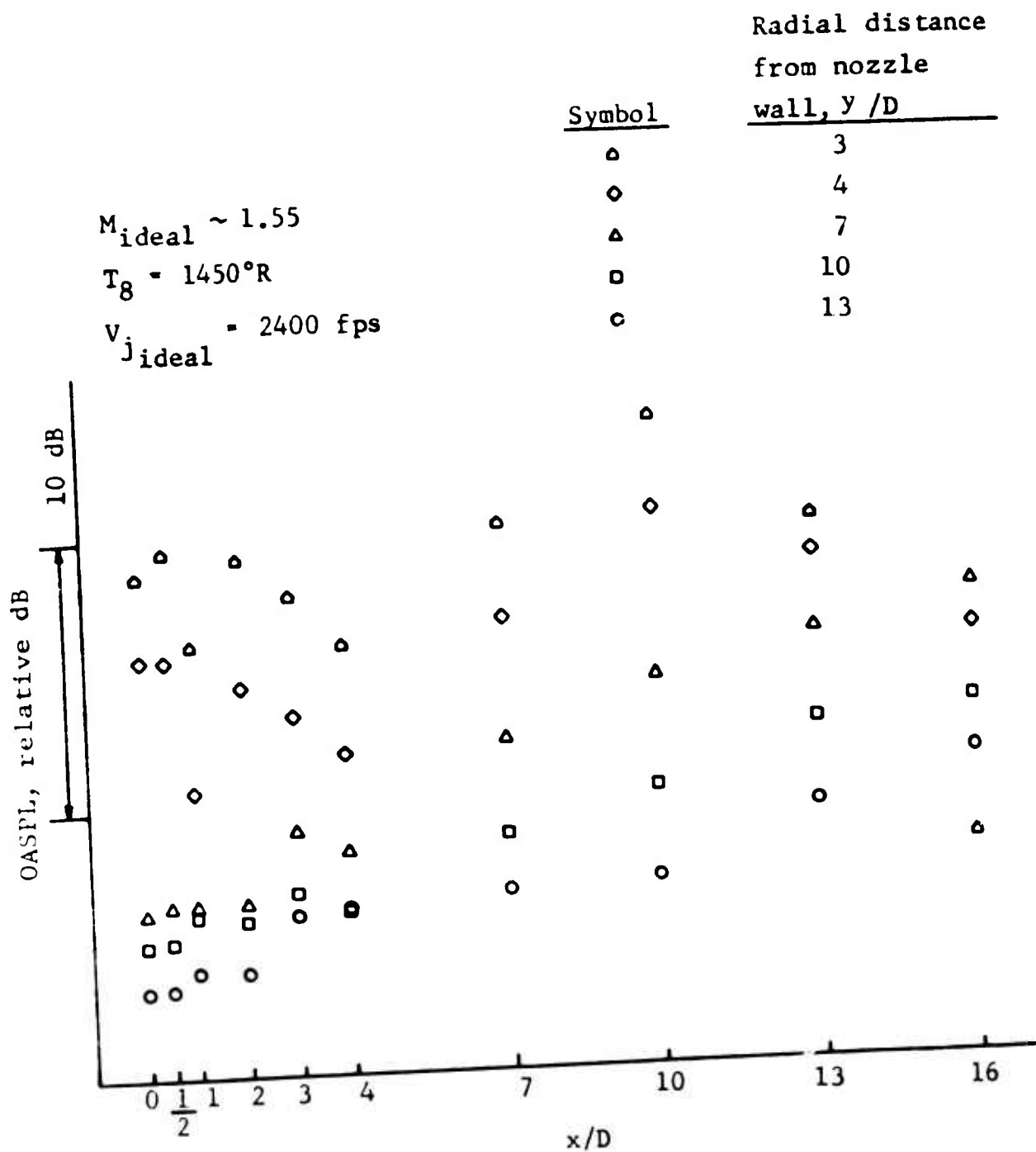


Figure 78 Variation of OASPL with Axial Distance from Nozzle Exit Plane at Different Radial Locations (4.31 in. Diameter Conical Nozzle)

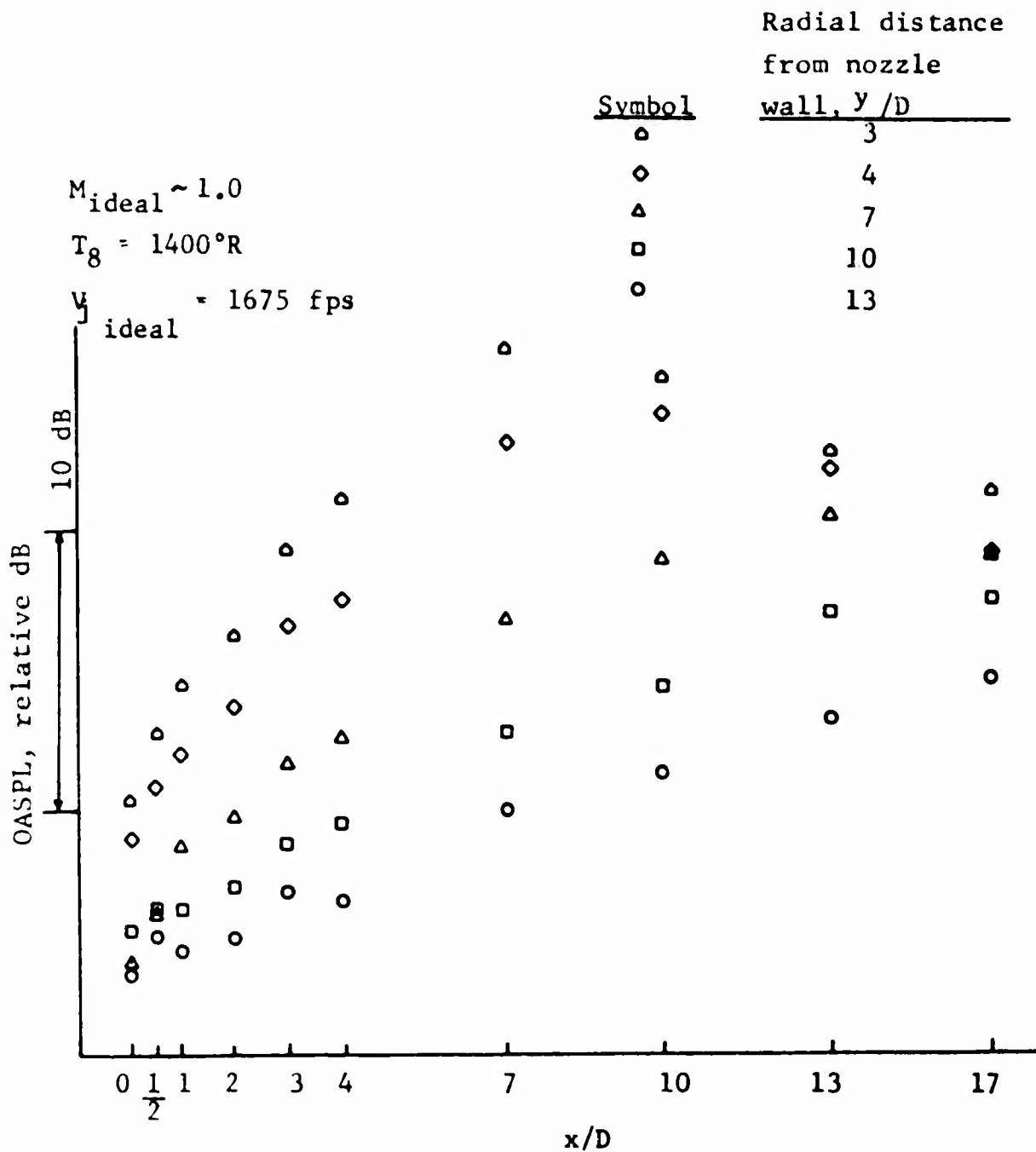


Figure 79 Variation of OASPL with Axial Distance from Nozzle Exit Plane at Different Radial Locations (4.31 in. Throat Diameter C/D Nozzle)

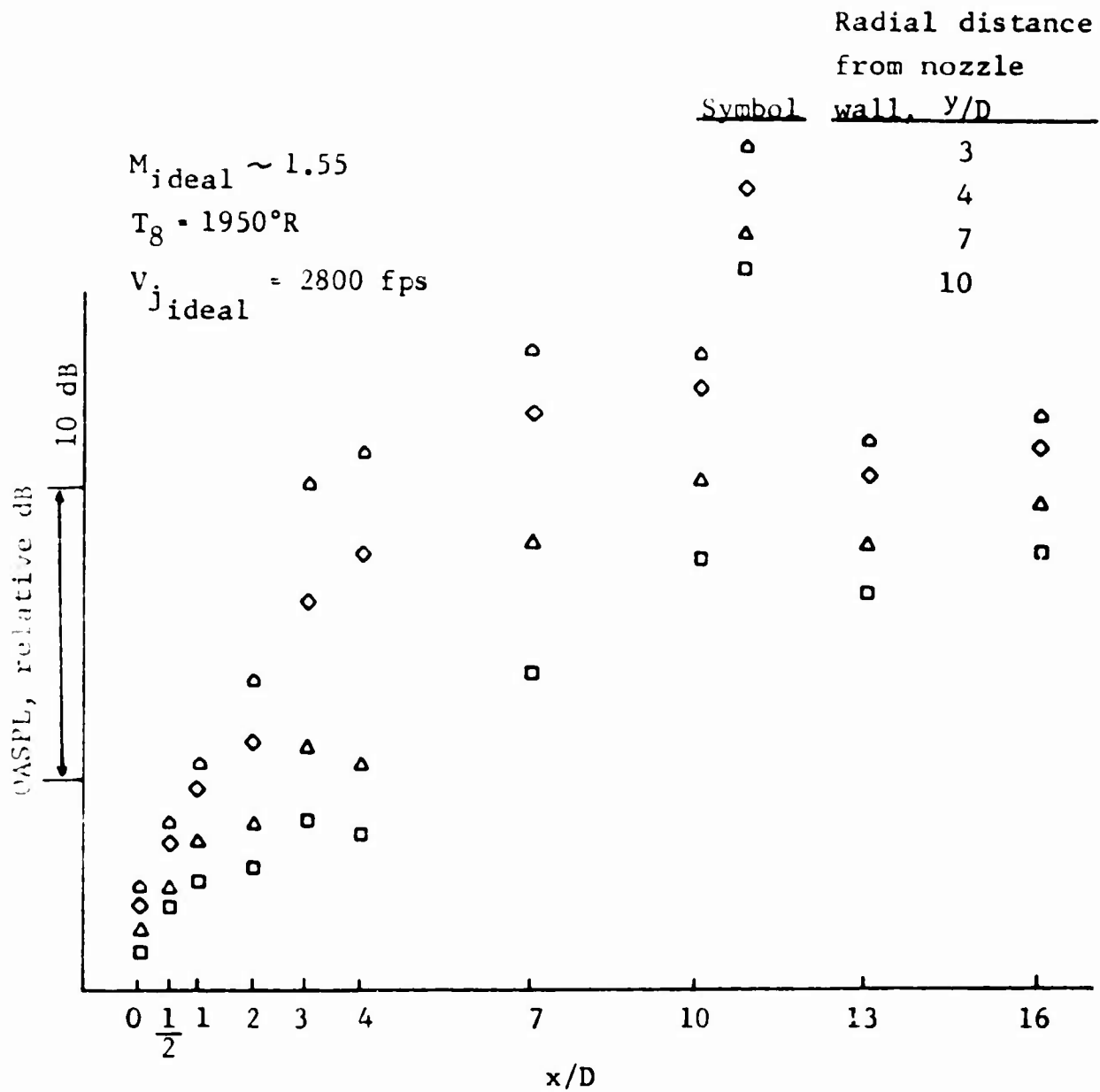


Figure 80 Variation of OASPL with Axial Distance from Nozzle Exit Plane at Different Radial Locations (4.31 in. Throat Diameter C/D Nozzle)

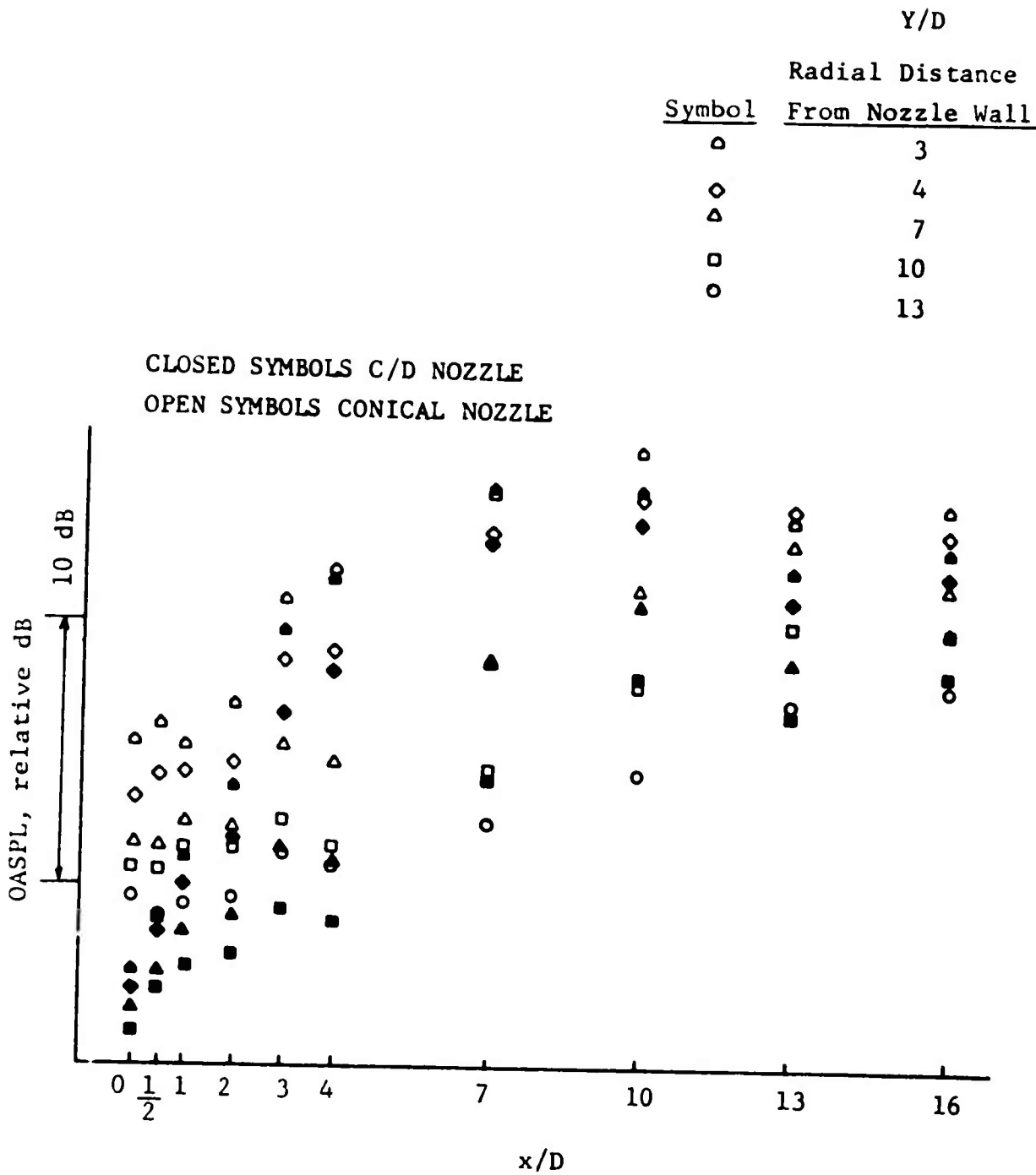


Figure 81 Comparison of OASPL vs. X/D Profiles for Conical and C/D Nozzles ($M = 1.55$, $V_j = 2800$ fps, $T_g = 2000^\circ R$)

$M_{ideal} = 1.55$
 $V_j = 2800 \text{ fps}$
 $T_j = 2000^\circ R$

○ CONICAL NOZZLE
 □ C/D NOZZLE

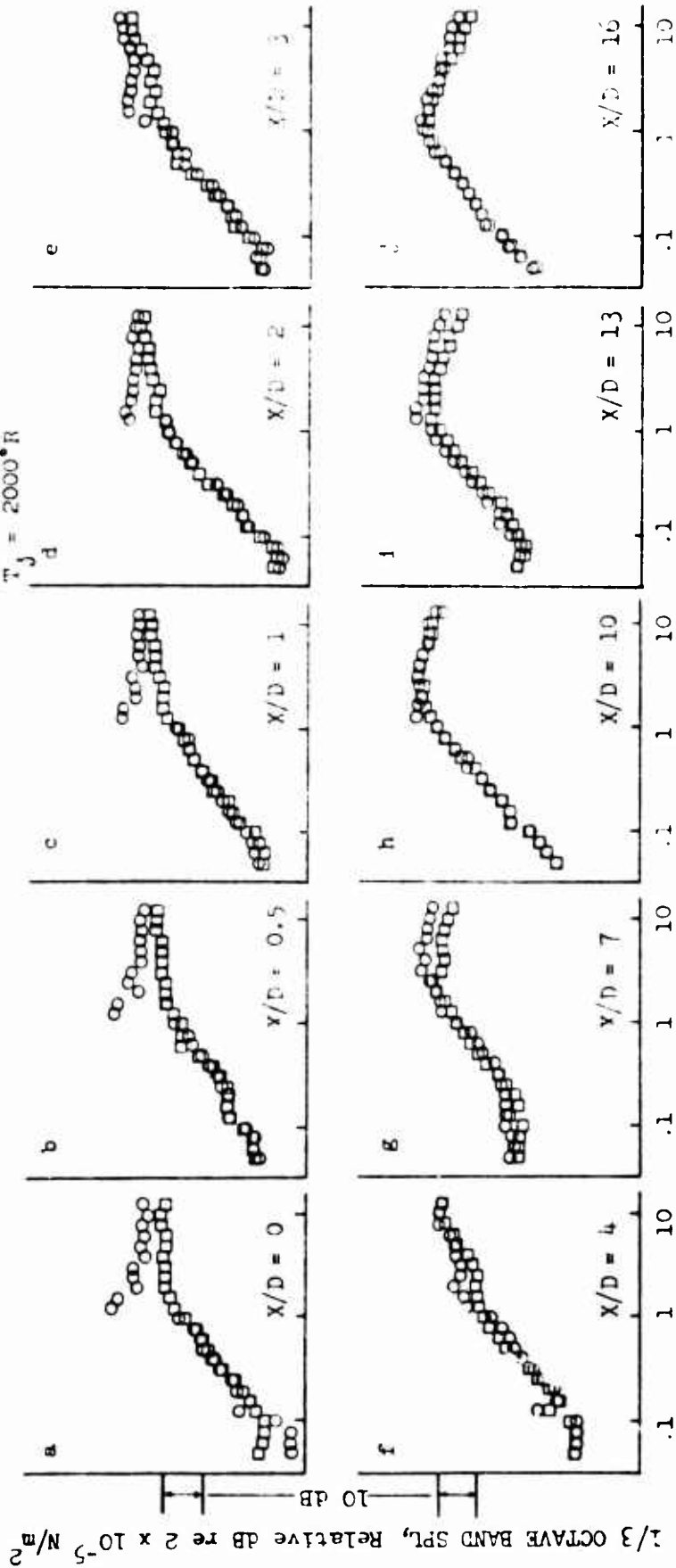


Figure 82 a-j 1/3 Octave Band Spectra from Conical & C/D Nozzles

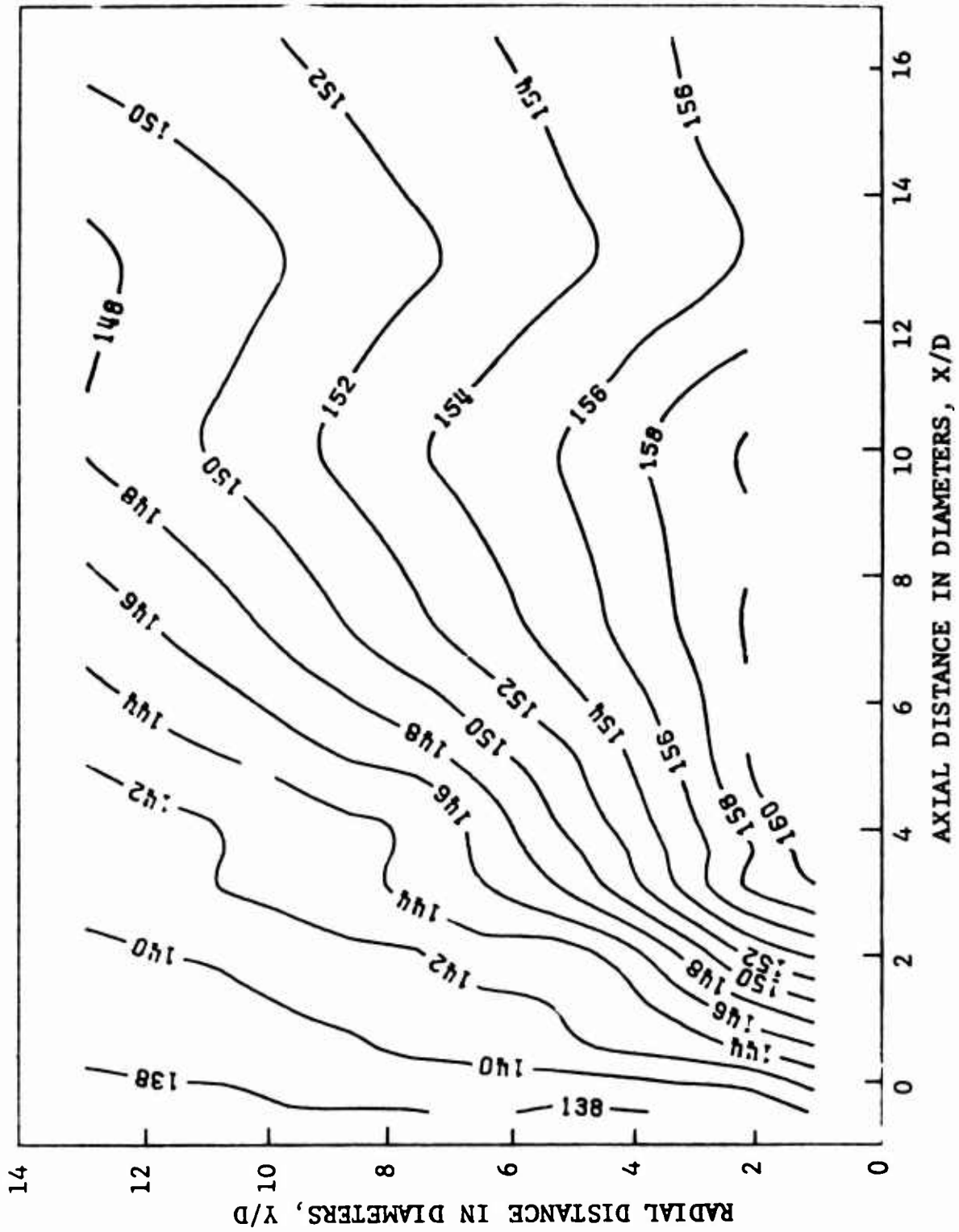


Figure 83 Overall Sound Pressure Level Contours: 4.31 in. Throat Diameter C/D Nozzle
 $V_j = 3100$ fps, $T_T = 2400^\circ R$

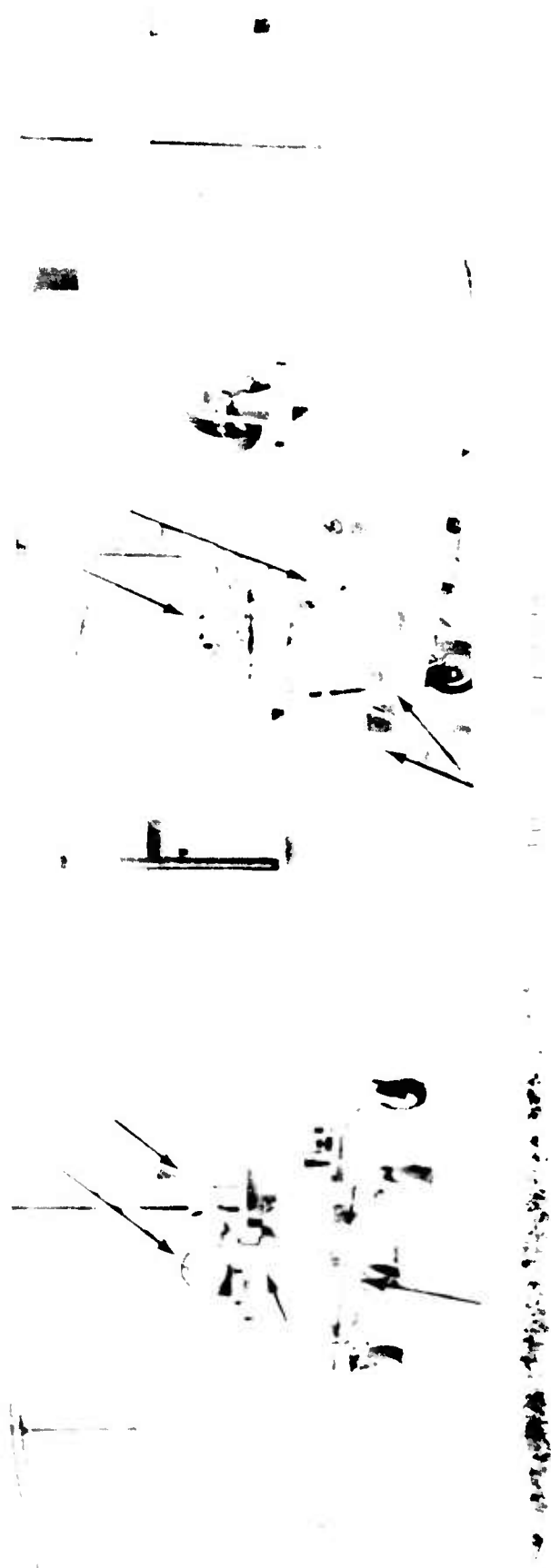


Figure 84 Simulated Setup for Schlieren System

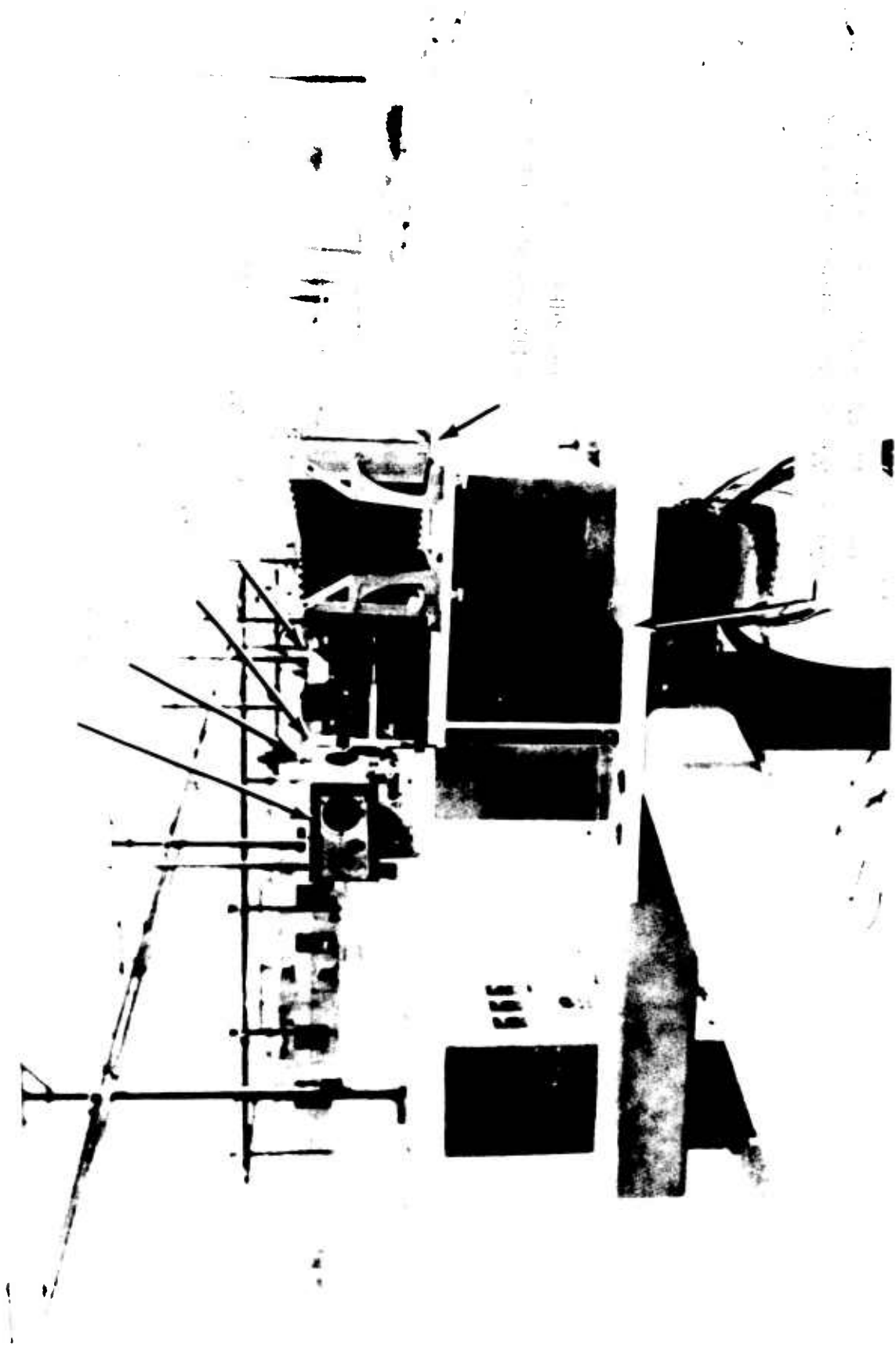


Figure 85 JEWOTS-Schlieren "Still" Photographic System

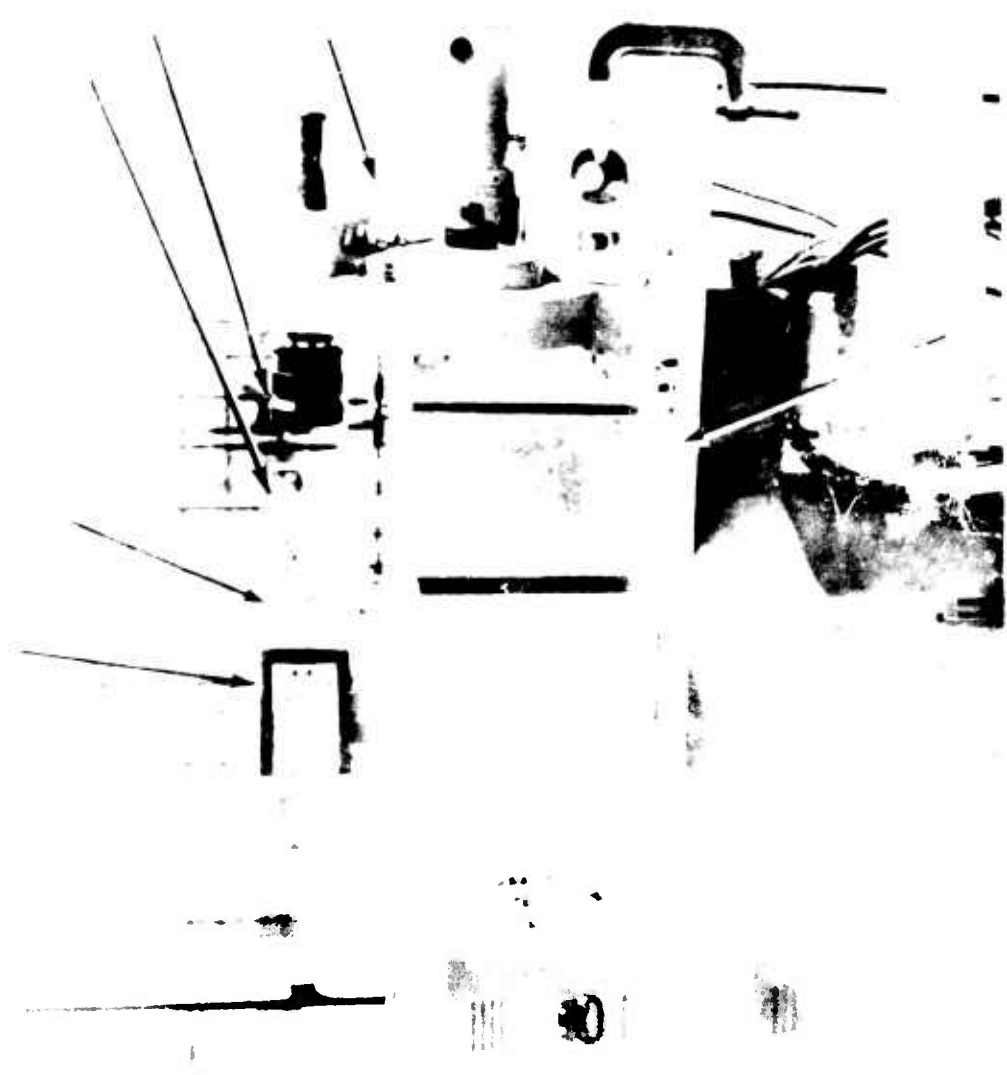


Figure 86 JENOTS-Schlieren "High-Speed" Movie System

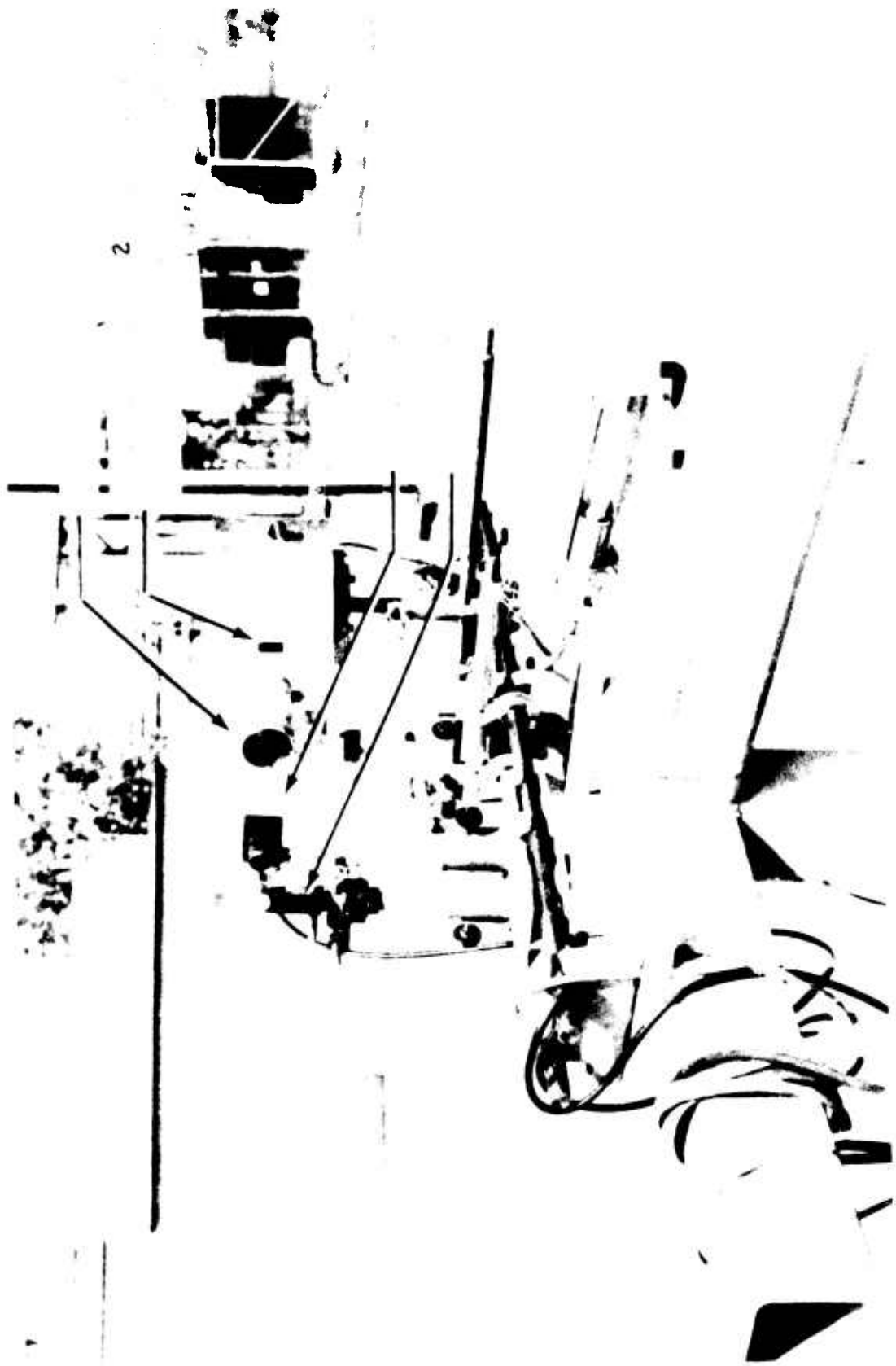


Figure 87 JENOTS-Schlieren Light Source Systems Setup for Still Flash Pictures

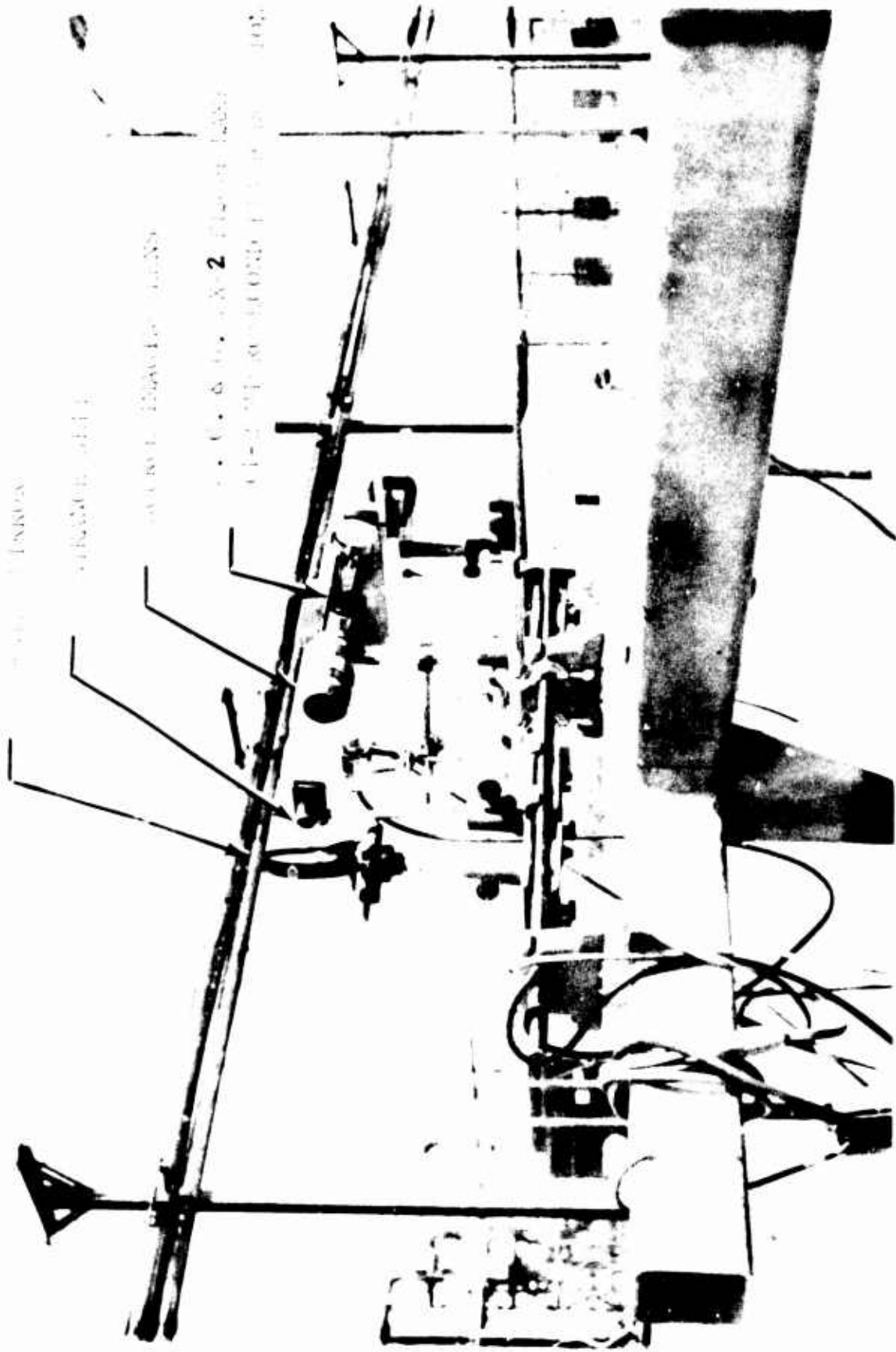


Figure 88 JENOTS-Schlieren Light Source Systems - Setup for High-Speed Movies

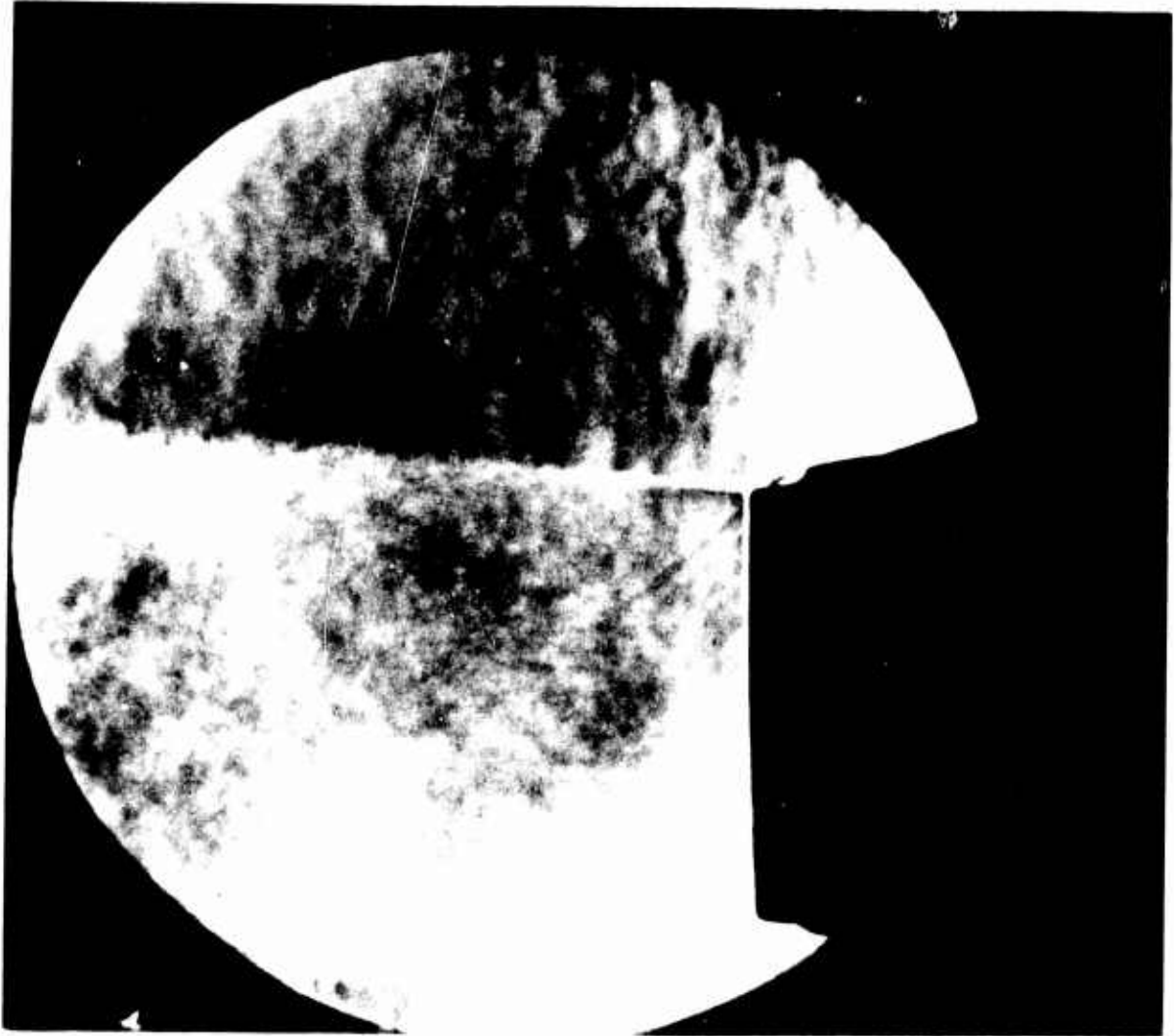


Figure 89 Schlieren Photograph of Shock Free Nozzle at Exit Plane

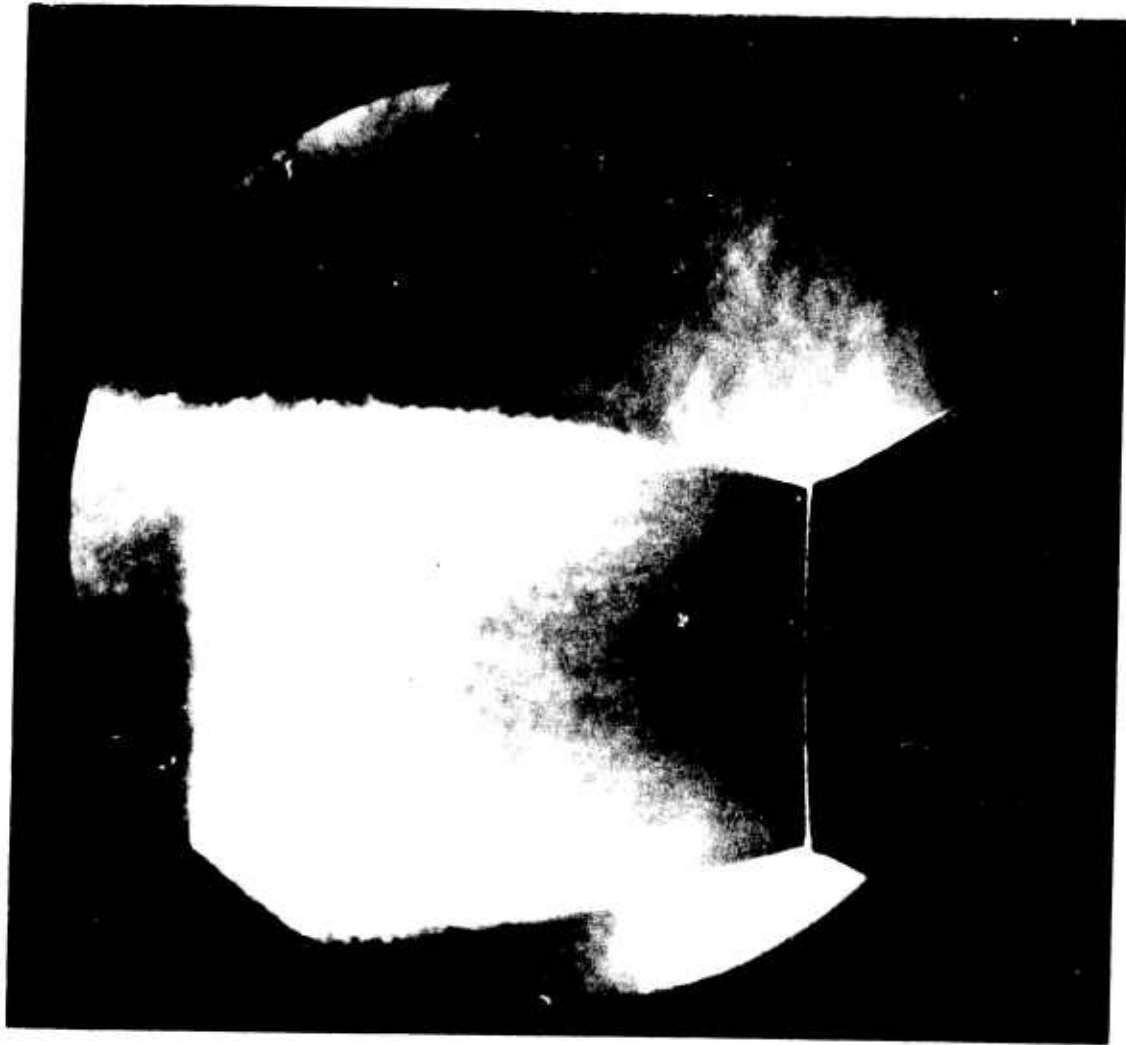


Figure 90 Schlieren Photograph of Thin Lip Conic Nozzle at Exit Plane

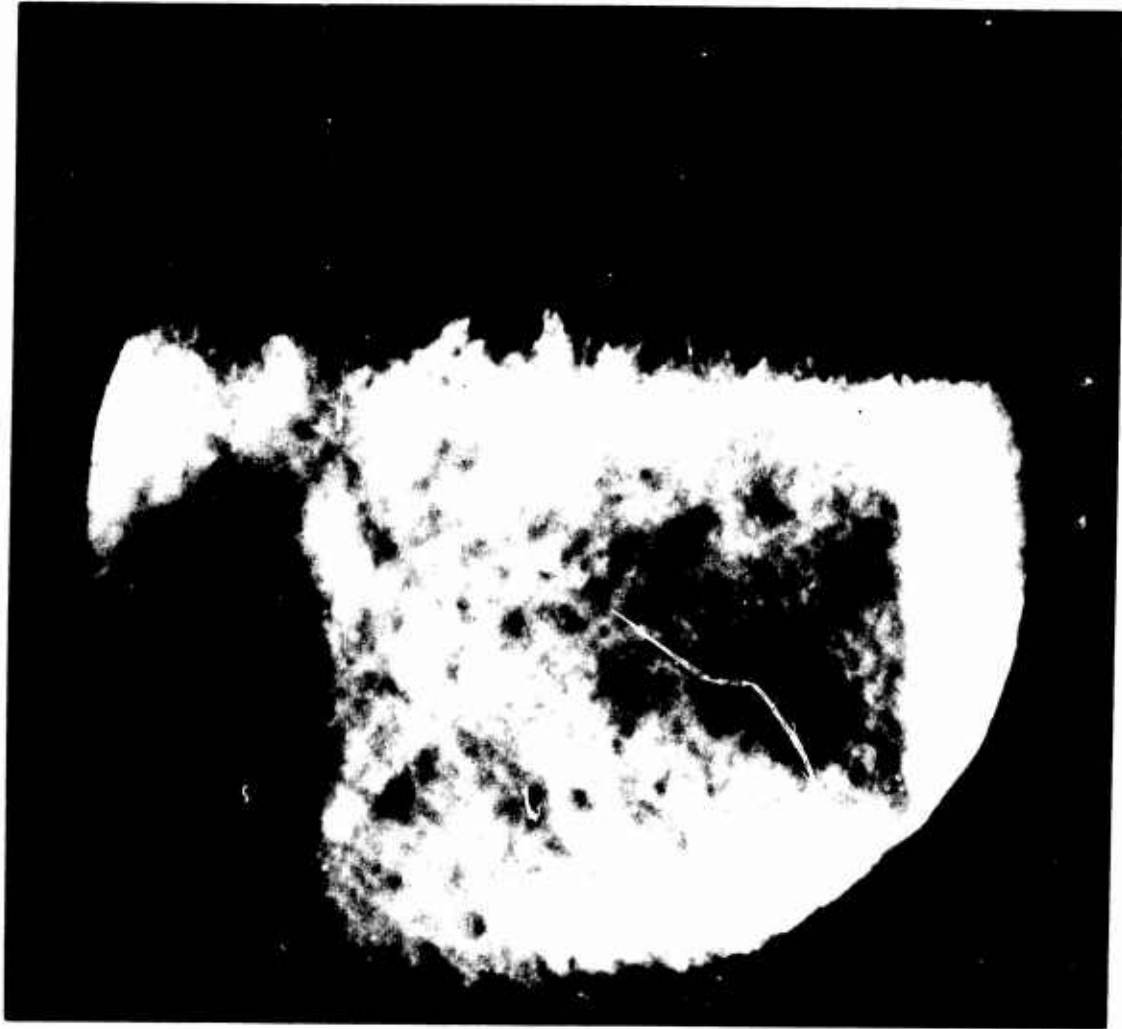


Figure 91 Schlieren Photograph of Thin Lip Conic Nozzle Downstream



Figure 92 Scalieren Photograph of Thick Lip Conic Nozzle at Exit Plane

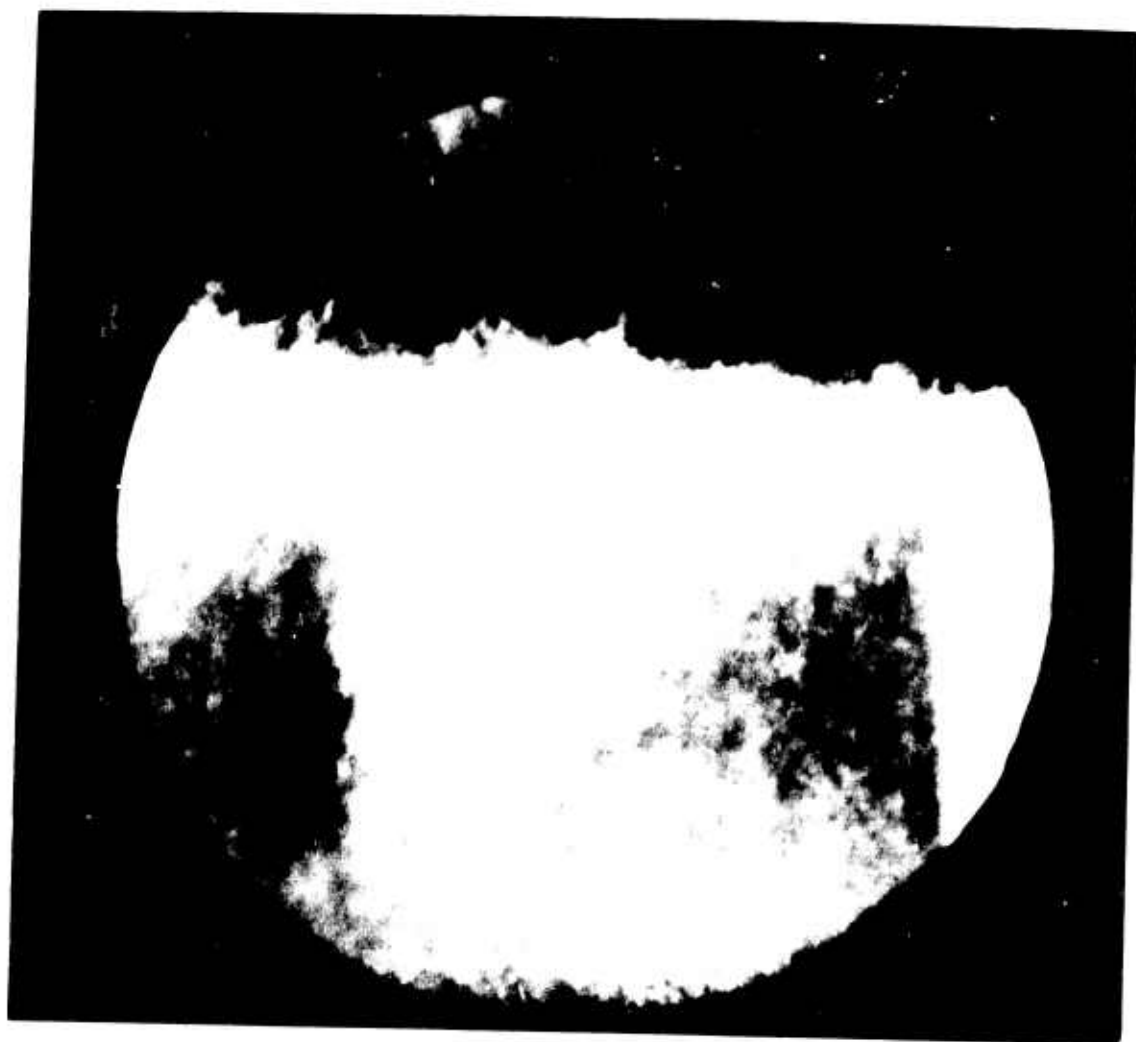


Figure 93 Schlieren Photograph of Thick Lip Conic Nozzle Downstream

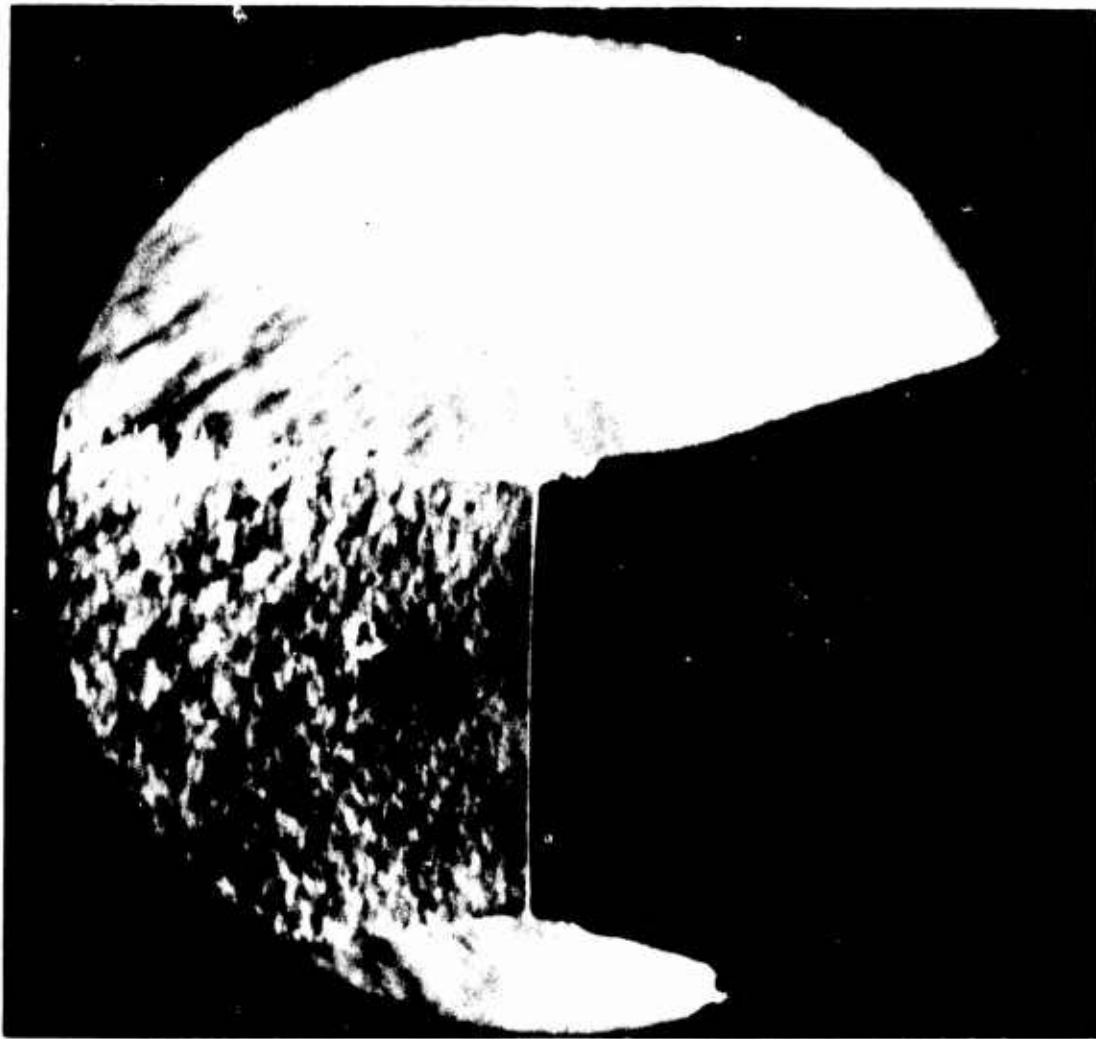


Figure 94 Spark Schlieren Photograph of Shock Free Nozzle at Exit Plane

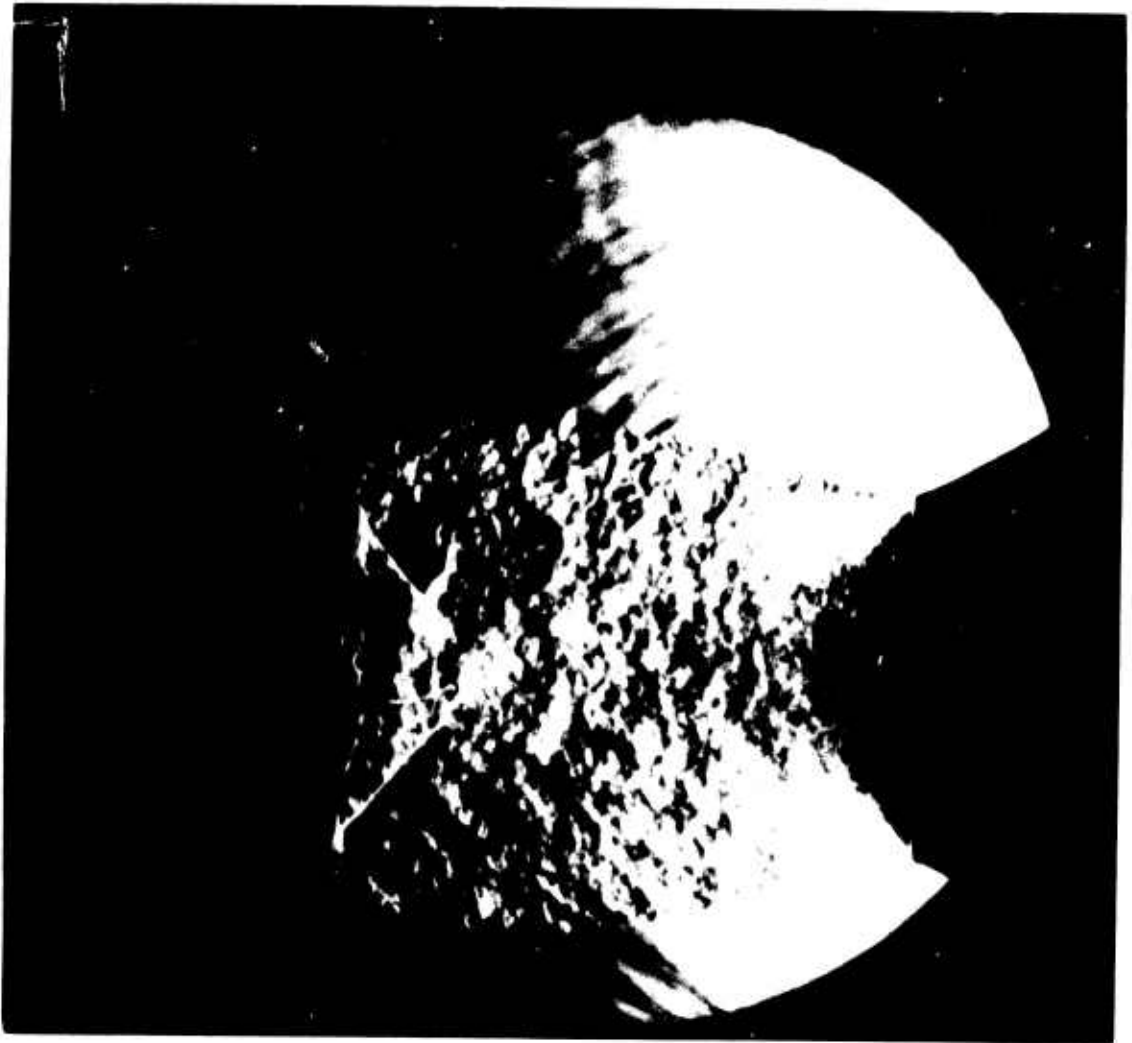


Figure 95 Spark Schlieren Photograph of Thin Lip Conic Nozzle at Exit Plane

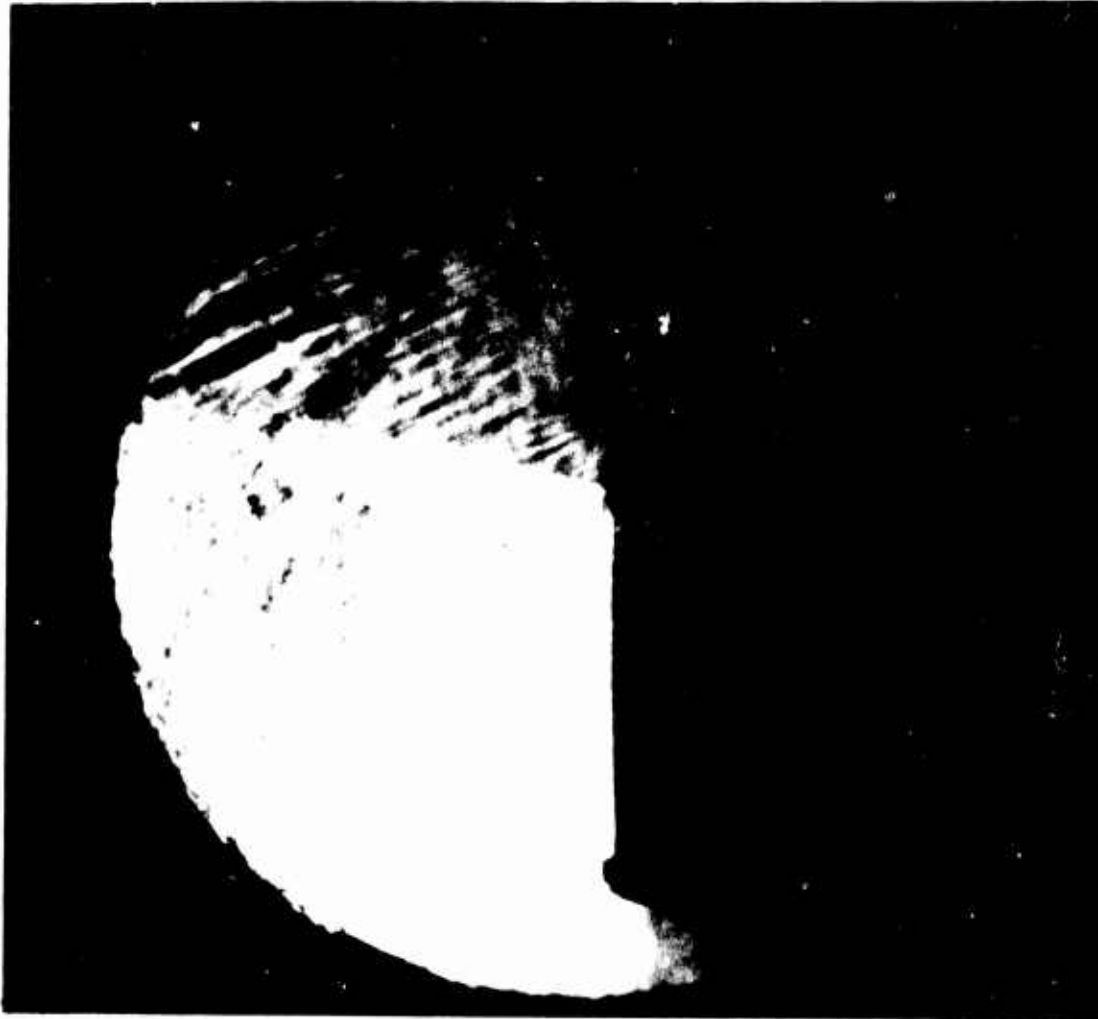


Figure 96 Spark Schlieren Photograph of Thick Lip Conic Nozzle at Exit Plane

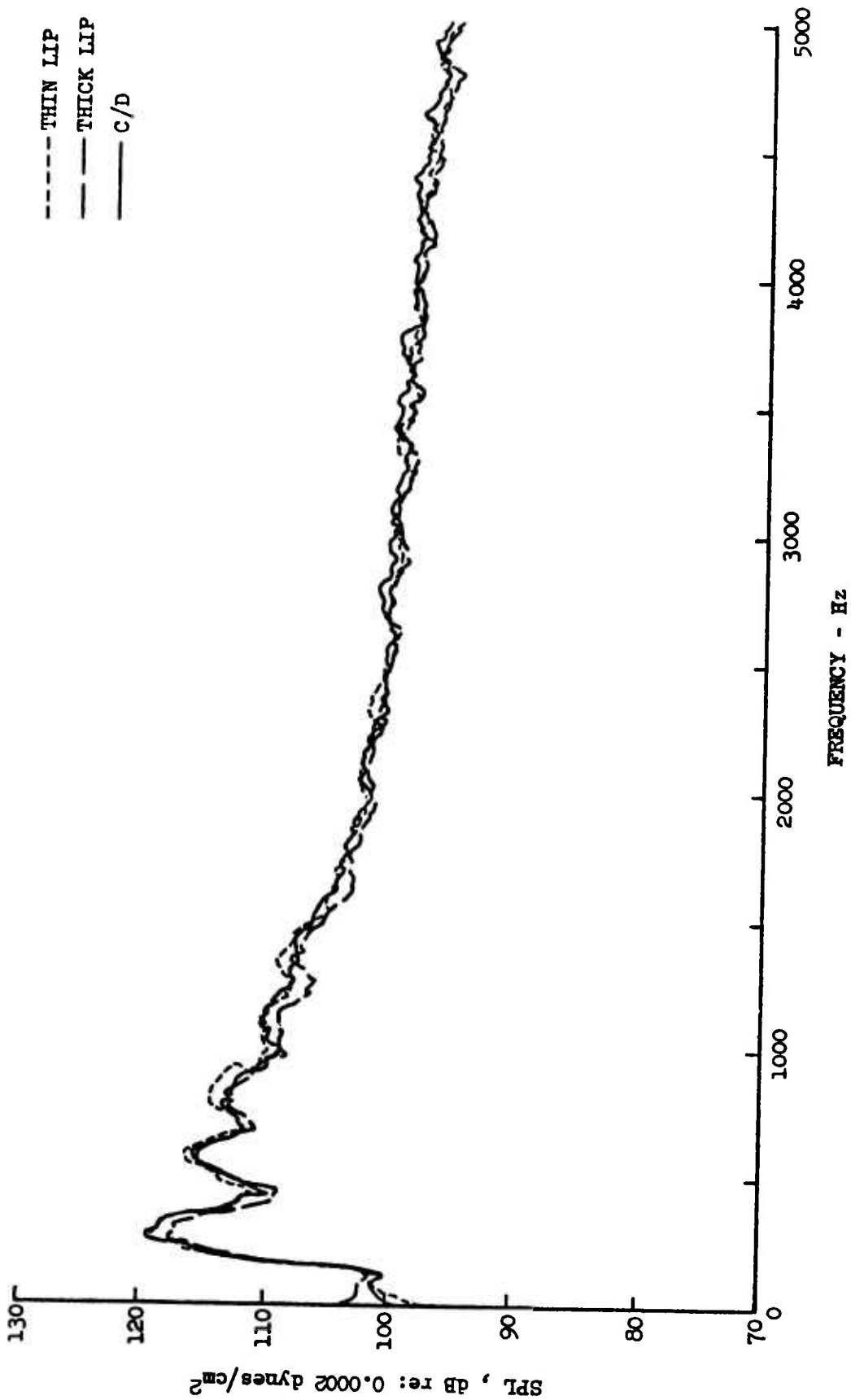


Figure 97 Far-Field Narrow Band Spectra Comparison of C/D and Conical Thin and Thick Lip Nozzles
 $\theta = 30^\circ$, $V_j = 2500$ fps, $T_T = 1400^\circ R$

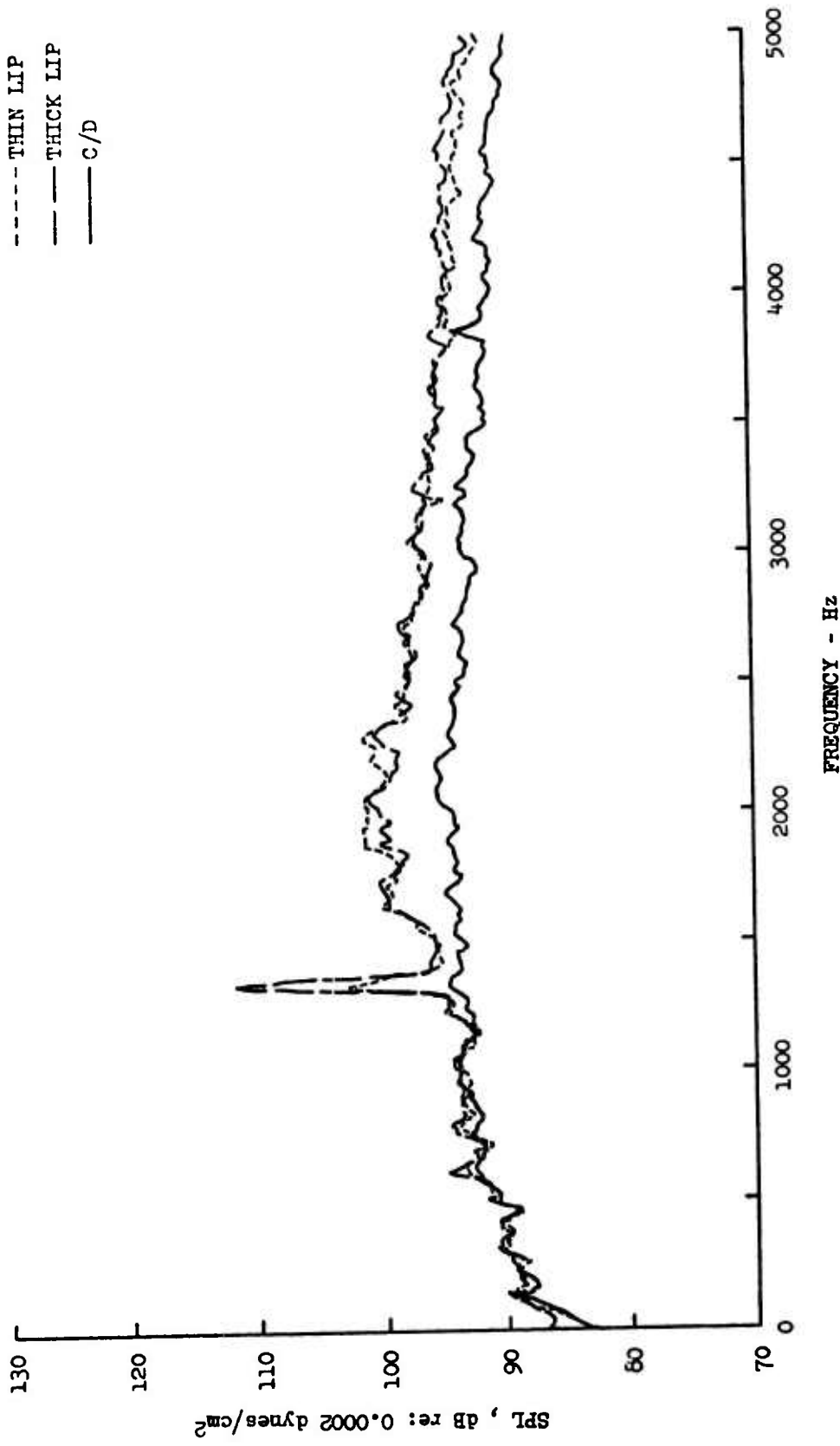


Figure 98 Far-Field Narrow Band Spectra Comparison of C/D and Conical Thin and Thick Lip Nozzles
 $\theta = 130^\circ$, $V_j = 2500\text{fps}$, $T_T = 1400^\circ\text{R}$

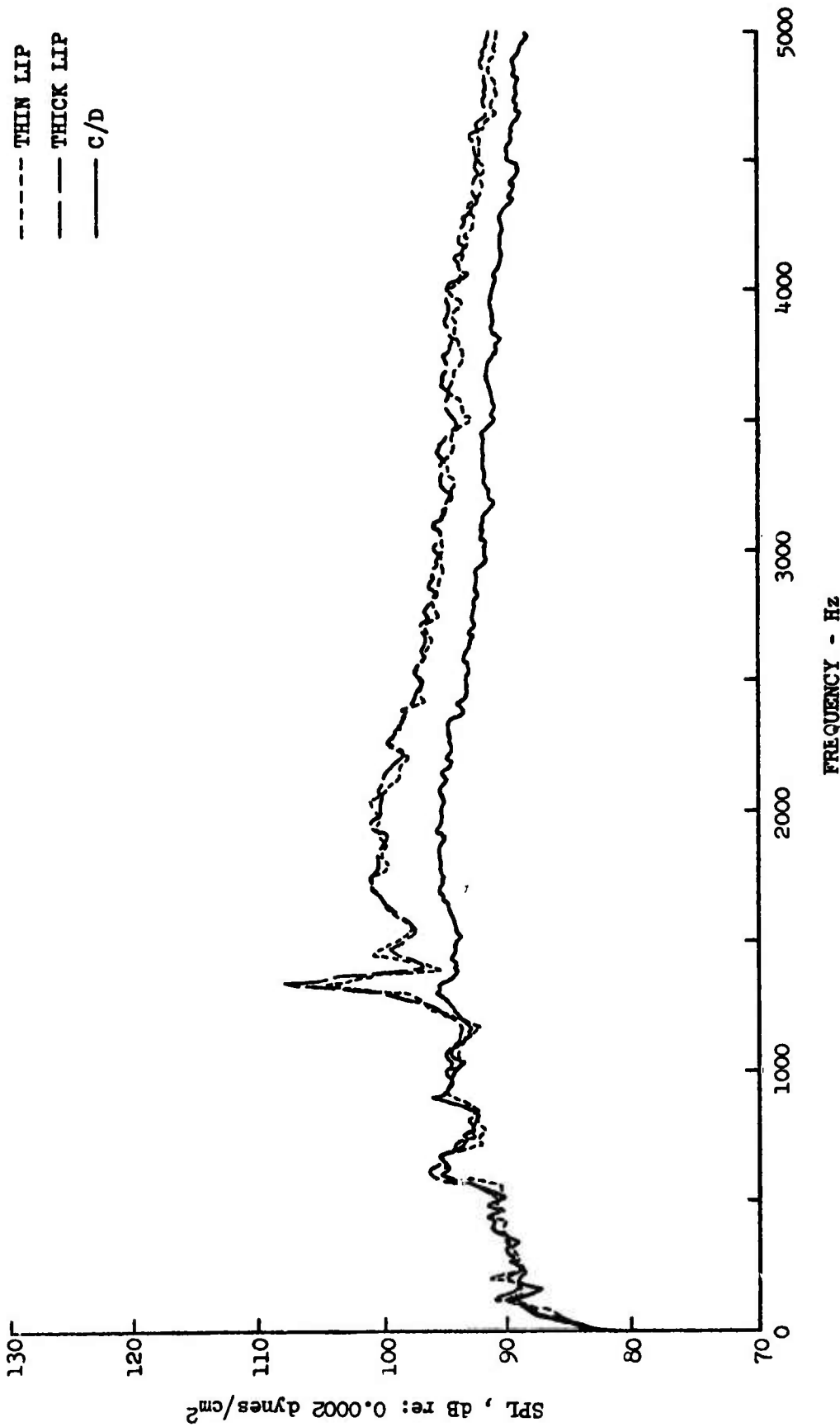


Figure 99 Far-Field Narrow Band Spectra Comparison of C/D and Conical Thin and Thick Lip Nozzles
 $\theta = 140^\circ$, $V_j = 2500$ fps, $T_T = 1400^\circ R$

IV. IN-JET NOISE SOURCE LOCATION STUDIES

1.0 LASER VELOCIMETER DEVELOPMENTS

P. Scott, P. Mossey, P. Knott

1.1 Theoretical Analysis for Turbulent Spectra

A method has been developed for determining the turbulent spectra of hot and cold jets using the LV device. Due to the random arrival of the velocity information in the LV device, conventional spectrum analyzers could not be used. Thus special computational techniques and hardware had to be realized before successful hot and cold jet spectra could be obtained. Future work in the area of LV spectra analysis consists of finalizing the analysis procedures, improvement of the LV processor to tailor it to the requirements of spectra analysis, and construction of a laboratory LV spectra system.

The difficulty in obtaining spectra from the LV device arises from the fact that the velocity estimate available at its output is not continuous. Successive estimates of the velocity are only available when particles traverse the probe volume. Conventional spectra estimation techniques assume that all values of the input signal are known in the analysis interval. Such knowledge is not available at the LV output. The effects of this are easily shown. If we assume:

1. Particles arrive at the probe volume with equal probability (Poisson probability distribution) in each time interval.
2. The arrival of a particle at the probe volume is statistically independent of the value of the jet velocity at the probe volume, we may signify the LV output signal, $y(t)$, as the product of the time velocity $v(t)$, and a sampling sequence, $s(t)$, consisting of impulses occurring at the particle arrival times.

Thus our model for the LV output becomes

$$y(t) = v(t) s(t)$$

with auto correlation function

$$R_{yy}(\tau) = R_{vv}(\tau) R_{ss}(\tau).$$

This follows from the assumption of independence of particle arrival time and velocity value.

If the particles arrive in a completely random manner, but at constant rate, λ , then the arrivals constitute a Poisson process and we may write

$$R_{ss}(\tau) = \lambda \mu_0(\tau) + \lambda^2$$

Using the above and the Wiener relation which states that the auto-correlation function and spectrum and wide sense stationary process are Fourier transform pairs, we obtain

$$S_{yy}(\omega) = \lambda^2 S_{vv}(\omega) + \frac{\lambda}{2\pi} \int_{-\infty}^{\infty} S_{vy}(\mu) d\mu.$$

Thus the process at the output of the LV device is the sum of the original velocity spectrum and a noise term. If the noise term is large compared to the velocity spectrum this spectrum will be obliterated. The ratio of the spectrum to the noise term, D , is

$$D = 2\pi \lambda \frac{S_{vv}(\omega)}{\int_{-\infty}^{\infty} S_{vy}(\mu) d\mu}$$

From this, one sees that there are two ways to reduce the effects of the noise term; either analyze narrow band processes (which increases $S_{vv}(\omega) / \int_{-\infty}^{\infty} S_{vy}(\mu) d\mu$) or increase the mean sampling rate λ . For spectra from known turbulent jets, it may be shown that the mean sampling rate required is 10^2 to 10^6 times that achievable with the LV device. Thus it is impossible to obtain spectra from turbulent jets by conventional techniques.

1.2 Method for Obtaining Spectra

We are interested in determining the spectrum of the jet velocity and not the actual time history of the velocity at some point in the jet. Thus if we can determine a technique for obtaining spectra without reconstruction of the time history, the problem associated with conventional techniques may be circumvented. A method for doing this may be based on the fact that the spectrum of a signal contains information about how a point relates to its neighbors. The "exact" time at which this point occurs is unimportant, an assumption which

is required if a signal is to have a unique, singly dimensioned spectrum. If the jet velocity is sampled in such a way that information about the adjacent relationships is not lost then there will be sufficient information in the sampled signal to reconstruct the original spectrum. We will develop a method for performing the reconstruction, stating in a more rigorous fashion the constraints on the sampling sequence. We will then present a model for the sampling sequence corresponding to particle arrivals in the LV device and show that it has the required properties.

The spectrum estimator may be derived one first considers the auto-correlation function of the sampled process. If $y(t)$ is the process available at the output of the LV device, we may model it as the product of a sampling sequence, $s(t)$, consisting of impulses at the sampling (particle arrival) times and $v(t)$, the original velocity signal. We will assume that $v(t)$ and $s(t)$ are statistically independent so that if

$$y(t) = s(t) v(t)$$

then

$$R_{yy}(\tau) = R_{ss}(\tau) R_{vv}(\tau)$$

where the $R(\tau)$'s are the appropriate auto correlation functions. This equation suggests a method for determining $R_{vv}(\tau)$, if we write

$$R_{vv}(\tau) = \frac{R_{yy}(\tau)}{R_{ss}(\tau)} .$$

We may determine $R_{vv}(\tau)$ if

$$R_{ss}(\tau) \neq 0$$

in the region of interest. This is the basic restriction on the sampling sequence. It can be shown that this is equivalent to stating that $s(t)$ must contain samples

τ apart for all required values of τ . Knowledge of $R_{VV}(\tau)$ allows us to determine the velocity spectrum $S_{VV}(\omega)$ by the Weiner relation.

$$S_{VV}(\omega) = \int_{-\infty}^{\infty} R_{VV}(\tau) e^{-i\omega\tau} d\tau$$

i.e. the auto-correlation function and spectrum of a signal are Fourier transform pairs.

We are now faced with the problem of determining $R_{yy}(\tau)$ and $R_{SS}(\tau)$. To facilitate this, we will change our measure of τ from continuous to a finite grid, so that

$$\tau \rightarrow nT$$

where T , a constant, is the grid spacing. The impulses of our sampling sequence, $s(t)$, will become pulses with width T and height $1/T$ (to preserve an area of one). These pulses will occur at times nT with a finite probability, P . We will assume that T is so small that $v(t)$ is constant in these intervals. Thus

$$y(t_0) \cong y(nT)$$

for

$$(n - 1/2) T \leq t_0 < (n + 1/2) T.$$

To estimate $R_{yy}(nT)$, we will use the conventional

$$\hat{R}_{yy}(n) = \frac{1}{M} \sum_{i=1}^M y(iT) y((i+n)T)$$

where for convenience we will assume the availability of $2M$ values of $y(i)$.

To determine $\hat{R}_{SS}(n)$, we observe that

$$\begin{aligned} R_{SS}(n) &= E \{s(i) s(i+n)\} \\ &= \sum_{s(i)=0}^1 \sum_{s(i+n)=0}^1 \frac{s(i) s(i+n)}{T^2} P\{S(i) = \frac{s(i)}{T}, S(i+n) = \frac{s(i+n)}{T}\} \end{aligned}$$

or

$$R_{ss}(n) = \frac{1}{T^2} P\{S(i) = \frac{1}{T}, S(i+n) = \frac{1}{T}\}.$$

We will use the last equality to estimate $R_{ss}(n)$ by writing

$$\hat{R}_{ss}(n) = \frac{1}{T^2} \hat{P}\{S(i) = \frac{1}{T}, S(i+n) = \frac{1}{T}\}$$

We now substitute the conventional estimate of $P\{S(i) = \frac{1}{T}, S(i+n) = \frac{1}{T}\}$, to obtain

$$\hat{R}_{ss}(n) = \frac{L(n)}{T^2 M}$$

where $L(n)$ is the number of times there is a sample pair n apart after observing M successive positions in the record. We combine these two estimates to obtain

$$\hat{R}_{vv}(n) = T^2 \sum_{i=1}^M y(i) y(i+n) / L(n)$$

In examining the sum above we note that $M - L(n)$ of the terms will be zero, corresponding to the positions where $s(i) = 0$, $s(i+n) = 0$ or both. Thus we may sum only the non-zero terms so that

$$\hat{R}_{vv}(n) = T^2 \sum_{i=1}^{L(n)} y(i) y(i+n) / L(n)$$

What the above equation says is "sum all the product pairs which occur in the sampled data at lag n and divide by the number of pairs summed": i.e., determine the sample mean of the $v(i) v(i+n)$ product for each lag n . This is easily related to the definition of the auto-correlation function as the expected value of $v(i) v(i+n)$.

In determining the spectrum of a turbolet jet we use the above to estimate the auto-correlation function on a fine grid. We then use the techniques of Blackman & Tukey¹ and Parzen² to take the weighted, discrete Fourier transform to obtain the spectrum estimate.

1.3 Error Analysis

In the previous section we have developed a method for estimating the auto-correlation function of velocity turbulence data obtained with a laser velocimeter. This estimate, under the assumption of an infinitely fine time grid, is bias free, i.e.:

$$E \left\{ \frac{\sum_{i=1}^M X_i X_{i+n}}{M} \right\} = \frac{\sum E \{X_i X_{i+n}\}}{M} = R_{xx}(n)$$

The introduction of a finite width time grid, however, introduces two bias errors. The reason for these errors may be seen by examining Figure 100.

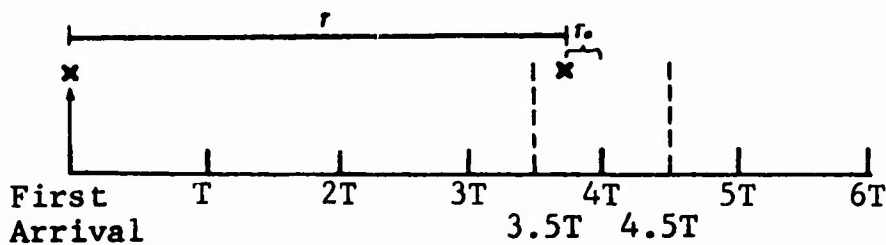


Figure 100

If the time between arrivals is measured in discrete intervals of length T , then our estimate of $R_{xx}(NT)$ really consists of the average of lag products $x(t)x(t+NT+\tau_0)$ where τ_0 is a random variable on interval

$$-T/2 \leq \tau_0 < T/2$$

These "jitters" in the lag of each product pair causes a bias error whose effect may be estimated using the techniques of Balakrishnan.³ This analysis appears as Appendix IV-1. It is shown that if the jitters have nearly the same density function then:

1. The spectrum is weighted by the characteristics function of the jitter's probability density.
2. This weighted spectrum will then be aliased about frequency which is the reciprocal of the grid spacing.

3. Differences in the jitter density function from interval to interval cause additional biases to be added to the spectrum these terms disappear at $f = 0$, and increase with frequency.

Experiment shows that the grid spacing for turbulent velocity spectra measurement should be at least a fifth of what would be chosen as the Nyquist spacing in convention "sample data" analysis. In the system used at General Electric a factor of one tenth was used.

One may wonder why an equally spaced grid used if it introduces these errors. We use it because:

- 1) It is required to get a finite probability of arrival for products at a given lag value.
- 2) It allows the use of the FFT in performing the spectrum calculation which makes this computation tractable in a small computer.
- 3) It allows the use of all of the arriving product pairs.

We will now consider the other parameters affecting the spectrum estimate. It is useful, since aliasing occurs about the grid interval, to consider the spectrum in the Z-domain here the grid interval is used as the sampling interval. If we define f_d as the frequency above which there is no significant power, then at one tenth grid spacing, the grid width, T , should be:

$$T = \frac{1}{20 f_d}$$

For turbulence spectra f_d is assumed to be 20 kHz so that for our system

$$T = 2.5 \times 10^{-6} \text{ sec.}$$

On the unit circle in the Z-domain, we have:

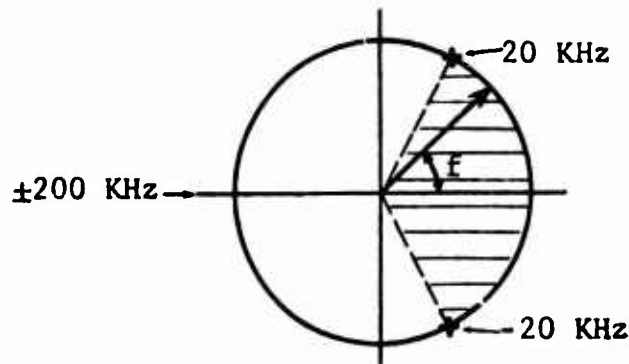


Figure 101

Hence we are only interested in determining the spectrum on the corresponding to the pie shaped shaded region in Figure 101. Let us now consider the bandwidth of the analysis. This is determined by the length (total number of lags computed) of the auto-correlation function (a.c.f.) and the "window" used in the spectrum estimate. The window function^{1,2} is used to reduce undesirable effects induced by the finite a.c.f. length. The window function used in the General Electric system is attributed to Parzen.² The bandwidth of the spectrum analysis may be shown to be³

$$BW_{3 \text{ dB}} = \frac{\mu}{(m-1)T}$$

where μ is a function of the window ($\mu \sim 1.4$ for Parzen), and m is the number of lags computed. If a bandwidth of about 100 Hz is required then a value of $m = 5120 = 512 \times 10$ may be used. Thus we must calculate 5120 averaged lag products to obtain a spectrum with 100 Hz. Band width. The spectrum may be calculated by taking the discrete Fourier transform of the weighted auto-correlation function. One way of doing this would be to use an FFT routine on a 5120 point block. Computation time and computer storage may be reduced if we compute the transform output points only over the segment shaded in Figure 101. It may easily shown that:

$$\hat{S}(\omega) = T \sum_{\ell=0}^{M-1} [F^R (2 R_{XX}((\ell + kN)T) \cdot \cos(\omega \ell T) - F^I (2 R_{XX}((\ell + kN)T) \cdot \sin(\omega \ell T))] - TR_{XX}(0)$$

where F^R and F^I are the real and imaginary parts of an m point FFT routine. In our case, $N = 10$, $M = 512$ and $\omega(J) = 2\pi(J)/NMT$ where T is the grid spacing.

The auto-correlation function and spectra equations were implemented in a combination of machine language and Fortran on a PDP8/E mini-computer. This machine is equipped with 8K bytes of core memory and two Dectape magnetic tape drives. A TZ digital interface was designed to link the laser velocimeter processor to the computer. This interface also measures the arrival time between successive particles and provides sixteen words of buffer memory. This high speed memory is required because the arrival time between successive particles can be faster than the computer's ability to absorb the data (even though the computer mean data read rate is considerably faster than the mean particle arrival rate). Analysis shows that the 16 word memory should overflow less than one in one billion arrivals if the mean particle arrival rate is less than 20 KHZ. A display scope was also interfaced to the computer and software was written to allow the display of the turbulence spectrum and auto-correlation function together with the sampling auto-correlation function, and the interarrival and velocity amplitude histograms.

1.4 Experimental Set-Up Used for Laser Velocimeter Turbulent Spectra and RMS Turbulent Plume Surveys

1.4.1 The Laser Velocimeter Arrangement

The arrangement used was similar to that of the 1971 A.F. Program as reported in AFAPL-TR-72-52 Chapter V⁴. The details of that report will not be repeated here. Instead, changes or new features and improvements will be described that have been used in this current reporting period. The basic optics system used was again the differential Doppler, backscatter, single package arrangement that has the proven feature of ruggedness for our rather severe environment. A substantial improvement in temperature stability of the optics alignment was made (on an internal G.E. Program) that also allowed greater range without sacrificing spacial resolution of the measurement volume. Figure 102 shows a schematic arrangement of the laser package used on this program. The laser beams no longer are coaxial with the receiving lens, but instead are projected from below the lens, forming an angle, α , that keeps the major axis of the control volume ellipsoid to a minimum. Compare this

figure to Figure V-B-4 (page 550) of the AFAPL-TR-72-52. The dimensions of the control volume are: major axis 0.25 inch, minor axis 0.020 inch. The range has been extended from 40 inches to 85 inches (fixed, as before). The extension has allowed backing off the package by 45 inches from the jet and the acoustic protection enclosure as used in 1971 is no longer necessary. The three steering mirrors and the beam splitter were remounted on adjustable supports, all the same aluminum alloy, and this eliminated the temperature-alignment problem seen in 1971 when we used some brass and stainless steel pieces. Figure 103 shows the Laser Velocimeter setup at GE's JENOTS facility.

The range extension to 85" brought about two problems, however. The first of these is the increased sensitivity to temperature gradients in the air intervening between the package and the sensitive volume. This has caused a small decrease in accepted data rate in cold weather where convection gradients occur right at the front of the package, where the laser beams emerge.

The data rate was estimated to drop by 20% to 30% when the outdoor temperature was 25° F. The package temperature is usually held to 60 to 80° F by a thermostat.

The second problem encountered in the range extension is that of a reduction in the return light power. This reduction in return light power is because a 6-inch diameter lens is being used at a greater distance (smaller solid angle of light collection). This reduction in light power collected was partly compensated for by increasing the electrical gain of the photomultiplier through use of higher supply voltage. This resulted, however, in greater shot (light quantum) noise reaching the LV processor. As a result, the percentage of laser Doppler bursts validated dropped by perhaps a factor of two.

1.4.2 Actuator and Seeding

A remotely actuated platform was again used but this time on all three axes: vertical, horizontal and axial. Travel capabilities were 32, 32, and 240 inches, respectively, all remote read-out. Resolution was $\pm 1/16$ inch for each axis, except the last 208 inches of the axial: $\pm 1/8$ inch.

Seeding was by injection of AL_2O_3 powder, nominal 1 micron diameter, into the supply air to the burner and also into the region of the nozzle, so as to seed the entrained air. The power feeder equipment used was as reported in AFAPL-TR-72-52 Chapter V section 3, except that the fluidized bed column supply air was heated to about 250° F to prevent power aggregation by moisture absorption.

1.4.3 Signal Processing and Recording

The laser velocimeter signal processor used was the G.E. developed direct-counter (time domain) type similar to that reported in AFAPL-TR-72-52 Chapter V, but with some improvements made during 1973 on a G.E. internal program. These improvements resulted in a lowered rate of false validations and improved linearity and resolution. The recording of turbulent velocity probability distributions (histograms) was again by the NS633 Pulse Height Analyzer, 256 Channel, dumped into an X-Y plotter. The recording of spectra was by the same equipment as used as discussed in Subsection 1.5.

1.5 Laser Velocimeter Turbulent Spectra Measurements

In the above subsection descriptions of the analysis and laser equipment used for estimating turbulent spectra were given. Described here are a set of demonstration experiments performed to measure the longitudinal component of turbulence spectra in the exhaust plume of a 4.3 inch diameter convergent nozzle (See Figure 54) at General Electric's JENOTS facility. Experiments were performed on a cold subsonic jet and in a sonic heated jet. These tests were performed in late December of 1973 and are preliminary.

1.5.1 Cold Jet LV Turbulence Spectra Results

The conical nozzle was set at $M_j = 0.5$, $T_g = \text{ambient}$. The location of the laser velocimeter measuring volume was at an $x/d = 6$, $r/r_o = 1$. Figure 104 shows the measured autocorrelation function and the interparticle-arrival histogram. Figure 105 shows the constructed histogram. The LV estimated turbulence spectrum for this jet using the analysis of Section 1.1 is shown on Figure 106. Also shown on Figure 106 is a hot film spectrum taken on the same jet at the same location. The agreement between the Laser Velocimeter

results analyzed to-date were for a limited data sample. The limited data sample is expected to give a larger variance at the high frequencies. To reduce the variance at the high frequencies, more data product pairs of the data samples will be processed.

1.5.2 Hot Jet LV Turbulence Spectra Results

Figures 107 to 109 illustrate LV measurements for a sonic jet ($V_j \sim 1500$ fps) with total temperature at 1500° R. The LV was set at $X/D = 10$, $r/r_0 = 0$, and was measuring the longitudinal component of turbulence. Figure 107 shows the constructed autocorrelation function for the heated high velocity jet. Figure 108 shows the constructed histogram, and Figure 109 shows the LV measured turbulence velocity spectrum. There are no other measuring devices that can measure the turbulence velocity spectra in this type of environment, and therefore, no comparisons will be available. As was indicated with the cold jet turbulent measurements the higher frequency data is expected to be in some error due to the limited data sample analyzed. Currently more data product pairs of the data samples are being processed to reduce the variance at the high frequencies and these results will be reported on at a later date.

The above results demonstrate the feasibility of using the laser velocimeter to construct turbulent velocity spectra in realistic exhaust jet environments. In addition to performing measurements on an ambient temperature $M_j = 0.5$ jet, turbulent velocity measurements were performed on a high temperature, high velocity jet. The laser velocimeter system used to perform the measurements is one which can be used for small or for the large model scale tests as performed above, or on an actual jet engine nozzle. These preliminary tests are a prelude to demonstration experiments planned for in-jet noise source location studies at hot supersonic exhaust jets.

1.6 Laser Velocimeter Jet Plume Surveys

As part of the development and evaluation of the laser velocimeter as a useful non-contact aero-acoustic probe, extensive surveys of the mean velocity and turbulent rms velocity characteristics were performed on subsonic and supersonic shock free and shocked hot jet exhaust plumes. Nearly 1000 data points

were taken. At the time of this writing the bulk of this data is being processed for data analysis. Reported here are some comparisons of LV measured flow properties with measurements taken with a hot film anemometer for a Mach 0.5 cold jet. Preliminary LV results are also shown illustrating the mean and turbulent flow characteristics of a shock-free ($M_j = 1.55$) heated ($T_T \sim 1500^\circ \text{R}$) jet.

The nozzles tested were the 4.3-inch convergent conical nozzle (See Figure 54) and the 4.3 inch throat diameter convergent-divergent nozzle (Figure 55). The laser velocimeter system used the one described in subsection 1.4. The comparison hot film anemometer probe for the cold jet test was a Thermo Systems model 1210. Figure 110 shows the arrangement used for the hot film measurements. An extension beam was attached to the automatic LV traversing cart so that accuracy of probe location could be obtained.

1.6.1 Cold Jet Laser Velocimeter/Hot Film Measurements

1.6.1.1 Axial Variation of Mean Velocity

Figure 111 shows the axial variation distribution of the centerline mean velocity as measured by the laser velocimeter and the hot film anemometer. For reference purposes hot wire measurements of Wooldridge and Wooten⁵ at $M_j = 0.3$ are shown as a solid triangle. The LV/Hot film/hot wire comparisons as seen to be in good agreement. The results show that the mean velocity in the core began to decrease at an axial location of $X/R = 6$. Between $X/D = 6$ and 15 the flow undergoes a complicated readjustment toward that of a self similar region.

1.6.1.2 Radial Variation of Mean Velocity

A mean velocity profile comparison between the laser velocimeter and the hot film measurements is shown in Figure 112. The radial profile shown is at an axial of $X/D = 2$. This station was chosen so that the results of Wooldridge and Wooten could also be use as a comparison. Good agreement between the LV, hot film, and hot wire measurements is observed.

1.6.1.3 Axial Variation of Turbulence Intensity

Figure 113 shows comparisons between laser velocimeter measurements and hot film anemometer measurements for axial variations of turbulence intensity along the jet centerline and at the jet lip ($r/D = .5$). Wooldridge and Wooten's measurements are again shown for comparison purposes. The agreement between all three instruments is again found to be good. The centerline variation of turbulence intensity is seen to vary smoothly from a very low value at the exit to a peak value around an X/D of about 10. The lip region variation of turbulence intensity is seen to rapidly increase from a low value at the exit plane to a rather large value at $X/D \sim 2$. From $X/D \sim 2 \rightarrow 8$ the intensity levels appear rather uniform.

1.6.2 Hot Supersonic Jet Laser Velocimeter Measurements

1.6.2.1 Axial Variation of Mean Velocity

The axial variation distribution of the centerline mean velocity is shown in Figure 114. A uniform distribution is observed until about 10 diameters downstream. Thereafter the usual axial velocity decay is observed. These results are in agreement with what would be expected for a supersonic shock-free exhaust jet.

1.6.2.2 Radial Variation of Mean Velocity and Turbulent Intensity

Figure 115 illustrates the LV measured radial distribution of mean velocity and turbulent intensity of the $M_j = 1.55$, $T_T \sim 1500^\circ R$ shock free exhaust at an axial location of $X/D = 9.6$. The mean velocity distribution is as expected and the turbulence intensity profile shows a peak in turbulence intensity near the nozzle lip region ($r/D \sim .5$).

1.6.2.3 Axial Variation of Turbulence Intensity

The axial variations of the supersonic jet turbulence intensity along the jet centerline and the nozzle lip is shown in Figure 116. The centerline distribution shows a very gradual increase in the turbulence intensity level out to about ten diameters. Past the 10 diameter location an abrupt increase in level is observed. The nozzle lip axial variation of the turbulence level

is also seen to be more gradual than was observed for the cold subsonic jet results (Figure 113). A peak value is observed to occur between 10 to 12 diameters downstream.

The above comparison between General Electric's Laser Velocimeter, the hot film anamometer, and other published results have shown good agreement for mean velocity and turbulent intensity variations. Preliminary laser velocimeter measurements of mean velocity and turbulent intensity have been shown for a shock free ($M_j \sim 1.55$) high temperature ($T_T \sim 1500^\circ \text{R}$) jet. These results are a first of a kind type of measurements and more of the measurements that were taken on this jet will be reported at a future date. A number of other LV measurements have been obtained on cold subsonic and heated supersonic exhaust jet over a varied range of velocities (1000 \rightarrow 3000 fps) and temperatures (1000 $^\circ$ R \rightarrow 3000 $^\circ$ R). These results are currently being reduced and analyzed for future reporting. The above results and the turbulence spectrum results discussed in section 1.4 clearly demonstrate the General Electric's Laser Velocimeter as a viable non-contact type of measurement device capable of measuring the needed detailed fluid dynamic turbulent flow characteristics of high velocity high temperature jets necessary for performing noise source location type of experiments.

2. STATIC PRESSURE PROBE DEVELOPMENT FOR JET NOISE SOURCE CORRELATION STUDIES

R.A. Kantola, J.F.C. Wang

Recent research activity in the area of jet noise has been heavily involved in cross-correlation measurements. These have included correlations of the unsteady pressure and velocities in the jet plume to the far-field acoustic signal and in-jet two point correlations of pressure, and pressure and velocity. This work is aimed at extending the techniques to high speed flows, particularly the in-jet correlations and resolving the discrepancies reported in earlier investigations.

2.1 Theoretical Background

The analytical basis for the correlation technique has been well documented and will only be briefly presented here as a point of reference. The starting point for this is the "dilatation equation", which has been shown to be equivalent to Lighthill's original formulation using acoustic quadrupoles. This dilatation equation is given as:

$$\frac{1}{c_o^2} \frac{\partial^2 p^{(1)}}{\partial t^2} + \nabla^2 p^{(1)} = \frac{1}{c_o^2} \frac{\partial^2 p^{(0)}}{\partial t^2} \quad (1)$$

where $p^{(1)}$ = propagating part of the pressure and the non-propagating portion of the unsteady jet pressure, $p^{(0)}$, is defined as

$$p^{(0)} + p^{(1)} = p - p_o \quad (2)$$

where p = instantaneous static pressure

and p_o = average static pressure

The right side of equation 1 is viewed as a forcing function of the wave equation for the acoustic pressure $p^{(1)}$. This wave equation assumes that the propagation is taking place in still air, not in a jet flow, and, therefore, the effects of refraction and convection are not accounted for. For farfield microphones sufficiently far from the sources and for the origin of the coordinate system sufficiently close to the sources, equation 1 can be solved in terms of Kirchoff's retarded potentials as

$$p^{(1)}(x,t) = \frac{-1}{4\pi C_0^2 x} \int_{\text{volume}} \frac{\partial^2 p^{(0)}(\bar{y},t)}{\partial t^2} \Big|_{\hat{t}} d\bar{y}^3 \quad (3)$$

where X = microphone arc
 C_0 = isentropic wavespeed
 \bar{y} = source location
 \hat{t} = retarded time = $t - \frac{x}{C_0}$.

Now assuming that the far-field fluctuating static pressure $p(x,t)$ is represented by $p^{(1)}(x,t)$ and then multiplying both sides of equation 2 by $p(x,t)$ evaluated at a new time $t + \tau$, the result can then be time-averaged to yield

$$\overline{p(x,t)p(x,t+\tau)} = \frac{-1}{4\pi C_0^2 x} \int_{\text{volume}} \overline{\left[\dot{p}^{(0)}(\bar{y},t) \right]_{\hat{t}} p(x,t+\hat{\tau})} d\bar{y}^3 \quad (4)$$

With statistically stationary variables only the time delay τ is important and results in the equation 4 reduce to:

$$\overline{p(x)p(x,\tau)} = \frac{-1}{4\pi C_0^2 x} \int_{\text{volume}} \overline{\left[\dot{p}^{(0)}(\bar{y}) p(x,\hat{\tau}) \right]_{\hat{t}} (d\bar{y}^3)} \quad (5)$$

This equation says that the rms value of the far-field acoustic signal can be found by setting $\tau = 0$, and evaluating the integral at $\hat{t} = x/C_0$ and then taking the square root. This will give the far-field acoustic pressure at one point due to all the sources in the jet plume. The time derivative shown here can be represented for stationary random variables, in other forms, as:

$$\overline{p^{(0)} p(\hat{\tau})} = \frac{-2}{2\tau} \overline{\dot{p}^{(0)} p(\hat{\tau})} = \frac{\partial^{-2}}{\partial \tau^2} \overline{p^{(0)} p(\hat{\tau})} \quad (6)$$

This development follows very closely that given in Reference 6.

2.2. PROBE SELECTION

2.2.1 In-Jet Pressure

2.2.1.1 Pressure Probe Selection Requirements

To adequately measure the fluctuating pressure within the jet plume and not cause extraneous readings in the in-jet pressure measurement and more critically in any correlation of the pressure signal to far-field measurement demands that the probe selection be done very carefully. Of course the insertion of any probe will cause some disturbance to the jet plume and radiate some sound, however, this must be minimized by the proper selection of probe size, jet diameter and probe type. For cold jets the criteria can be given as follows:

- o Probe Frequency Response
- o Probe Contamination Factor
- o Repeatability

A. Probe Frequency Response

Probe amplitude and phase response must be reasonably flat to frequencies greater than the signal content in the jet plume and the far-field. Fuchs⁵ has measured the fluctuating pressure in the jet and found that at 3 diameters downstream, on the jet centerline, the power spectral density is down by 40 dB at a Strouhal number, S_T , of 2.5 compared to the peak value at $S_T=0.45$. Rakl⁶ and Siddon⁷ made measurements of the in-jet pressure field with a small airfoil-like probe and these indicate that the major portion of the correlated "pseudo sound" is below a Strouhal number of 2.0. Rakl⁶ used a far-field microphone at 45° from the jet center line and cross-correlated this signal with the in-jet sensor, or pseudo sound measurement.

Lee and Ribner⁸ correlated an in-jet hot-wire measurement of the fluctuating velocity to a far-field microphone and their data indicates that little information existed above $S_T=2.5$. Scharton and Meecham¹¹ also measured the fluctuating pressure in the jet plume and found that the 1/3 octave band sound pressure level was 20 dB down at $S_T=4$ from the maximum. Based on these previous investigations it can be said that a Strouhal number of no greater than 4 is required to adequately measure a cold subsonic jet. For a 2 inch

diameter jet with a 1000 fps exit velocity the maximum frequency of interest is then 24 KHz.

Several probe possibilities exist and will be discussed briefly below:

- i) Conventional microphones, of the 1/8" size, have an adequate response greater than 50 KHz. With an aerodynamically shaped nose cone, this is a strong candidate.
- ii) Siddon's probe has a minimized dipole radiation, but in its present form has a linear amplitude response range of less than 2.5 KHz and an unspecified phase response.
- iii) Long snouted adaptors can be applied to conventional microphones to reduce the volume of the probe, at the sensing point, and still have adequate amplitude response. However, the phase response suffers due to the long transmission path. For a probe with a 3 inch transmission tube the phase shift at 24 KHz is approximately 2000 degrees.

B. Probe Contamination Factor

Rakl⁶ and Siddon⁷ have defined a probe contamination factor which is the ratio between the mean squared acoustic pressure due to dipole type radiation from the probe surface to the mean squared acoustic pressure due to quadrupole type radiation from the adjacent eddy of the fluid. For cylindrical probes this factor, C, can be expressed as

$$C = \frac{4420}{(u'_{rms}/U)^2 M^2} \left(\frac{d}{x} \right)^4 \left(\frac{dp}{d} \right)^4$$

where: u'_{rms} = RMS value of the fluctuating velocity
M = Local Mach number
d = Jet diameter
 d_p = Probe diameter
X = Downstream distance
U = Local velocity

A sample calculation is given below:

$$\begin{aligned}\text{For } M_{\text{exit}} &= 0.8 \\ X &= 5d, \quad M = M_{\text{exit}} \\ u'_{\text{rms}}/U &\approx 0.25 \\ d_p &= 1/8'' \\ d &= 2'' \\ C &= 0.0027\end{aligned}$$

This calculation indicates that a 1/8" microphone is probably adequate for high subsonic jets and subsonic portions of supersonic jets with reasonable exit diameter. The probe used by Rakl and Siddon had a $C = 0.1$.

C. Repeatability

It is important that accurate means exist to calibrate the probe to an absolute scale. In this respect the commercially available probes generally will be better.

2.2.1.2 Pressure Probe Selection

The 1/8" condenser microphone with an aerodynamically shaped nose cone and a long 90° probe support to align the probe with the flow was selected as in-jet acoustic probe. It was felt that an airfoil probe such as used by Rakl⁶ and Siddon⁷ could not have been developed in time, with an adequate frequency response. Consultation with Prof. T.E. Siddon revealed that their present probe resonated, indicating an inductive-capacitance type action, and it was necessary to fill the microphone cavity with cotton to dampen this oscillation. Therefore, enlarging the hole size would have little effect on the dynamic response. Siddon felt that this present probe is not the ultimate, but rather, a first model of this type, and he is actually pursuing a refined, more miniaturized version of this probe. Using conventional 1/8" microphones, it should be possible to develop a Siddon-type probe with a 5-6 KHz response, but this is still too low.

2.2.2 Probe Selection

Velocity mapping in the 2" diameter cold jet exhaust at Mach number of 0.8 was performed using hot film anemometers with single and "x" probes. The special "x" hot film probe, mounted on a wedge shape stem, was purchased from

Therm-System Inc. for two dimensional velocity measurements. Figure 117 shows a schematic picture of this "x" hot film probe which consists of two hot films on the wedge at 45° with respect to the jet axis and perpendicular to each other viewed from side. Thus, by taking the sum and the difference of the signals from these two films, the axial and the radial components of the jet flow can be obtained, respectively (Reference 9). A single film probe, TSI model 1210-20, was chosen to provide injet velocity measurements with minimum disturbance in the flow for the velocity and the in-jet pressure cross correlation investigation.

2.3 Experiments

Jet noise experiments were conducted on an outdoor test facility with cold air exhausting through a 2 inch diameter convergent nozzle. This nozzle is fed by a 12 inch plenum equipped with straightening screens and honeycomb, which is in turn fed by a long 4 inch line. The jet axis is parallel to a grass covered, ground plane at a height of 5.5 feet.

Far-field acoustics are measured with a 1/2" Bruel and Kjaer microphone on a 10 foot arc (in the same horizontal plane as the jet axis) and ranging from 19° to 146° from the jet axis. In-jet and farfield acoustic signals are fed to a large indoor Sangamo (Sabre IV) tape recorder and processed through a Hewlett Packard mini-computer, General Radio 1921 Real Time Analyser, and a Saicor Correlator (400 point).

The temperature difference between the jet total temperature and the ambient temperature ranged from 22° F to a maximum of 40° F with the ambient temperature ranging from a low of 43° F to 63° F.

The ambient noise level for this facility is quite low, 65 to 67dB, (re. 0.0002μbar), and the far-field data ranged from 100 to 115 dB so that the ambient contamination is very low.

Several types of experimental data were gathered and are listed below:

Far-field acoustics

In-jet unsteady pressure measurements

In-jet unsteady velocity measurements

Simultaneous measurements of unsteady jet pressure and far-field acoustics

Two-point unsteady jet pressure measurement
Simultaneous measurements of unsteady jet velocity and far-field acoustics.

2.3.1 In-Jet Measurements

2.3.1.1 Static Pressure Fluctuations

The fluctuating static pressure within the plume of the 2" jet, has been mapped with a nozzle pressure ratio of 2 (slightly under-expanded). Initial trials at a pressure ratio of 3 showed that the pressure field was very intense, and except for very large downstream distances, greater than 15 diameters, the 1/8" B&K microphone could not tolerate the high amplitudes and therefore, a nearly sonic jet was used. Before taking these measurements it was necessary to determine the response of the 1/8" B&K microphone and 90° angle support to the jet-induced vibration. This was accomplished by covering the static pressure opening of the microphone nose cone with silicone rubber. This microphone was then subjected to an intense acoustic field, which would have produced a rms signal of 100 times the quiescent signal if the opening had not been sealed. The sealing technique prevented the acoustic signal as the output signal did not change in the presence of the field. The microphone was then submerged in the jet and the vibration induced "rms" signal was mapped. Comparing this rms signal to the signals achieved with an unblocked nose cone showed that the acoustic plus vibration signals were from 14 dB to 20 dB greater than that of the vibration alone. Since this is a random signal, the correction to obtain a pure acoustic signal is less than 0.1 dB.

Four downstream stations were measured at 1,3,5 and 10 diameters downstream. At each of these points a radial traverse of the overall average (rms) jet pressure signal was plotted on a X-Y recorder. These plots are shown on Figures 118 through 121. Measurements of this type have been made before by Scharton and White.¹⁰ The measurements reported here show more definite peaks and valleys at the shorter downstream distances; this is to be expected since the probe to jet diameter ratio was smaller for the current measurements. Scharton and White show that maximum "rms" pressure on the jet center line occurs at 5 diameters downstream while these measurements indicate that the overall jet

pressure rises uniformly along the center line from one diameter to 10 diameters downstream. The maximum jet pressure does not occur on the center line for x/d of 5 and less. The radial position and the maximum value of the jet pressure for each axial station are shown on Figure 122. The absolute maximum jet pressure measured was 4% of the plenum gage pressure or 5.7% of the jet dynamic pressure. This level agrees well with the Scharton and Meecham¹¹ results on a sonic jet, formed by the exhaust of turbojet and with the low velocity results ($m = 0.35$) of Planchon and Jones¹² and Rakl⁶. These results indicate that the maximum overall jet pressure level is rather insensitive to jet diameter, temperature and upstream turbulence. The radial locus of the jet pressure maximum lies somewhat inside corresponding measurements of the fluctuating axial velocity.

The shape of the maximum jet pressure level versus axial distance is very similar to the noise source distribution for a 2.8 inch diameter hot jet (1150° F) given by MacGregor and Simcox.¹⁴ An even better fit could probably be obtained by making a comparison based on a cross-sectional area weighting of the jet pressure level.

Along this locus of maxima, a 1/3 Octave band analysis was made of the signal. An example of this is shown on Figure 123; the spectral shape is very similar for all axial locations with the closer axial stations having a slightly more peaked spectrum. The Strouhal number of the peak 1/3 octave band level is shown on the insert to Figure 123.

2.3.1.2 RMS Velocity Mapping

Figure 117 shows a schematic diagram of the apparatus for obtaining the hot film velocity data. Signals from both films of the "x" probe were linearized and calibrated to an accuracy of $\pm 0.25\%$ of the velocity measured between 400 to 1000 ft/sec. Two dual channel Hewlett Packard differential amplifiers with unity gain were used to obtain the sum and difference from the hot film signals, and give the axial and radial velocity components, i.e., u' and v' . The mean axial and radial velocities, i.e., \bar{u} and \bar{v} were obtained from the sum and the difference of the average voltage readings at the outputs of the two hot film linearizers. A TSI Model 1060 RMS meter was employed at the out-puts of the HP differential amplifiers to give the turbulence levels of the axial and

radial velocities. The time-varying axial and radial velocities from the HP differential amplifiers were recorded on the Sangamo Tape recorder simultaneously with the far-field pressure signal from a microphone located 10 ft away from the nozzle exit and at 43.8° from the jet axis. The mean velocity and the turbulence level distributions in the Mach 0.8 jet exhaust are shown in Figure 124. Good agreements of the mean axial velocity distribution and turbulence level distribution are found between the present measurements and those presented in References 15 and 16. The radial velocity of the jet was found to be about 10% of the jet exit velocity and decaying slightly in the downstream direction. The turbulence levels in the axial direction were found to be about two times of those in the radial direction at most locations in the jet exhaust.

2.3.2 Pressure Probe Contamination

Probe contamination of the far-field signal is always of concern in this type of measurement and can be determined by comparing the far-field signal with and without the inlet probe. On Figure 125 it can be seen that the "rms" value of the far-field SPL is severely affected by the presence of the in-jet probe at the higher angles. This result is due to the different radiation patterns of moving (jet) and fixed (probe contamination, dipole-like) noise sources, with the moving sources having a radiation pattern biased towards the shallower angles and therefore, less contaminated. Subsequent results show clearer correlations at the shallow angles. The contamination is also seen to be greater as the downstream distance is increased; part of this is due to the greater insertion required to reach the maximum "rms" jet pressure level. One-third octave band analysis of the far-field signals (with and without the in-jet probe) reveals that the contamination appears at frequencies higher than the peak intensity (Strouhal) frequency.

2.3.3 In-Jet to Far-Field Correlations

2.3.3.1 Jet Pressure to Far-Field

Cross-correlations of an $1/8$ " B&K microphone, buried in the plume of a 2" convergent jet, with a far-field microphone have been found to be sensitive to the far-field microphone position and in-jet axial location. At the four

axial stations of $x/d = 1, 3, 5$ and 10 the in-jet microphone was placed on the radial point of maximum overall (rms) jet pressure level and then cross-correlated with several microphone positions, ranging from 20° to 60° from the jet axis. These correlations were for the most part processed using a 400 point Saicor correlator and checked with a Hewlett Packard Fourier Analyser and mini-computer.

Figure 126 shows these results for the unfiltered cross-correlations. Band pass filtering of the signals will undoubtedly improve the correlation, and may allow a discernible correlation at the shallow angles. In particular, note that larger downstream distances have much higher correlations. When the probe is placed at the larger axial distances it encounters a larger scale of turbulence and should yield a better correlation. Work not reported here, but currently carried out in suppressor models, with much finer turbulent scales, shows a much lower level of correlation with a similar directivity effect. Similar measurements were made by Meecham and Hurdle¹⁸ with in-jet probe at 5.2 diameters downstream of a 6.5" jet ($M=0.99$) and one diameter off-axis. The correlation levels are in good agreement and the directivity only slightly poorer agreement with the results presented here (see Figure 10 of Reference 18).

Siddon and Rakl^{6,7} measured a correlation coefficient of 0.02 with the far-field at 90° and the injet probe at $x/d = 5$ and $r/d = 1$. This result is in agreement with the present findings and those of Meecham and Hurdle.¹⁸

Noise source location methods suggested by Meecham and Hurdle,¹⁸ Rakl⁶ and Siddon⁷ require the complete mapping of the correlation function for the entire jet plume and then taking the second time derivative of these correlations. The correlograms themselves, without differentiation, range from fairly definitive to very marginal, so that this process is tenuous, at best. Figures 127 through 129 show the unfiltered cross-correlation shapes for one axial position and they illustrate the range of clarity that exists. The shape of the correlation functions shown here tends to more anti-symmetric than symmetric shapes predicted by others. When closer to the jet and at larger far-field angles the correlation shape is completely obscured by noise. The use of cross-correlations of in-jet pressure to the far field acoustic pressure as a noise source location method does not appear to be very attractive as it requires a very tedious and marginal procedure. An improved correlation method to determine the axial source distribution would be to place a small probe

close to the jet flow (to obtain good definition of source location) but not in the plume to eliminate probe contamination of the far-field and probe pick-up of self-noise. In this manner, the distribution along the jet axis of the near-field radiation to the far field could be determined.

2.3.3.2 In-Jet Velocity to Far-Field Pressure

If \vec{r} is the directional vector connecting the injet sound source point and the far-field microphone location, the cross correlation between the square of the injet velocity component, $V_{\vec{r}}$, and the far-field pressure, $P(\phi)$, can be obtained by the cross-correlation of the axial and radial velocity components, i.e. u and v , with the far-field pressure in the following manner (Reference 12): where ϕ is the angle between \vec{r} and the jet axis and t is the time delay. The advantages of employing the above formula are twofold: (1) velocity components u and v are usually easier to obtain than $V_{\vec{r}}$; and (2) for an experimental set up with more than one far-field microphone, the cross-correlation of the velocity vs. the pressure signal from every microphone can be calculated with one simultaneous measurement. The measurement of the velocity component, $V_{\vec{r}}$, is usually made by using a single hot wire probe oriented in the direction parallel to \vec{r}_{ξ} (Reference 4). This kind of measurement can not be easily justified as an absolute $V_{\vec{r}}$ measurement, because a single hot wire probe can not provide one dimensional velocity measurement unless the flow field is purely one dimensional. For an axisymmetric flow field such as jet exhaust from a round nozzle, the transverse velocity perpendicular to $V_{\vec{r}}$ and the wire will always be measured along with $V_{\vec{r}}$. On the other hand, if a proper "x" hot wire probe is used (Reference 9), the velocity components u and v can be resolved and measured with no difficulty. The objective of using the special "x" hot film probe for the 2" Diameter Jet Velocity Mapping (Section 2.2.2) is to provide the u and v measurements for the cross-correlation of the in-jet velocity to the farfield microphone pressure signal.

Because the correlations between velocity and pressure are very weak, (about 5%), the narrow band analysis procedure has to be adopted (Reference 13). Figure 130 shows a block diagram of the instruments used for the cross correlation study. A typical narrow band cross correlation $\Delta R_{V_{\vec{r}}, 2p}^{\vec{r}}(t)$ is shown in Figure 131 where f is the filter central frequency. Due to some mismatch

between the two narrow bandpass filters, the noise associated with the cross correlation output is high and masks the correlation. Better in-jet velocity and farfield pressure cross correlation results should be obtained in the near future. The in-jet pressure correlations to the farfield acoustic signal are much clearer as evidenced by the fact that a discernible correlation could be obtained at these same conditions without filtering (see Figure 126).

2.4 In-jet Correlations

A. Radial Coherence

Simultaneous measurements of fluctuating static pressure in the jet plume were made at two points and cross-correlated to determine the tangential and radial coherence. Cross correlation of the jet pressure and fluctuating velocity are used to determine the axial coherence. The primary goal of these experiments were to see if the results of Fuchs¹⁹ would be valid at higher jet Mach numbers. Fuchs used a 4 inch diameter jet and 1/4" Bruel and Kjaer microphones at a jet Mach number of 0.12, while these experiments used a 2" jet with 1/8" Bruel and Kjaer microphones so that the principal difference will be due to the effects of higher speed. The high degree of radial coherence found by Fuchs (at zero time delay) does not hold at this high flow velocity ($M=1$). Figure 132 shows the zero time delay cross correlation as well as that for the optimum time delay with one microphone on the jet centerline and the other microphone at various radii. The structure of the jet pressure field (at this Mach number) is quite unlike that of Fuch's results. The zero time delay point is just one point on a cross-correlation function and is not necessarily the most interesting. It does not yield any information on propagating disturbances and will only indicate the level of coherence. The correlations, however, show strong indications of repetitive wave-like motion in the radial direction. Figure 133 shows these function for $r = 0.711$ "; the regularity of the peaks and the asymmetric behavior near the origin are the predominant features. From these peaks and valleys a reflection length $r = 1.54$ " was determined. Another point of interest is the appearance of a sign inversion at the origin (zero time delay), as can be seen on Figure 134. On the right side of Figure 134 the outer microphone signal is delayed so that inward going pressure waves are being correlated, and on the left side the centered microphone is delayed so

that outward going waves are being correlated. For no sign inversion the correlation function should be symmetric about the origin and going to unity as r tends to zero. The sign inversion seen here appears also on the other correlation functions for the larger radial separations. A source ring can also be postulated since the time delay for the correlation peak closest to the origin changes sign as the radial separation increases; this can be seen on Figure 132. The location of this source ring is found to be $V_g=0.67$ " connecting the time delays of two radial separation points with a Mach line. This radial source location is used on Figure 133 to predict the location of the second minimum and the corresponding repetitions. The agreement of these predicted peaks and valleys with the actual correlation function is quite good and tends to verify the model employed here. A complete Mach wave diagram was constructed using another observation, that the signals reverse sign as they pass through the reflection radius, V_f . Although this is a most unusual phenomenon, agreement of the predicted position and the signs of the correlation peaks with the data is quite good particularly since a very simple acoustic propagation model (Mach line) was employed. This experimentally deduced reflective model of the jet agrees in principle with some of the later theoretical models (Reference 20) that suggest that the jet flow acts like a wave guide to internal sources. Also the model of a large scale pulsating cell as proposed by Scharton and White¹⁰ does not seem to be supported by this evidence; it would require the correlation functions to be symmetrical about the time origin and show peaks and valleys on both sides. The peak and valley seen here could be due to a harmonic content of the signal, as both the 1/3 octave spectra of the jet pressure (see Figure 123) and the far-field (at 90°) microphone peak near the 4.4 KHz frequency that corresponds to the peak to peak wave length, but auto-correlations of the jet pressure did not show any sign of harmonic content.

The cross-correlation technique has been seen to be a powerful technique to define the nature of the jet pressure structure rather than just to determine the zero time delay coherence as has been the primary result of previous investigators.

B. Circumferential Coherence

Circumferential coherence measurements were taken at two different radii, one on the outside edge of the jet ($r/d = 1.43$) and one buried in the jet ($r/d = 0.36$). For the outer edge, these results (Figure 135) are of the same magnitude as those of Fuchs¹⁹ and confirm that the outer edges of the jet do undergo some sort of toroidal motion as observed by Crowe and Champagne.²¹ In the interior of the jet, however, the coherence is down by a factor of ten with very little coherence except at $\Delta\theta = 45^\circ$. This indicates that even if the outer layers are exhibiting coherent (toroidal) motion the interior portion has a much lower level of coherence.

C. Axial Coherence

To determine the axial characteristics of the jet pressure field would require two microphones to be placed on an axial line. This would cause a probe interference problem on the downstream microphone and was not attempted. A hot film probe was used instead as the upstream probe, since the upper velocity limit on the hot film probe is about $M = 0.9$, (the jet Mach number was reduced to 0.8) to assure probe survival. The microphone was fixed at the axial station and the hot film probe traversed upstream away from the microphone. Both the unsteady axial velocity u' and $(u')^2$ were correlated to the jet pressure. A typical correlation function is shown on Figure 136 with the corresponding convection velocity shown on Figure 137. The convection velocity at $\Delta x = 0.23$, is about 50% of the local mean velocity (at the microphone) with an increase to 80% of the local mean velocity at the maximum separation.

Contrary to Fuchs¹⁹ low speed observations, no evidence of wave-like disturbances appeared. The correlation monotonically decreases as the separation increased as shown on Figure 138. Fuchs' data was taken on the jet center-line and is not directly comparable; however, the wave-line character appears in nearly all of his other correlations. Some were taken with one microphone on the jet axis and the other slightly off-axis ($0.5d$) and moved parallel to it. Apparently this axial wave-like character does not exist at the higher jet velocities and is a low speed phenomenon. Fuchs used the

zero time-delay correlation. If that point were used here, the level of correlation would be reduced to about one-tenth of the optimum time delay value. By squaring the linearized hot film signal, the $(u')^2$ signal was obtained and correlated to the jet pressure. Figure 139 shows that the level of correlation is only about 1/3 to 1/2 of that of velocity to pressure correlation indicating that the cross product of unsteady velocity u' and mean velocity (shear noise) contributes more strongly to the jet static pressure fluctuation than the square of the unsteady velocity (self noise).

APPENDIX IV - 1

Effects of Grid Spacing on LV Spectra Estimation

LV spectra will be estimated by reconstructing the auto-correlation function by evaluating the average of each lag-product value. When this is done, an error is introduced because lag time values are quantized on a grid. If the grid has spacing T, then the lag estimate for $T = NT + T \pm T/2$. We must determine how small to make T so that the induced error is sufficiently small. This error may be analyzed in the manner of Balakrishnan†: Consider the auto-correlation function estimate:

$$\hat{R}_{xx}(\tau) = E \{x(\tau) x(t + \tau + \xi(\tau))\}$$

where τ is the nominal lag time value
 ξ is the random variable describing the variation in the lag product of τ
 x is the process under analysis

If x and ξ are independent, and if all processes are stationary and ergodic, then

$$\hat{R}_{xx}(\tau) = E_{\xi} \{R_{xx}(\tau + \xi(\tau))\}$$

where E is the expectation over ξ .

If the auto-correlation function is sampled on a grid of T, then $-T/2 \leq \xi(\tau) \leq T/2$ and

$$\hat{R}_{xx}(\tau) = E_{\xi} \{T R_{xx}(\tau + \xi(nT)) + \sum_{n=-\infty}^{\infty} \mu_0(\tau - nT)\}$$

The spectrum is then the Fourier transform of Equation (3), which is

$$\hat{S}_{xx} = E_{\xi} \left\{ \int_{-\infty}^{\infty} S_{xx}(\omega - \mu) e^{j\xi(nT)(\omega - \mu)} \sum_{n=-\infty}^{\infty} \mu_0(\mu - \frac{2\pi n}{T}) d\mu \right\}$$

We now consider cases of the above. First if the $\xi(\tau)$ are identical (which would be the case of Poisson sampling, neglecting $R_{xx}(0)$), then

$$\xi(\tau) = \xi$$

Interchanging integration and expectation, we find

$$\hat{S}_{xx}(\omega) = \int_{-\infty}^{\infty} S_{xx}(\omega - \mu) \phi_{\xi}(\omega - \mu) \sum_{-\infty}^{\infty} \mu_0 \left(\mu - \frac{2\pi n}{T} \right) d\mu$$

where $\phi_{\xi}(\omega) = E[e^{j\xi\omega}]$ = characteristic function of the r.v. ξ .

Thus, the spectrum becomes

$$\hat{S}_{xx}(\omega) = \sum_{-\infty}^{\infty} S_{xx}\left(\omega - \frac{2\pi n}{T}\right) \phi_{\xi}\left(\omega - \frac{2\pi n}{T}\right)$$

which is the aliased version of the original spectrum times the characteristic function. If we assume that ξ is uniformly distributed, then

$$\phi_{\xi}(\omega) = \frac{2 \text{Sin}(\omega T/2)}{\omega T}$$

Thus, the error is zero at $\omega = 0$ (a general result since $\phi(0) = 1$ for all characteristic functions) and increases with frequency. Reasonable values of T (i.e., complying with the Nyquist criterion) limits this error at high frequencies to about 3dB.

This model, however, neglects some important effects. First, the estimate of $R_{xx}(0)$ will contain no jitter. Second, near $T = 0$, there will be different distributions for $\xi(\tau)$ (i.e. ξ will be function of τ) due to the finite par-tical transit and processor dead times. In a similar manner, we may show that

$$\begin{aligned} \hat{S}_{xx}(\omega) &= \sum_{-\infty}^{\infty} S_{xx}\left(\omega - \frac{2\pi n}{T}\right) \phi_{\xi}\left(\omega - \frac{2\pi n}{T}\right) \\ &+ \sum \frac{T}{2} \int_{-\infty}^{\infty} [S_{xx}(\omega - \mu)] [\phi_{\psi_L}(\omega - \mu) - \phi_g(\omega - \mu)] e^{-j\mu\tau} d\mu \end{aligned}$$

where "most" of the jitters are identical with $\phi_g(\omega)$ their characteristic functions and the exception lag values, τ_L , have jitters ψ with characteristic functions $\phi_{\psi_L}(\omega)$.

From the above we may determine:

1. A "noise" error (second term) is added to the spectrum if the jitters have different distributions.
2. Since all $\phi(\omega) = 1$ at $\omega = 0$, the smaller the grid spacing and frequency, the smaller the noise error, since

$$[\phi_{\psi_L}(\omega) - \phi_g(\omega)] \rightarrow 0$$

Several simulations were conducted under various assumptions simulating expected L_1V_1 spectra conditions. From these it was concluded that if $T \leq T_n/5$, where T_n is the Nyquist period, the induced errors were at least 30 dB below the peak of the original spectra. Thus a grid spacing of

$$T \leq T_n/5$$

should be used in LV spectra estimates. Thus, if 40 KHz is assumed as the required Nyquist frequency, then a grid spacing of

$$T \leq 5\mu \text{ sec}$$

is required in the analysis system.

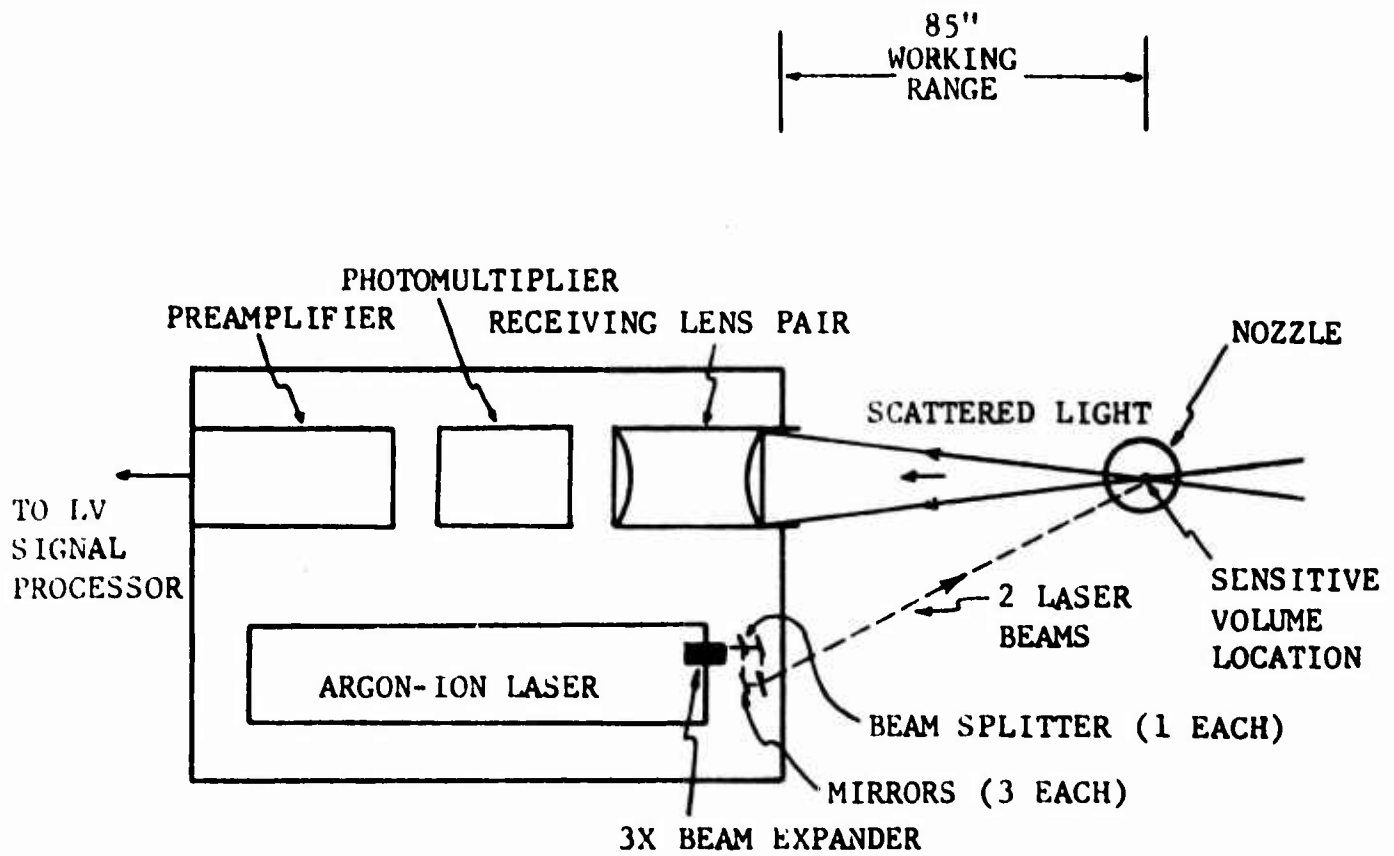


Figure 102 Laser Velocimeter Optics Package

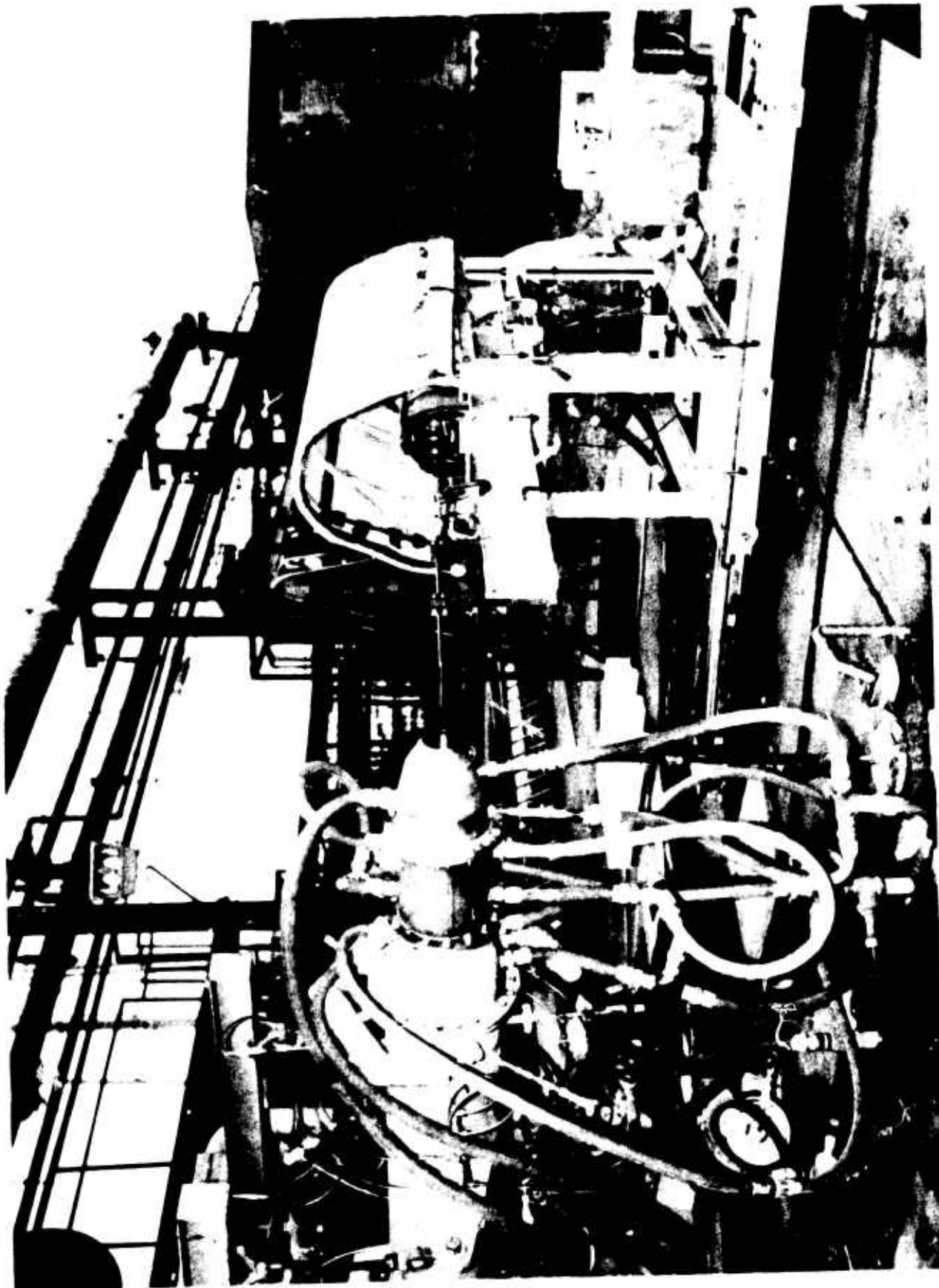


Figure 103 Laser Velocimeter Setup at JENOTS

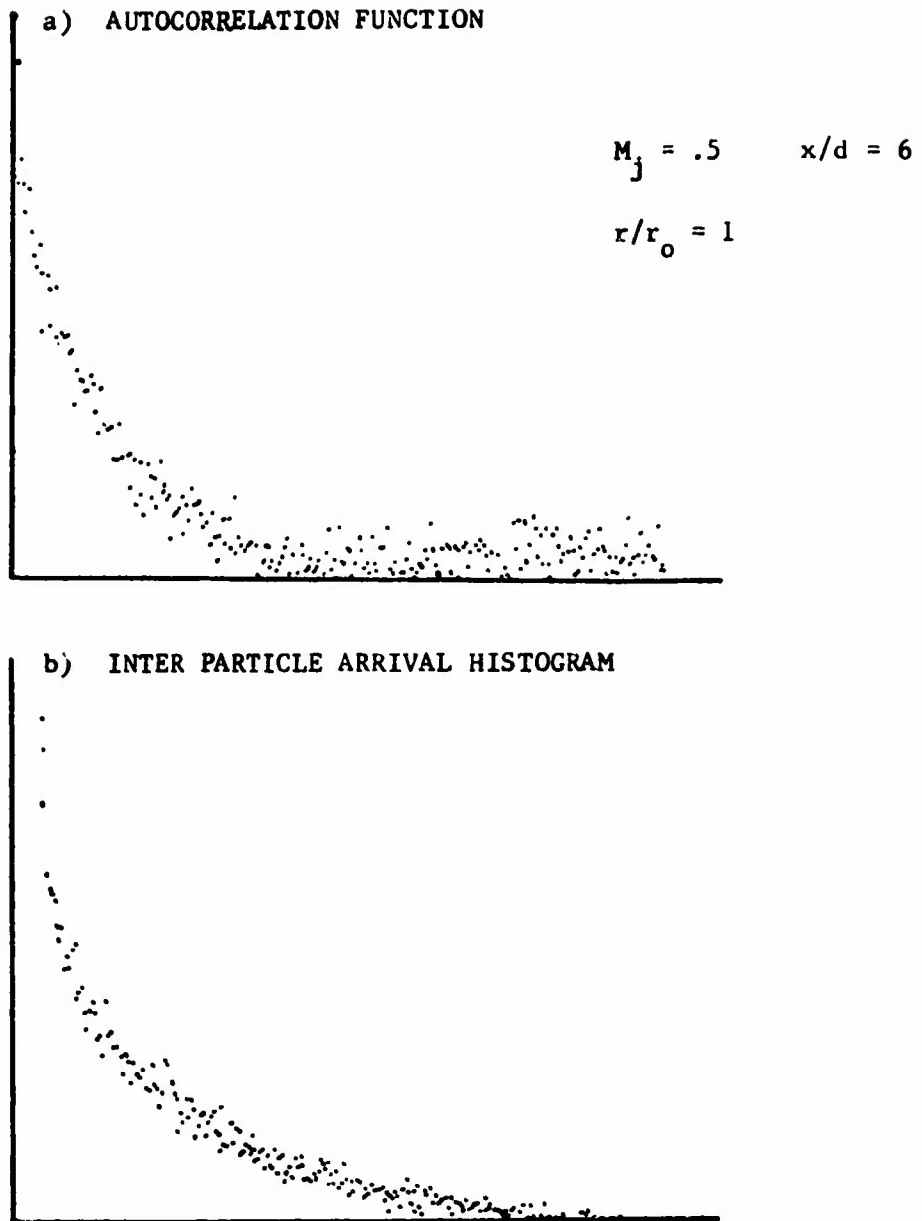


Figure 104 Laser Velocimeter Estimated Autocorrelation Function and Inter-Particle Arrival Histogram

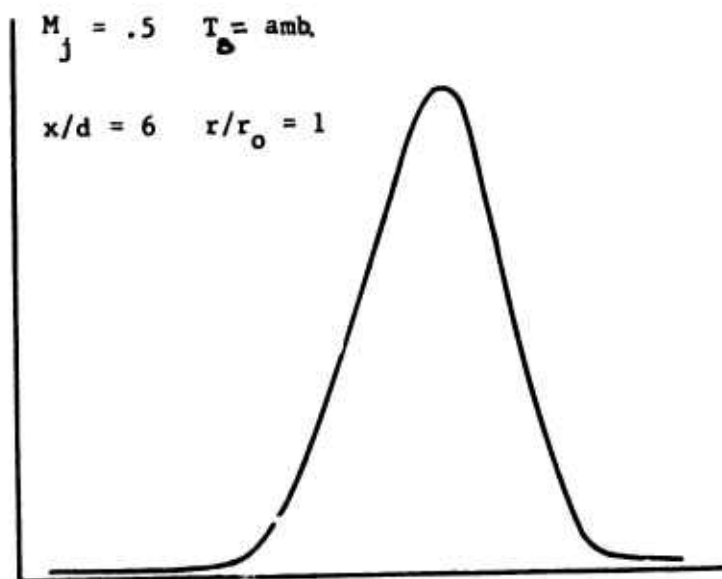


Figure 105 Velocity Histogram

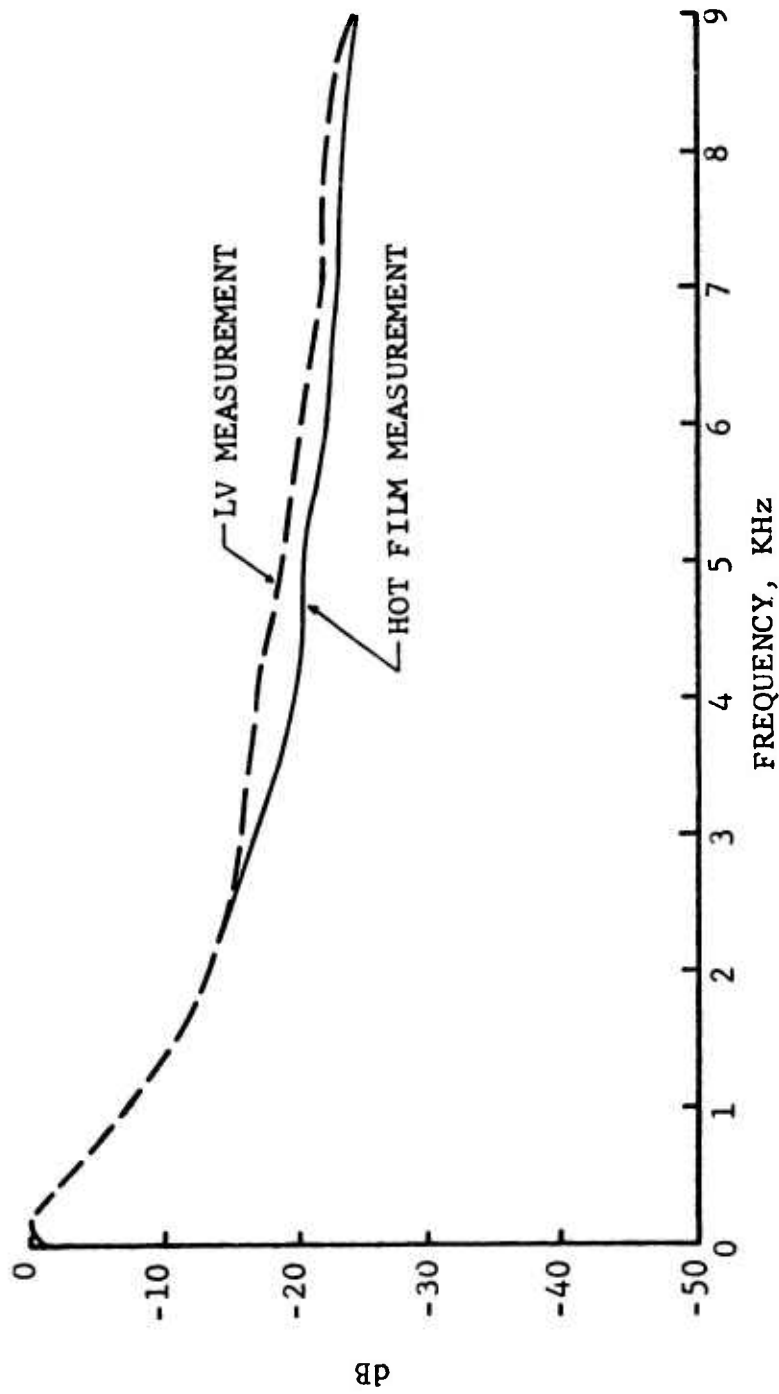
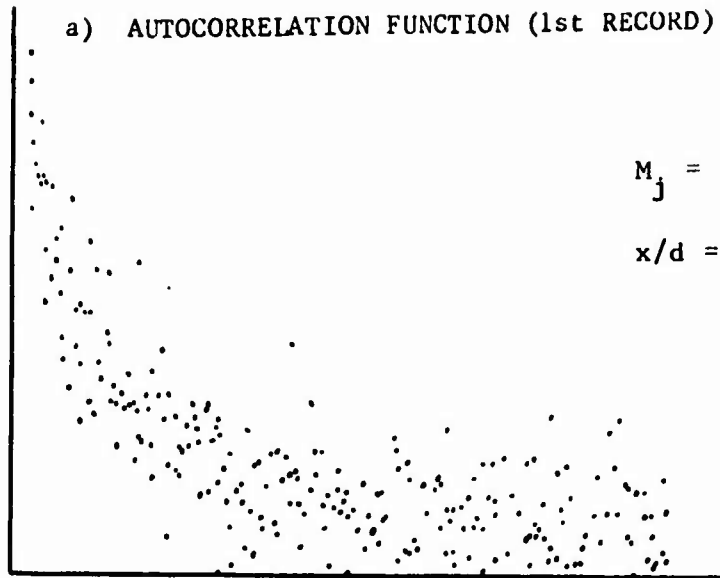


Figure 106 Comparison of Laser Velocimeter and Hot Film Turbulence Spectra
 $M_j = 0.5$, $X/D = 6$, $r/r_0 = 1$, 80 Hz Bandwidth



$$M_j = 1.0$$

$$T_T = 1500^\circ R$$

$$x/d = 10$$

$$r/r_0 = 0$$

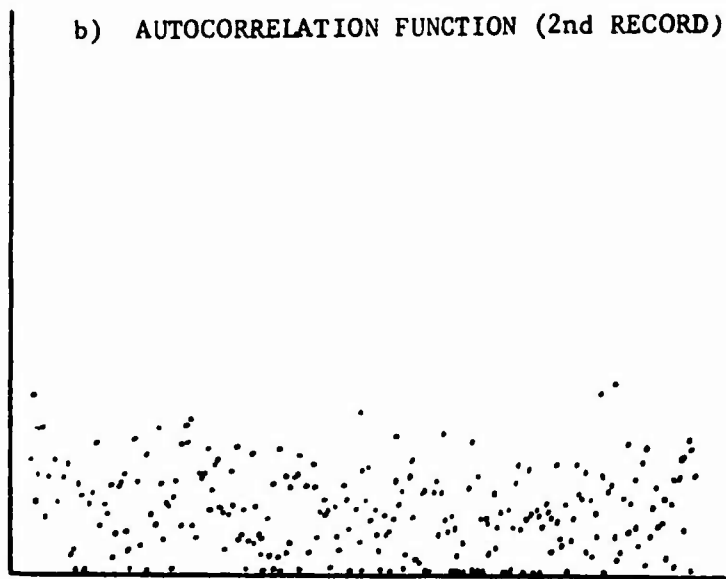


Figure 107 Autocorrelation Function

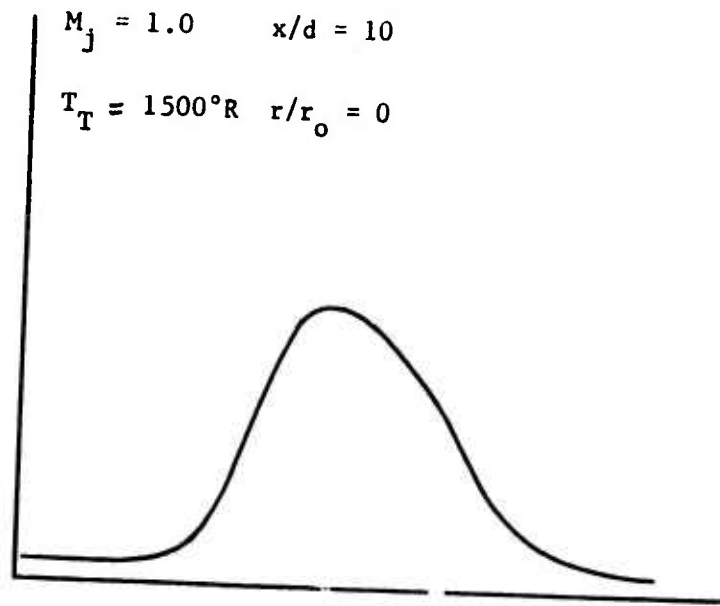


Figure 108 Velocity Histogram

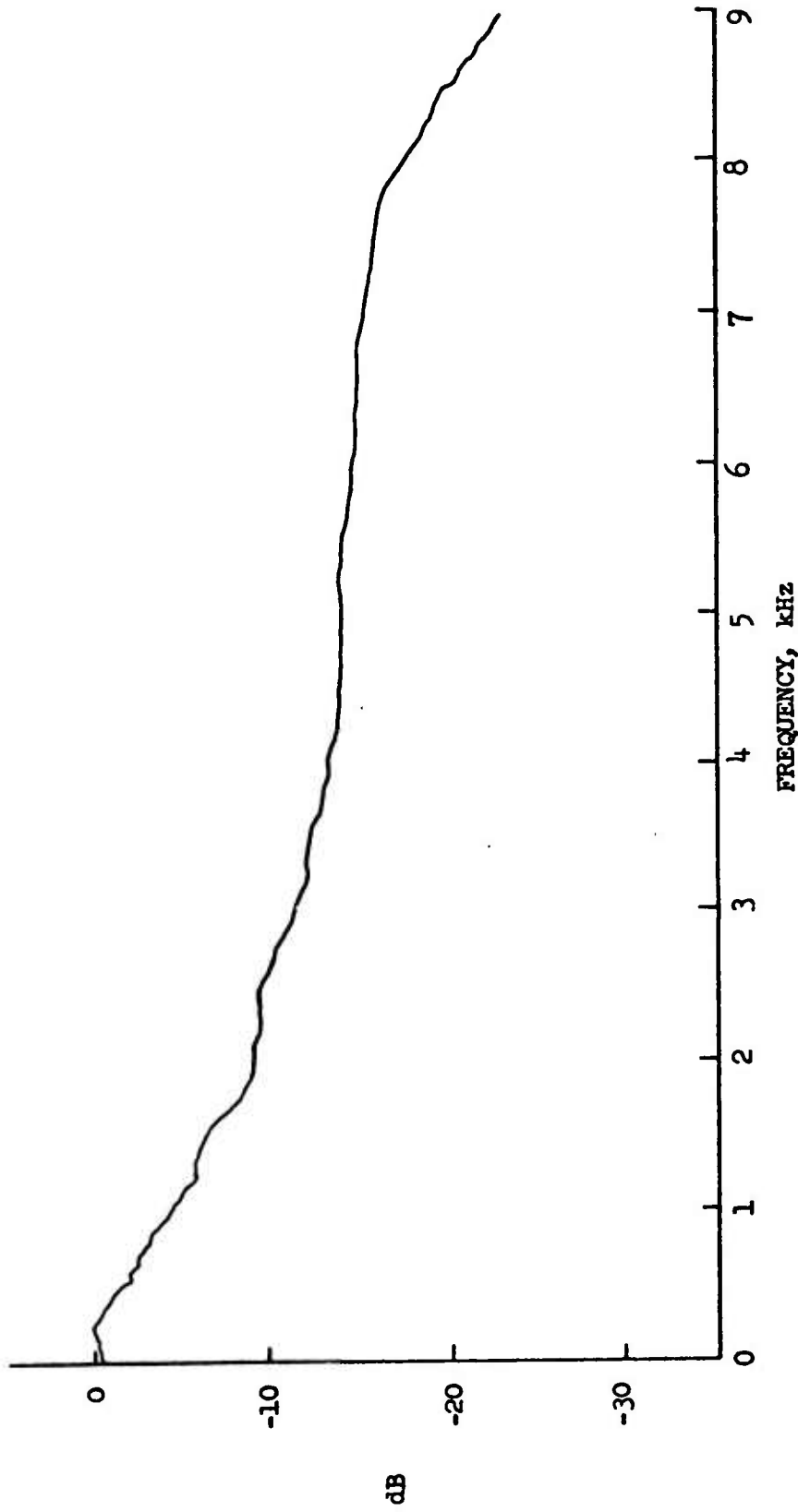


Figure 109 Measured Laser Velocimeter Turbulent Spectrum for a Hot Sonic Jet
 $M_j = 1.0$, $T_8 = 1500^\circ R$, $X/D = 10$, $r/r_0 = 0$

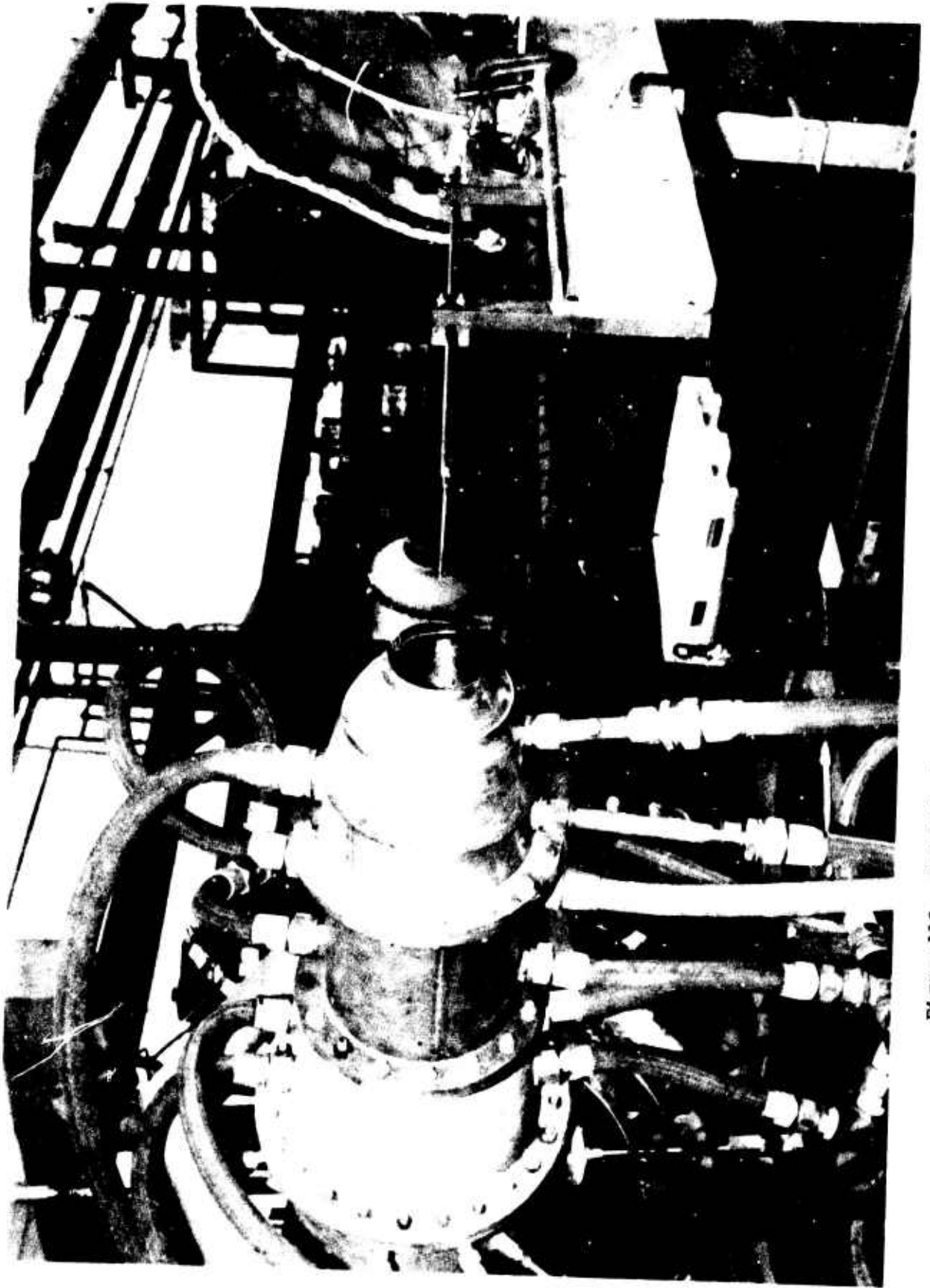


Figure 110 Hot Film Arrangement on Laser Velocimeter Cart

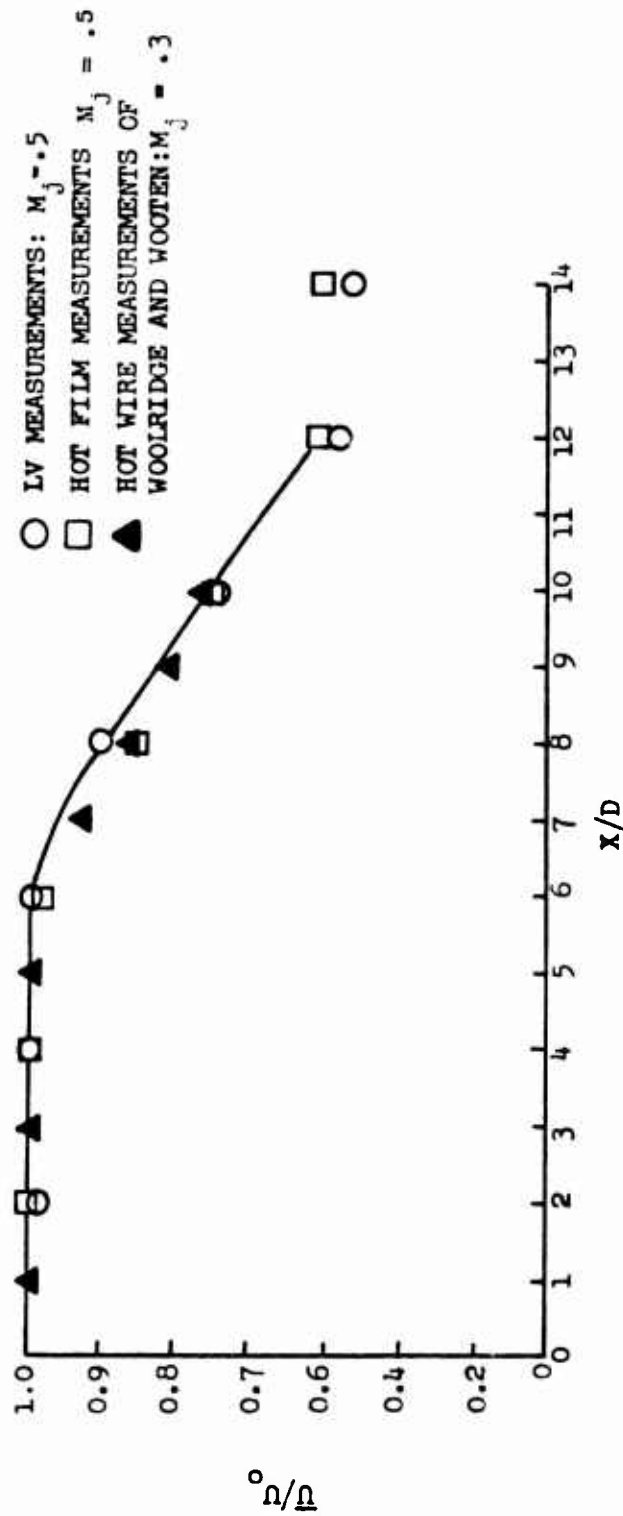


Figure 111 Axial Variations of Mean Velocity: Comparison of LV with Hot Film
 $M_j = 0.5$

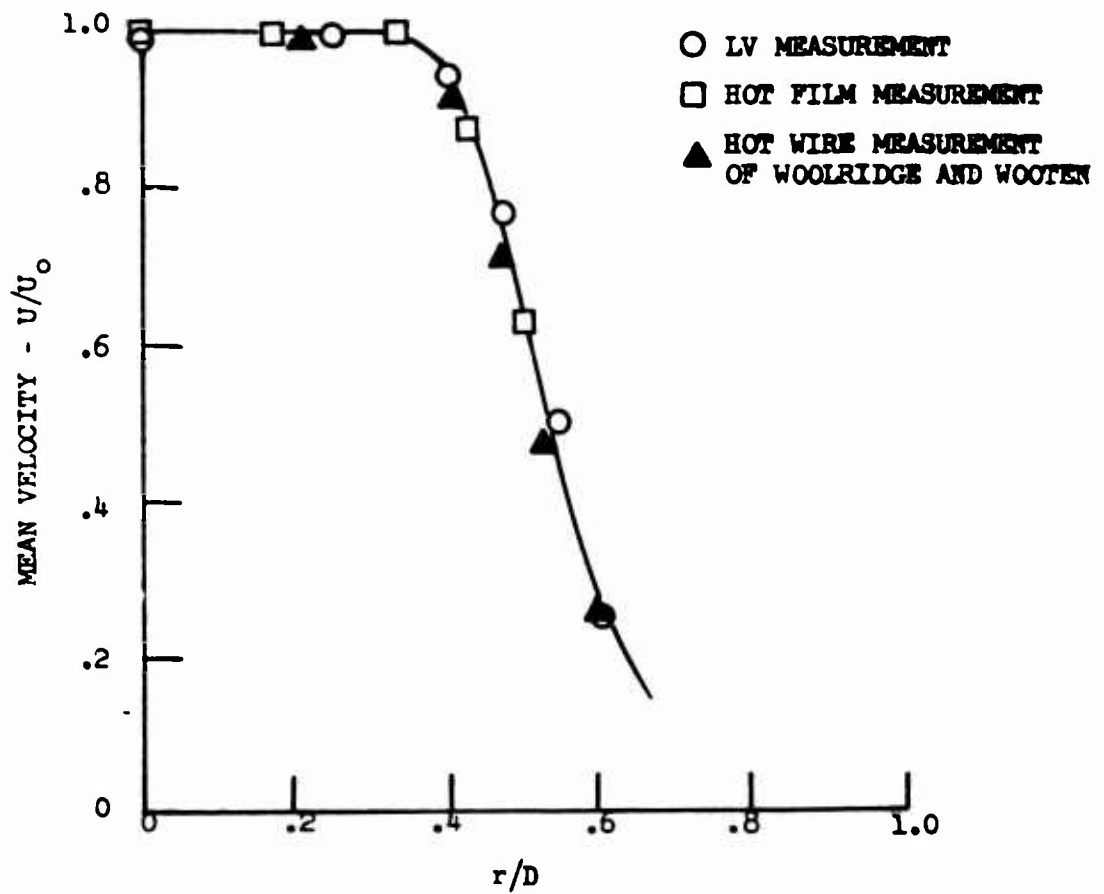


Figure 112 Mean Velocity Profile Comparison of LV with Hot Film
 $X/D = 2.0, M_j = 0.5$

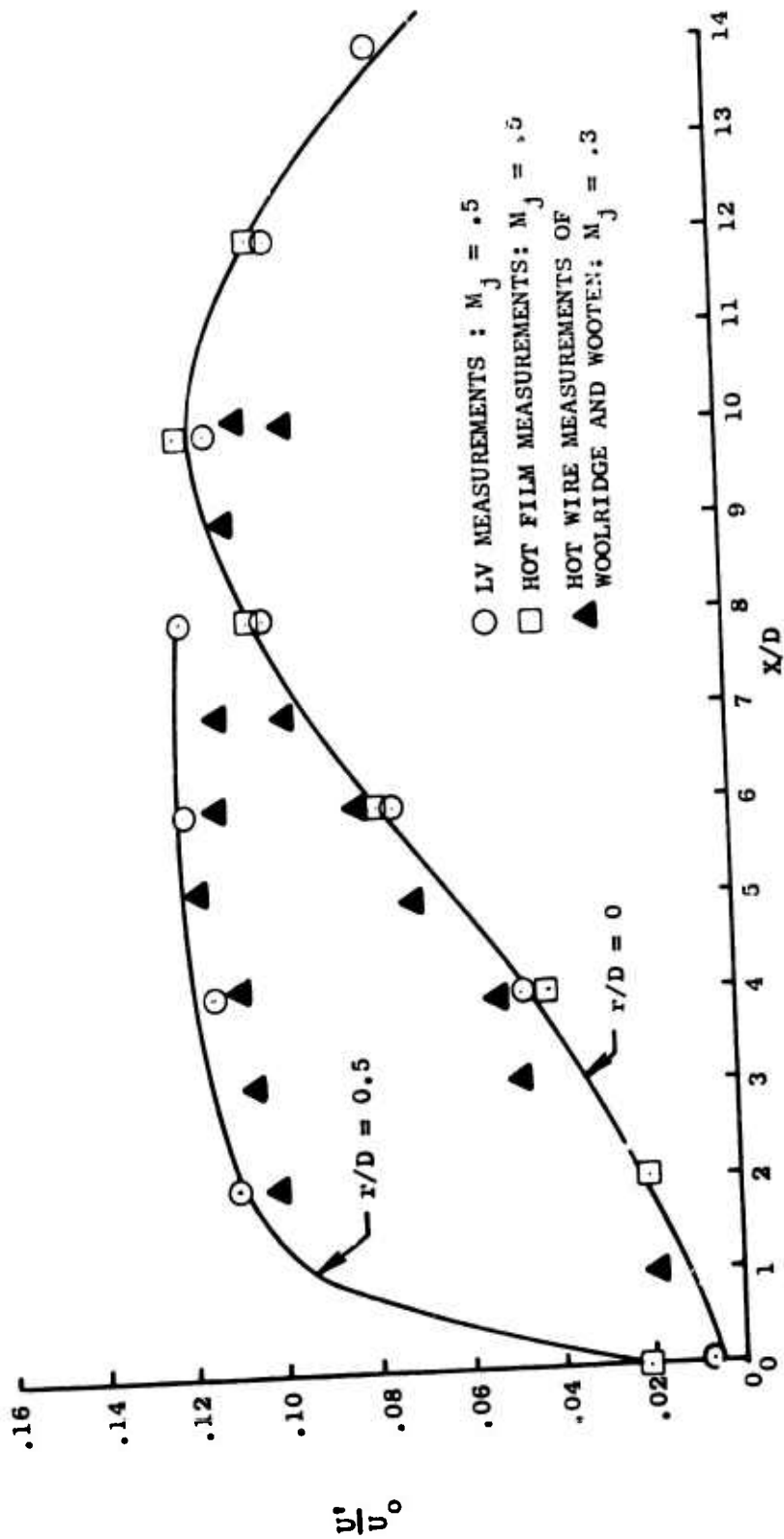


Figure 113 Axial Variation of Turbulence Intensity: Comparison of LV with Hot Film
 $M_j = 0.5$

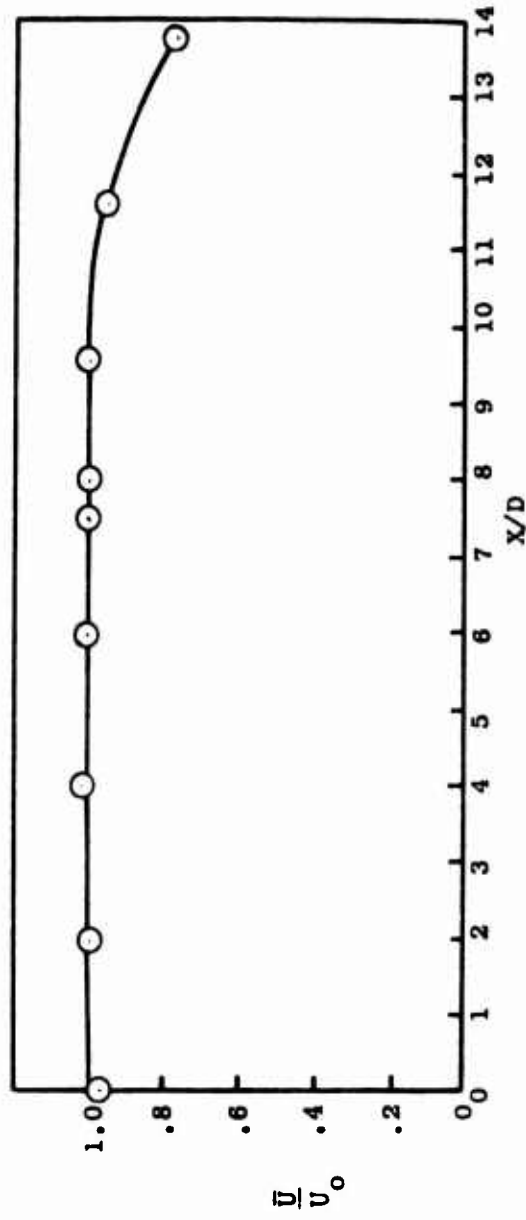


Figure 114 Laser Velocimeter Measured Axial Profile of Mean Velocity for a Perfectly Expanded Hot Supersonic Jet; $M_j = 1.55$, $T_T = 1500^\circ R$

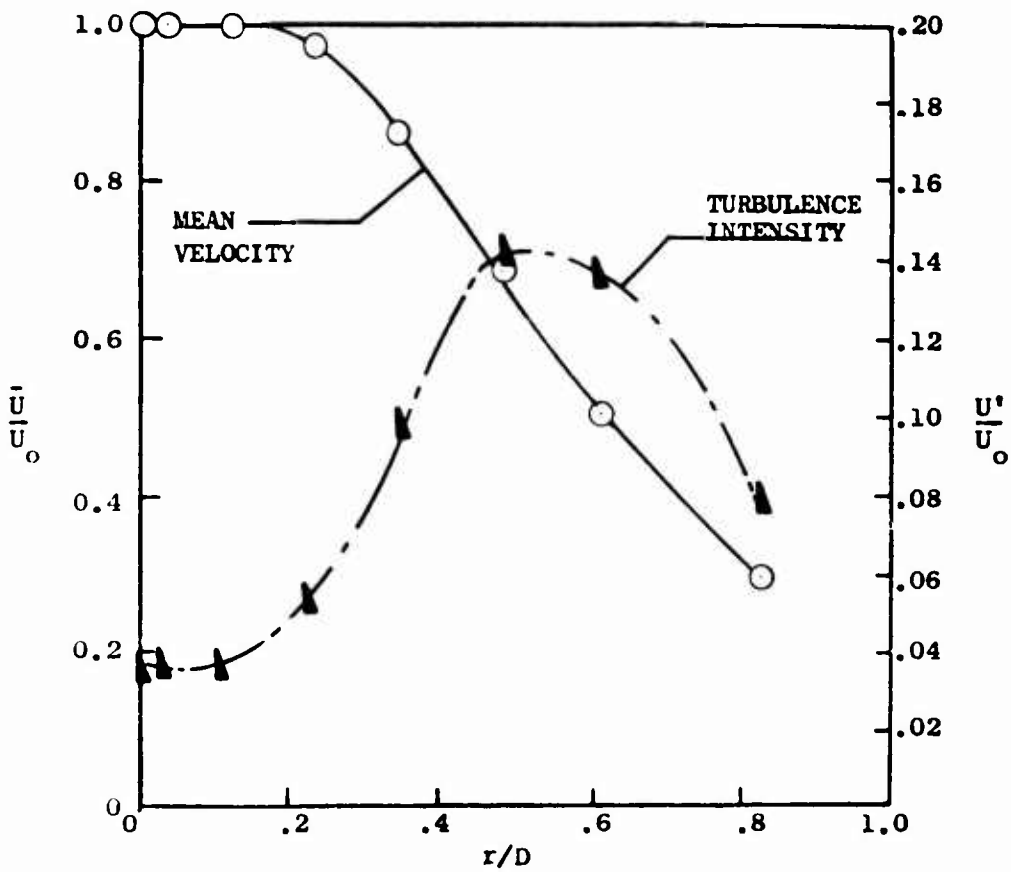


Figure 115 Laser Velocimeter Measured Mean Velocity and Turbulence Intensity Radial Profiles; $M_j = 1.55$, $T_T = 1500^\circ R$, $X/D = 9.6$

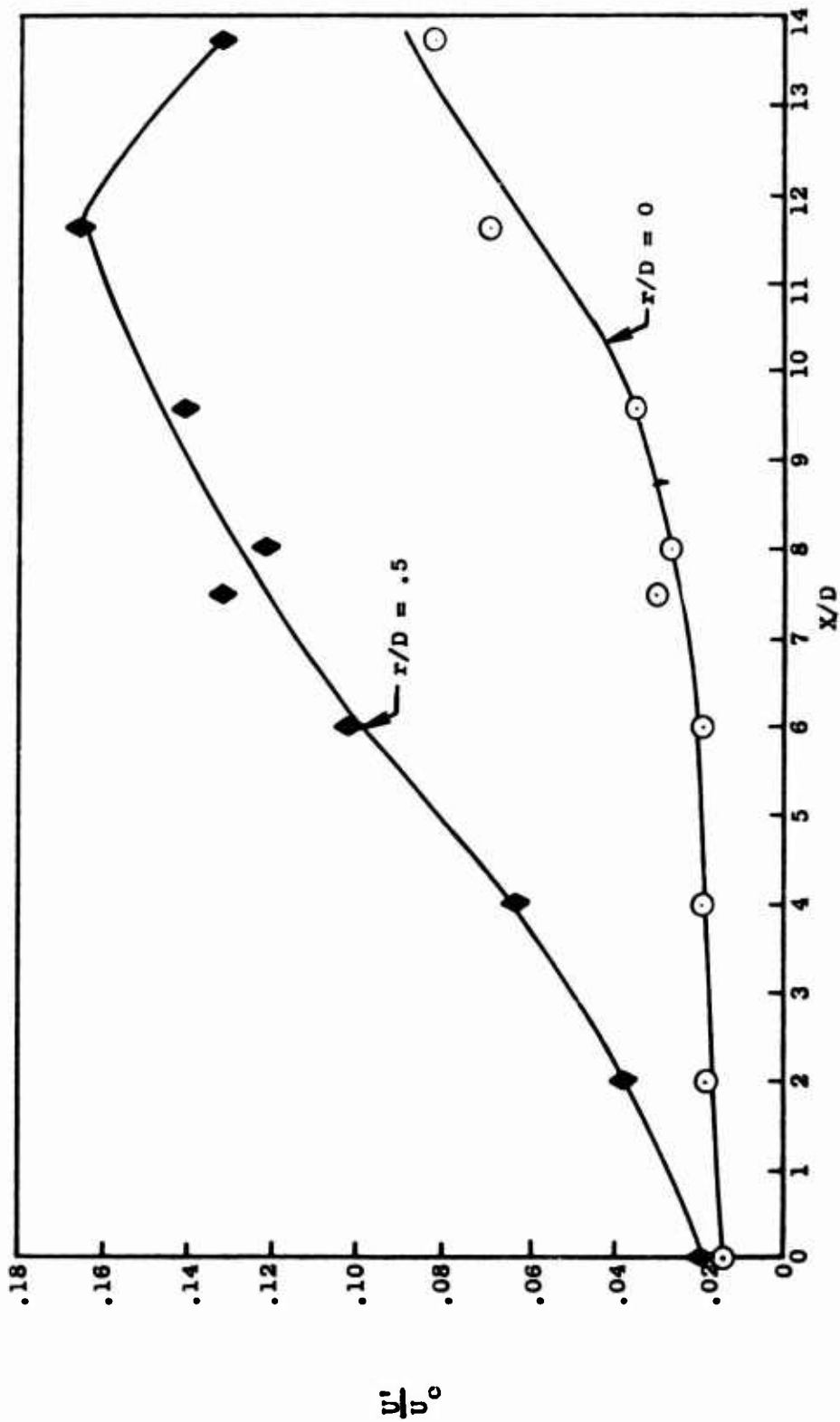


Figure 116 Laser Velocimeter Measured Axial Variation of Turbulence Intensity for Shock-Free Flow: $M_j = 1.55$, $T_T = 1500^\circ R$

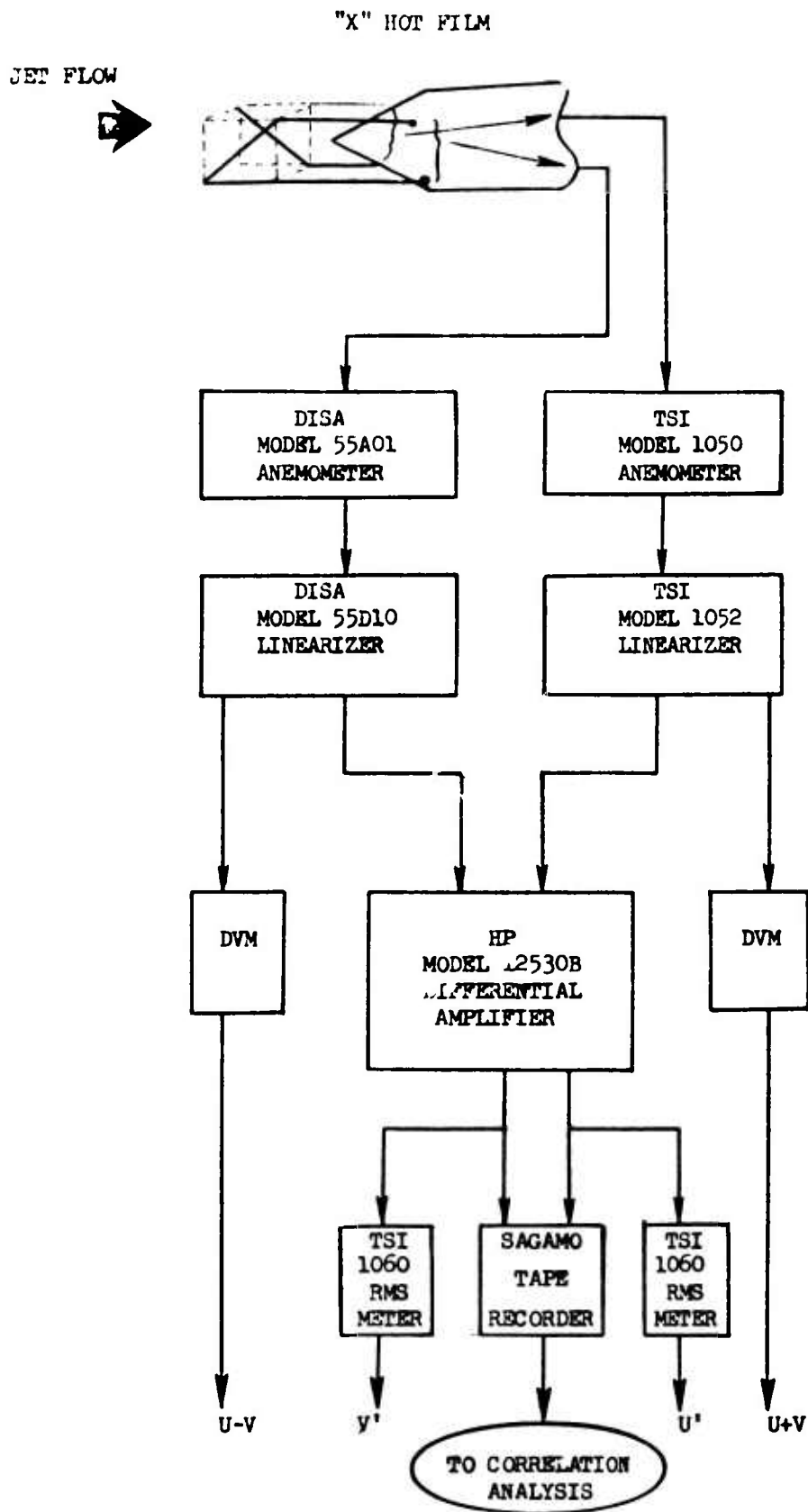


Figure 117

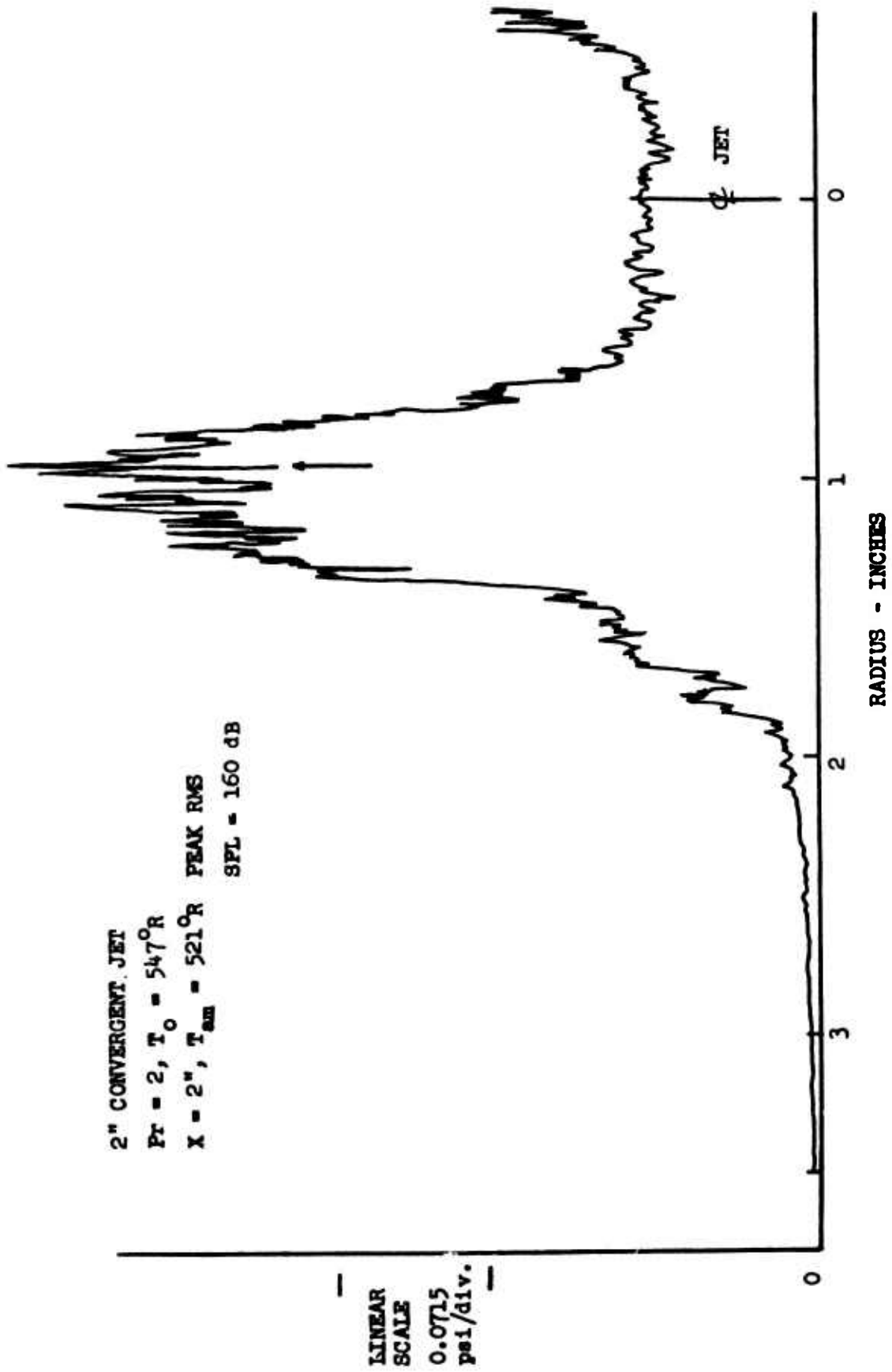


Figure 118 In-Jet Static Pressure "RMS" Profile

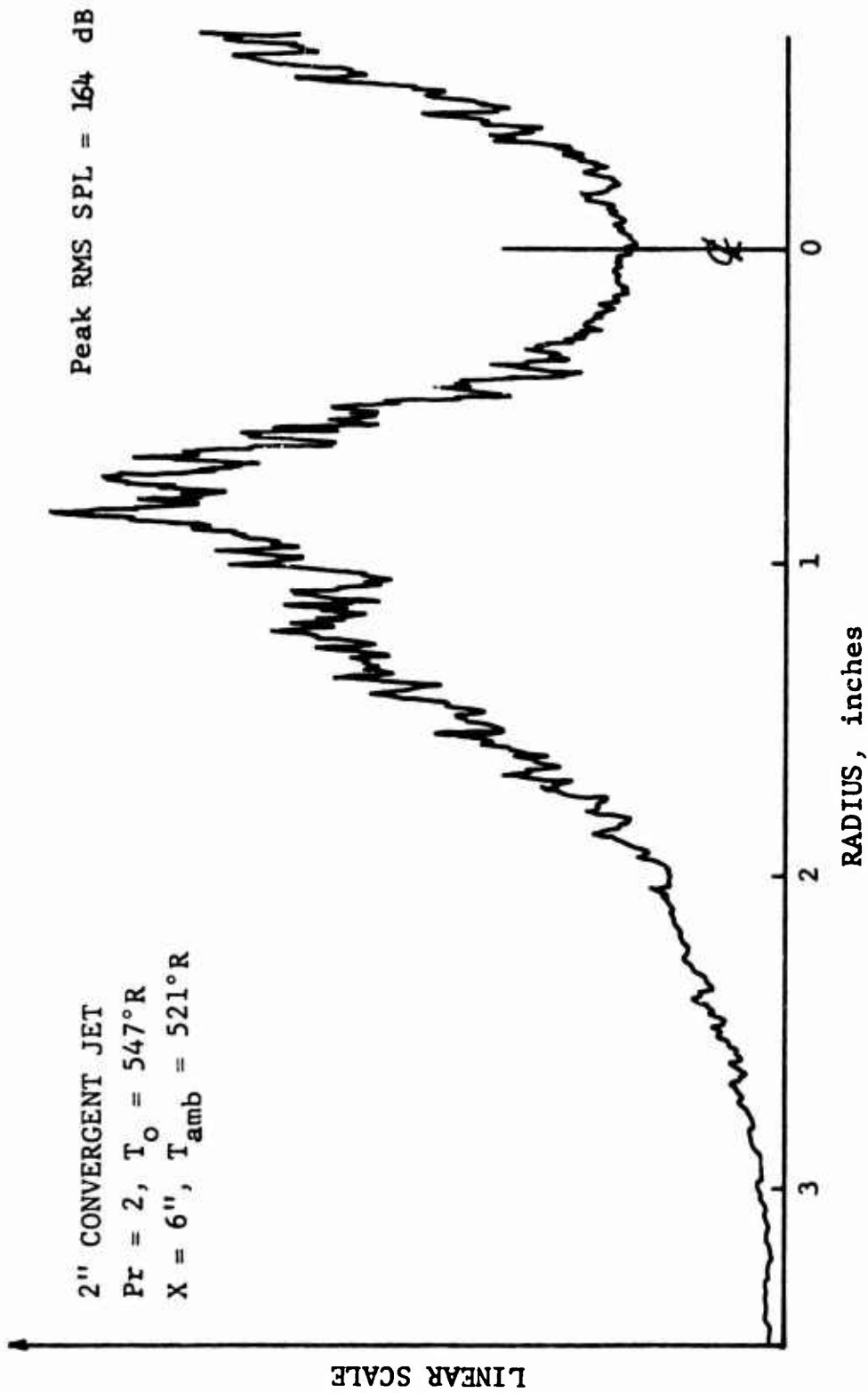


Figure 119 In-Jet Static Pressure "RMS" Profile

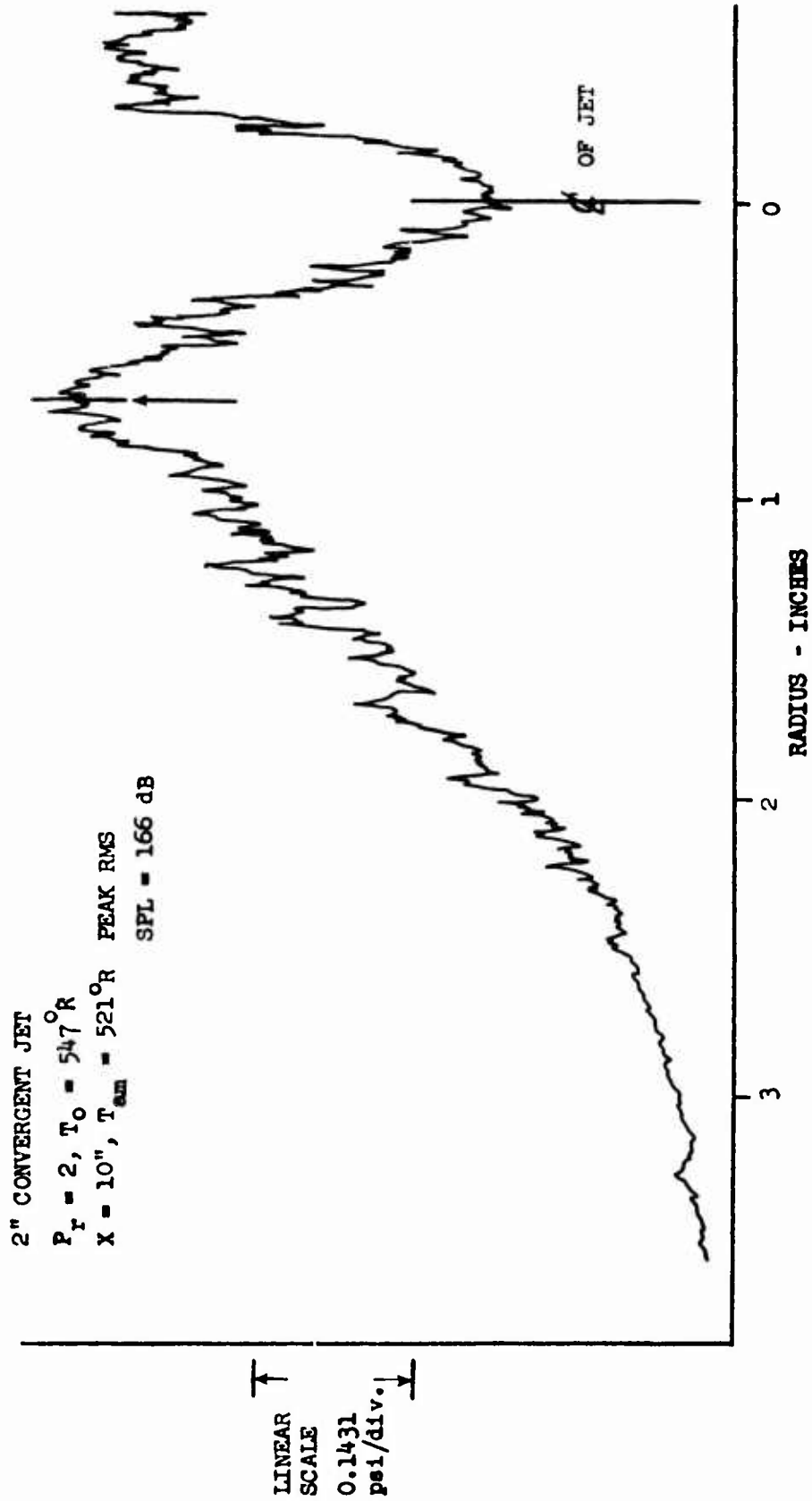


Figure 120 In-Jet Static Pressure "RMS" Profile

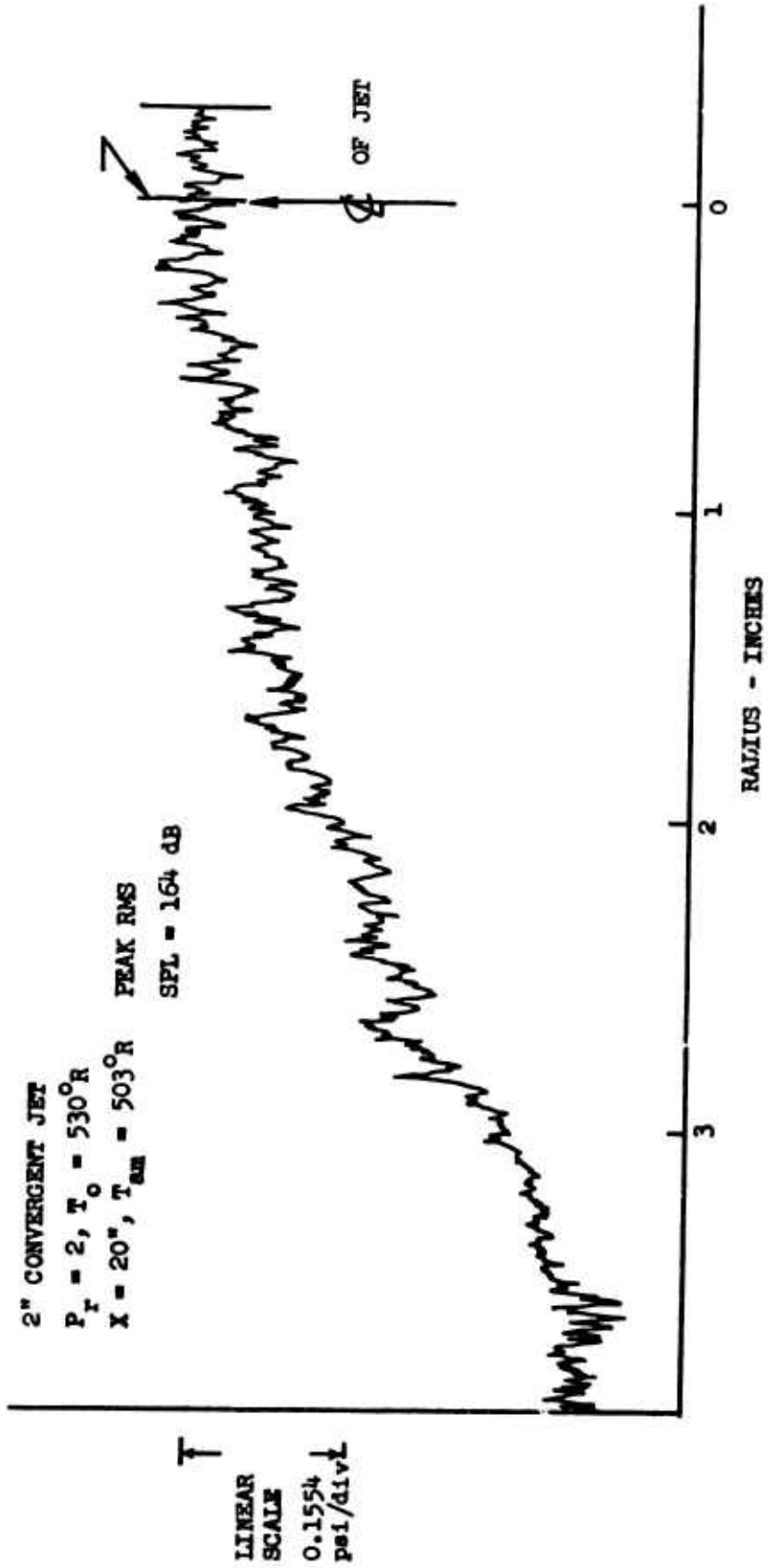


Figure 121 In-Jet Static Pressure "RMS" Profile

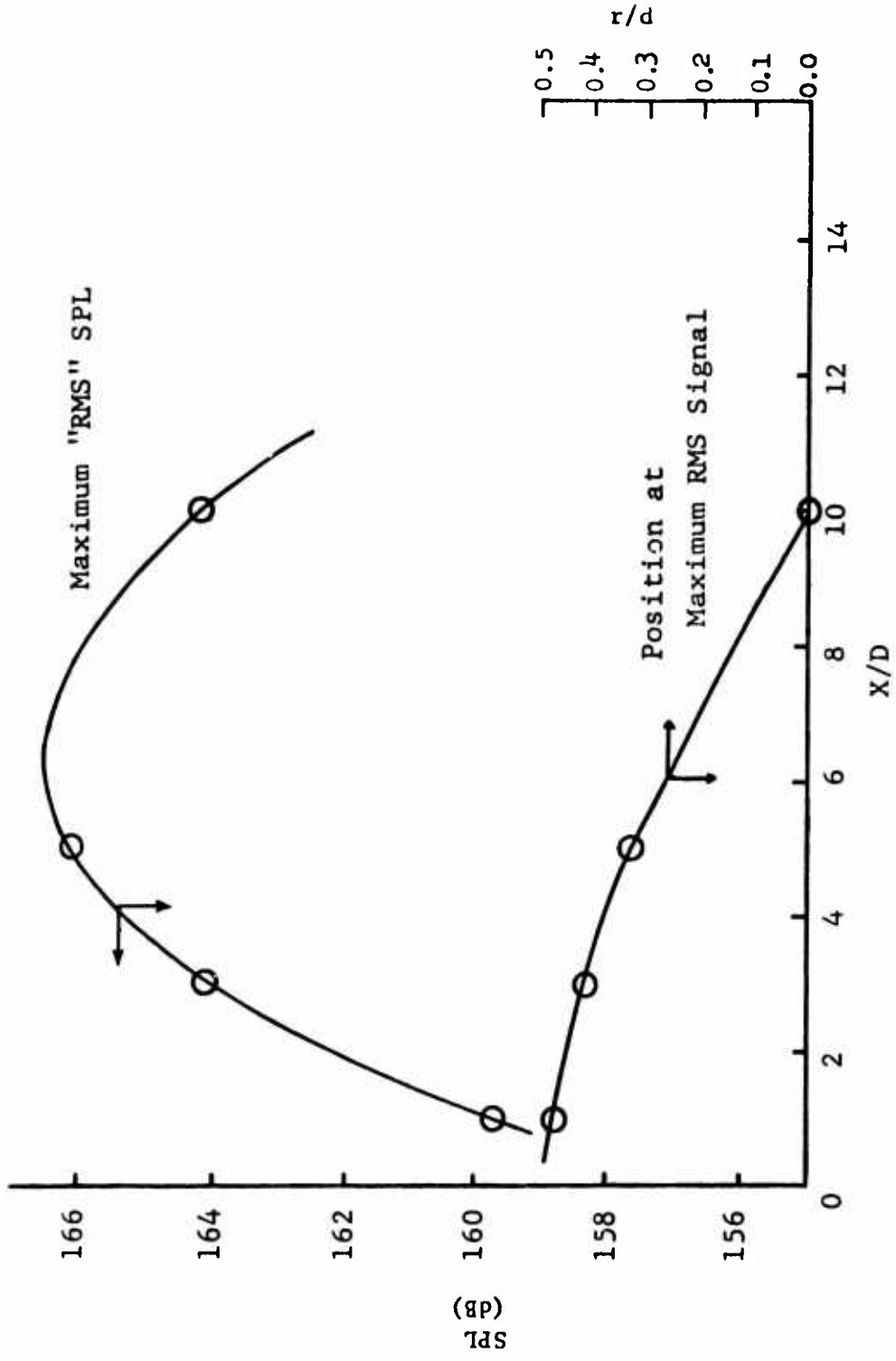


Figure 122 In-Jet Fluctuating Pressure Maximum Level and Radial Position versus Downstream Distance, X; Convergent Jet, D = 2 in., Pr = 2

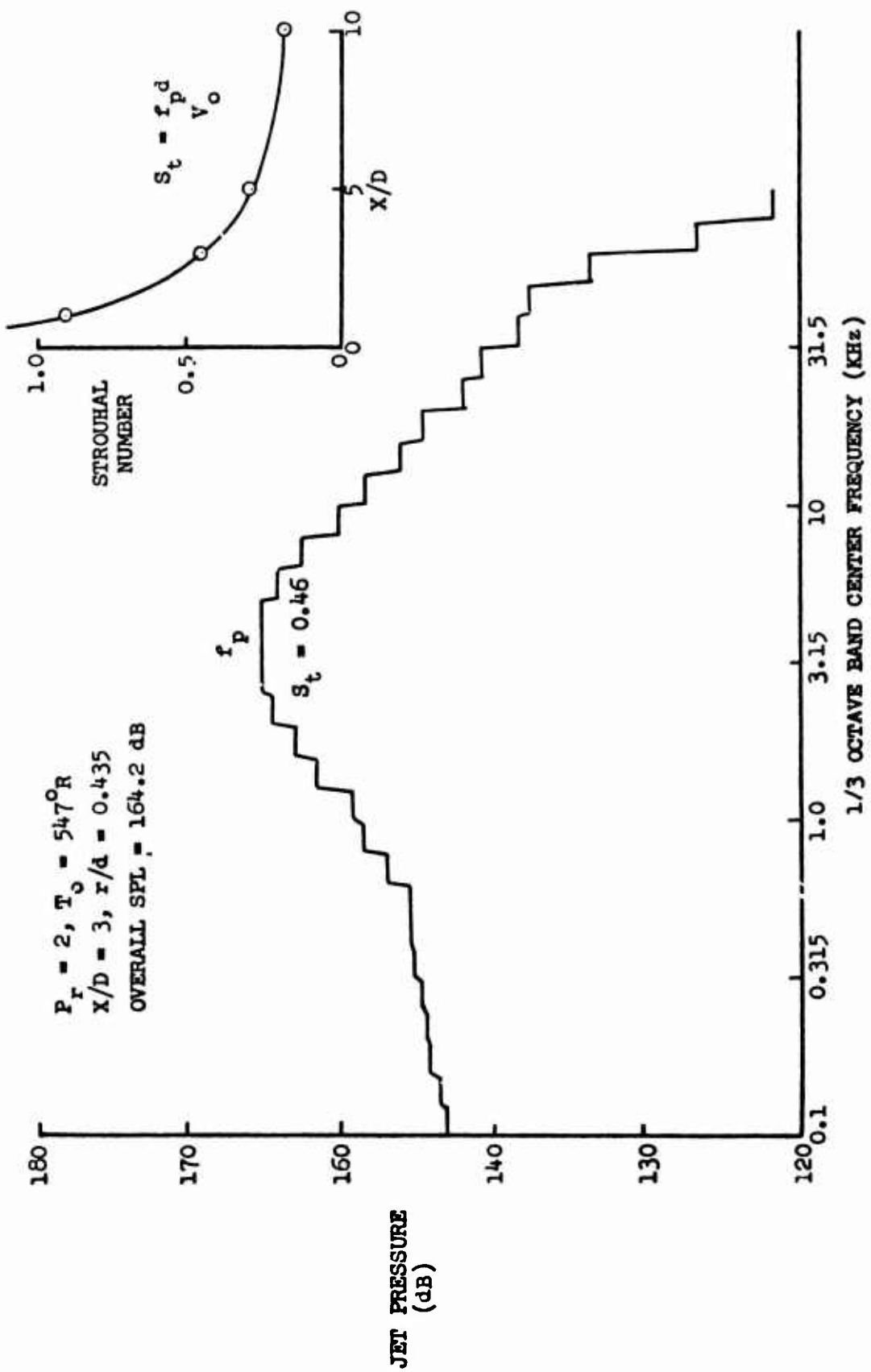


Figure 123 Jet Pressure 1/3 Octave Band Spectrum

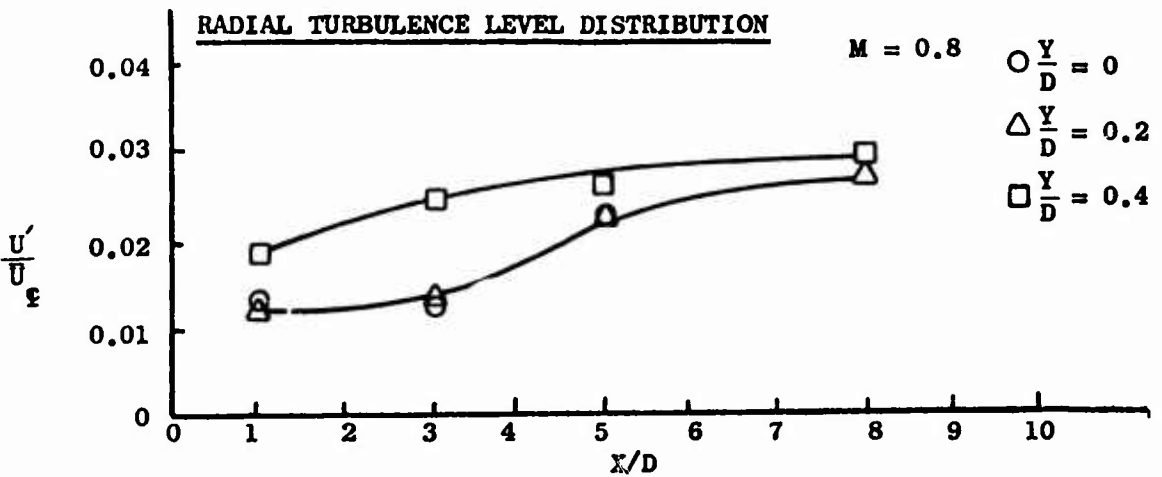
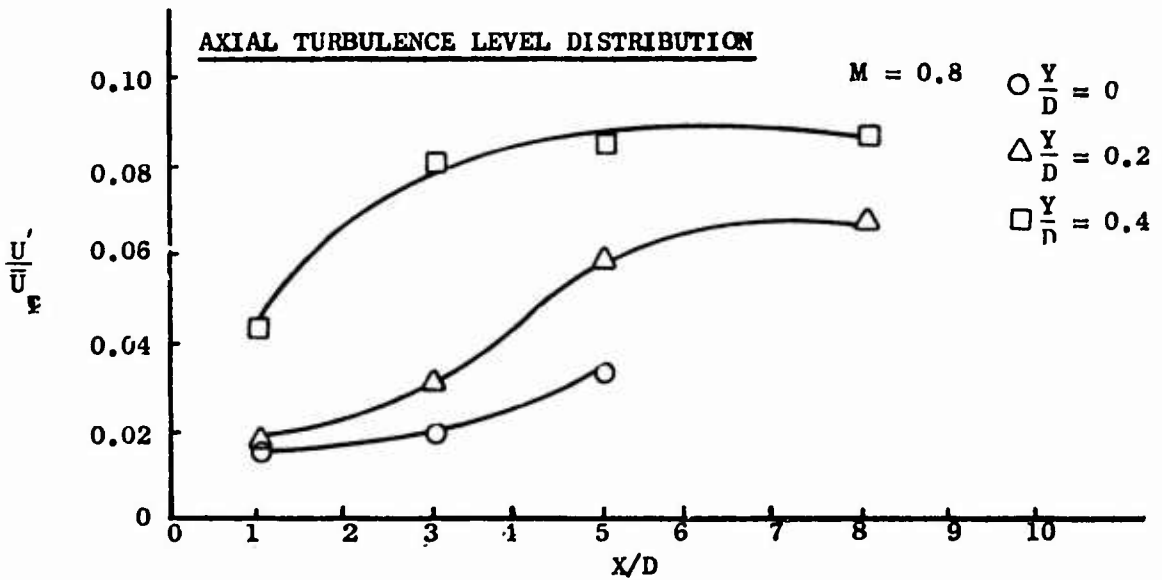
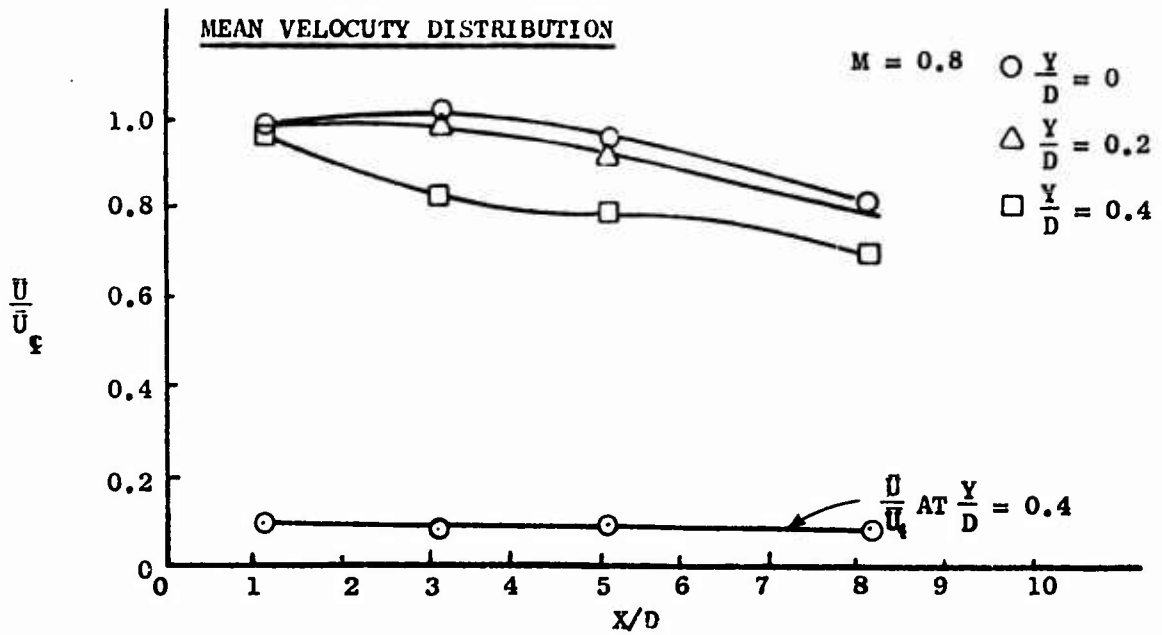


Figure 124

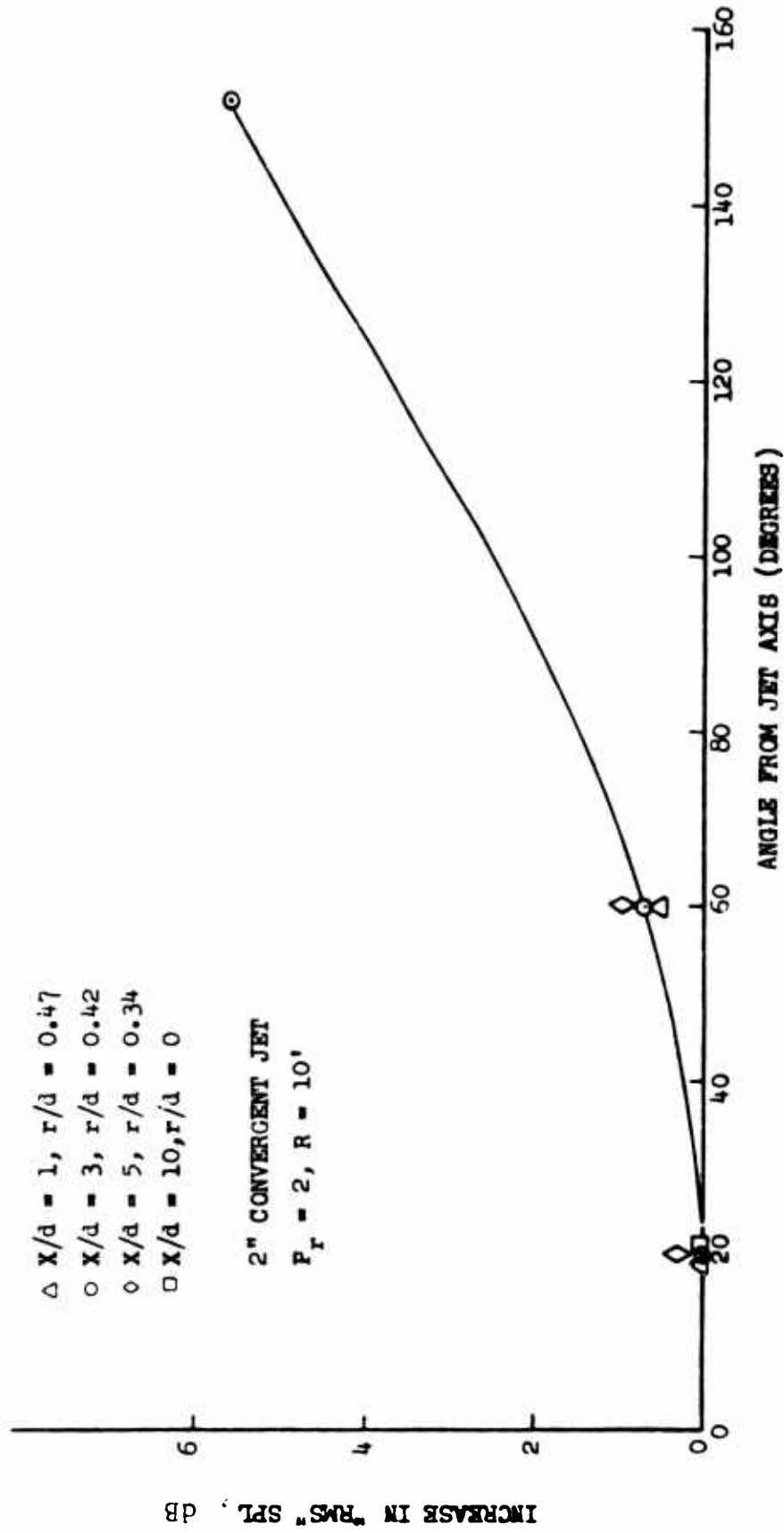


Figure 125 Probe Contamination of Far-Field SPL versus Far-Field Microphone Position

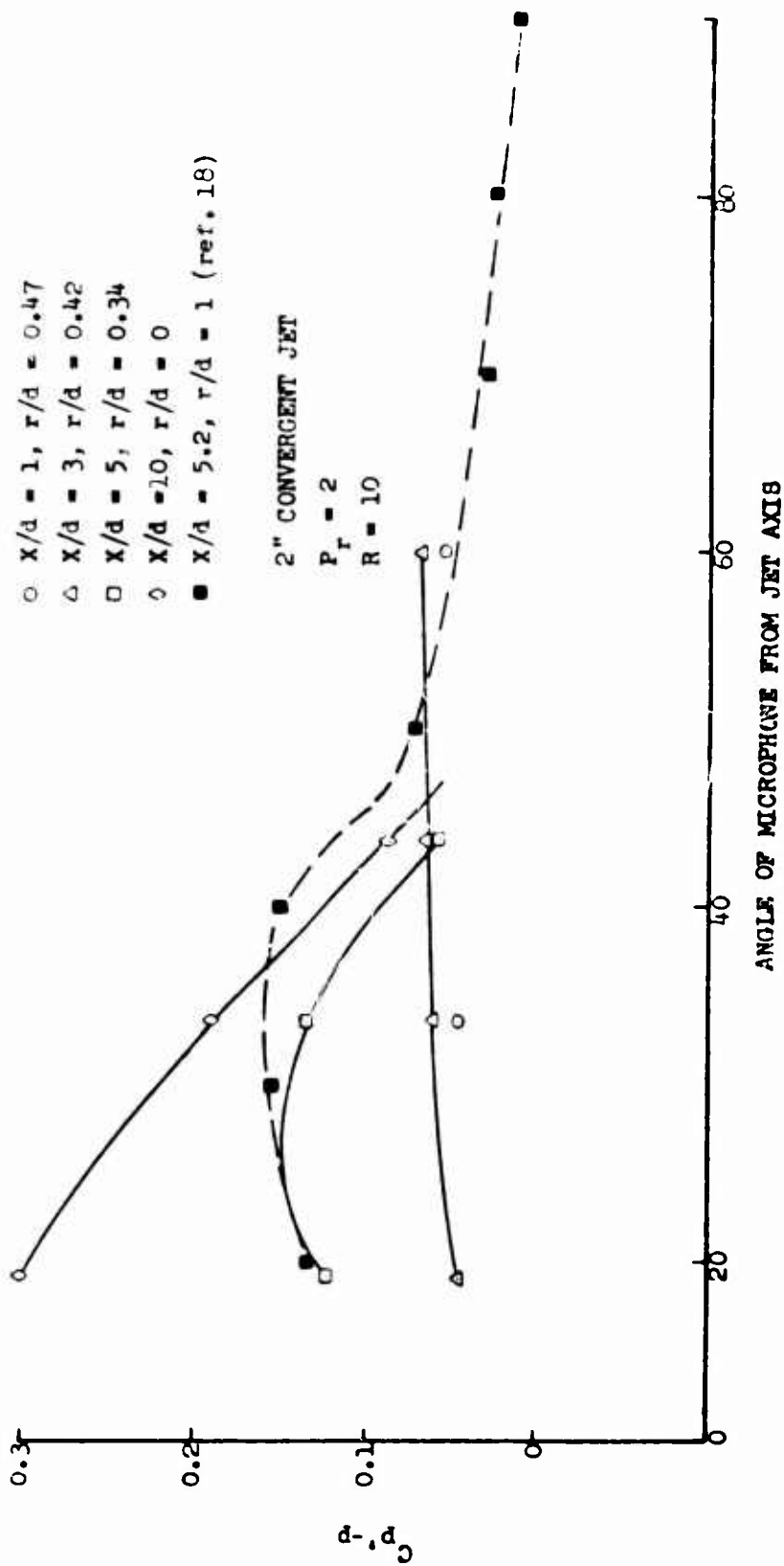


Figure 126 Normalized Cross-Correlation of In-Jet Microphone with Far-Field Microphone
 In-Jet Microphone at Point of Peak "RMS" Signal

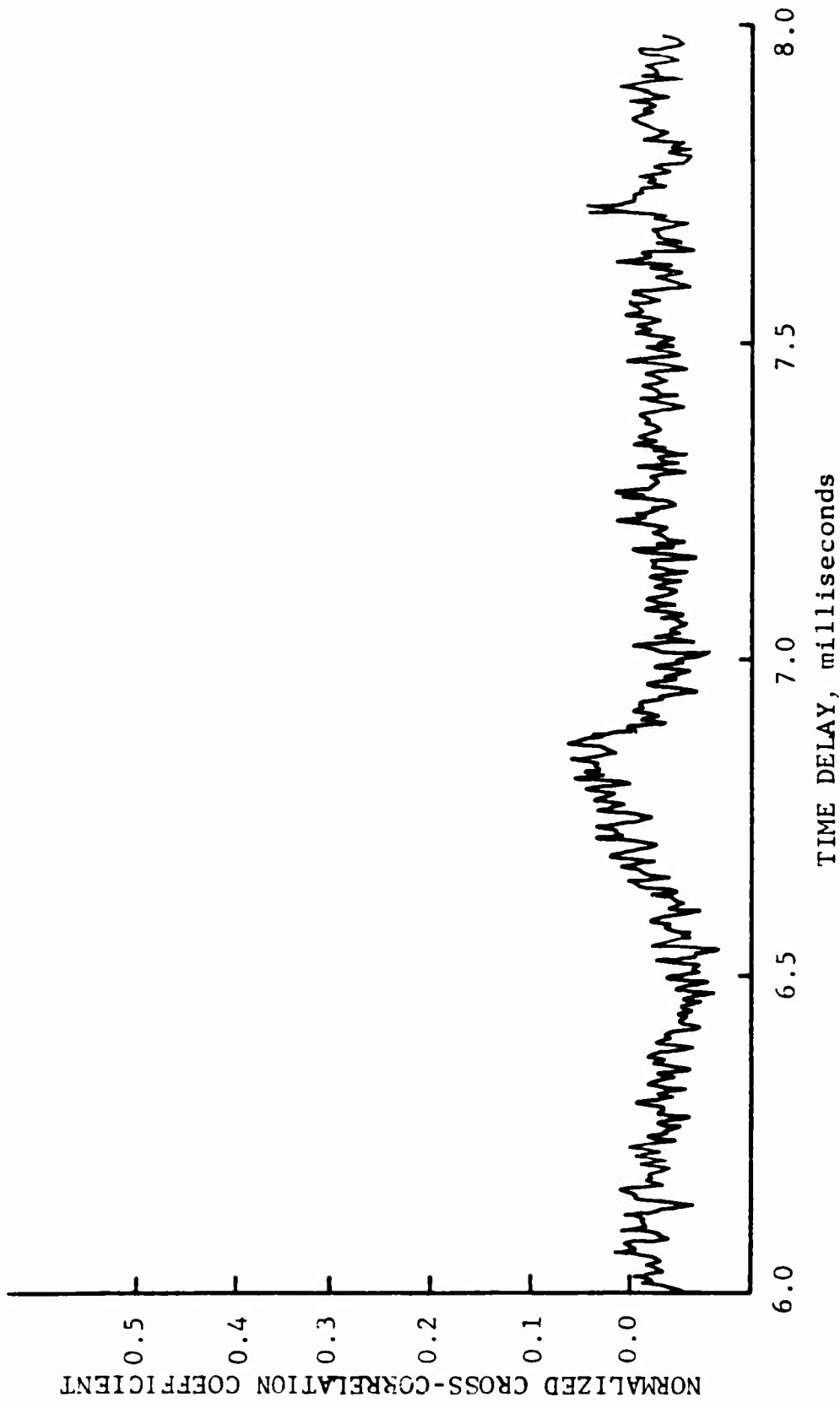


Figure 127 Unfiltered Cross-Correlation of In-Jet Microphone and Far-Field Microphone:
 2 in. Diameter Convergent Jet at Pr = 2, In-Jet at X = 20 In. on Centerline;
 Far-Field at R = 10 ft. 43.8° from Centerline

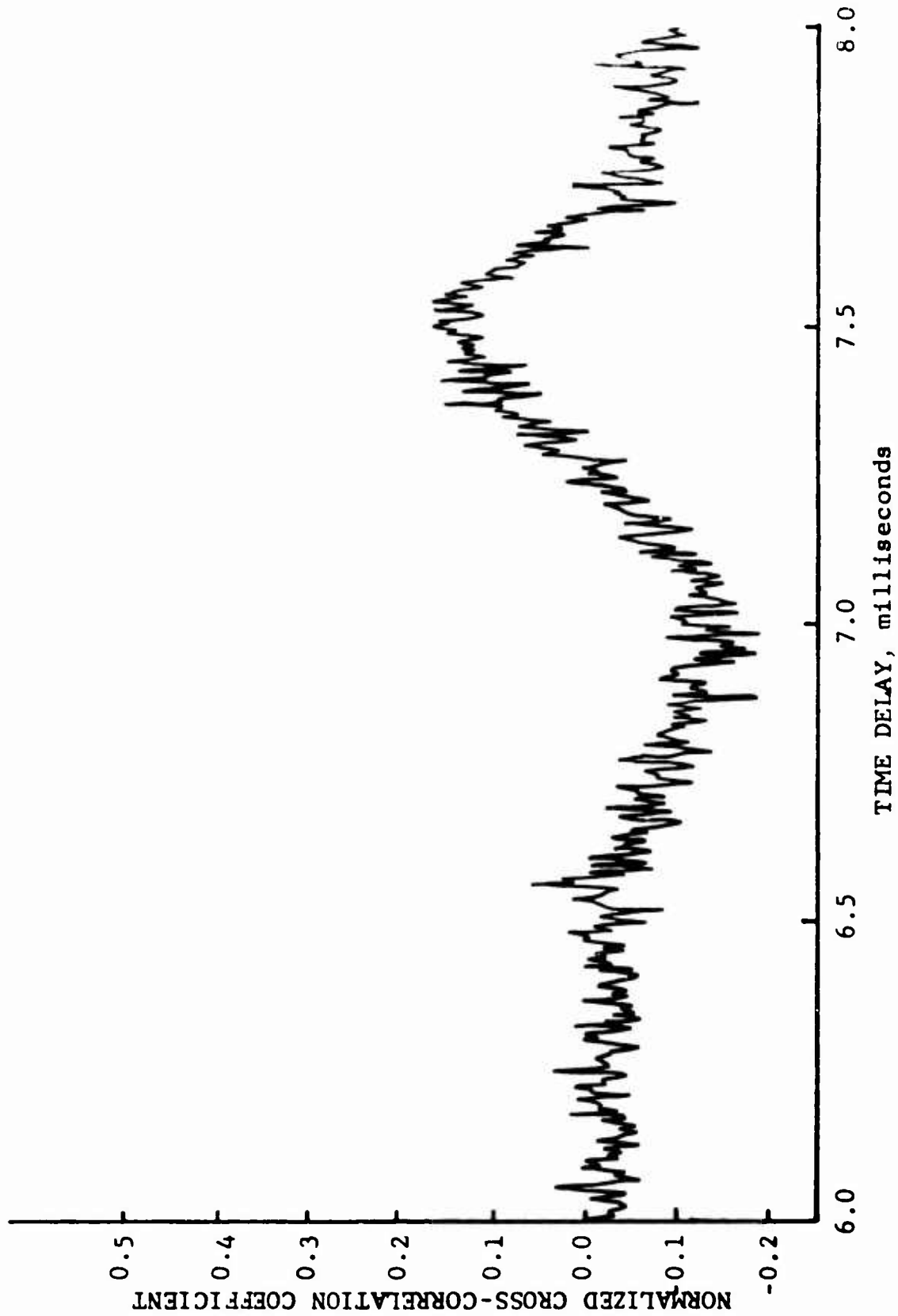


Figure 128 Unfiltered Cross-Correlation of In-Jet Microphone and Far-Field Microphone:
 2 in Diameter Convergent Jet at Pr = 2, In-Jet at X = 20 In. on Centerline,
 Far-Field at R = 10 ft. 33.6° from Centerline

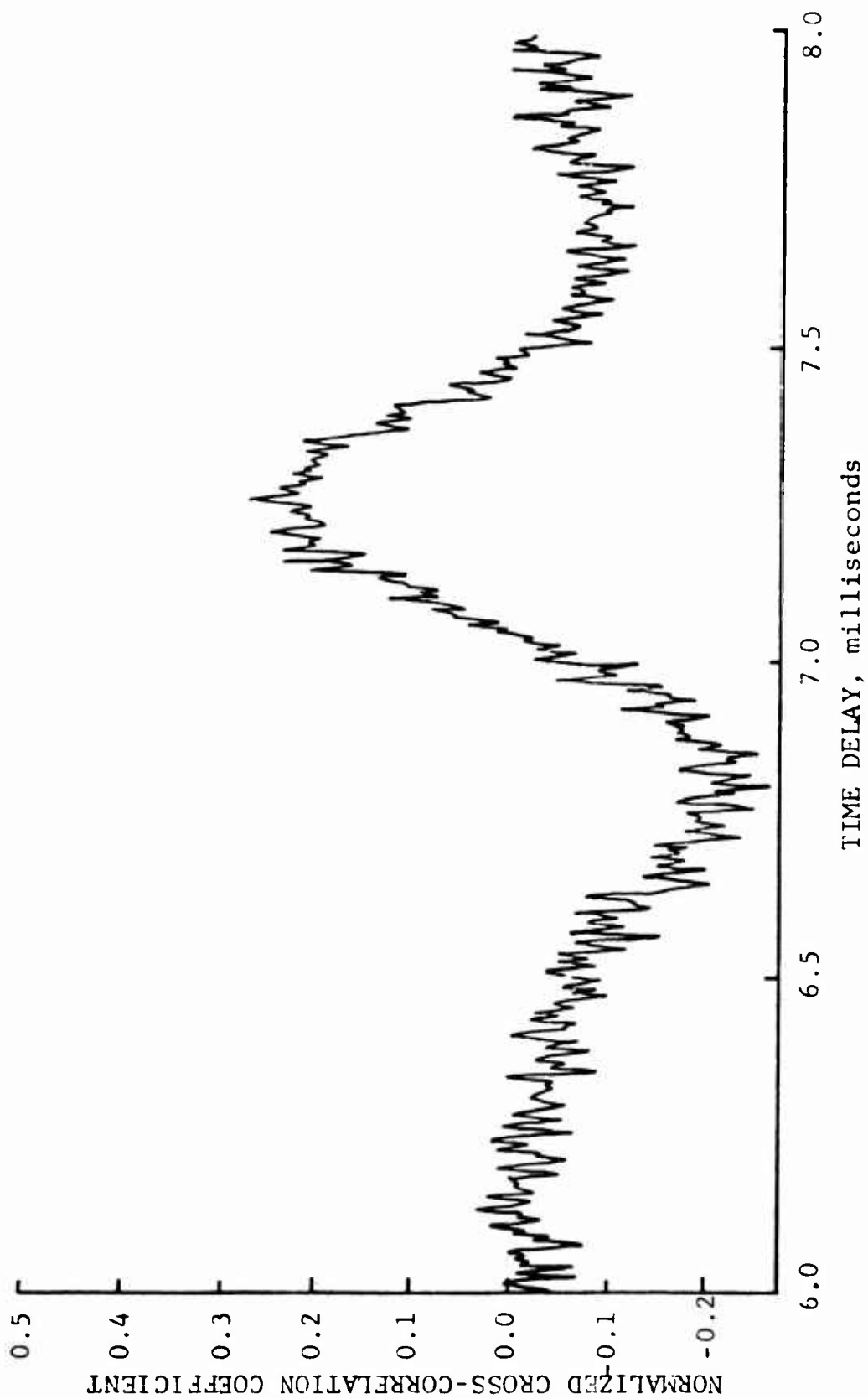


Figure 129 Unfiltered Cross-Correlation of In-Jet Microphone and Far-Field Microphone:
 2 in. Diameter Convergent Jet at $Pr = 2$, In-Jet at $X = 20$ in. on Centerline,
 Far-Field at $R = 10$ ft. 19.1° from Centerline

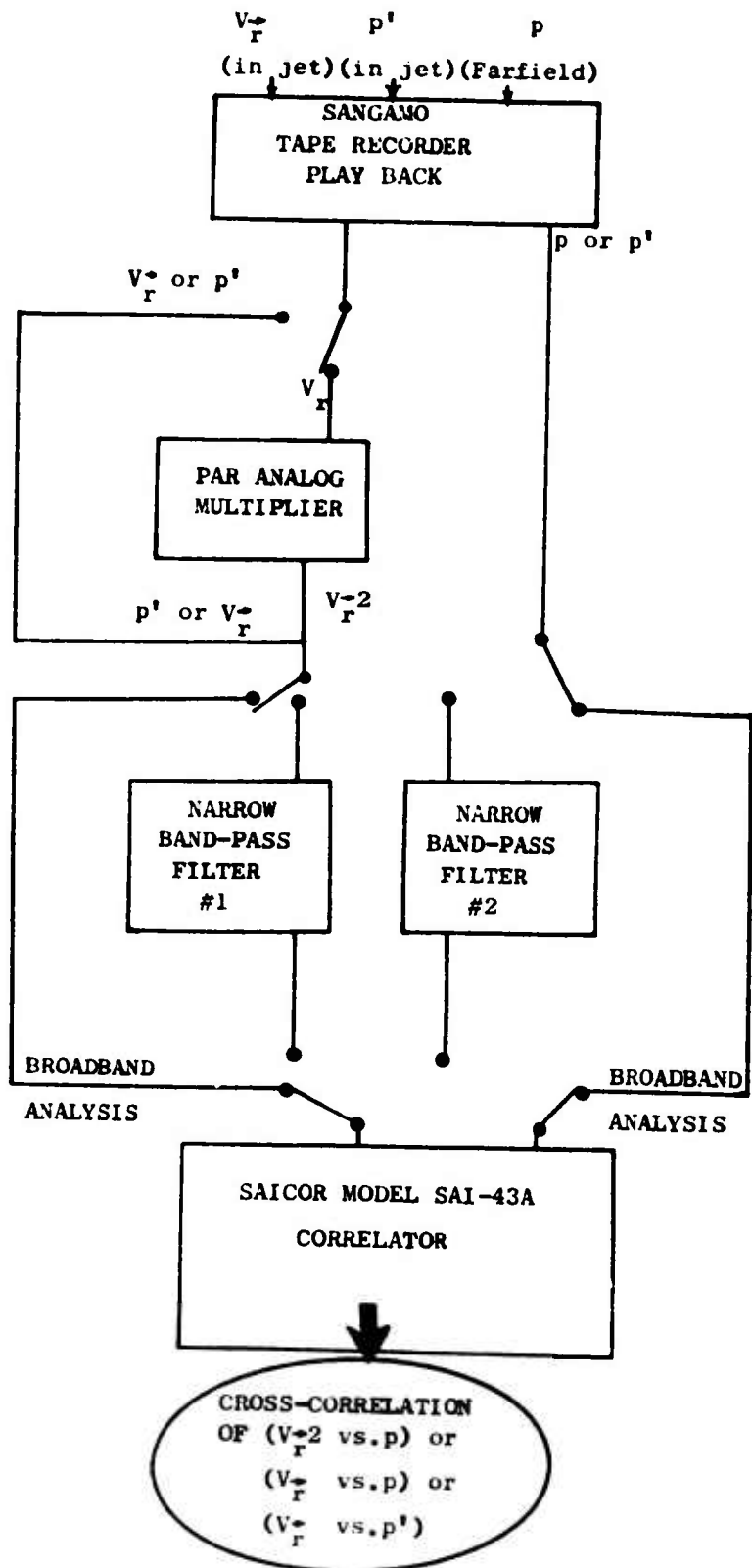


Figure 1.30 Block Diagram for the Cross-Correlation Measurements

2" CONVERGENT JET

M = 0.8 X/d = 3
r/d = 0.355

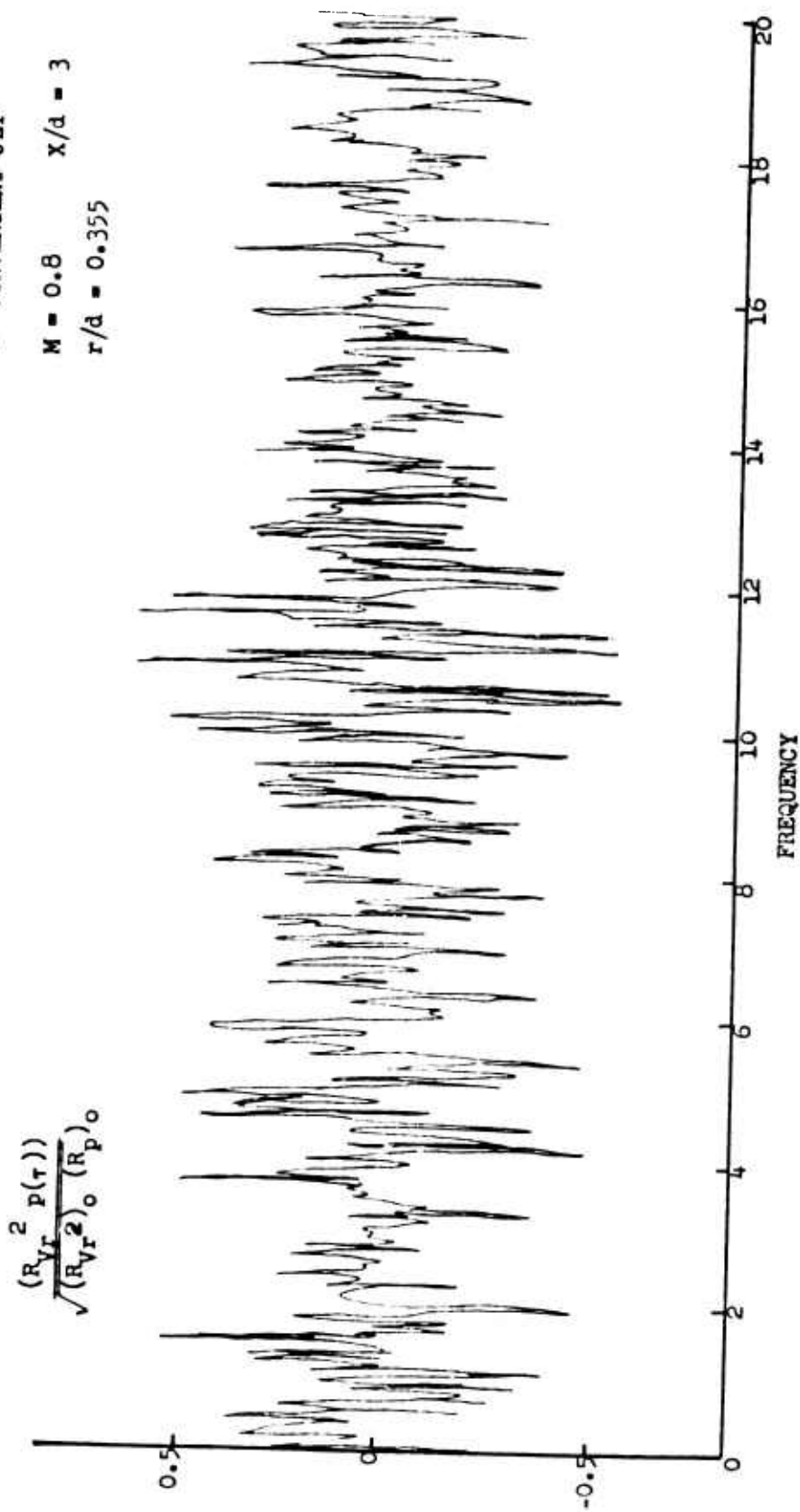


Figure 131 Normalized Cross-Correlation of V_r^2 and Far-Field Acoustics

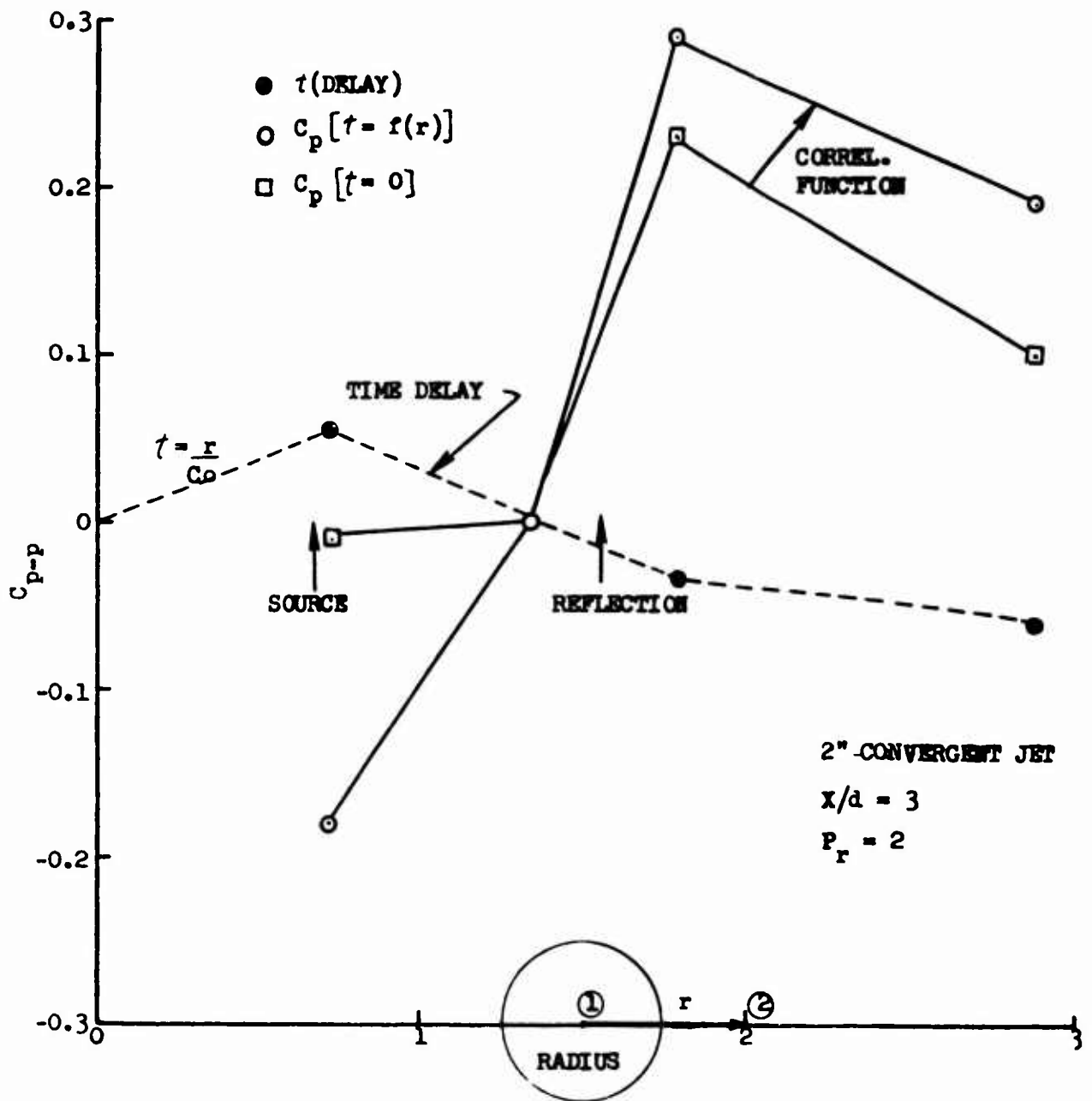


Figure 132 Normalized Cross-Correlation Coefficient for In-Jet Microphones

2" CONVERGENT JET
 $X/d = 3, r = 0.711$
 $P_r = 2$

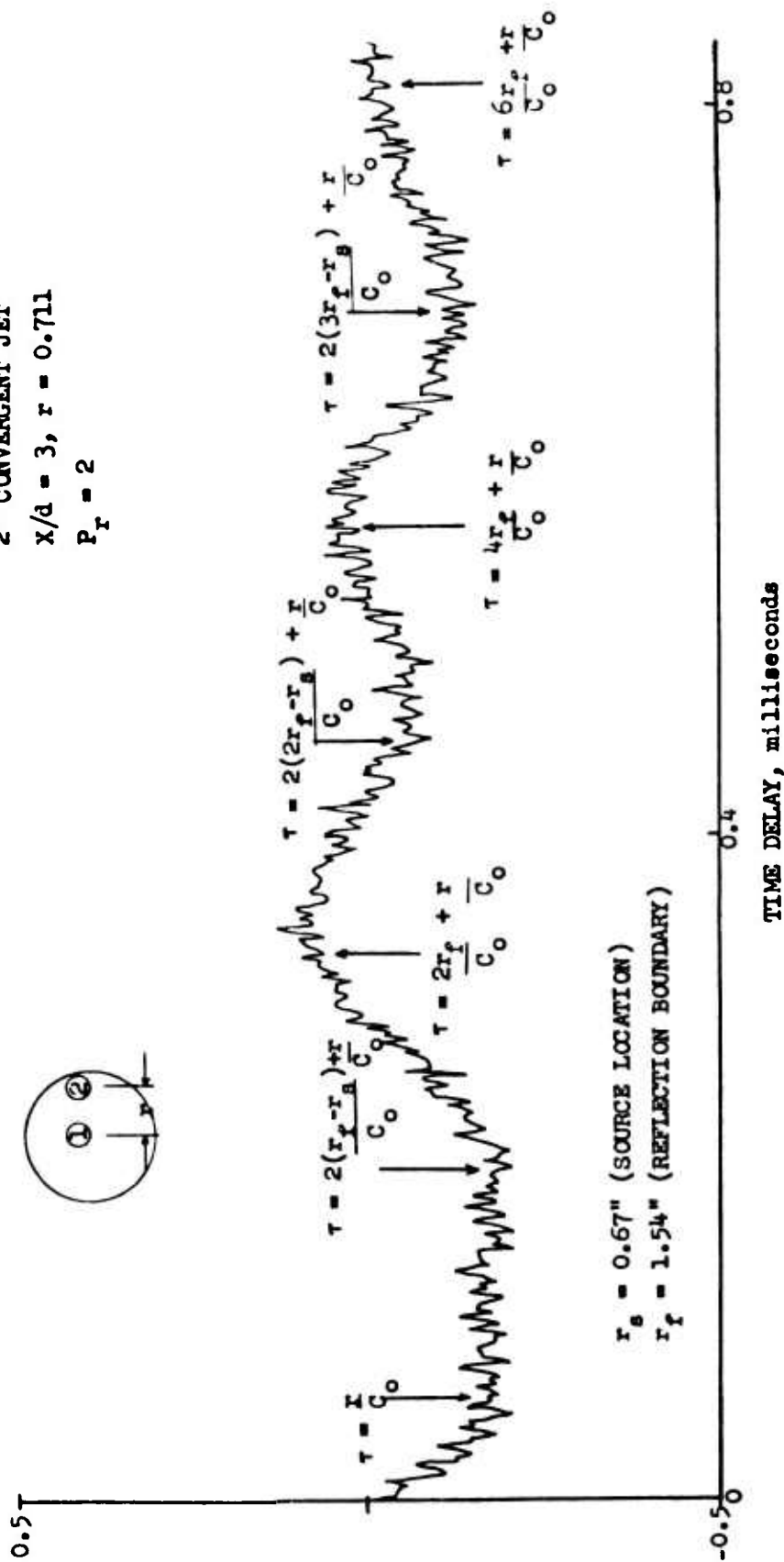


Figure 133 Radial Cross-Correlation Function

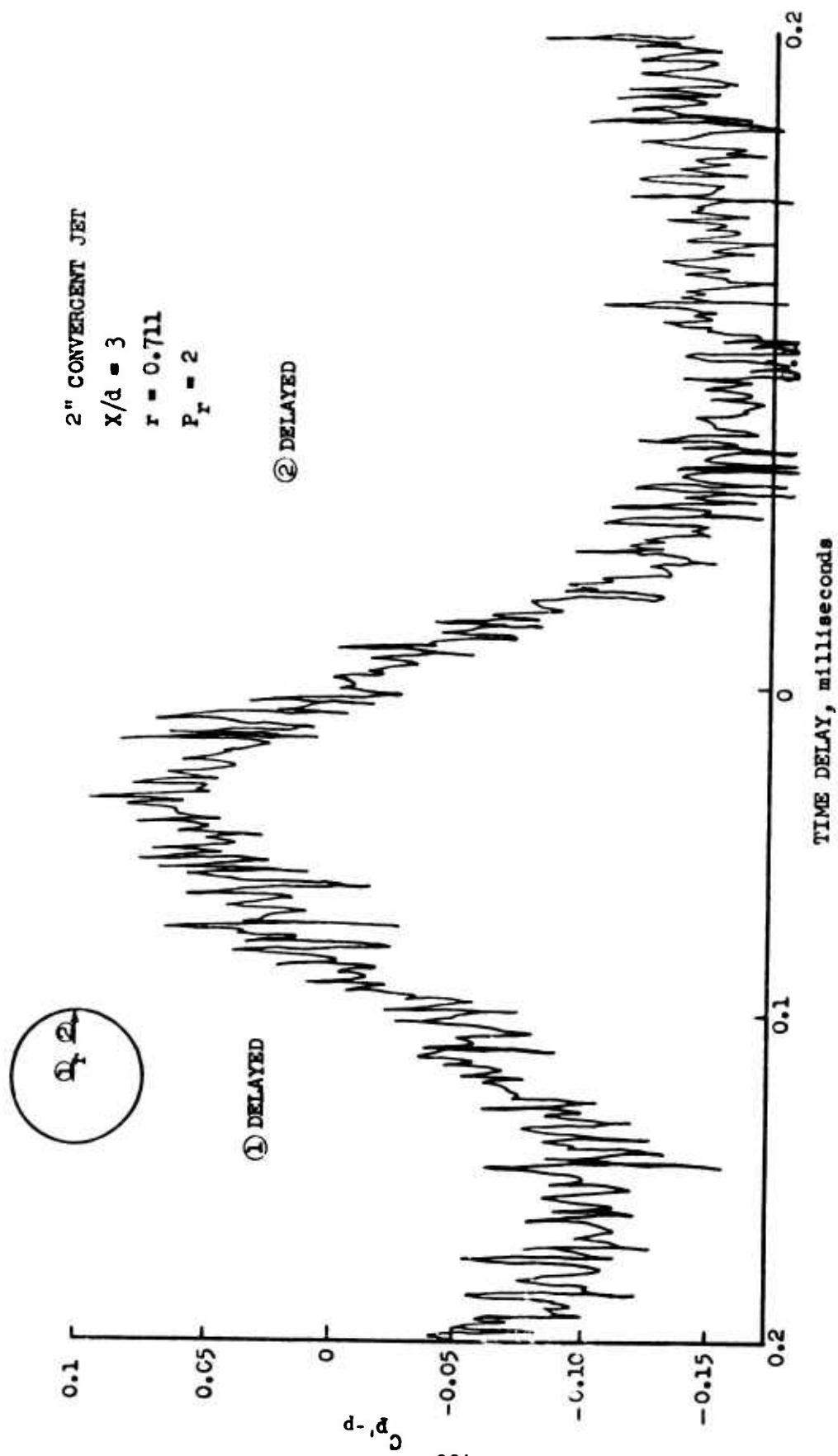


Figure 134 Radial Cross-Correlation Function

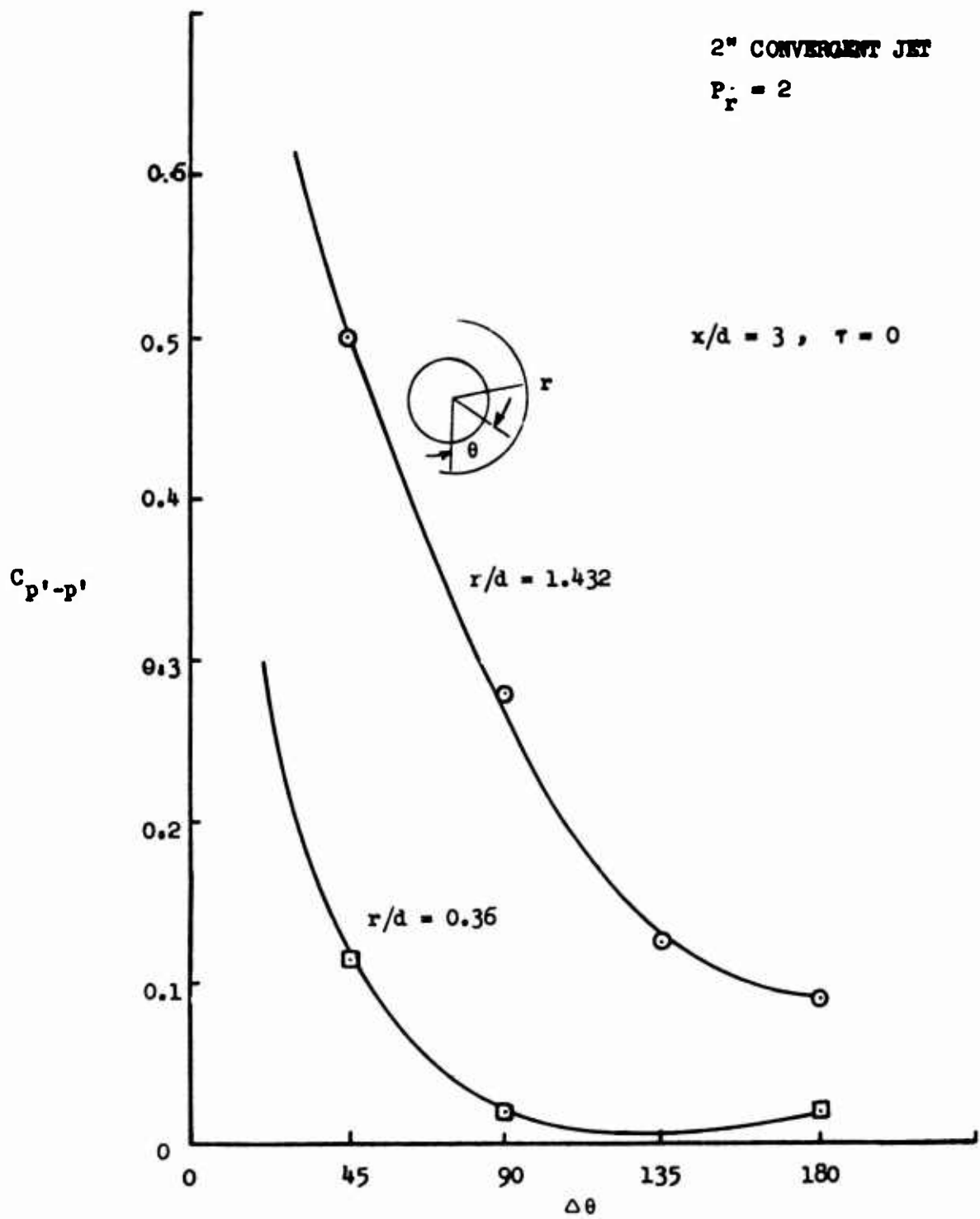


Figure 135 Circumferential Cross-Correlation Unfiltered Microphone

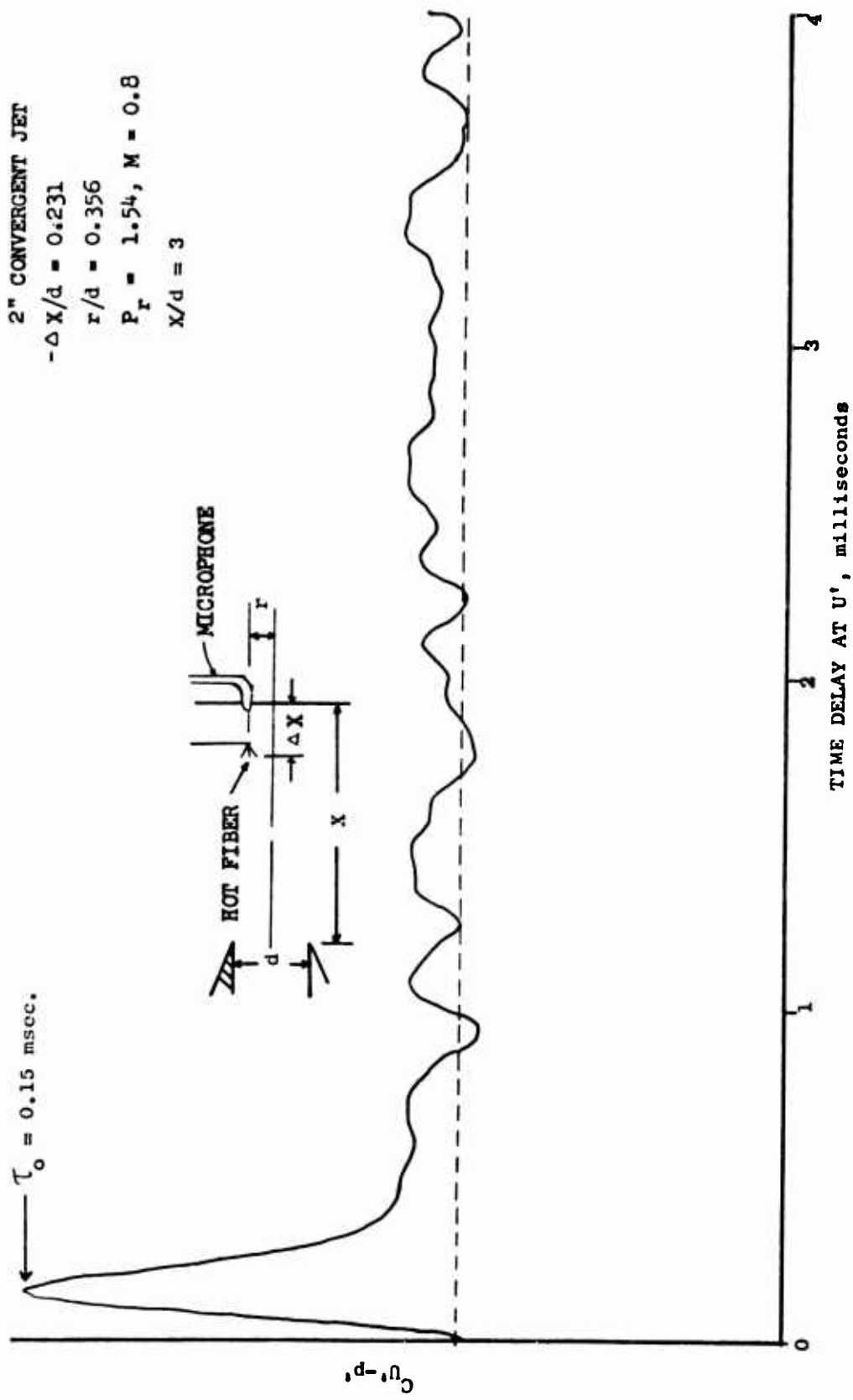


Figure 136 Normalized Cross-Correlation Function of Unsteady Velocity, U' , and Jet Pressure, p'

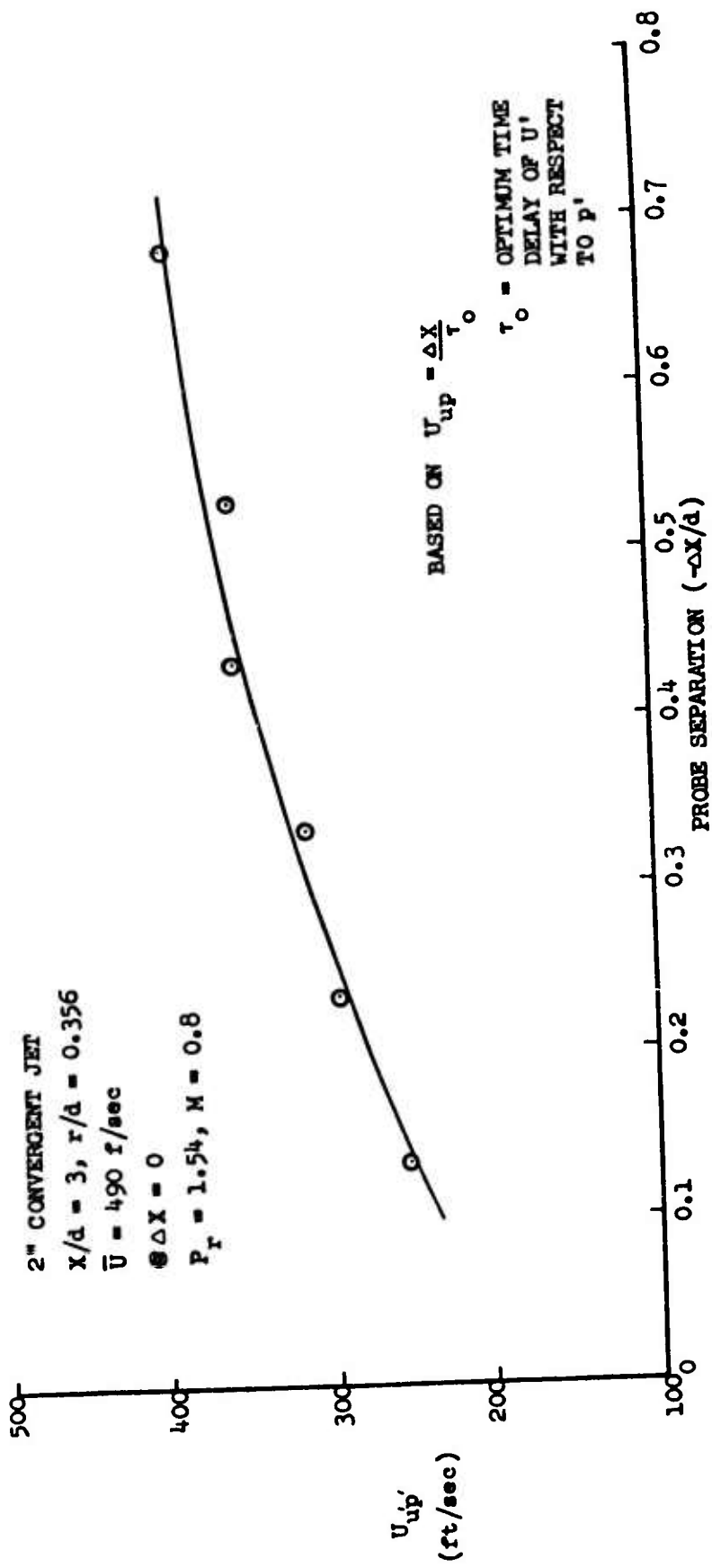


Figure 137 Eddy Convection Velocity as a Function of Probe Separation

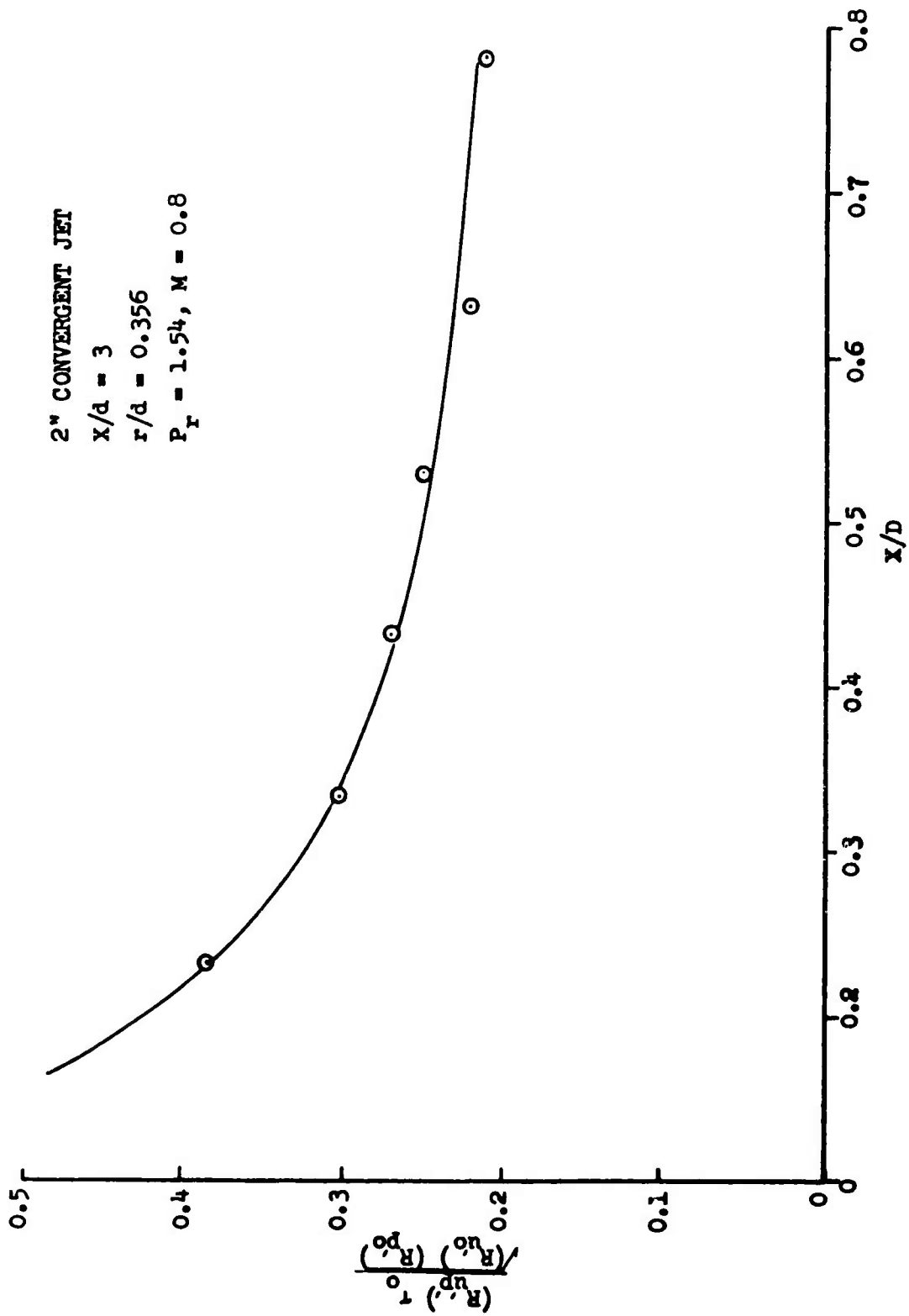


Figure 138 Axial Cross-Correlation Coefficient of Unsteady Velocity, U' , and Jet Pressure, p'

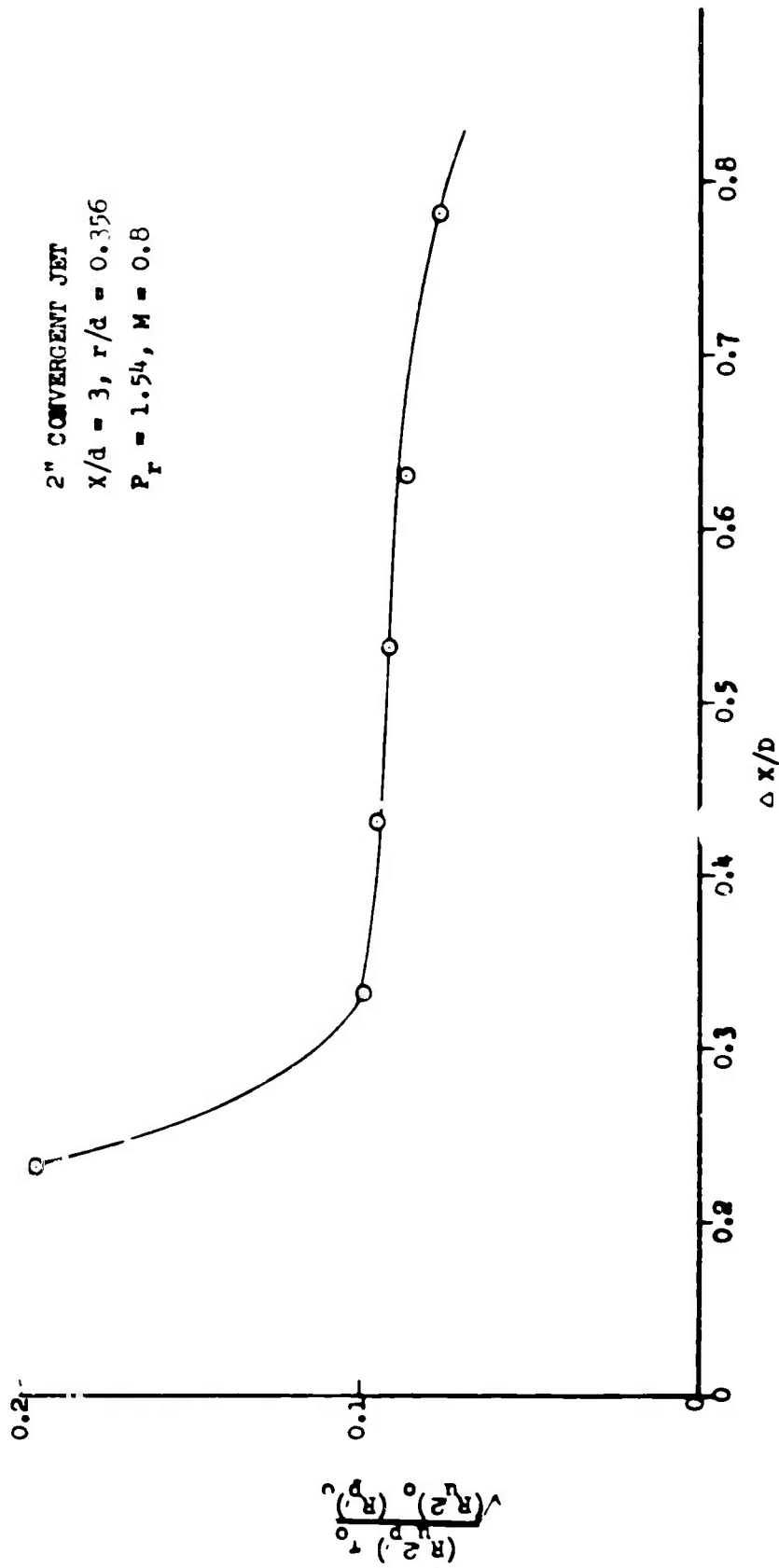


Figure 139 Axial Cross-Correlation Coefficient of Unsteady Velocity Squared, U'^2 , and Jet Pressure, p'

REFERENCES I

1. Rotta, J., "Statistical Theory of Non-homogeneous Turbulence," Part II, NASA TT FF-11, 696, June 1968.
2. Glushko, G.S., "Turbulent Boundary Layer on a Flat Plate in an Incompressible Fluid," NASA TTF-10, 080, 1965.
3. Spalding, D.B., and Patankar, S.V., Heat and Mass Transfer in Boundary Layers, Morgan-Grampian: London, 1967.
4. Heck, P.H., and Ferguson, D.R., "Analytical Solution for Free Turbulent Mixing in Compressible Flows," AIAA Paper 71-4, 1971.
5. Heck, P.H., and Merkle, C.L., Analytical Flow Field Analyses for Compressible Turbulent Jets. Chap. 1 of "Supersonic Jet Exhaust Noise," Benzakein, M.J., and Knott, P.R., eds., AFAPL-TR-72-52, Air Force Aero Propulsion Lab., Wright-Patterson AFB, Ohio, August, 1972.
6. MacCormack, R.W., and Paullay, A.J., "Computational Efficiency Achieved by Time Splitting of Finite Difference Operators," AIAA Paper 72-154, 1972.
7. Knott, P.R. and Benzakein, M.J., "Analytical and Experimental Supersonic Jet Noise Research," AIAA Paper 73-188, January, 1973.
8. Ribner, H.S., "Connection of a Pattern of Vorticity Through a Shock Wave," NACA TN 1164, 1954.
9. Ribner, H.S., "Shock Turbulence Interaction and the Generation of Noise," NACA TN 1233, 1955.
10. Ribner, H.S., "Acoustic Energy Flux from a Shock-Turbulence Interaction", J. Fluid Mech., Volume 35, p. 299, 1969.
11. Simcox, C.D. "Effect of Temperature and Shock Structures on Choked Jet Noise Characteristics," AIAA Paper 71-582, 1971.
12. Chan, Y.Y., "A Simple Model of Shock Cell Noise Generation and its Reduction," NRC (CANAOA) Aero. Rept. LR-564, October, 1972.

13. Love, E.S., Grigsby, C.E., Lee, L.P., Woodling, M.J., **Experimental and Theoretical Studies of Axisymmetric Free Jets,** NASA TR-R-6, 1959.
14. Oswatitsch, K., Gas Dynamics, New York: Academic, 1956.
15. Abbett, M., "The Mach Disc in Underexpanded Exhaust Plumes," AIAA Paper: 70-231, 1970.
16. Averenkova, G.I., Ashratov, E.A., and Volkonskaia, T.G., "Investigation of the Parameters of Axisymmetric Underexpanded Ideal Gas Jets," *Vychislitelnye Metody: Programmirovaniye*, No. 15, Moscow Univ. Press pp. 92-101, 1970.
17. Fox, J.H. "On the Structure of Jet Plumes," AIAA J. V12 No. 1, p. 105, January, 1974.

REFERENCES II

1. Phillips, O.M., "On the Generation of Sound by Supersonic Turbulent Shear Layers," *J. Fluid Mech.*, 9, pp. 1-28 (1960).
2. Morse, P.M. and Ingard, K.U., Theoretical Acoustics. New York: McGraw-Hill. See pages 728-732 (1968).
3. Csanady, G.T., "The Effect of Mean Velocity Variations on Jet Noise," *Journal of Fluid Mechanics*, 26, pp. 183-197 (1960).
4. Lush, P.A., "Measurements of Subsonic Jet Noise and Comparison with Theory," *Journal of Fluid Mechanics*, 46, pp. 477-500 (1971).
5. Kari, R., "A Moving Source Problem Relevant to Jet Noise," *Journal of Sound and Vibration*, 25, pp. 337-347 (1972).
6. Mrofey, C.L. and Tanna, H.K., "Sound Radiation from a Point Force in Circular Motion," *Journal of Sound and Vibration*, 15, pp. 325-351 (1971).
7. Eversman, W. and Beckemeyer, R.J., "Transmission of Sound in Ducts with Thin Shear Layers - Convergence to the Uniform Flow Case," *Journal of the Acoustical Society of America*, 52, #1 (Part 2), p. 216 (1972).
8. Ribner, H.S., "Reflection, Transmission and Amplification of Sound by a Moving Medium," *Journal of the Acoustical Society of America*, 29, p. 435 (1957).
9. Miles, J.W., "On the Reflection of Sound at an Interface of Relative Motion," *Journal of the Acoustical Society of America*, 29, p. 226 (1957).
10. Batchelor, G.K. and Gill, A.S., *Journal of Fluid Mechanics*, 14, p. 529.
11. Landahl, M.J., *J. Fluid Mech.*, 29, 441.
12. Lighthill, M.J., "Jet Noise," *American Institute of Aeronautics and Astronautics Journal*, 1, pp. 1507-1517 (1963).
13. Bishop, K.A., *J. Fluid Mech.*, 50, 21.
14. Ribner, H.S., "Aerodynamic Sound from Fluid Dilatations: A Theory of Sound from Jets and Other Flows," University of Toronto, Institute for Aerospace Studies, Rept. 86 (AFOSR TN 3430) 1962.

15. Hoch, R.G., et al., "Studies of the Influence of Density on Jet Noise," presented at the First International Symposium on Air Breathing Engines, Marseille, France, June 19-23, 1972.
16. Rollin, V.G., NACA TN 4217 (1958).
17. Pao, S.P., "Rocket Noise Prediction Model Using the Phillips Theory," UAI Report, University of Alabama in Huntsville, September, 1973.
18. Pao, S.P. "Aerodynamic Noise Emission from Turbulent Shear Layers," J. Fluid Mechanics, July, 1973.

REFERENCES III

1. Hoch, R.G. et al., "Studies of the Influence of Density on Jet Noise," Presented at the First International Symposium on Air Breathing Engines (June 1972).
2. Bhat, W., Jaeck, C., "A Study of the Effect of Density Variations on Clean Jet Noise," Boeing D6-40604 (October 1972).

REFERENCES IV

1. Blackman, R.B., Tukey, J.W., The Measurement of Power Spectra, Dover Publications, New York (1958).
2. Enochson, L.D., Ontes, R.K., Programming and Analysis for Digital Time Series Data, Shock and Vibration Center, U.S. Dept. of Defense (1968).
3. Balakrishnan, A.V., "On the Problem of Time Jitter in Sampling," IRE Transactions on Information Theory, April 1962 (p. 226-236).
4. Benzakein, M.J., Knott, P.R., Supersonic Jet Exhaust Noise, Technical Report AFAPL-TR-72-52.
5. Fuchs, H.V., J. Sound and Vibration, 22, (3), pp. 361-378 (1972)
6. Raki, R., "Two Casualty Correlation Techniques Applied to Jet Noise," Ph.D. Thesis, University of British Columbia, April 1973.
7. Siddon, T.E., Proceedings of INTER-NOISE 1972 Conference, October 4-6, 1972, Washington, D.C., pp. 452-457.
8. Lee, H.K. and Ribner, H.S., Journal of the Acoustical Society of America, 52, pp. 1280-1290 (1972).
9. General Anemometer Catalog, Section III, Thermo-System Inc.. (1973).
10. Scharton, T.D. and White, P.H., JASA, Volume 52, No. 1 (Part 2) pp. 399-412, 1972.
11. Scharton, T.D. and Meecham, W.E., "Preliminary Experimental Investigation of the Simple Source Theory of Jet Noise," J. Acoustical Soc. of Amer., 51, pp. 383-386 (1972).
12. Planchon, H.P. and Jones, B.G., "A Study of Local Pressure Field in Turbulent Shear Flow and Its Relation to Aerodynamic Noise Generation," Stanford Symposium, March, 1973.
13. Nagamatsu, H.T., and Sheer, R.E., "Supersonic Jet Exhaust Noise," Chapter V, Technical Report AFAPL-TR-72-52 (1972).

REFERENCES IV (CONCLUDED)

14. McGregor, G.R. and Simcox, C.R., "The Location of Acoustic Sources in Jet Flows by Means of the Wall Isolation Technique," AIAA 73-1041, October, 1973.
15. Lush, P.A., "Measurements of Subsonic Jet Noise and Comparison with Theory," Journal of Fluid Mechanics, 46, pp. 477-500 (1971).
16. Ribner, H.S. and Mani, R., private communication.
17. Laurence, J.C., Intensity, Scale, and Spectra of Turbulence in Mixing Region of Free Subsonic Jet," NACA Report No. 1292, (1957).
18. Meecham, W.C. and Hurdle, P.M., AGARD Conference Pre-Print No. 131, pp. 8-1 to 8-12, Brussels, September 1973.
19. Fuchs, H.V., "Space Correlations of the Fluctuating Pressure in Subsonic Turbulent Jets," J. Sound and Vibration, (1972) 23(1), 77-99.
20. Mani, R., "A Moving Source Problem Relevant to Jet Noise," J. Sound and Vibration, 25, pp. 337-347 (1972).
21. Crow, S.C., and Champagen, F.H., "Orderly Structure in Jet Turbulence," J. of Fluid Mechanics, 48, pp. 547-591 (1971).